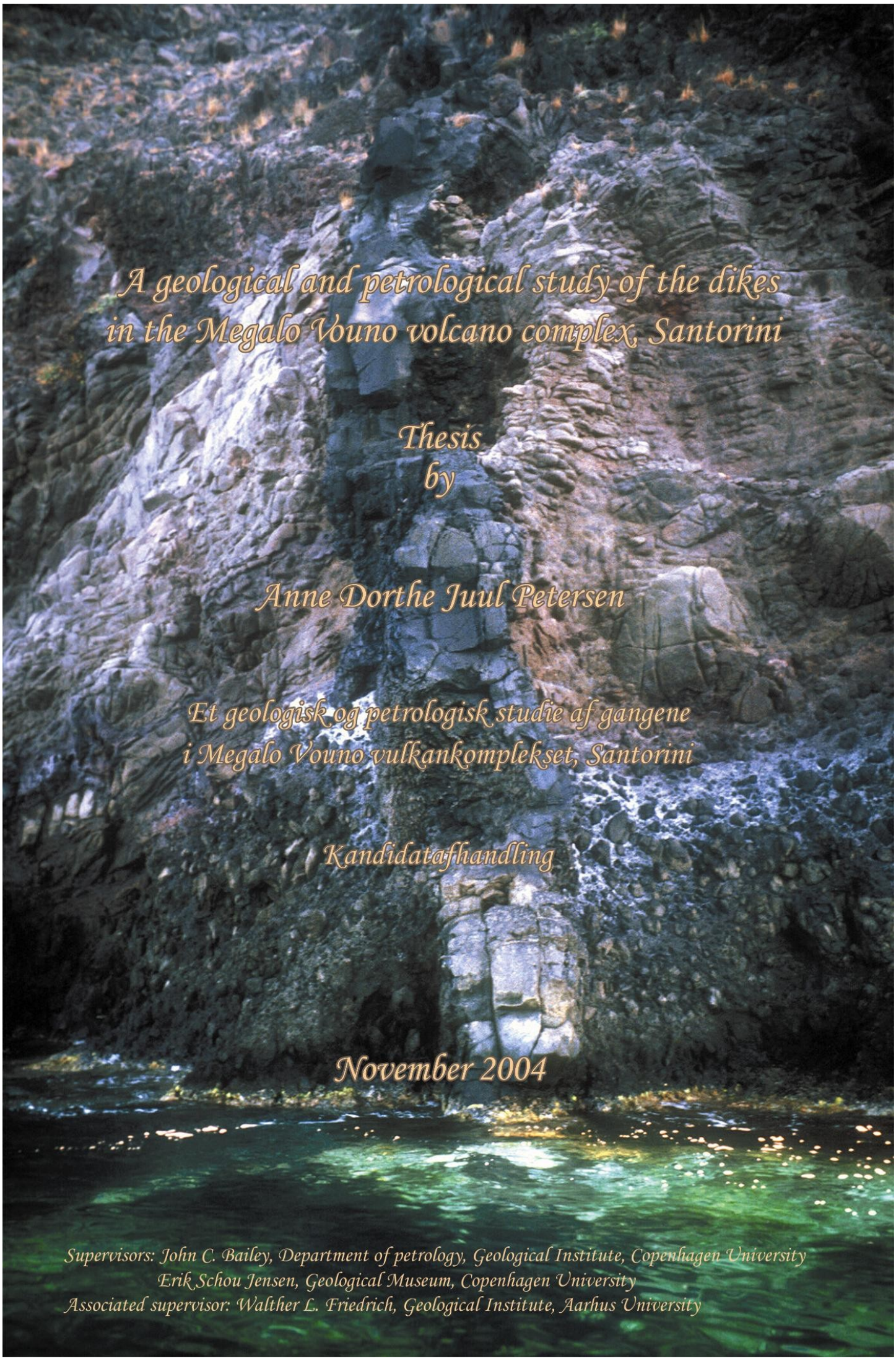

# A geological and petrological study of the dikes in the Megalo Vouno volcano complex, Santorini

Thesis
by

Anne Dorthe Juul Petersen

Et geologisk og petrologisk studie af gangene i Megalo Vouno vulkankomplekset, Santorini

Kandidatafhandling

November 2004

Supervisors: John C. Bailey, Department of petrology, Geological Institute, Copenhagen University
Erik Schou Jensen, Geological Museum, Copenhagen University
Associated supervisor: Walther L. Friedrich, Geological Institute, Aarhus University

# Table of contents

## Appendices



**+ CD-ROM with thesis in PDF**

## Abstract

Thirty-six dikes cutting through the Megalo Vouno volcano complex (northeastern Santorini, Greece) were sampled and analysed for major and trace elements. Fifteen selected dike samples were analysed for Sr, Nd and Pb isotopes along with five lava flows from the Peristeria 3 unit, sampled by Hansen (1997).

The volcanism on Santorini is a consequence of the subduction of the African plate beneath the Aegean microplate. All dikes were intruded prior to the ca. 22 ka Cape Riva eruption and the youngest dikes, cutting all the way to the top, may be related to the Thirassia-Skaros complex.

The dikes and lavas were divided into two separate groups on the basis of Sr and Nd isotopic data. The low-Nd series comprises 11 samples of basaltic to trachytic composition, varying in Sr and Nd isotopic ratios from 0.704693-0.707115 and 0.512636-0.512558, respectively. The high-Nd series is defined by seven samples, ranging from basaltic andesite to trachyandesite, displaying a variation in Sr and Nd isotopic ratios from 0.703783-0.705004 and 0.512844-0.512700, respectively. The two groupings overlap in Pb isotopic composition within the ranges: $^{206}Pb/^{204}Pb$: 18.799-18.927, $^{207}Pb/^{204}Pb$: 15.640-15.688 and $^{208}Pb/^{204}Pb$: 38.824-39.084.
Spider diagram patterns confirm the different mantle source compositions of basaltic rocks belonging to the low-Nd and high-Nd series. Four different groupings can be made on the basis of spider diagrams: low-HFSE (to which all basaltic high-Nd samples belong), medium-HFSE (no isotopic analyses), high-HFSE (to which the single analysed low-Nd basalt belongs) and a low-Th group defined by a single dike sample (plus a basaltic sample from the Second eruptive cycle collected by Zellmer (1998)). The low-Th sample has a distinct isotopic composition at low Nd and low Sr isotopic ratios, and has the highest $^{206}Pb/^{204}Pb$ and lowest $^{207}Pb/^{204}Pb$ ratios of all the studied rocks.
It was not possible to confirm whether the medium-HFSE rocks have a distinct source composition due to lack of isotopic analyses. These rocks may result from smaller degrees of melting of a low-HFSE source, or mixing between the low-HFSE and the high-HFSE source.

Despite the fact that the dikes are not comagmatic, well-defined trends on variation diagrams appear to be consistent with fractional crystallisation of olivine, clinopyroxene, plagioclase, ± orthopyroxene, ± Fe-Ti oxides. Magmatic evolution took place along both the calc-alkaline and tholeiitic differentiation trend. This is believed to be a consequence of the different source compositions possibly combined with subsequent magma mixing.

Crustal contamination contributed to the observed variation in isotopic ratios within the low-Nd and high-Nd series. Comparison with Santorini basement rock compositions indicated that the two series assimilated different upper crustal materials.

## Resumé

Seksogtredive dikes (lavagange) der gennemskærer Megalo Vouno vulkankomplekset i det nordøstlige hjørne af Santorini (Grækenland), blev indsamlet og efterfølgende analyseret for hoved- og sporgrundstoffer. Femten udvalgte prøver blev analyseret for Sr, Nd og Pb isotoper sammen med prøver af fem lavastrømme fra Peristeria 3 enheden (indsamlet af Hansen (1997)).

Vulkanisme på Santorini er en følge af subduktionen af den afrikanske plade under den ægæiske mikroplade. Samtlige dikes intruderede komplekset inden Cape Riva udbruddet (ca. 22 ka), og de yngste dikes, som skærer hele vejen igennem til toppen, kan tænkes at være relateret til Thirassia-Skaros vulkankomplekset.

Dikes og lavastrømme inddeltes i to separate grupper på basis af deres Sr og Nd isotopdata: "lav-Nd"serien omfatter elleve prøver af basaltisk til trakydacitisk sammensætning, med varierende Sr og Nd isotopratioer på henholdsvis 0.704693-0.707115 og 0.512636-0.512558. "høj-Nd"serien er defineret af syv prøver, der varierer i sammensætning fra basaltisk andesit til trakyandesit, med en variation i Sr og Nd isotopratioer på henholdsvis 0.703783-0.705004 og 0.512844-0.512700. De to grupperinger overlapper i Pb isotopsammensætning inden for intervallerne: $^{206}Pb/^{204}Pb$: 18.799-18.927, $^{207}Pb/^{204}Pb$: 15.640-15.688 og $^{208}Pb/^{204}Pb$: 38.824-39.084.

Mønstre i multigrundstofdiagrammer bekræfter, at basaltiske bjergarter tilhørende "lav-Nd" og "høj-Nd"serierne har forskellige kildesammensætninger. Fire forskellige grupperinger kan foretages på baggrund af multigrundstofdiagrammer: "lav-HFSE"(hvortil alle basaltiske "høj-Nd"prøver hører), "medium-HFSE"(ingen isotopanalyser), "høj-HFSE"(hvortil den analyserede "lav-Nd"basalt hører) samt "lav-Th"gruppen, som defineres af en enkelt dike (plus en basaltisk prøve fra den Anden Eruptive Cyklus indsamlet af Zellmer (1998)). "lav-Th"prøven adskiller sig i isotopsammensætning ved en kombination af lave Nd- og lave Sr isotopratioer, og har tilmed de højeste $^{206}Pb/^{204}Pb$ og laveste $^{207}Pb/^{204}Pb$ ratioer af alle de studerede prøver. Som følge af manglende isotopanalyser var det ikke muligt at bekræfte om "medium-HFSE"prøverne har en afvigende kildesammensætning. Det er muligt, at disse i stedet er dannet som følge af lavere grad af opsmeltning af "lav-HFSE"kilden, eller ved mixing mellem "lav-HFSE" og "høj-HFSE"kilderne.

På trods af at prøverne ikke er co-magmatiske, stemmer veldefinerede trends på variationsdiagrammer overens med bortfraktionering af olivin, klinopyroxen, plagioklas, ± orthopyroxen, ± Fe-Ti oxider. Magmatisk udvikling har fundet sted langs såvel den calc-alkaline som den tholeiitiske differentiationstrend. Dette tænkes at være en konsekvens af de forskellige kildesammensætninger, muligvis i kombination med efterfølgende magma mixing.

Efterfølgende skorpekontaminering medvirkede til de observerede variationer i isotopratioer inden for "lav-Nd" og "høj-Nd"serierne. Sammenligning med basementbjergarter fra Santorini indikerede, at de to serier assimilerede forskellige typer af skorpemateriale.

# 1. Introduction and aims

The samples collected for this study are from the Greek volcanic island Santorini, which is situated centrally in the Aegean Arc (Fig. 1.1). The volcanic island was formed in a subduction zone environment as a consequence of African oceanic lithosphere subducting beneath thinned, continental European lithosphere. Construction of several volcanic centres interrupted by violent caldera formations shaped the island as it appears today. A number of dikes cut the volcanic products of Micros Profitis Ilias, Peristeria and Megalo Vouno volcanoes in the north-eastern corner of Santorini (Fig. 1.2). Thirty-six of these dikes were sampled and investigated for the present thesis and it was tried to establish how the dikes fit in with the known geological and petrological evolution of the area.

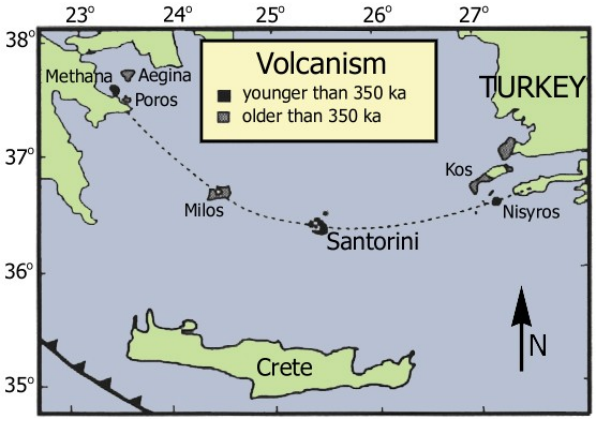


**Fig. 1.1.** Location of Santorini in the Aegean Arc, Greece. Map modified after Zellmer (1998).

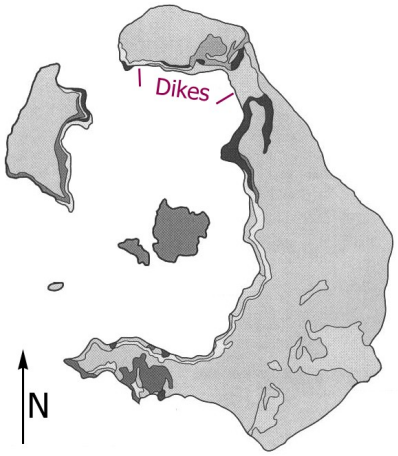


**Fig. 1.2.** Map of Santorini indicating the area in which dikes cut through the products of the caldera wall. Modified after Zellmer (1998).

Major and trace element contents plus selected isotopic ratios were determined for the sampled dikes in order to develop a better understanding of the complex evolution of the north-eastern volcanic centres on Santorini.

Hansen (1997) studied lava flows of the north-eastern volcanic centres and discovered that the products had developed along two different trends. As some of the dikes cut through these products it was interesting to determine whether the dikes can be assigned to either of these trends or if they are, perhaps, a product of unrelated younger or older activity. It was also sought to establish relations between the dikes since other scientists have suggested that they were erupted over a long period of time, and may not originate from a single magma chamber (Puchelt et al., 1990).

Many source components and processes are thought to have influenced the final volcanic products, the most important being: heterogeneous subcontinental mantle, slab fluids and sediments along with subsequent magma chamber processes involving fractional crystallisation, magma mixing and assimilation of crustal rocks. These components and processes were discussed in relation to the geochemistry of the collected dike samples.

## 2. Tectonic setting

The evolution of the Eastern Mediterranean region from the Palaeozoic up till now has been complex and there has been considerable disagreement among scientists about the evolution of the area. Several models for the opening of Neotethys in early Mesozoic have been proposed; they mainly build on palaeomagnetic data, subsidence data, and timing of stratigraphic and tectonic events. Robertson et al. (1996) compiled some of the models suggested for the reconstruction of the area in Late Permian through to the Cretaceous and these vary greatly. In the following short summary of the events that led to the present-day appearance of the Eastern Mediterranean and the Aegean area, the work of Robertson & Grasso (1995) has mainly been used, along with the most recent study by Stampfli & Borel (2002), which was based on combined stratigraphic, sedimentary, palaeontological, palaeomagnetic and palaeobiogeographical data.

### 2.1 Evolution of the Eastern Mediterranean

Palaeotethys opened as a back-arc basin around 420 Ma ago, and through much of the Palaeozoic and Mesozoic this large ocean basin was sited between Gondwana and Laurussia, a part of it covering the area which is now the Eastern Mediterranean (Fig. 2.1.A).

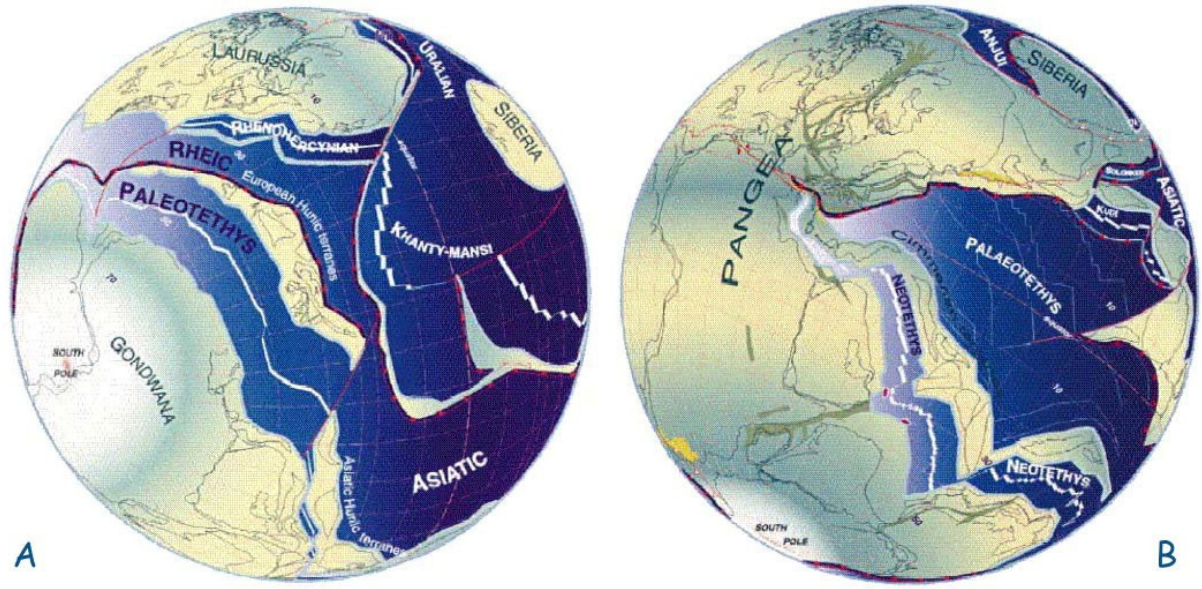


**Fig. 2.1.** Orthographic projections by Stampfli & Borel (2002) with Europe fixed in its present-day position.
***A)*** Opening and widening of Palaeotethys here shown ca. 400 Ma ago. Palaeotethys opened as a back-arc basin between Gondwana and Laurussia due to slab roll-back of the Rheic and Asiatic oceans (Stampfli & Borel, 2002). The Hunic terranes drifted northwards leading to the Variscan orogeny in Europe and finally closed the Rheic Ocean around 340 Ma ago. The projection is centred 10N/20E.
***B)*** Opening of Neotethys here shown around 260 Ma ago. See text for further explanation. The projection is centred 20N/20E.

Palaeotethys was finally closed in the Late Triassic-Early Jurassic as a result of the opening of Neotethys that began in the Late Carboniferous. This opening, and the resulting closure, is thought to be associated with the Cimmerian terranes that detached from the north Gondwanan margin and drifted northwards, thereby opening Neotethys to the south. Subduction of Palaeotethys under the present Eurasia is thought to have created enough slab pull to initiate the rifting process (Fig. 2.1.B).

Neotethys existed through much of the Mesozoic but commenced closure when subduction of the Neotethyan northern margin began around 195 Ma ago. This subduction created a slab-pull force that is thought to have contributed to the opening of the central Atlantic Ocean and the break-up of Pangea in the Early Jurassic (Fig. 2.2.C). Later the subduction of the Neotethyan mid-oceanic ridge influenced the break-up of Gondwanaland, which began around 130 Ma ago. Since the Late Jurassic, Africa and Eurasia have been converging and the Neotethyan ocean basins in the Mediterranean have progressively been eliminated (Fig. 2.2.D). Garfunkel (1998) argued that spreading in the easternmost Mediterranean was active until mid-Cretaceous, and suggested a maximum age of 90-92 Ma for the onset of convergence. According to Faccenna et al. (2001) Africa has been slowly converging toward stable Eurasia on a NNE path at an average of about 1-2 cm/year for the past 80 Ma, changing to a more northerly path around 40 Ma ago.

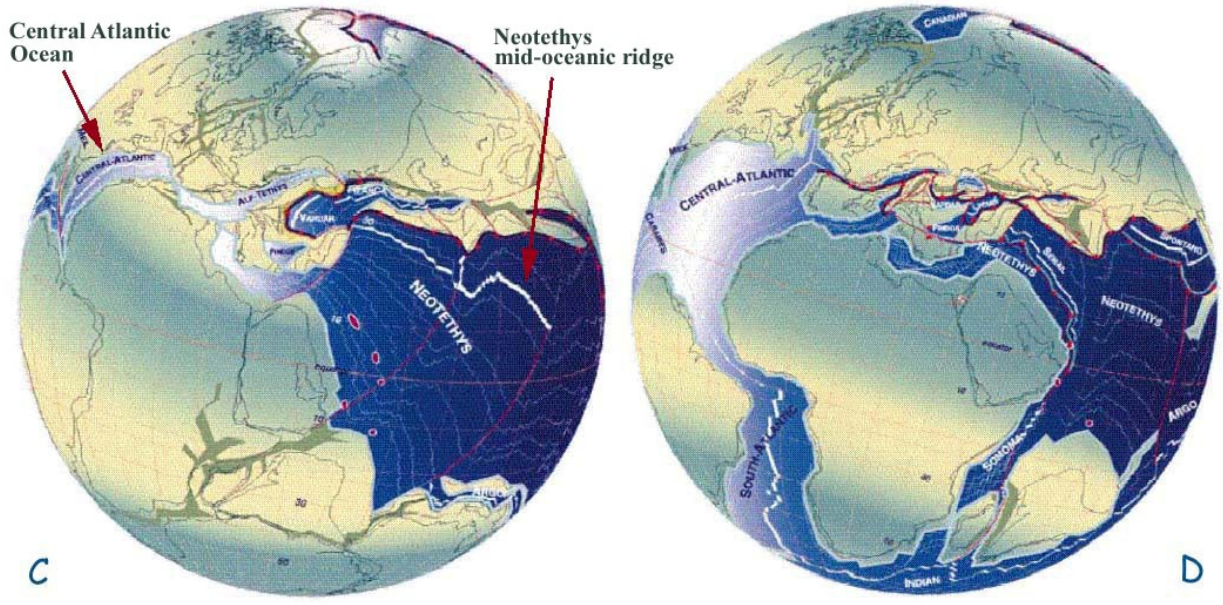


**Fig. 2.2.** Orthographic projections by Stampfli & Borel (2002) with Europe fixed in its present-day position.
***C)*** The consumption of Neotethys here shown around 156 Ma ago. Processes thought to have led to the break-up of Pangea are discussed in text. The projection is centred 20N/20E.
***D)*** Break-up of Gondwanaland and convergence between present-day Africa and Europe here shown around 85 Ma ago. Further explanation in text. The projection is centred 20N/20E.

A complex history of opening and closure of several ocean basins, together with rifting and movement of associated microcontinents, is thought to have dominated the Eastern Mediterranean through the Mesozoic and Cenozoic.

During the Tertiary, subduction zones were developed in the Western and Eastern Mediterranean. The subducting plate beneath the Eastern Mediterranean is thought to be Neotethyan oceanic crust, but according to Robertson & Grasso (1995) the slab being subducted at present could be highly thinned North Africa-related continental crust. New seismic data, on the other hand, suggest that the subducted slab is purely oceanic, and that the slab being subducted in the Hellenic Trench today is oceanic African lithosphere (Bohnhoff et al., 2001). During the Late Mesozoic-Early Tertiary, collisional belts such as the Taurides, Hellenides, Albanides and Dinarides were formed in southern Europe, and in mid-Tertiary the just formed eastern subduction zone began to migrate southwards and back-arc extension increased its southward curvature (Kissel & Laj, 1988). These processes gave rise to the present-day plate boundaries in the Eastern Mediterranean (Jackson, 1994; Robertson & Grasso, 1995).

## 2.2. The Aegean area

Santorini and the Aegean Arc are located within the Aegean microplate, which was first delineated by McKenzie (1970). Its boundaries are defined by the Kephalonia Fault zone (KF) in the west, the North Anatolian Fault zone (NAF) in the north and the Hellenic Trench (HT) in the south (Fig. 2.3). The Hellenic Trench system is composed of several individual trenches: Ionian, Matapan, Gortys and Poseidon in the west and Ptolemeus, Pliny and Strabo in the east (Fig. 2.8). To the east the border of the Aegean microplate is defined by earthquakes (Jackson, 1994).

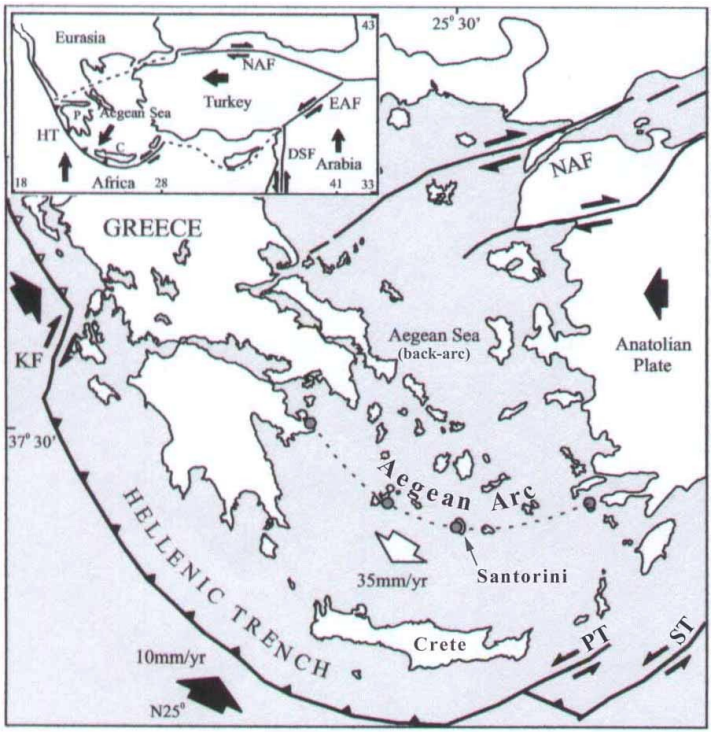


**Fig. 2.3.** Plate movements in the Aegean area showing the convergence between Africa and stable Eurasia, the northward movement of the Arabian plate exerting pressure upon the Anatolian Plate (inset), and some of the most prominent morphological features. The Aegean Arc is shown together with the best defined fault systems in the area: Kephalonia Fault zone (KF), North Anatolian Fault zone (NAF), Hellenic Trench (HT) and the easternmost faults of the Hellenic Trench: Pliny (PT) and Strabo (ST) trenches. The back-arc area comprises the extensional region in the Aegean Sea, north of the Aegean Arc. Inset abbreviations: DSF: Dead Sea Fault, EAF: East Anatolian Fault and P: Peloponnese. Filled circles indicate volcanic centres of the Aegean Arc. Modified after Doutsos & Kokkalas (2001).

Further northeast the Aegean microplate seems to amalgamate with Turkey and the only visible boundary in the east is the East Anatolian Fault (EAF) (Fig. 2.3 (inset)).
The southernmost part of the Aegean microplate is moving southwest (with respect to Eurasia) at ca. 32-35 mm/year (e.g., McKenzie, 1970, 1978; Jackson, 1994; Kahle et al., 1998) overriding the subducting African plate which is in turn moving in a north-easterly direction at ca. 10-11 mm/year (Jackson 1994).

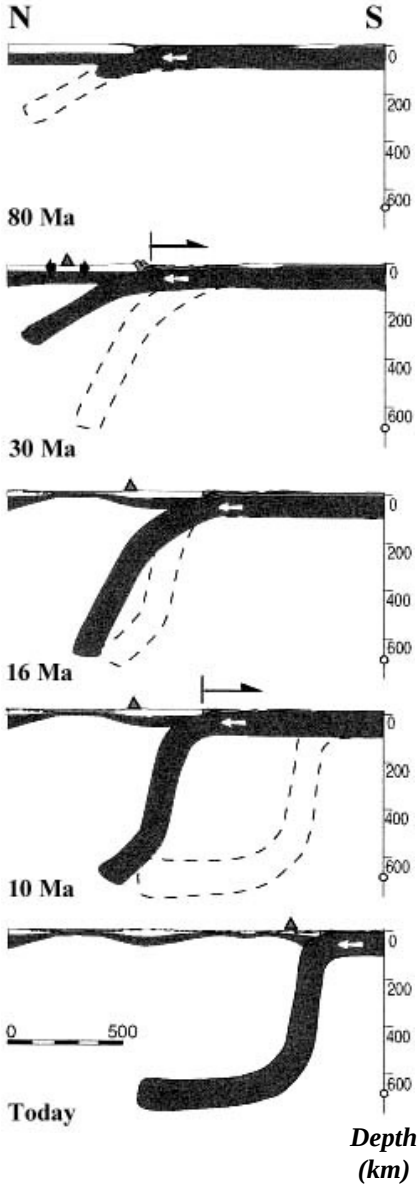


The south-westward movement of the Aegean plate is a result of combined slab-pull extension working in the back-arc area and pressure exerted by the west-moving Anatolian plate (Fig. 2.3). Slab-pull and roll-back are processes which are thought to arise when the cool African plate sinks into the asthenosphere and creates a drag upon the entire back-arc basin (Fig. 2.4). Palaeomagnetic data indicate that the southward curvature of the Aegean Arc began to develop during the Middle Miocene (Kissel & Laj, 1988), and this curvature is widely assumed to relate to rotations in the Aegean area, combined with an uneven southward migration of the subduction zone.

**Fig. 2.4.** Tectonic reconstruction of the evolution of subduction and back-arc extension. The diagram shows five stages of the subduction in the Aeolian Arc in the Central Mediterranean: 80, 30, 16, 10 Ma ago and today. Each panel shows the shape and location of the slab from the next panel (dashed lines). White arrows indicate the approximately constant amount of African convergence, whereas black arrows identify phases of trench migrations.
Tomographic images of the subducted Aegean slab in the Eastern Mediterranean (Fig. 2.10) show a less evolved shape for today and the shape of the slab more resembles the 10 Ma panel in this sketch. Other processes shown in the panels (volcanism, crustal thinning, uplift, roll-back (hinge migration)) and establishment and migration of a volcanic arc are similar in both areas. Modified after Faccenna et al. (2001).

The westward movement of Anatolia appears to date from the Late Miocene-Early Pliocene (ca. 5 Ma) when pressure from the north-moving Arabian plate caused motion along the North Anatolian and East Anatolian transform faults (Ergün & Özel, 1995). The relative importance, with respect to the extension in the south Aegean, of the push from the east and the pull from the south is uncertain but, according to Jackson (1994), geodetic results imply that the force of the Turkey-Eurasia motion is more important. Gautier et al. (1999) claim to have found

evidence that extension was already taking place in Lower Miocene before the Anatolian plate began to move (Middle or Upper Miocene), and therefore state that extension was not a result of the plate movement. Instead, gravity spreading of the continental lithosphere that had previously been thickened during Alpine collision is thought to have initiated extension (Fig. 2.5) (as previously suggested by Le Pichon & Angelier, 1981). However, the westward movement of Anatolia is contributing to plate movement plus extension in the area and is furthermore thought to have influenced the rotations of crustal blocks in much of the Aegean (Avigad et al., 1998; Gautier et al., 1999).

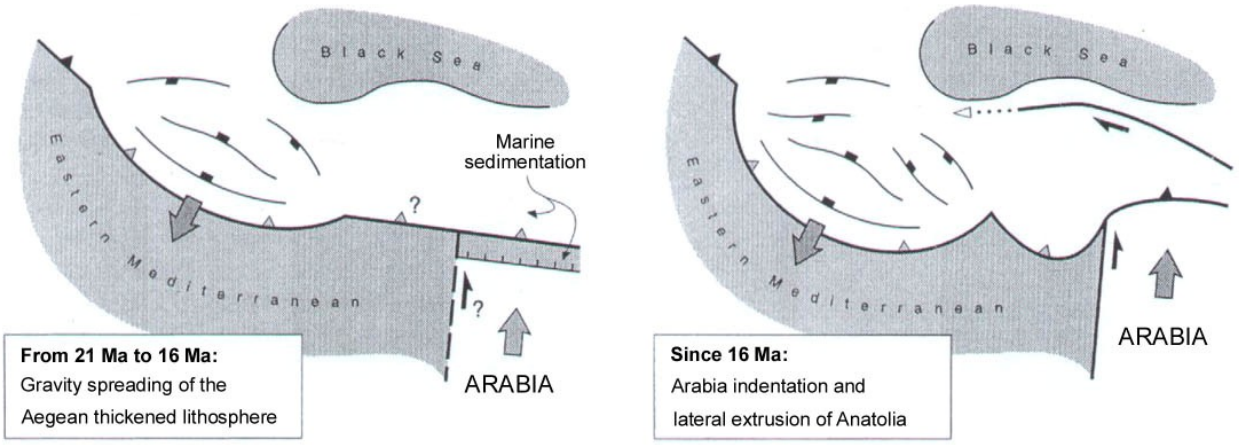


**Fig. 2.5.** The geodynamic evolution of the Eastern Mediterranean from ~21 Ma onwards. According to Gautier et al. (1999) only gravity spreading of the lithosphere (and simultaneous roll-back) was important with regard to extension in the Aegean between 21 and 16 Ma ago. 16 Ma is proposed as a maximum age for the onset of the Anatolian plate adding to the extension. After Gautier et al. (1999).

The result of the above processes can be seen in the calculated crustal thicknesses in the Aegean area. These calculations were first performed by Makris (1978) and were based on gravity and seismic refraction observations showing that the crust beneath Greece and Turkey is between 40 and 60 km thick, whereas the crustal thickness varies between 20 and 32 km beneath the Aegean Sea.

Gautier et al. (1999) made experiments to estimate the total amount of Aegean extension. They calculated that in the last at least 21 Ma the front of the subduction zone (Hellenic Trench) must have migrated ca. 445 km south, of which only 90 km can be attributed to pure transfer of the westward motion of Anatolia (Fig. 2.6). Internal extension of the Central Aegean is now around 12 mm/year and has been roughly constant for the last 11 Ma (Gautier et al., 1999).

Rapid Miocene extension of the Aegean area combined with subduction roll-back is thought to have resulted in southward migration of the volcanic arc (e.g. Fytikas et al., 1984, Pe-Piper & Piper, 2002). This is expressed by extension-related Eocene-Oligocene volcanism and plutonism in Greece and Bulgaria, early Miocene volcanism on the north Aegean islands, plutonism in the Cyclades and finally subduction-related Plio-Quaternary volcanism in the modern Aegean Arc (Fig. 2.7). Extension during the Plio-Quaternary resulted in extensional

unroofing of metamorphic core complexes, e.g. in the Cyclades (Fig. 2.6) (Lister et al., 1984; Avigad & Garfunkel, 1991).

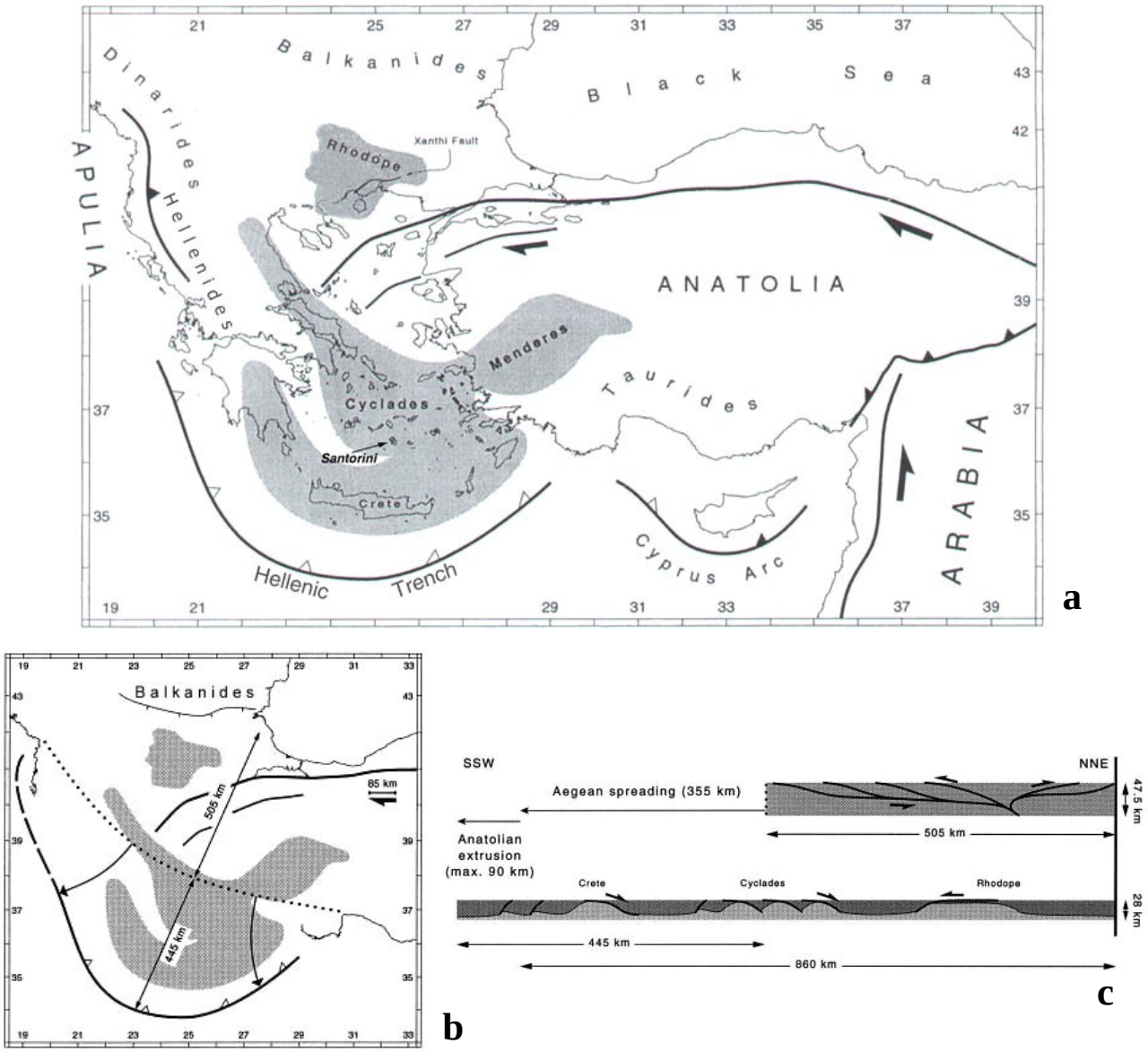


**Fig. 2.6.** Schematic estimation of the total amount of Aegean extension.
The front of the subduction zone (Hellenic Trench) is calculated to have migrated ca. 445 km SSW in the last 21 Ma. Only 90 km could be attributed to the westward motion of Anatolia. Modified after Gautier et al. (1999).

**a**) Structures of the Aegean area. Major active fault zones are shown as thick lines and grey shading indicates areas with metamorphic complexes of Cenozoic age, or probable Cenozoic age in the case of the Rhodope massif.
**b**) Simplified map of the Aegean area; the dotted line representing the assumed initial shape of the Aegean subduction zone (Hellenic Trench) and the shading showing areas with metamorphic complexes of Cenozoic age.
**c**) Schematic cross sections along the central axis of the Aegean area, showing the initial (top) and present (bottom) situations as sketched in map **b**, above and below the dotted line, respectively. Geometry of thrusts and fault systems is speculative for the initial situation.

Uplift rates peaked in the late Early Miocene, and uplift continued during Plio-Quaternary time. The rocks in the Cyclades are metamorphic of Late Palaeozoic to Mesozoic age with several granitoid intrusions. The exposed basement geology in the Aegean only represents upper crustal lithologies and the nature of the deeper crust is a matter of speculation. According to Druitt et al. (1999) the deeper crust may be Proterozoic gneisses as in other deeper parts of the Hercynian crust of southern Europe.

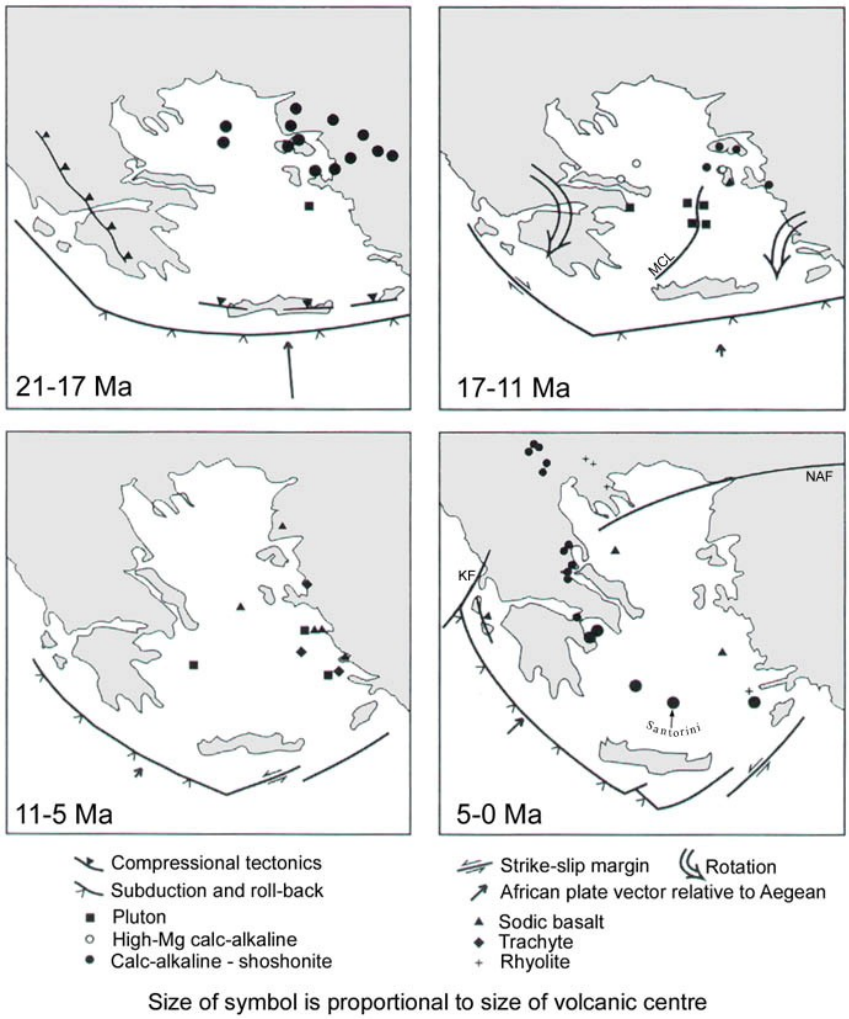


**Fig. 2.7.** Evolution of the curvature of the Hellenic Trench.
Palaeomagnetic data have been used to reconstruct these maps, showing the change in curvature from 21 Ma ago to the present. Early extension-related volcanism in Greece and Bulgaria as well as volcanism and plutonism in the Aegean Sea is related to subduction because the latter is thought to have added to the extension with a roll-back process.
Direct subduction-related volcanism is not present until max. 5 Ma ago but Pe-Piper & Piper (2002) think that extension may have had greater influence on this volcanism than formerly assumed (see Section 2.3).
Abbreviations on maps:
KF: Kephalonia Fault, MCL: Mid-Cycladic Lineament and NAF: North Anatolian Fault.
After Pe-Piper & Piper (2002).

At the present time, in the southern Aegean, the most prominent morphological features are the volcanic Aegean Arc, the Cretan Trough, the sedimentary fore-arc, the Hellenic Trench, and the Mediterranean Ridge (Fig. 2.8).

The Cretan Trough (or South Aegean Trough), situated just north of Crete, is a 2000 m deep structure that contains sediments that were eroded off the uplifted southern Aegean Cyclades Massif (Perissoratis, 1995).

The islands of Kythira, Antikythira, Crete, Kasos, Karpathos and Rhodes form the sedimentary fore-arc, also called the outer non-volcanic arc. These islands consist of Palaeozoic to Tertiary rocks deformed during the Alpine orogeny (Makropoulos & Burton, 1984).

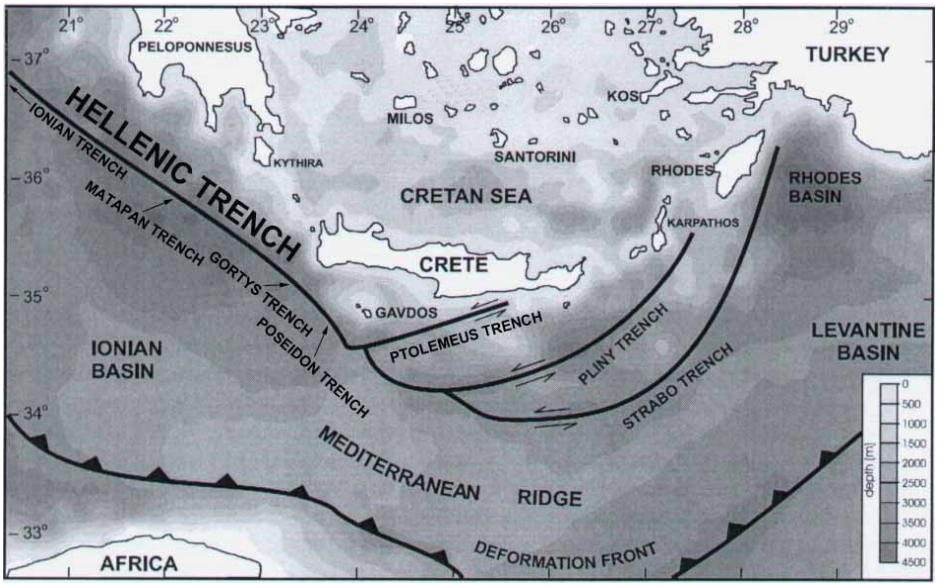


**Fig. 2.8.** Major structural features of the southern Aegean area (bathymetry in shading). Arrows in the western part of the Hellenic Trench indicate only approximate location of individual trenches of the complex trench system. Modified after Ten Veen & Meijer (1998).

The island of Crete represents a horst structure that was developed within the last 5 Ma. It is of particular interest because geophysical data have suggested that a microcontinent on the northern edge of the African plate was subducted together with the oceanic lithosphere sometime in the Oligocene (~30 Ma ago), giving rise to the unusual thickness of Crete (Bohnhoff et al., 2001). The microcontinent is thought to have been buried to a depth of about 35 km and later exhumed about 19 Ma ago by so-called buoyant escape (Fig. 2.9).

The Hellenic Trench is the morphological expression of the Aegean subduction zone itself, reaching a water depth of ca. 5000 m. Oceanic lithosphere is subducted in a NNE direction in the Hellenic Trench beneath the continental lithosphere of the Aegean. This leads to the formation of an inclined seismic zone dipping NE with the active volcanoes of the Aegean Arc above it.

The Mediterranean Ridge lies ca. 200 km south of the sedimentary fore-arc and is a 150-300 km wide structure rising 1-2 km above the surrounding sea floor. It probably began to take form during the Neogene as a direct result of the subduction process (Kastens, 1991). It consists of intensively folded and faulted rocks of the African margin, which are interpreted as sediments which failed to subduct; these are mainly thought to be Messinian evaporites (Le Pichon & Angelier, 1981; Limonov et al., 1996).

The existence of a subduction zone in the southern Aegean Sea was inferred mainly from the presence of a volcanic arc and associated earthquakes. It was first widely accepted when seismological observations revealed a well-developed Wadati-Benioff zone down to 150-180 km below the central Aegean Sea (e.g. Papazachos & Comninakis, 1971, 1978; Makropoulos & Burton, 1984; Papadopoulos et al., 1986; Christova & Nikolova, 1998). The angle of the

subducted slab was determined to be 30-40° (Papazachos & Comninakis, 1971) and in 1988 seismic tomography showed that the Benioff zone could be followed down to at least 600 km beneath the central Aegean (Spakman et al., 1988) (Fig. 2.10). Spakman et al. (1993) carried out further studies which showed that the slab can be followed down to at least 670 km and possibly down to 800-1000 km.

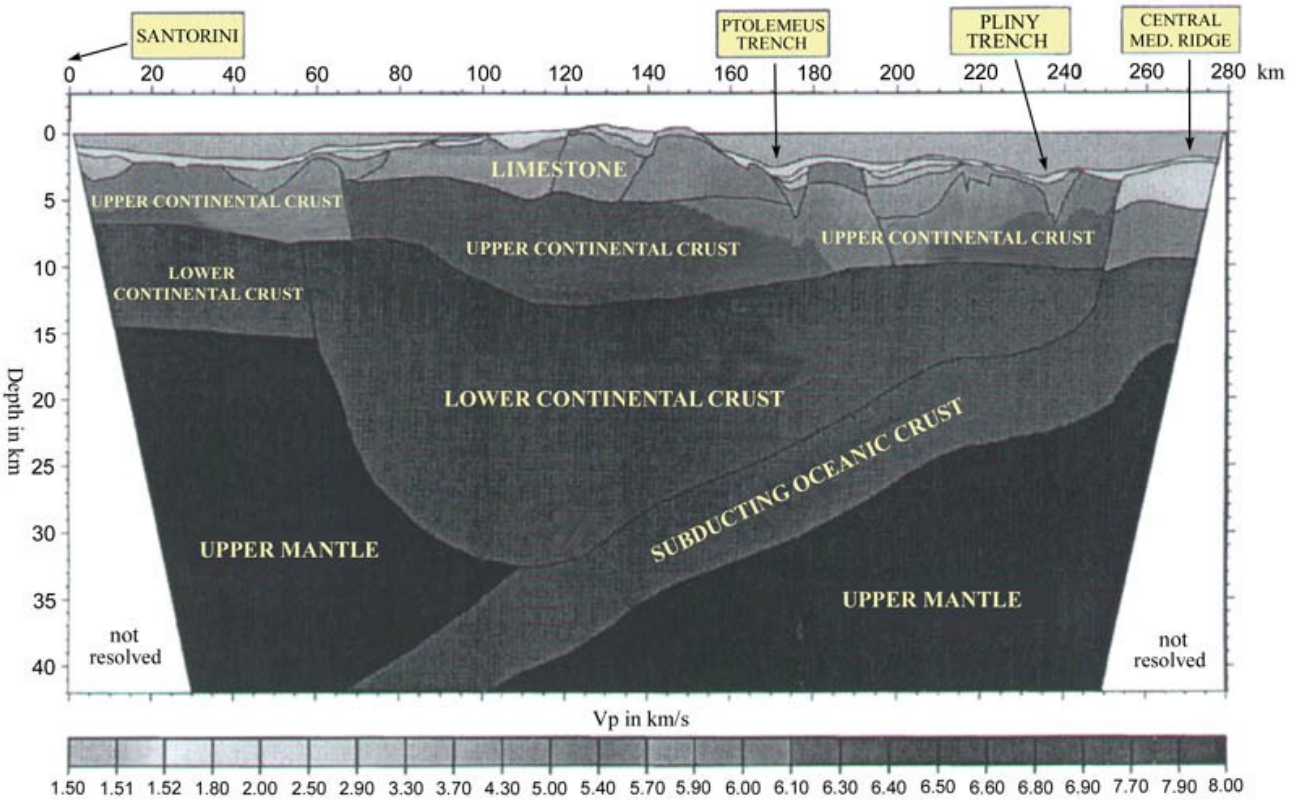


**Fig. 2.9.** North-south traverse across Crete. 2D P-wave velocity-depth model with a vertical exaggeration of 3.3 showing the greater continental thickness beneath Crete. The model given here suggests that the excessive thickness is due to subduction of a microcontinent. The downgoing slab is ca. 5-7 km thick oceanic crust of the African plate. Modified after Bohnhoff et al. (2001).

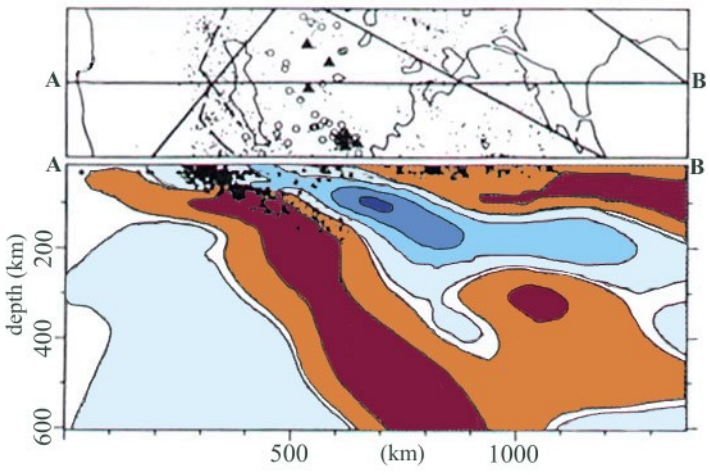


**Fig. 2.10.** Tomographic image of the Aegean upper mantle in cross section.
The upper panel displays a small location map for orientation: The profile line A-B oriented SSW NNE passes from the North African coast through Crete and Turkey to the Black Sea. The lower panel displays the inferred P-wave velocity heterogeneity. Red and orange colours indicate positive anomalies, and blue nuances indicate negative anomalies. White areas are regions with poor resolution and the dark red area crossing the lower panel and reaching to depths of over 600 km represents the subducted slab. The dashed line in the upper panel indicates the Hellenic trench system, and black triangles represent calc-alkaline volcanism. Black circles in the lower panel show earthquake foci and open circles in upper panel indicate focal depths of 100-180 km. Modified after Spakman et al. (1988).

Most authors believe that the present subduction in the Hellenic Trench was established, perhaps in a slightly different form, sometime in the Miocene. Le Pichon & Angelier (1981) estimated that the subduction system began about 13 Ma ago, based on the age of the oldest volcanic rocks (just under 5 Ma) in the present arc, and an assumption about the shape of the underlying slab. McKenzie (1978) and Mercier (1981) have suggested a much shorter period of subduction of around 5-10 Ma, while Jolivet & Patriat (1999) and Spakman et al. (1988, 1993) suggest older ages of ca. 25 Ma and 26-40 Ma, respectively. Apparently the discrepancies result from different opinions of the length of the subducted slab and plate movement rates through time. Spakman et al. (1988, 1993) propose an early onset of subduction (Oligocene or Eocene) based on a slab length of at least 600 km and a subduction rate of 15-23 mm/year. If, on the contrary, subduction of this slab had only taken place during the last 5 Ma, the result is a higher subduction rate of up to 160 mm/year. The 5 Ma age was, however, based on a slab length of only ca. 200 km (as estimated before the introduction of tomographic imaging).

Based on the present-day ~35mm/year south-western movement of the Aegean microplate, and the ~11mm/year north-moving African plate, combined with a subduction to >670 km depth (as inferred from the tomographic images), simple calculations give a minimum age for the onset of subduction of 15 Ma. It must also be taken into account that initial subduction of the African plate could have been rather slow as suggested by Spakman et al. (1988). On the other hand, subduction was probably faster than the present-day rates over a long period of time, due to the loading of the overriding plate onto the sinking one combined with slab pull (Christova & Nikolova, 1998).

Christova & Nikolova (1993, 1998) used mapping of velocity structures to determine the geometry of the Wadati-Benioff zone beneath the Aegean Sea (Fig. 2.11). The Wadati-Benioff zone seems to be composed of an eastern and a western flank, which have different dips and therefore do not intersect. The eastern flank has a dip of 40° to the northwest and reaches a depth of at least 170 km, whereas the western flank dips 20-30° to the northeast and reaches down to at least 180 km.

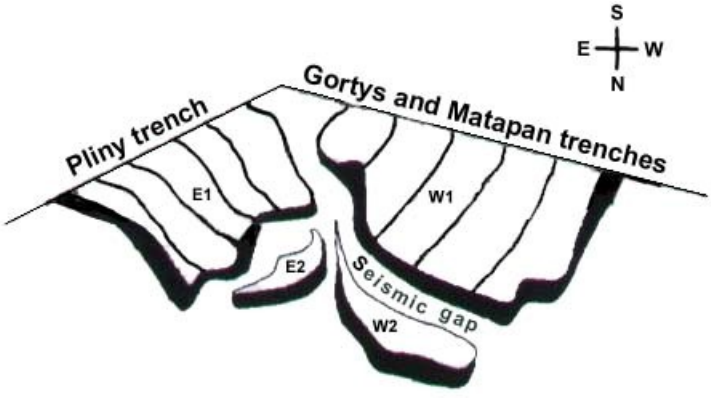


**Fig. 2.11.** Diagram of the geometry of the Hellenic Wadati-Benioff zone. E1 and W1 are the upper parts of the eastern and western flanks of the subduction zone, E2 and W2 are the lower parts. The model was based on work by Vanek et al. (1987) correlating the spatial distribution of Aegean earthquakes with geological, volcanic and tectonic phenomena. The seismic gaps probably represent partial melts in the mantle wedge above the subducting slab approximately 130-150 km below the volcanic arc. Notice the arrangement of the four points of the compass. Modified after Christova & Nikolova (1993).

The seismic gaps, which were detected in both flanks (Vanek et al., 1987; Christova & Nikolova, 1993, 1998; Papazachos et al., 2000), were interpreted by Vanek et al. (1987) as a" partially melted part of the subducted slab where stress concentration cannot occur and therefore no major seismic activity is observed ."The active volcanoes of the Aegean Arc are situated in a smooth curve directly above the seismic gaps of both flanks. The seismic gaps however, are more likely to represent partial melts in the mantle wedge above the subducted slab, as melting of slab material would seem very unlikely in this environment.

Papazachos (1990) inferred from seismic data that the Benioff zone can be further separated into a shallow part (40-80 km) with a mean dip angle of 23° and a deep part (80-180 km) with a mean dip angle of 38°. This suggests that the oldest part of the slab is sinking more freely than the upper part which is still interacting with the continental Aegean lithosphere (Papazachos, 1990).

## 2.3. The Aegean volcanic arc

The Aegean (or Hellenic) volcanic arc is a curved chain of a dozen active, dormant and inactive volcanoes (Fig. 2.12). It is approximately 500 km long and 20-40 km wide and extends from the Saronic Gulf in the west to the Anatolian coast in the east. Of the islands belonging to the Aegean Arc, the most important volcanic centres are Milos, Santorini, Nisyros, Yali and Kos (Keller et al., 1990; Papazachos & Panagiotopoulos, 1993; Volti, 1999). Other volcanic centres along the arc include Sousaki, Aegina, Methana and Poros. Only Santorini, Nisyros and Methana exhibit major volcanic activity in historic times while on Sousaki, Milos and Kos there is minor activity in the form of solfatara or fumarole fields.

Volcanism along the arc began ca. 4.4 Ma ago (Keller et al., 1990) and is related to the NE-SW trending rupture zones recognized by Papazachos & Panagiotopoulos (1993) (Fig. 2.12).

Aegina, Sousaki, Poros and Milos were the earliest active centres along the arc and began their

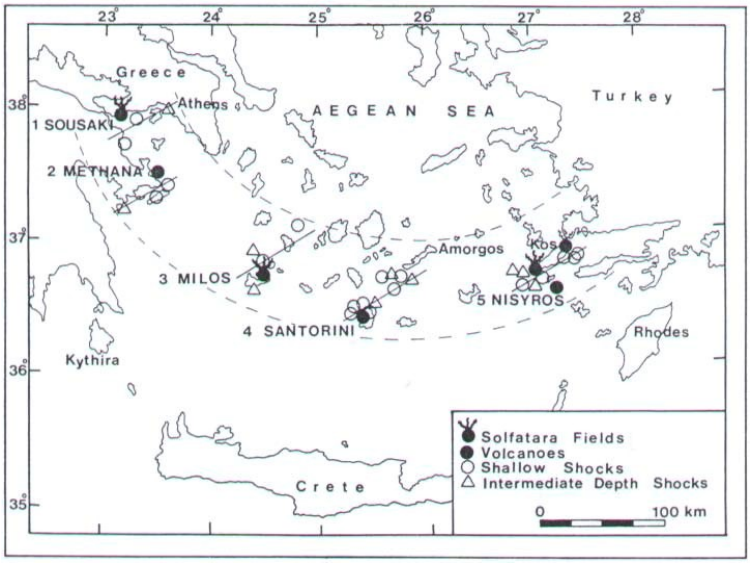


**Fig. 2.12.** Five distinct linear clusters defined by epicentres of shallow and intermediate depth strong earthquakes as well as volcanic centres (volcanoes, fumaroles and solfatara fields). The epicentres of the earthquakes and the centres of the volcanic activity in each cluster have a tendency to form a line with an approximately NE-SW direction (ca. 60°NE), corresponding to five normal faults in the crust beneath the Aegean Sea.
After Papazachos & Panagiotopoulos (1993).

activity in the early Pliocene. There was a period of less activity in the late Pliocene (except on Milos) followed by renewed activity during the Quaternary. The rest of the volcanic centres were only active during the Quaternary (Santorini, Methana, Nisyros, Yali and Kos) (Pe-Piper & Piper, 2002). For further description of the geology of the islands and geochemistry of the volcanic products, see Keller et al. (1990), Morris (2000), Pe-Piper & Piper (2002) and Sachpazi et al. (2002). The geology of Santorini is described in Chapter 3.

Some preliminary comments linking the geological setting of the Aegean Arc to the magmatic products of the arc can now be pointed out.

Continental crust underlies the whole Aegean area and varies in thickness from 20 to 32 km (Le Pichon & Angelier, 1981). This is much less than the surrounding land masses due to the extension of the Aegean area. When magmas rise to the surface, they pass through upper continental materials consisting of several kilometres (5-8 km according to Le Pichon & Angelier (1981)) of pre-Messinian sediments of unknown lithology (Limonov et al., 1996), up to 1 km of Messinian evaporites and finally a few hundred metres of Plio-Quaternary marls (Le Pichon & Angelier, 1981). These materials are likely to affect the geochemistry of the rising magmatic products. Also thought to affect magmatic geochemistry is the amount and type of sediment subducted with the downgoing slab. According to Le Pichon & Angelier (1981) the Messinian evaporites are scraped off and deposited on the Mediterranean Ridge, so only the underlying pre-Messinian sediments are thought to descend with the slab. According to Bohnhoff et al. (2001) sediments cannot be detected on the seismic images, and are therefore thought to be less than 1.5 km thick (the uncertainty of their method).

Pe-Piper & Piper (2002) suggest that, along with the subduction process, changes in the amount of extension in the Aegean area may have had an influence on the timing and locus of volcanism. All volcanoes along the arc have produced calc-alkaline volcanic rocks typical of a subduction zone environment, and range in composition from basalts, basaltic andesites and andesites to dacites and rhyolites (Mitropoulos et al., 1987; Pe-Piper & Piper, 2002). Mitropoulos and Tarney (1992) suggested that the greater amount of lithospheric extension in the central part of the Aegean Arc could result in greater upwelling of asthenosphere, and thus explain the greater abundance of basaltic and andesitic rocks on Santorini. In the Aegean Arc, only on Santorini are tholeiitic basalts and andesites found intercalated with calc-alkaline rocks (Pe-Piper & Piper, 2002).

Volcanic activity began on Santorini on the southern Akrotiri Peninsula (less than 2 Ma ago) while most of the volume of the exposed volcanics on Santorini was erupted during the last 200,000 years.

## 3. Geology of Santorini

Santorini is a group of islands located in the central part of the Aegean Arc (36°27N, 25°24E). It is a volcano complex consisting of five islands: Thera (main island), Thirassia, Aspronisi, Palaea Kameni and Nea Kameni (Fig. 3.1). The prevolcanic basement together with the remnants of the volcanic centres of the three first mentioned islands form the shape of an oval surrounding the submerged caldera, in the middle of which the two recent Kameni islands have appeared.

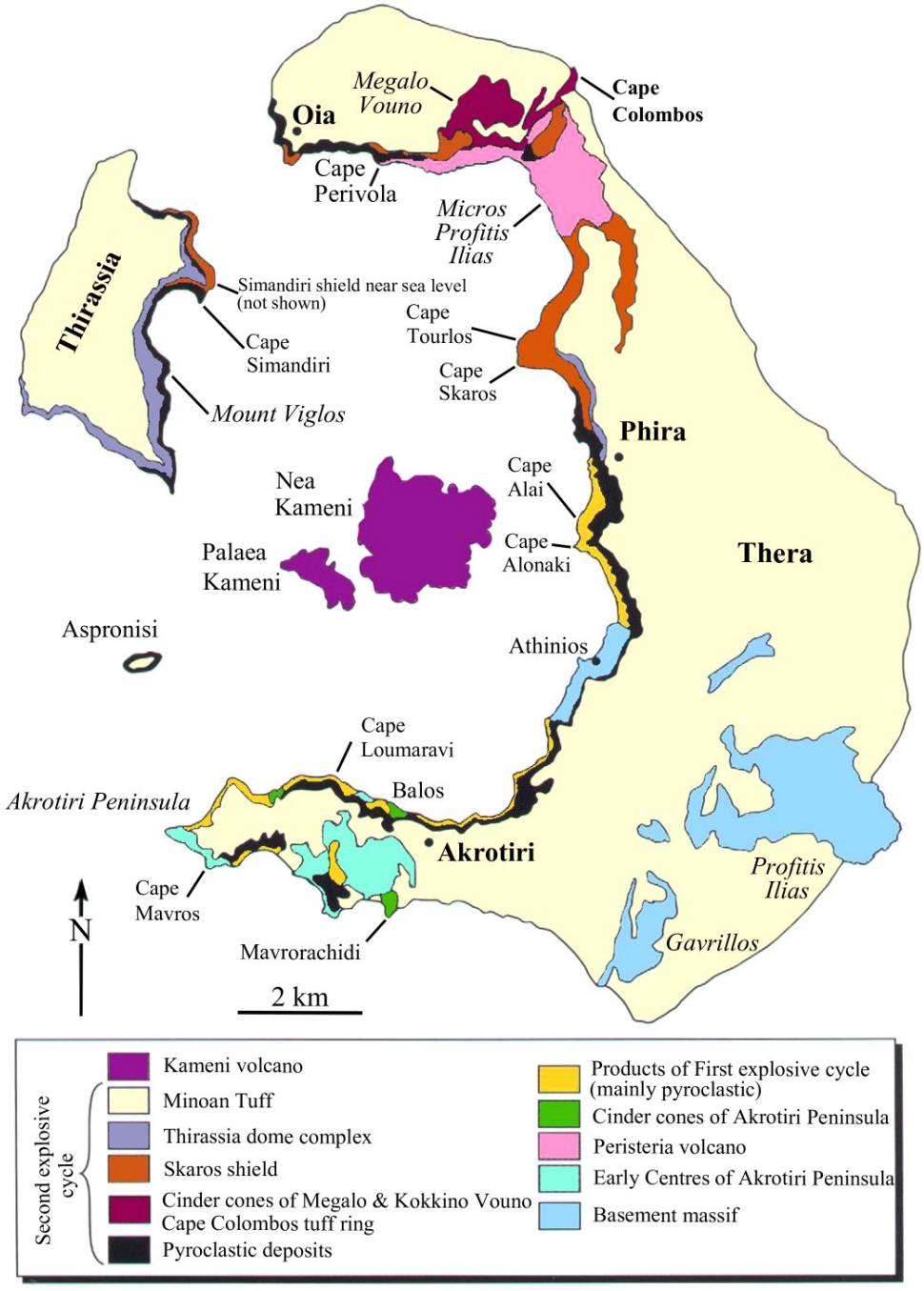


**Fig. 3.1.** Simplified geological map of Santorini modified after Druitt et al. (1999).

The area of the islands is ca. 90 km$^2$ and the caldera is roughly 8 x 5 km across. The caldera is divided into two main basins. The southern -which can further be subdivided into three smaller basins: the eastern, southern and western -consists of three max. 280 m deep depressions formed during the eruption of the Lower Pumice series (Caldera 1). These depressions have later been deepened by subsidence associated with formation of the northern ca. 380 m deep basin, which attained its present shape during the Minoan Eruption (Caldera 4) (Heiken & McCoy, 1984; Druitt et al., 1989). From the bathymetry of the area, it can be seen that all four basins are separated by ridges rising just tens of metres above the otherwise flat sea floor (Perissoratis, 1995).

Santorini lies on a major NE trending lithospheric rupture zone defined by earthquakes (Figs. 2.12 and 3.2). The majority of the dikes in the caldera wall in north-east Santorini trend NE or NNE, and roughly parallel this lineament. Associated with the volcanism on Santorini are also the Colombos Maar volcano ca. 7 km NE of Santorini and the Christiani Islands ca. 18 km SW of Santorini. These, together with Santorini, lie on the two tectonic lineaments the Colombos Line and Kameni Line (Fig. 3.2). The Christiani Islands are thought to be several hundred thousand years old and may be related to the earliest volcanism on Santorini (Friedrich, 2000).

The stratigraphic relationship between the basement and the many volcanic products is described briefly below and can be seen schematically in Table 3.1 and Fig. 3.1.

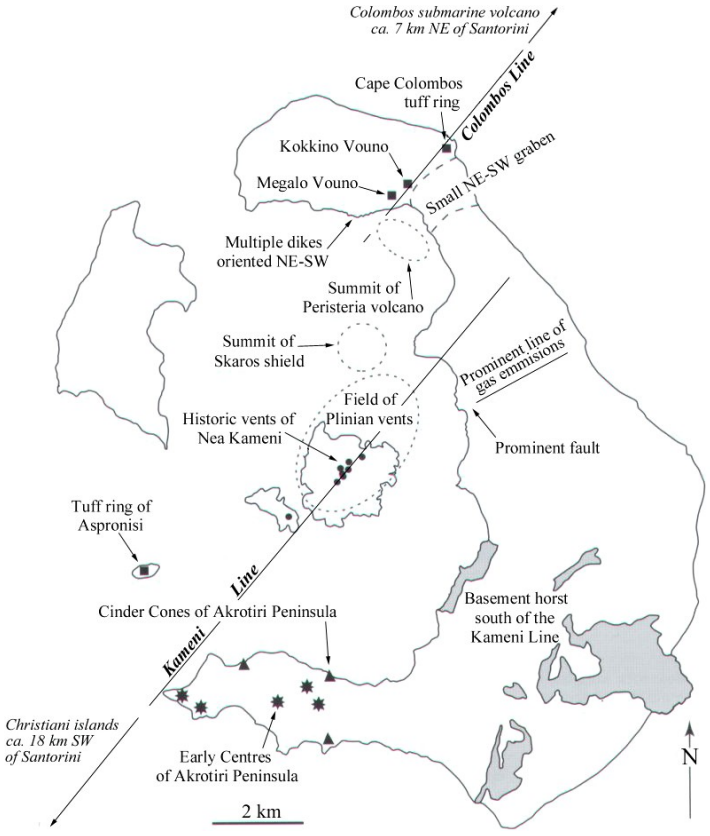


**Fig. 3.2.** Structural map of Santorini showing the tectonic lineaments that are thought to have influenced Santorini volcanism.
Both the young well-defined Kameni Line (defined by flank eruptions on the Kameni Islands) and the older Colombos Line (defined by the cinder cones of Megalo Vouno and Kokkino Vouno together with Cape Colombos tuff ring and Colombos Bank maar volcano) are approximately parallel to the regional NE-SW trending graben system. The relation between the many dikes in the caldera wall of north-east Thera and the regional structure (perhaps in combination with a volcanic event) is presented in Chapter 4.
Modified after Druitt et al. (1999).

## 3.1 Prevolcanic basement

The basement massif is a fragment of the Cyclades Massif. As mentioned in Section 2.2., the Cyclades is a metamorphic core complex located in the Aegean Sea north of the Aegean Arc, which experienced prolonged periods of uplift and finally extensional unroofing during the Plio-Quaternary. It has two main components on Santorini (Fig. 3.3):

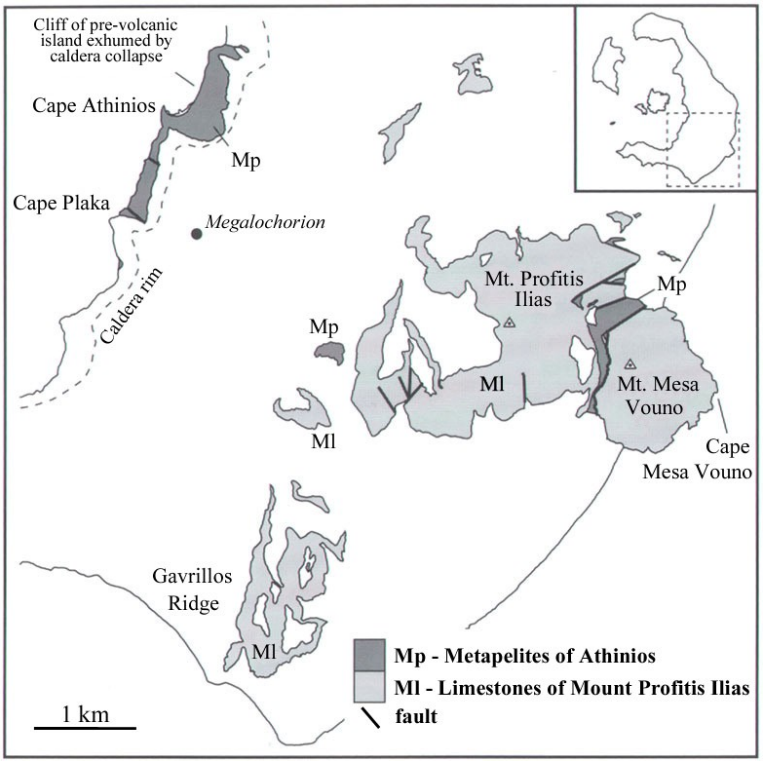


**Fig. 3.3.** Geological map of the basement massif in the south-east corner of Santorini. After Druitt et al. (1999).

(a) low-grade metapelites (phyllites and schists) mainly exposed along the caldera wall in the area around Athinios harbour, Cape Plaka and Cape Therma, but also between Mount Profitis Ilias and Mesa Vouno, plus a small outcrop between Gavrillos Ridge and Mount Profitis Ilias.

(b) crystalline limestones that form the massifs of Mount Profitis Ilias, Gavrillos Ridge and Mount Mesa Vouno.

These formations were once sediments deposited on the sea floor of Tethys (probably in the Triassic and Jurassic (Pichler & Kussmaul, 1980) and were later folded, metamorphosed and finally uplifted during the Cenozoic. The metapelites have been metamorphosed to blueschist facies and later overprinted by greenschist to amphibolite facies. According to Davis & Bastas (1978), older studies suggested the limestones were of Triassic age and fossil remains showed a

Palaeocene-Eocene age for the metapelites. Both units have been described by Davis & Bastas (1978) and Skarpelis & Liati (1990).

## 3.2 Early centres of the Akrotiri peninsula

The earliest volcanism on Santorini (650-550 ka; Druitt et al., 1999) is situated on the Akrotiri Peninsula (Fig. 3.1) and mainly consists of silicic lavas and tuffs, which differ from the rest of the volcanism on the island by being amphibole-bearing. There is evidence of submarine eruptions in the form of pillow lavas, hyaloclastite aprons, tuffs with ripple marks and the presence of vitric tuffs containing marine sediments and fossils or containing siliceous sponge spicules. These early volcanic centres have been uplifted, so that the marine sediments today lie 100 m or more above sea-level. According to Friedrich (2000), palaeontological data published in 1992 suggested ages as old as 1.6 Ma for sediments of the Akrotiri peninsula and zircon fission-track data have previously yielded ages of 940-1950 ka (Seward et al., 1980).

## 3.3 Peristeria Volcano

The existence of this old volcano in northern Thera (Fig. 3.4) was first proposed in the works of Reck from 1936 and has now been revived by Druitt et al. (1999). Many other studies (often based on the map by Pichler & Kussmaul (1980)) have assigned these products to the younger Megalo Vouno volcano – a cinder cone on top of Peristeria volcano.

Local people furthermore use Megalo Vouno as a location name because it is the name of the tallest point in the area. In this thesis the common name "Megalo Vouno" or preferably the "Megalo Vouno volcano complex" will be used when referring to the volcanic complex as a whole (Peristeria volcano and Megalo Vouno cinder cone). To avoid confusion, when mentioning the separate units they are further specified as Peristeria volcano or Megalo Vouno cinder cone.

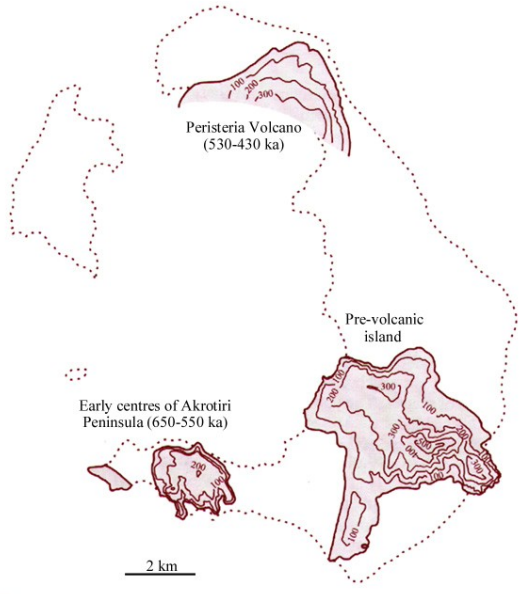


**Fig. 3.4.** Reconstruction of the pre-volcanic island, and the early centres of the Akrotiri Peninsula and Peristeria Volcano.
The outlines of the present-day islands are shown dotted and the topographic contours are in hundred metres.
After Druitt et al. (1999).

Megalo Vouno and its neighbouring volcanoes –Skaros, Micros Profitis Ilias (now also thought to belong partly to Peristeria) and Thirassia (see Fig. 3.1) –have previously been linked chemically and petrographically (the so-called Main Series of Nicholls (1971)) and it was thought that they were erupted simultaneously over a period of ca. 100 ka (Nicholls, 1971; Pichler & Kussmaul, 1980; Mann, 1983; Huijsmans, 1985; Huijsmans & Barton, 1990 among others). New K-Ar data, however, show that Peristeria, comprising most of what was previously termed Megalo Vouno and all of Micros Profitis Ilias, was erupted between 530-430 ka and could not have erupted simultaneously with either the Skaros or Thirassia volcanoes which are both much younger (Druitt et al., 1999).
A stratigraphic description of Peristeria volcano is given in Section 4.2.

## 3.4 Thera Pyroclastic Formation (TPF)

Pyroclastics of this formation can be found over most of Santorini and, apart from the basement, make up the major part of the main island Thera. Thera Pyroclastic Formation has been studied in detail (stratigraphically and geochemically) by i.a. Pichler & Kussmaul (1980), Vitaliano et al. (1990) and Druitt et al. (1989, 1999). The latter have divided it into two explosive cycles. The First explosive cycle (ca. 360-180 ka) and Second explosive cycle (180-3.6 ka) both commenced with explosive eruptions of andesitic and dacitic magma (alternating with effusion of basaltic and andesitic lavas), and culminated in two large silicic pyroclastic eruptions. Judging from the thickness and distribution of the ejecta layers, most of the major eruptions are thought to have discharged magma volumes of the order 1-10 $km^3$ or more (Druitt et al, 1989). The following description of the pyroclastic units is based on Druitt et al. (1989, 1999):
Briefly, the First explosive cycle consists firstly of the three Cape Therma eruptions which have all produced various amounts of alternating ignimbrite, spatter agglomerates and pumice deposits and secondly, of the two Lower Pumice eruptions consisting mainly of pumice and lithic lag breccia. These eruptions were followed by caldera collapse, today recognised by a steep unconformity in the caldera wall. This caldera is called the Lower Pumice caldera or Caldera 1 (Fig. 3.5, Table 3.1).
The Second explosive cycle comprises the seven units: Cape Thera, Middle Pumice, Vourvoulos, Upper Scoriae 1 & 2, Cape Riva and the Minoan Eruption. These units laid down varying deposits of pumice, ignimbrite, lithic breccias, spatter agglomerates, scoria and ash beds while, in between, constructive volcanism built up the Simandiri shield (base of Thirassia island), the Skaros shield and the Thirassia dome complex (Table 3.1). According to Druitt et al. (1999) other minor products in between the twelve major units of Thera Pyroclastic Formation can be grouped as 1) scoria-fall deposits, 2) ash fall layers, 3) base-surge layers, 4) wind-reworked ash and lapilli and 5) palaeosols representing long periods of dormancy.

The Second explosive cycle saw three caldera collapses (Fig. 3.5, Table 3.1):
Caldera 2, which cannot be linked to a specific eruption, but seems to have been the culmination of the Middle Tuff period,
Caldera 3, or the culmination of the Cape Riva eruption, which destroyed the central parts of the Thirassia-Skaros complex and finally,
Caldera 4, or the Minoan Eruption, the products of which drape the walls of the pre-existing caldera and give evidence that the Skaros shield and the overlying Thirassia-Skaros complex had, indeed, collapsed before the Minoan Eruption (Druitt & Francaviglia, 1990; Eriksen et al., 1990).
The Minoan Eruption, and its possible link with the destruction of the Minoan culture on Crete, has been intensely studied through the years and, therefore, the eruption will be described separately below, even though it is classified as belonging to the Second eruptive cycle by Druitt et al. (1989, 1999).

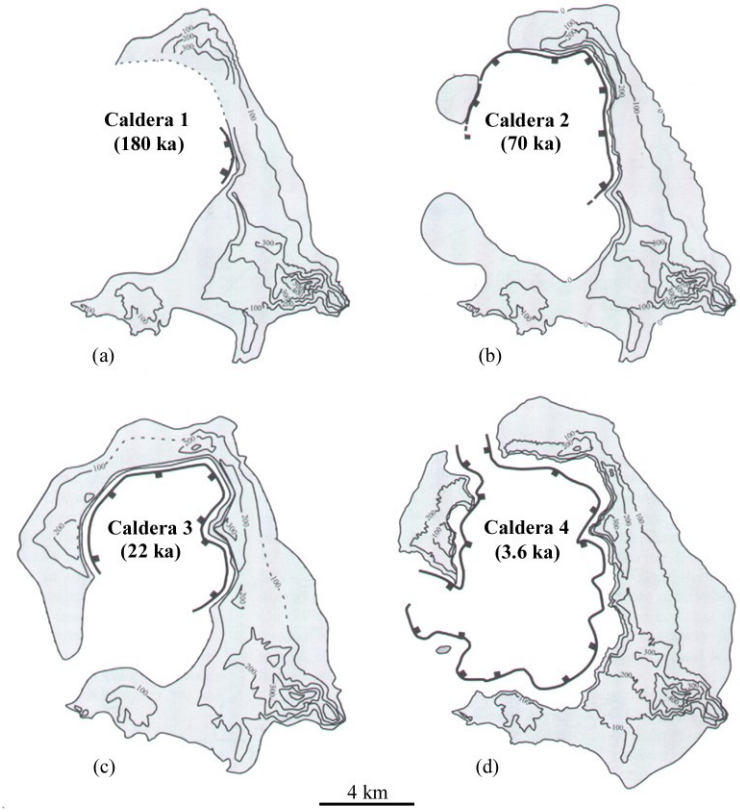


**Fig. 3.5.** Reconstruction of the four calderas of which there is evidence in the existing caldera wall (based on the works of Pichler & Friedrich (1980), Pichler & Kussmaul (1980) and Heiken & McCoy (1984)). Contours in 100 metres.
a) Caldera 1: Thought to have formed during the Lower Pumice 2 eruption.
b) Caldera 2: Probably a result of one or more of the eruptions of the Middle Tuff series.
c) Caldera 3: Also termed the Cape Riva eruption. Formed at the collapse of the Thirassia-Skaros complex.
d) Caldera 4: The Minoan Eruption and the resulting present-day caldera.
After Druitt et al. (1999).

## 3.5 The Minoan Eruption

The Minoan Eruption has been studied intensively by i.a. Heiken & McCoy (1984), Druitt & Francaviglia (1990), Pyle (1997) and McCoy & Heiken (2000).

The Minoan Eruption was dated on Greenlandic ice cores to 1645 ± 7 years BC (Hammer et al., 1987). The eruption is thought to have taken place from a shallow, flooded caldera containing a

central island (Eriksen et al., 1990) from which the black, glassy dacite and dacitic hyaloclastite in the Minoan deposits seem to originate (Druitt & Francaviglia, 1990).
The eruption is divided into several phases. The first was a Plinian eruption that created pumice airfall from a sub-aerial vent near the present Nea Kameni island. The column is thought to have reached a height of 36-38 km (Pyle, 1990) and Pichler & Friedrich (1980) speculated that the phase was very short and may have lasted for only a few hours. When seawater came in contact with the vent, violent phreatomagmatic eruptions followed and emplacement of base surges and tuff took place (second phase). In the third phase, pyroclastic flows were emplaced, and these contained stromatolitic blocks formed in shallow water of the pre-existing water-filled caldera. In these deposits can also be found very large blocks of dacite and dacitic hyaloclastite up to 10 m in diameter (Eriksen et al., 1990).
During a possible phase four, lithic breccias and ignimbrites were discharged in large amounts covering much of Santorini (Heiken & McCoy, 1984; Bardot et al., 1996). Pichler & Kussmaul (1980) mapped these units as reworked deposits, and Friedrich (2000) agrees with this interpretation. The final phase ended with formation of Caldera 4 also termed "the Minoan Eruption ."
Based on ash fall in Rhodes, Turkey and on Santorini, the eruption is in all estimated to have vented around 30-36 $km^3$ of magma (Druitt & Francaviglia, 1990; Pyle, 1990). The ashes from the Minoan Eruption have been distributed as far as Anatolia and pumice pebbles can today be found on beaches of several islands in the Mediterranean and as far as the Nile delta (Stanley & Sheng, 1986).

A simplified summary of the history of the Santorini volcanic field is given in Table 3.1, and is shown in the form of a cartoon in Kann & Petersen (2003).

## 3.6 Main Series of Nicholls (1971)

As mentioned above, Megalo Vouno, Micros Profitis Ilias, Skaros and Thirassia have previously been thought to have erupted simultaneously and, because of their geochemical similarity, classified as belonging to the same geochemical series – the Main Series. Rocks of the Main Series range from basalt to rhyodacite. Many authors have used this classification up to now and, even though it now seems that these volcanoes were not erupted simultaneously, much evidence still shows that the volcanoes of northern Thera and Thirassia are indeed petrographically and geochemically similar. The reason for this similarity could be that overall there are only minor chemical variations among the source magma chambers, or that the products of northern Santorini all originate from the same magma chamber, which has not evolved greatly through time. The present study in fact reveals that significantly different geochemical series are present.

For this study, the stratigraphy of Druitt et al. (1999) will mainly be used because it is based on the most recent age data for the area studied. The former published stratigraphic descriptions are also mentioned where these are relevant.

## 3.7 Post-Minoan volcanics

The two central islands of the caldera, Palaea Kameni and Nea Kameni (together the Kameni Islands), are the result of the most recent volcanic activity in Santorini. They have been formed by eleven eruptions between 197 BC and AD 1950 (nine eruptions according to Fytikas et al. (1990)), which were studied chemically and petrographically by Barton & Huijsmans (1986). The lavas are calc-alkaline dacites that have evolved from more mafic parental magmas via fractional crystallisation. Analyses show that the underlying shallow magma chamber (depth 2-4 km) is compositionally zoned (Barton & Huijsmans, 1986).

At present solfatoric and fumarolic activity occurs on the islands. Eruptions seem to have taken place along a 50° NE trend reflecting the fissures through which the lavas erupted (Heiken & McCoy, 1984).

Based on their distinctive chemistry, the Kameni Islands are usually interpreted as representing the onset of a new volcanic cycle, (Barton & Huijsmans, 1986; Druitt et al., 1989, 1999; Huijsmans & Barton, 1990). Heiken & McCoy (1984) on the other hand suggested that the Kameni lavas represent the last dregs from the Minoan magma chamber due to their low volatile content.

Besides the eruptions in the caldera, Colombos – the submarine maar volcano 7 km north-east of Santorini – has also been active in historic times. Volcanic activity was recorded in AD 1650, when earthquakes triggered eruption of large amounts of ash and pumice, and Thera s' eastern shores were severely damaged by an accompanying tsunami. In addition, the large amounts of sulphur-rich gases proved to be dangerous to the inhabitants on Santorini. A pyroclastic cone resulted from the eruptions but was rapidly eroded, so that the top of the volcano is now ca. 20 m below sea-level (Fytikas et al., 1990).

**Table 3.1.** Summary of the Santorini volcanic field and stratigraphic relationships between the units (excluding superficial formations). The numbers 1-4 (following Caldera collapse) refer to the four known calderas (see also Fig. 3.5). The name of each unit indicates the deposit of its first products relative to the first products of other centres. The table does not indicate for how long each volcanic centre was active. Modified after Druitt et al. (1999).

| **Kameni Volcano**<br>Dacites of the Kameni Islands | | |
|---|---|---|
| | | |
| **Central Thera/Thirassia/Aspronisi** | **Northern Thera** | **Akrotiri Peninsula** |
| **Caldera collapse (4)** | | |
| Minoan Tuff | Minoan Tuff | Minoan Tuff |
| **Caldera collapse (3)** | | |
| Cape Riva Tuff | Cape Riva Tuff | Cape Riva Tuff |
| Rhyodacites of Thirassia | Andesites of Oia | |
| Upper Scoriae 2 | Upper Scoriae 2 | Upper Scoriae 2 |
| Andesites and basalts of Cape Skaros | Andesites and basalts of Cape Skaros | |
| Dacites of Cape Skaros | | |
| **Caldera collapse (2)** | | |
| *Middle Tuffs:* | *Middle Tuffs:* | *Middle Tuffs:* |
| Upper Scoriae 1 | Upper Scoriae 1 | Upper Scoriae 1 |
| Vourvoulos Tuff | Vourvoulos Tuff | Vourvoulos Tuff |
| Tuff ring of Aspronisi | Kokkino & Megalo Vouno cinder cones | |
| | Tuff ring of Cape Colombos | |
| Middle Pumice | Middle Pumice | Middle Pumice |
| Cape Thera Tuff | Cape Thera Tuff | Cape Thera Tuff |
| Andesites & basalts of Cape Simandiri | | |
| **Caldera collapse (1)** | | |
| *Lower Pumices:* | *Lower Pumices:* | *Lower Pumices:* |
| Lower Pumice 2 | Lower Pumice 2 | Lower Pumice 2 |
| Lower Pumice 1 | Lower Pumice 1 | Lower Pumice 1 |
| Cape Therma 3 Tuff | Cape Therma 3 Tuff | Cape Therma 3 Tuff |
| Rhyodacites of Cape Alonaki | Rhyodacites of Cape Alonaki | |
| (thin Cape Therma 2) | | (thin Cape Therma 2) |
| Cape Therma 1 Tuff | | Cape Therma 1 Tuff |
| Andesites of Cape Alai | | |
| | **Peristeria Volcano:** | Cinder cones of the Akrotiri Peninsula |
| | Andesites, basalts & dacites of Peristeria 3 | Andesites and basalts of Akrotiri |
| | Andesites of Peristeria 2 | |
| | Andesites of Peristeria 1 | |
| | | **Early Centres of the Akrotiri Peninsula:** |
| | | Rhyodacites & tuffs of Akrotiri, andesites of Mount Loumaravi, and dacites of Cape Mavros |
| | | |
| **Basement Formation:** | | |
| Metapelites of Athinios | | |
| Limestones of Mount Profitis Ilias | | |

# 4. Dikes of the Megalo Vouno volcano complex

A distinct suite of dikes cuts through the Megalo Vouno volcano complex in the northern caldera wall. The aim of the present study has been to collect as many samples as possible from the dikes, to describe their petrology and to integrate them into the petrological evolution of the Megalo Vouno and Peristeria volcanoes. Several other studies have concentrated on the lava flows and pyroclastics of the complex, and hopefully the geochemistry and petrography of the dikes can help to clarify the evolution of the volcano complex.

Previous work by Huijsmans & Barton (1990) showed that the oldest lavas in the complex had considerably higher Sr content than the younger products, reflecting progressive depletion of the upper mantle due to fractional crystallisation. A few of the young lavas, however, showed the same high Sr contents, perhaps indicating mixing between a relatively evolved magma and a Sr-rich component (Huijsmans & Barton, 1990).

Hansen (1997) suggested that at least two magma series are represented among the volcanic products erupted by Megalo Vouno volcano. The 22 collected samples followed two well-defined trends in major and trace element diagrams, and were interpreted as two separate magma series that had mainly developed through separate processes –fractional crystallisation and magma mixing. The magmas were suggested to originate either from a common layered chamber or from a magma chamber feeding two separate chambers at shallower levels.

This chapter gives an introduction to the general volcanology of the area and to the dikes studied in the north-eastern corner of the Santorini caldera wall.

## 4.1. Stratigraphy of Megalo Vouno

The overall stratigraphy of the Megalo Vouno volcano complex has been described in some detail by Pichler & Kussmaul (1980), Druitt et al. (1989), Huijsmans & Barton (1990), Hansen (1997) and most recently by Druitt et al. (1999).

The stratigraphy has long been based on the extensive work by Pichler & Kussmaul (1980) but was recently revised in the comprehensive works of Druitt et al. (1989) and Druitt et al. (1999). The latter have changed the previously used names of the geological units so that it can be challenging to read about and compare the stratigraphy. Some units have merely changed name whilst others have been assigned to other units or stratigraphic levels completely. These changes are mainly based on new stratigraphic observations and dating of samples from several units.

The northern volcanoes Thirassia, Megalo Vouno, Skaros and Micros Profitis Ilias used to be regarded as four separate volcanoes: three volcanic shields and a steep stratovolcano (Micros Profitis Ilias). Druitt et al. (1999) on the other hand assign the lower parts of Megalo Vouno and all of Micros Profitis Ilias to the shield volcano Peristeria (Figs. 4.4 and 4.7), while the upper part of Thirassia is thought to be a part of the Thirassia-Skaros volcanic complex. The

stratigraphy of the volcanoes was previously based mainly on recognition of stratigraphic units seen elsewhere in the caldera wall, whereas the study by Druitt et al. (1999) used K-Ar dating on many units resulting in some (rather drastic) changes to the stratigraphy in the area (Table 4.1).

**Table 4.1.** Chronology of Pichler & Kussmaul (1980) compared with that of Druitt et al. (1999) for the volcanic centres of northern Santorini. As can be seen there is a great discrepancy between the two studies (see also text).

| Stratigraphic unit | Sample location (Druitt et al., 1999) | Determined age by Druitt et al. (1999) (ka) | Chronology by Pichler & Kussmaul (1980) (ka) |
|---|---|---|---|
| Cinder cone of Megalo Vouno | Welded spatter, 1 km N of Megalo Vouno summit | 54 ± 23 | ~18 |
| Cinder cone of Megalo Vouno | Andesite spatter, 1 km N of Megalo Vouno summit | 76 ± 28 | ~18 |
| Simandiri shield | 400 m N of Cape Simandiri, Thirassia | 172 ± 33 | ~79 |
| Peristeria 3 | Lava below tuff ring deposits, Cape Colombos | 308 ± 10 | >18 |
| Peristeria 3 | Lava below Lower Pumice, Oia | 431 ± 13<br>435 ± 11 | ~100 |
| Peristeria 3 | Topmost lava of Micros Profitis Ilias | 457 ± 7<br>472 ± 7 | <79 |
| Peristeria 3 | Topmost flow of Megalo Vouno succession | 480 ± 7 | >18 |
| Peristeria 2 | Second flow from base, Micros Profitis Ilias | 489 ± 23<br>502 ± 23 | ~79 |
| Peristeria 1 | Lowest flow at sea-level, Cape Heptapedio, Megalo Vouno | 551 ± 12<br>505 ± 11 | >100 |

The stratigraphy of Huijsmans & Barton (1990) was based on the work of Pichler & Kussmaul (1980) which is described briefly here. Pichler & Kussmaul made a geological map of Santorini in 1969/1970 and also interpreted some cross sections of the caldera. One of the latter shows Megalo Vouno (Fig. 4.1) which has been divided into three stratigraphic series: Lower Series ($M_1$ & $M_2$), Cape Colombos (Ko ~~not~~ not present in Fig. 4.1), and Upper Series ($M_3$, $M_4$, $M_5$ and $M_6$).

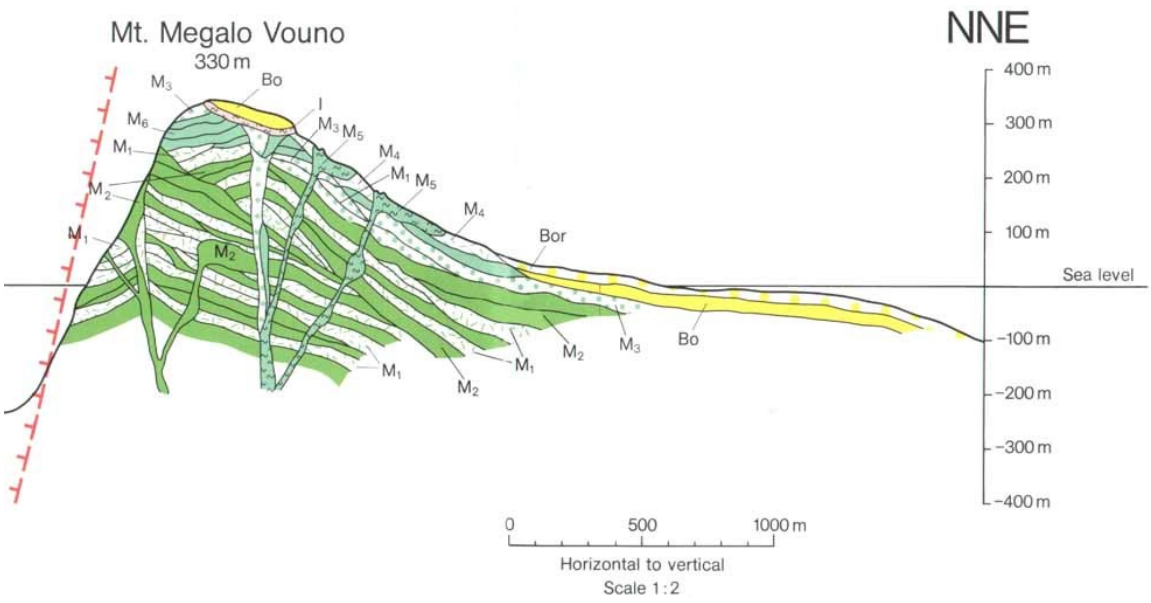


**Fig. 4.1.** Interpretation of the stratigraphy of Megalo Vouno from Pichler & Kussmaul (1980). **$M_1$**: quartz-latiandesitic scoriae, lapilli, and ashes; **$M_2$**: quartz-latiandesitic lavas; **$M_3$**: black andesitic lapilli; **$M_4$**: reddish andesitic scoriae; **$M_5$**: highly welded andesitic scoriae; **$M_6$**: andesitic lavas; **I**: dacitic to quartz-latiandesitic ignimbrites; **Bo**: rhyodacitic ash-flow and pumice-fall deposits: **Bor**: reworked Bo material.

These deposits have later been covered by ignimbrite flows of the Cape Riva eruption (I), rhyodacitic ash-flows and pumice fall of the Upper Pumice series (Bo) as well as reworked products of the Upper Pumice series (Bor).

According to Huijsmans & Barton (1990) Megalo Vouno can be divided into six stratigraphic units: MV1-MV6 (Fig. 4.2). MV1 (east) and MV2 (west) comprise the core of the complex and consist of an old ca. 150 m high lava shield built up by basaltic andesites in the lower part and low-silica andesites in the upper part. Depressions in the irregular surface of this shield are thought to be filled by Lower Pumice (LP) deposits followed by large, flow-banded domes and lavas of high-silica andesite. Some partly welded red scoria assigned to Upper Scoria 1 and 2 (US1 & US2) were also observed in these depressions (Fig. 4.2).

MV3 consists of grey-black cinders containing numerous flows and domes of MV5, which have basaltic to andesitic composition (shown as lines on Fig. 4.2).

MV4 denotes the red cinders covering much of the top of Megalo Vouno. These are thought to have been erupted by the Megalo Vouno and Kokkino Vouno cinder cones along with basaltic to dacitic lava flows (belonging to MV5) in the north-eastern flank of the complex.

Basaltic lava flows west of the Megalo Vouno core complex cover the stratigraphic units of MV3, MV5 and US2 and are collectively named MV6. As described below new studies have shown that these lavas are not a product of Megalo Vouno and have instead been assigned to the Skaros volcano by Druitt et al. (1999).

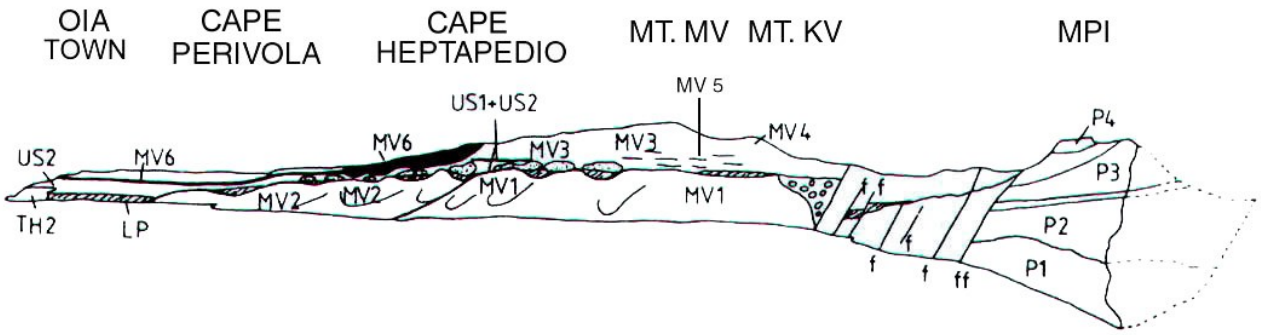


**Fig. 4.2.** Interpretation of the stratigraphy of the northern caldera wall by Huijsmans & Barton (1990). **P1-P4**: units of Micros Profitis Ilias volcano (MPI) after Huijsmans (1985); **f**: fault; **MV1-MV6**: units of Megalo Vouno volcano (see text for detailed description of products); **US1-US2**: deposits of Upper Scoriae 1 and 2 (units of Pichler & Kussmaul, 1980); **LP (hatching)**: Lower Pumice (LP1 and LP2; units of Pichler & Kussmaul, 1980); **TH2**: lavas of Thirassia volcano (unit of Pichler & Kussmaul, 1980); **MT. MV**: Mount Megalo Vouno; **MT. KV**: Mount Kokkino Vouno; **MPI**: Micros Profitis Ilias volcano.
Modified after Huijsmans & Barton (1990).

Hansen (1997) gave a detailed stratigraphic description of the uppermost part of Megalo Vouno and its relations to the neighbouring volcanoes, Micros Profitis Ilias and Thirassia. Hansen uses the eruption chronology of Pichler & Kussmaul (1980) (with minor modifications by Druitt et al. (1989)), which deviates a lot from the revised ages of Druitt et al. (1999) (Table 4.1). Nineteen of her collected samples belong to the MV5 unit of Huijsmans & Barton (1990) (or

Peristeria 3 of Druitt et al. (1999) ~~s~~see following pages) and three samples were dikes cutting through the Megalo Vouno complex.

The latest work on the stratigraphy of Megalo Vouno (as well as the rest of Santorini) gives some new subdivisions primarily based on new field work and dating of rock samples (Druitt et al., 1999). As can be deduced from Nicholls (1971) this latest stratigraphy has mainly been based on the old stratigraphic divisions made by Reck in 1936.
According to Druitt et al. (1999) the Megalo Vouno volcano complex is subdivided into three units (Figs. 4.3 and 4.4) followed by scoria eruptions from the Megalo Vouno and Kokkino Vouno cinder cones:
(1) a core of andesitic lavas and tuffs (Peristeria 1 ~~**av1**~~),
(2) massive silicic andesite lava flows (Peristeria 2 ~~**av2**~~), and
(3) a succession of thin andesitic and basaltic lavas, with subordinate dacites (Peristeria 3 – **av3**).

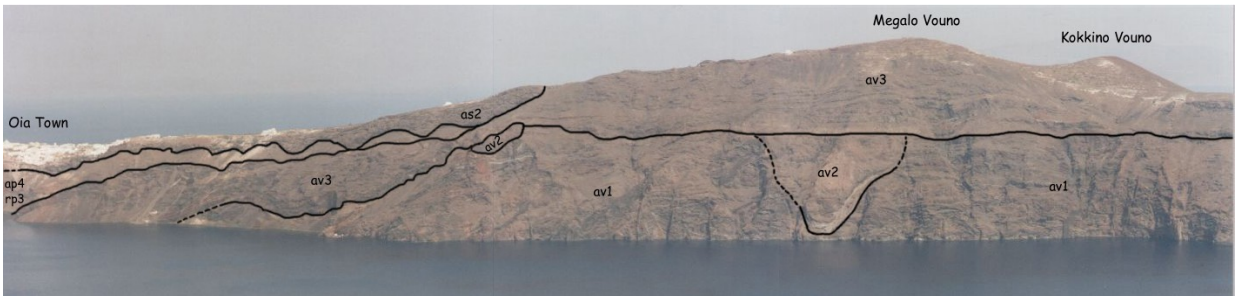


**Fig. 4.3.** Stratigraphic interpretation of Peristeria volcano (only the Megalo Vouno area is shown on photo). Units after Druitt et al. (1999): **av1**: Peristeria 1; **av2**: Peristeria 2; **av3**: Peristeria 3; **rp3**: Lower Pumice 1 & 2; **ap4**: Middle Tuff; **as2**: Skaros lavas. Several of the dikes sampled in this study can be faintly seen in the caldera wall. **av3** is partly covered by scoria of Megalo Vouno and Kokkino Vouno cinder cones.

Peristeria 1 comprises the lower 120-180 m of the cliffs below the Megalo Vouno summit and consists of andesitic lava flows, tuffs, breccias and hyaloclastites cut by several dikes. This fits well with the stratigraphic units MV1 and MV2 of Huijsmans & Barton (1990) except that Druitt et al. (1999) include the whole of the neighbouring volcano Micros Profitis Ilias into Peristeria 2 and 3 (Fig. 4.4), while Huijsmans & Barton (1990) believe it to be a separate volcano.
Dating of a Peristeria 1 andesite from the lowest stratigraphic level yielded an age of 528 ± 23 ka (Fig. 4.4).
Peristeria 2 is thought to occur in three different places:
(a) as small silicic andesite domes that occur sporadically at the contact between Peristeria 1 and 3 (Figs. 4.3, 4.4 and 4.7).
(b) as a funnel-shaped mass of silicic andesite lined with tuff directly below the Megalo Vouno summit. This is thought to represent either remains of a lava-filled vent or a skin of lava adhering to an ancient cliff (Fig. 4.5).

(c) as massive silicic andesite flows that form the base of the caldera wall of the neighbouring volcanic complex Micros Profitis Ilias. A sample from the base of Micros Profitis Ilias yielded a K-Ar date of 496 ± 16 ka (Fig. 4.4).

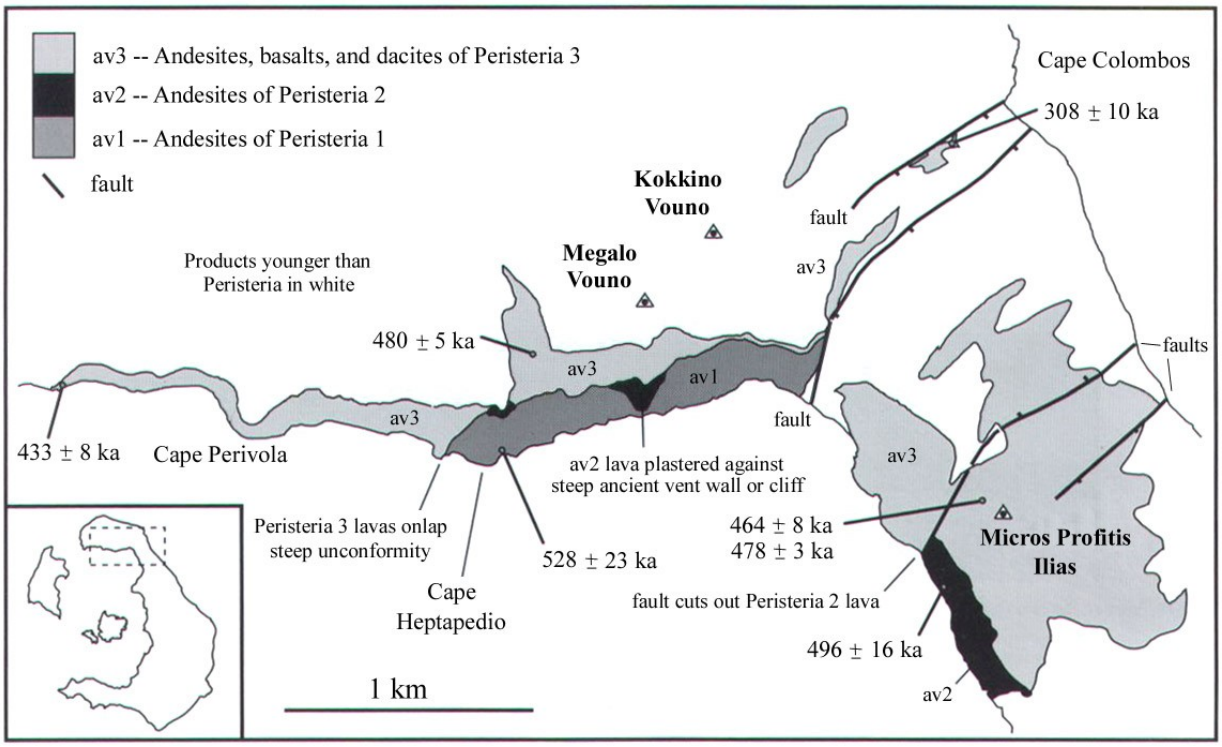


**Fig. 4.4.** Geological map of the remains of Peristeria Volcano. Products younger than Peristeria are shown in white. After Druitt et al. (1999).


**Fig. 4.5.** Funnel-shaped silicic andesite (**av2** of Druitt et al. (1999)) below MV summit interpreted as the wall of an ancient vent (Druitt et al., 1999). Several dikes can be seen crossing the strata on either side.

The three mentioned occurrences have been assigned to the same stratigraphic unit based on similar chemical compositions and stratigraphic positions. The existence of both Lower Pumice (LP) and Upper Scoria 1 & 2 (US) in the area between Peristeria 1 and 3, as suggested by Huijsmans & Barton (1990), is ruled out by Druitt et al. (1999) because of new age data from the overlying products of Peristeria 3 (MV5 of Huijsmans & Barton (1990)). Dating of a Peristeria 3 lava from Megalo Vouno has yielded a K-Ar age of 480 ± 5 ka (Fig. 4.4), which is much older than the dates previously obtained for the pyroclastics:

LP1: 203 ± 24 ka (Druitt et al., 1999), 67-138 ka (Seward et al., 1980); LP2: ca. 160 ka (Keller, 1981), 172 ± 33 (Druitt et al., 1999); US2: 37.9 ± 0.2 ka (Mellors & Sparks, 1991), 79 ± 8 ka and 54 ± 3 ka (both Druitt et al., 1999). Furthermore it is possible to see Peristeria 3 lying stratigraphically below Lower Pumice deposits below the town of Oia (Figs. 4.3 and 4.6).

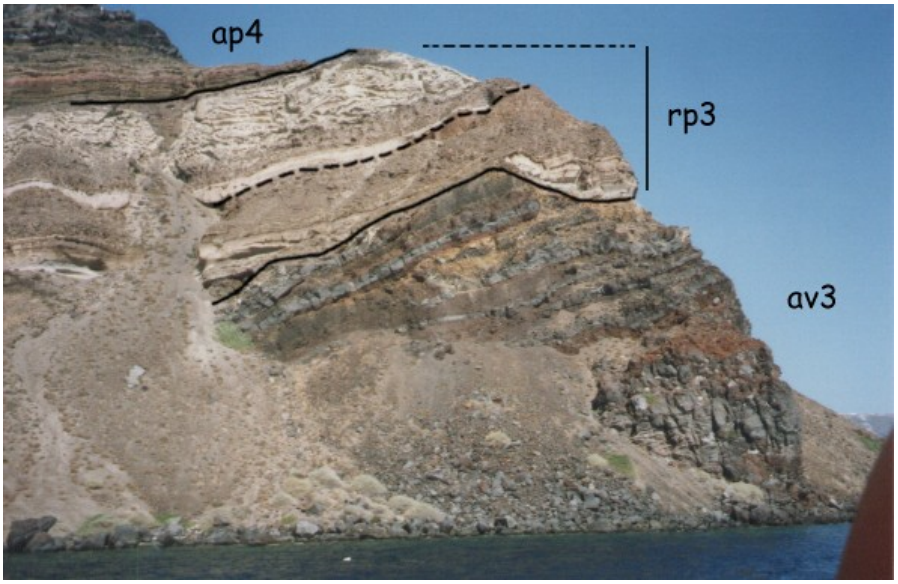


**Fig. 4.6.** Profile in the caldera wall in the westernmost part of Megalo Vouno (near Cape Perivola). The profile is seen from the inside of the caldera just east of and below Oia. Units after Druitt et al. (1999): **av3**: lavas of Peristeria 3; **rp3**: Lower Pumice tuffs (the dashed line in the cliff separates Lower Pumice 1 and Lower Pumice 2); **ap4**: Middle Tuff sequence. Just above ap4 there are lava flows of Skaros volcano (as2) not visible in this photo. This sequence can be seen on Fig. 4.3.

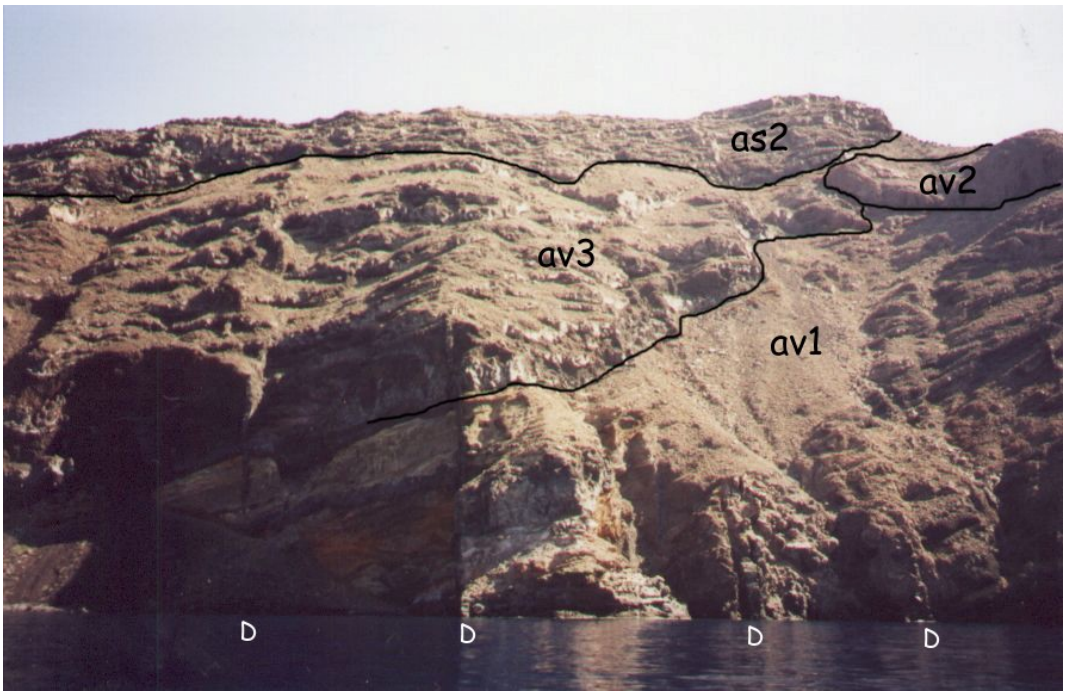


**Fig. 4.7.** Stratigraphy of the Megalo Vouno volcano complex (near Cape Heptapedio) using the units of Druitt et al. (1999): **av1**: the eroded remains of Peristeria 1; **av2**: silicic andesite lava thought to belong to Peristeria 2 along with the funnel-shaped vent shown in Fig. 4.5 and the base of Micros Profitis Ilias; **av3**: lavas and tuffs of Peristeria 3; **as2**: lava flows that overflowed the Skaros shield —termed "Andesites of Oia" in Table 3.1 (also Fig. 4.8). **D**: some of the dikes sampled in this study: From left to right: MVD-B 00-14, MVD-B 00-15, MVD-B 01-17 and MVD-B 01-18 (MVD-B 01-16 is concealed in the bay and therefore not visible in this photo).

Peristeria 3 comprises aphyric to plagioclase-phyric lavas and tuffs up to 140 m thick. Some of the dikes cutting Peristeria 1 are thought to have fed the Peristeria 3 lava flows (Nicholls, 1971; Druitt et al., 1999). It is uncertain whether an andesitic lava flow near Cape Colombos is the result of continued flank eruptions on Peristeria (dated at 308 ± 10 ka; Fig. 4.4). Although Druitt et al. (1999) have mapped it as belonging to Peristeria 3, it does not seem related to the other eruptions.

In general Druitt et al. (1999) have described Peristeria volcano as being a composite stratovolcano four kilometres in diameter; its summit lay about 350 m above the contemporary sea-level, which is only 20 m above the present height. Druitt et al. (1999) have also calculated the sub-aerial volume of the volcano to have been at least 2 $km^3$. According to the obtained ages, construction of the complex must have begun about 530 ka and lasted until at least 430 ka. South-east of Peristeria the neighbouring Skaros volcano laps up against the remains of Peristeria volcano (the part also known as Micros Profitis Ilias). K-Ar dating on a Skaros sample below Imeroviglio has yielded an age of 67 ± 9 ka (Fig. 4.8) (Druitt et al., 1999). The western margin of Peristeria (below Oia) is overlapped by pyroclastic deposits of the Lower Pumice 1 and 2 (203 ± 24 ka; Druitt et al., 1999) and Middle Tuff sequences, followed by lava flows of the Skaros volcano ( Andesites of Oia in Table 3.1) (Figs. 4.3, 4.6 and 4.8).

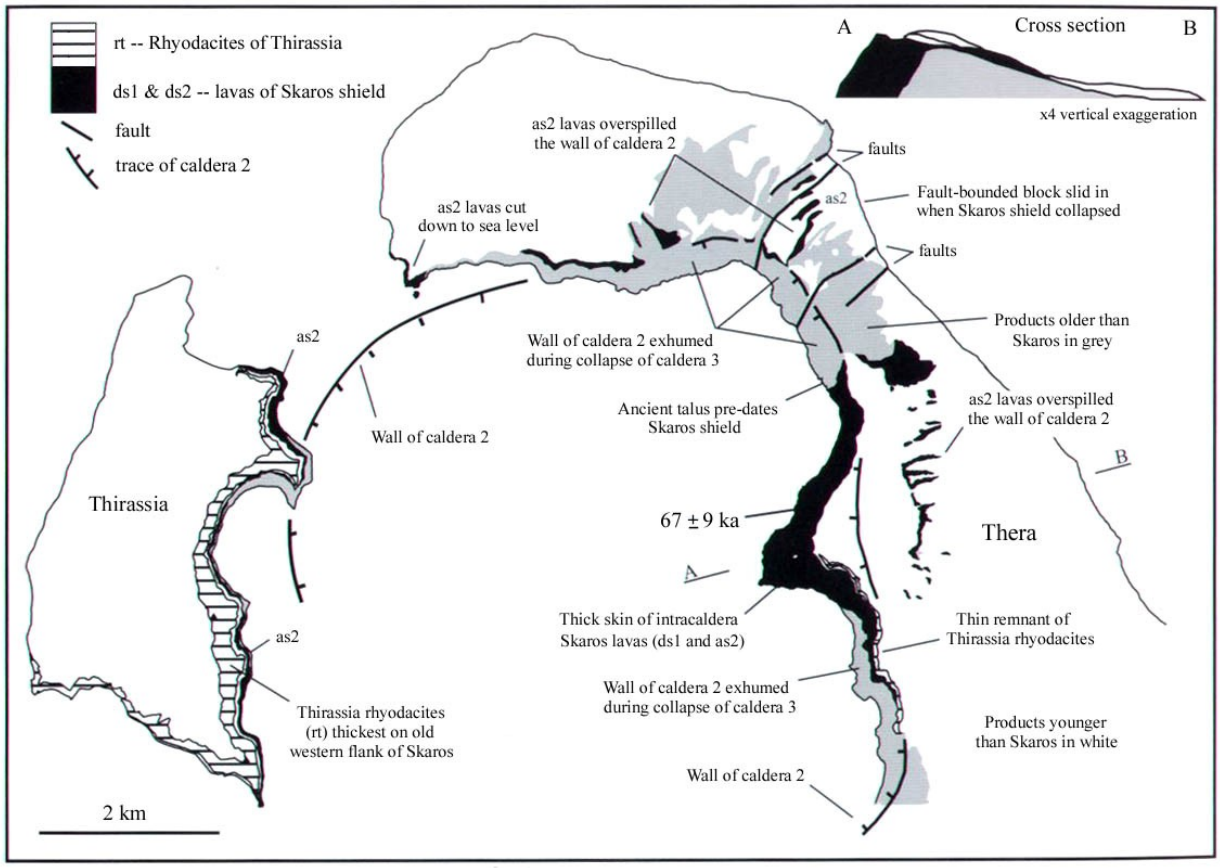


**Fig. 4.8.** Map of Thirassia and northern Thera showing the remains of the Thirassia-Skaros complex and its relations with the eroded Peristeria volcano. The profile A-B (top right corner) shows how the volcano shield infilled and overspilled the pre-existing caldera. After Druitt et al. (1999).

The cinder cones of Megalo Vouno and Kokkino Vouno were erupted on top of the eroded Peristeria volcano in the Middle Tuff period (Table 3.1). The two cinder cones together with products of the Colombos tuff ring lie on a NE-SW lineament thought to be connected with the presence of a basement fault (Fig. 4.9).

The products of the two cones form a single sheet and therefore must have erupted simultaneously. Within the scoria beds welded spatter can be seen which has locally remobilised as lava flows. The spatter is suggested by Druitt et al. (1999) to have been fed by lava fountains from a NNE-SSW fissure separating the two cones. Several of the dikes seen in the caldera wall can be faintly traced up the cliffs of the Megalo Vouno volcano complex into the scoria and may be related to this fissure.

As indicated on Figs. 4.9 and 4.10 four NE-SW-trending faults (F1-F4) have been located in the north-east corner of Thera in the area between Megalo Vouno and Micros Profitis Ilias. According to Druitt et al. (1999) it was the widespread Cape Riva eruption (caldera 3) and collapse of the Thirassia-Skaros complex (Table 3.1; Fig. 3.5) that triggered insliding of a large (800 m wide) block along two curved faults (F2 and F3: Fig. 4.10). This is the reason why Peristeria 2 of Micros Profitis Ilias is seen at and just above sea-level while Peristeria 2 products are found much higher in the cliffs on Megalo Vouno (Fig. 4.4).

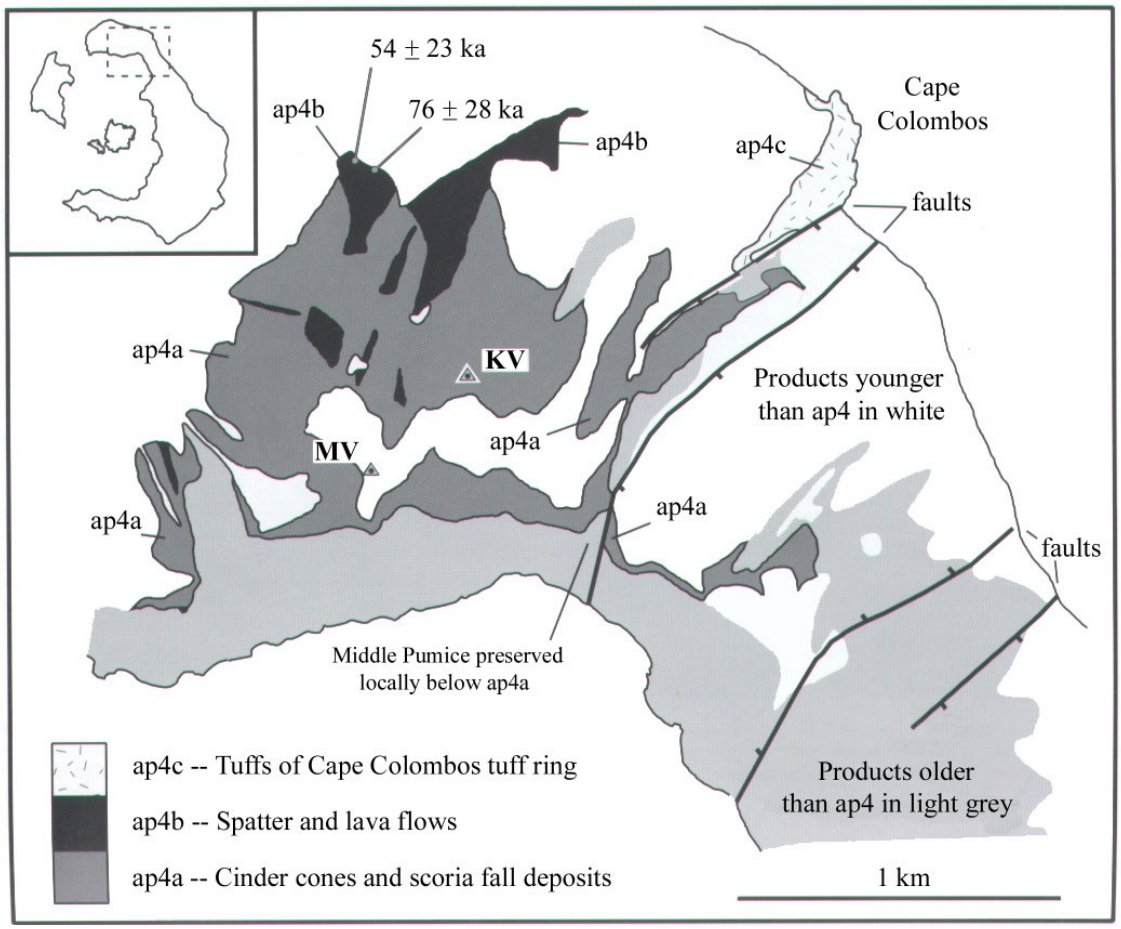


**Fig. 4.9.** Simplified map of products of the Megalo Vouno (MV) and Kokkino Vouno (KV) cinder cones and the Colombos Tuff Ring. After Druitt et al. (1999).

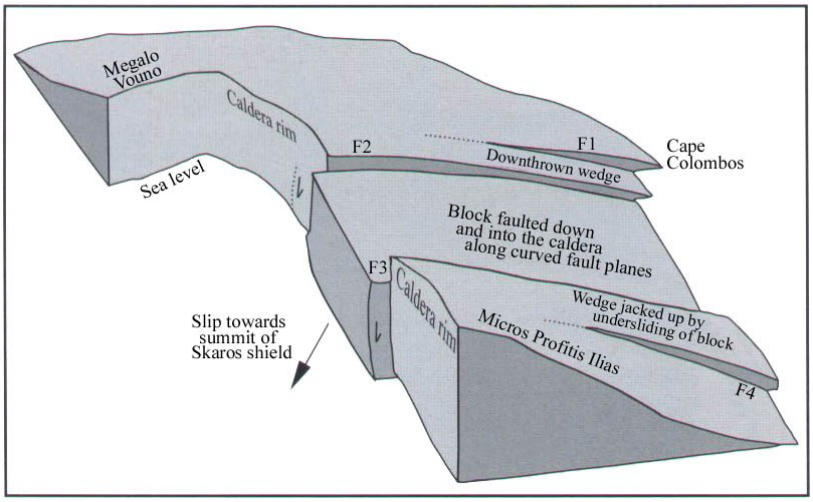


**Fig. 4.10.** Field relationships in the caldera wall of north-east Thera. The Cape Riva eruption and collapse of the Thirassia-Skaros complex triggered insliding of the large block between faults F2 and F3. According to Druitt et al. (1999) earlier studies suggested that the resulting graben was of purely tectonic origin because it parallels the regional fault trend. Druitt et al. (1999) on the other hand think that the insliding took place when the Thirassia-Skaros complex collapsed and left a depression and tectonic instability in the north-east area. After Druitt et al. (1999).

Following the foot path on top of Megalo Vouno it is possible to see a few remains of products that are not related to the Peristeria (or Megalo Vouno) volcano; these are welded ignimbrites of the Cape Riva eruption (18 ka; Pichler & Friedrich, 1976 or 22 ka; Bard et al., 1990) (Fig. 4.11) and rhyodacitic tuff of the younger Minoan Eruption.

**Fig. 4.11.** Welded ignimbrite on top of Megalo Vouno. The ignimbrite is a product of the ca. 18-22 ka old Cape Riva eruption.

## 4.2. Field observations

Thirty-six dikes cutting the Megalo Vouno volcano in northern Santorini were collected in the years 2000 and 2001. Furthermore, to supplement the work of Hansen (1997), a lava flow in the caldera wall was sampled via boat (MV-B 01-38) and a piece of scoria from the Megalo Vouno cinder cone was collected near the top (MV-T 01-37).

Twelve of the 36 dikes were collected on top of Megalo Vouno (sample numbers: "MVD-T"), either along the foot path by the steep caldera wall (ca. 300 m above sea-level) or on the north-western side of the Megalo Vouno cinder cone. These are all examples of dikes that have reached the top, as opposed to the majority of dikes, which stop at different levels in the caldera wall. Some of the dikes are thought to have fed lava flows (Nicholls, 1971 and subsequently cited by Druitt et al., 1999; Friedrich, 2000) but this has not been observed. Due to weathering, the dikes can now be seen to stand out because the surrounding unconsolidated lapilli has been more easily eroded (Fig. 4.12).

The other 24 dikes were sampled at sea-level from a rubber dinghy (sample numbers: "MVD-B"). This way of sampling presented great difficulty; firstly because the sea in both field seasons was rough and sailing on most days was too dangerous, and secondly because the caldera wall near sea-level is practically vertical and there are only two places along the entire wall where it is possible to go ashore. When the weather allowed, samples were collected directly from the boat by holding it as close to the wall as possible whilst at the same time avoiding a puncture on the protruding rocks.

The dikes collected at sea-level are all more or less weathered and since most have been partially altered because of interaction with seawater it was difficult to get fresh samples.

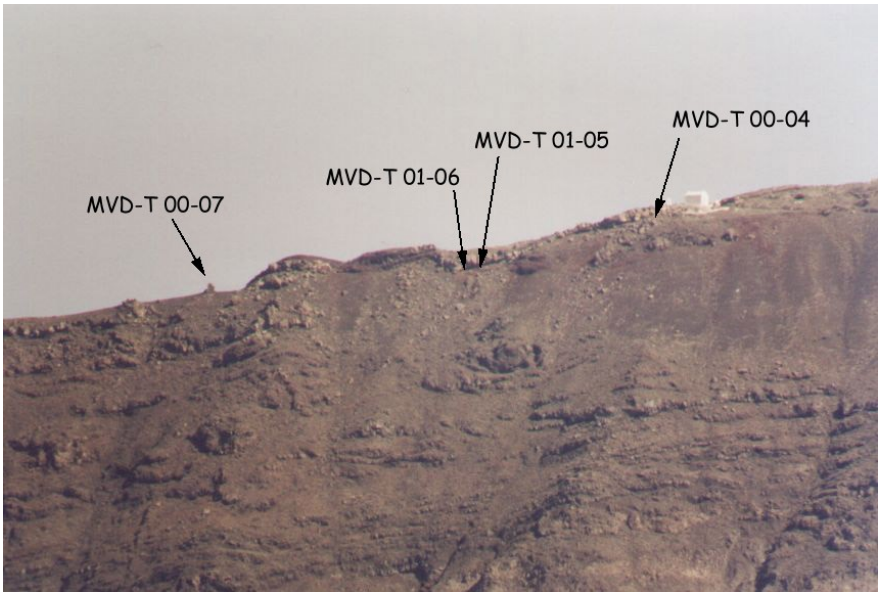


**Fig. 4.12.** Location of four of the dikes sampled on top of Megalo Vouno. As can be seen it is difficult to determine which dikes are the same as the dikes collected at sea-level, because none of the dikes are well defined all the way down the caldera wall.

The strike of the dikes has been measured and the exact position of the sampling site has been mapped with GPS using the WGS 84 datum (Lat°min.min/1000; Long°min.min/1000) (Table 4.2).

The exact position of the sampled dikes has been mapped (Fig. 4.13) using a section of the map of Santorini by Pichler & Kussmaul (1980) as base. Two fixed points were used: Cape Colombos (N 36°28.402; E 25°25.297) and the end of the pier in Ammoudi harbour below Oia (N 36°27.626; E 25°22.192).

The strike of the dikes can be very variable even over short distances because most of the dikes curve. The strike of some of the dikes could not be measured because they were only seen in two dimensions in the caldera wall and some were so wide that the strike was impossible to gauge. However, the strike has been recorded for most of the dikes to give an idea of their general orientation. The majority have a N-S strike or NNE-SSW (around 24°N) while only four dikes strike towards the NW.

The dip of the dikes has not been recorded, because most of the dikes were too uneven to get a precise measure or they were so curved that the dip changed completely over a few meters. In general they seemed to be near vertical (dip ca. 70-90°).

**Table 4.2.** Strike, width and sampling position of the 36 dikes sampled along the caldera wall and on top of Megalo Vouno in this study.

| Sample No | Width (cm) | Strike (°N) | Latitude | Longitude |
|---|---|---|---|---|
| MVD-T 00-01 | 15-50 | 7-20 | N 36°27.795 | E 25°24.491 |
| MVD-T 01-02 | 20 | 10 | N 36°27.774 | E 25°24.458 |
| MVD-T 00-03 | 40-70 | 11-14 | N 36°27.759 | E 25°24.430 |
| MVD-T 00-04 | 50-100 | 22 | N 36°27.709 | E 25°24.237 |
| MVD-T 01-05 | 30-100 | 3 | N 36°27.701 | E 25°24.190 |
| MVD-T 01-06 | 30-70 | 357 | N 36°27.708 | E 25°24.179 |
| MVD-T 00-07 | 50-80 | ca. N-S | N 36°27.700 | E 25°24.114 |
| MVD-T 01-08 | 40 | 357-3 | N 36°27.602 | E 25°23.790 |
| MVD-T 00-09 | 120 | 18-24 | N 36°27.859 | E 25°24.244 |
| MVD-T 00-10 | 40 | 22 | N 36°27.793 | E 25°24.224 |
| MVD-T 00-11 | 100-200 | 2-5 | N 36°27.809 | E 25°24.187 |
| MVD-T 00-12 | 80 | 3-5 | N 36°27.777 | E 25°24.168 |
| MVD-B 00-13 | 80-100 | not measured | N 36°27.489 | E 25°23.739 |
| MVD-B 00-14 | 80-100 | not measured | N 36°27.470 | E 25°23.752 |
| MVD-B 00-15 | 100-150 | 17-28 | N 36°27.455 | E 25°23.778 |
| MVD-B 01-16 | 400-500 | 15 | N 36°27.466 | E 25°23.830 |
| MVD-B 01-17 | 200-400 | 322 | N 36°27.466 | E 25°23.854 |
| MVD-B 01-18 | 50 | 22 | N 36°27.456 | E 25°23.865 |
| MVD-B 01-19 | 20-40 | 24 | N 36°27.457 | E 25°23.875 |
| MVD-B 01-20 | 100 | 338 | N 36°27.440 | E 25°23.923 |
| MVD-B 01-21 | 300-350 | 26 | N 36°27.461 | E 25°23.998 |
| MVD-B 01-22 | 150 | 320 | N 36°27.490 | E 25°24.014 |
| MVD-B 01-23 | 150-180 | 320 | N 36°27.479 | E 25°24.060 |
| MVD-B 01-24 | 100-250 | 358 | N 36°27.487 | E 25°24.061 |
| MVD-B 01-25 | 400 | 28 | N 36°27.486 | E 25°24.066 |
| MVD-B 01-26 | 250-300 | 18 | N 36°27.486 | E 25°24.081 |
| MVD-B 01-27 | 15-40 | 24 | N 36°27.485 | E 25°24.093 |
| MVD-B 01-28 | 30-60 | 25 | N 36°27.513 | E 25°24.108 |
| MVD-B 01-29 | 500-800 | 6 | N 36°27.515 | E 25°24.153 |
| MVD-B 01-30 | 200 | 356 | N 36°27.528 | E 25°24.185 |
| MVD-B 00-31 | 70-80 | 358 | N 36°27.590 | E 25°24.619 |
| MVD-B 00-32 | 300 | 6-12 | N 36°27.596 | E 25°24.633 |
| MVD-B 00-33 | 300 | 6-12 | N 36°27.597 | E 25°24.634 |
| MVD-B 00-34 | 300-400 | 4 | N 36°27.593 | E 25°24.636 |
| MVD-B 00-35 | 800-1000 | not measured | N 36°27.590 | E 25°24.687 |
| MVD-B 00-36 | 60 | 350 | N 36°27.573 | E 25°24.728 |

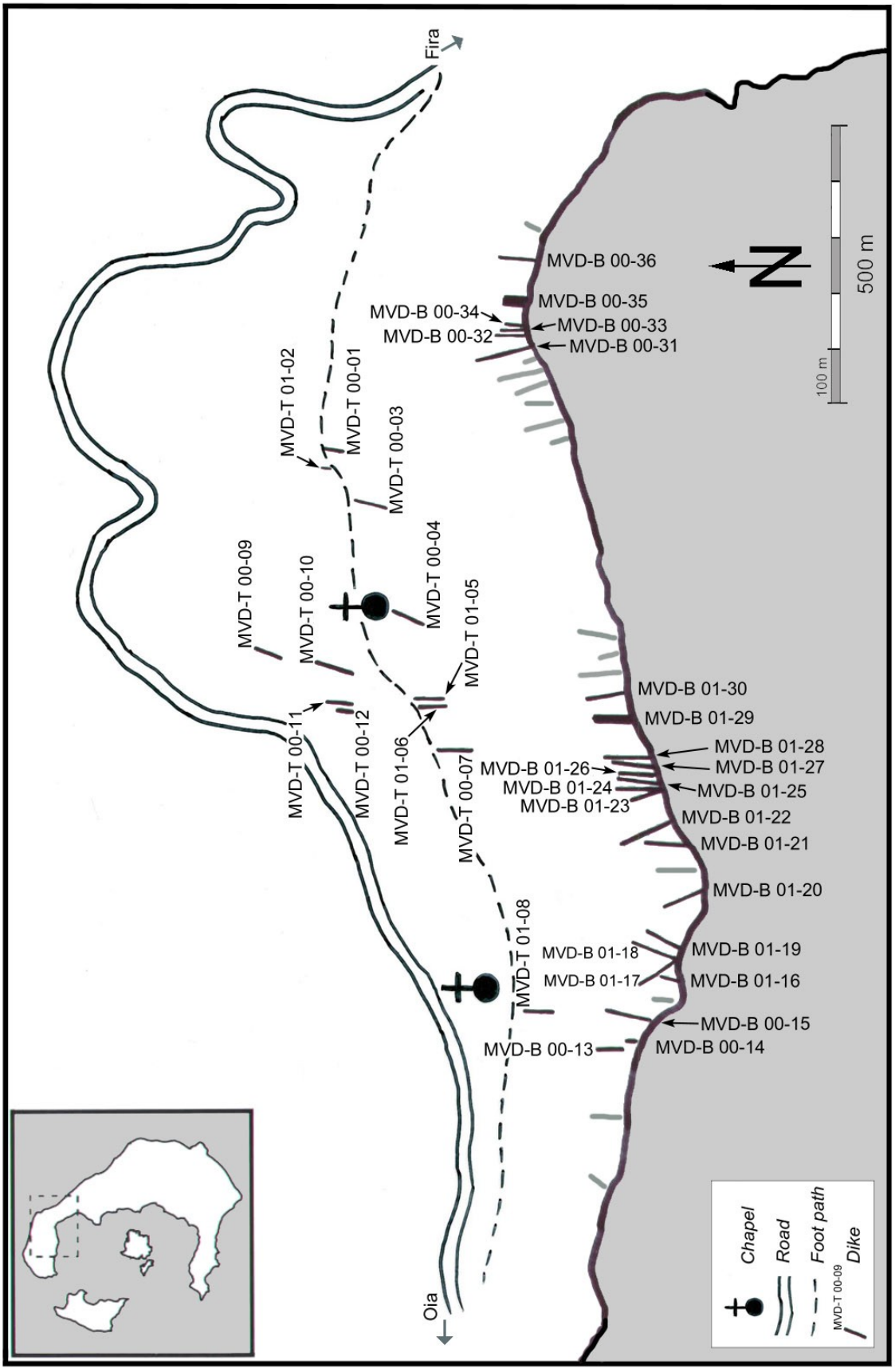


**Fig. 4.13.** Map of the Megalo Vouno area in the north-east corner of Thera, showing locations of the dikes sampled in this study. The exact position of the dikes has been measured by GPS and mapped using two fixed coordinates and the map by Pichler & Kussmaul (1969/70) as a base. The strike of the dikes shown is true, whereas the length and width of each dike are approximate. Unnumbered dikes shown in grey represent dikes that were not sampled due to inaccessibility. Position and strike of these dikes were not obtained and their locations on the map are only to indicate their presence. The field work for the mapping was carried out in the years 2000 and 2001.

The dikes are spread quite evenly throughout the Megalo Vouno complex, and only make up a very small percentage of the total cliff (<5%) from Cape Perivola to the fault between Megalo Vouno and Micros Profitis Ilias (Figs. 4.2 and 4.4). Below the town Oia (west of Cape Perivola) only two dikes were observed along a ca. 1.5 km stretch. Along the following ca. 2 km (to the east), at least 38 dikes were observed near sea-level and several more could be seen further up in the cliffs of the Megalo Vouno complex (Fig. 4.14). Some dikes were only few metres apart, others several tens of metres apart. There seemed to be a gap of ca. 200 metres in the area of the funnel-shaped andesite (Figs. 4.3, 4.4 and 4.5), where no dikes were observed (Fig. 4.13). More dikes can be observed cutting through the av2 part of the neighbouring Micros Profitis Ilias volcano (Fig. 4.4) but none of these were sampled for this study.

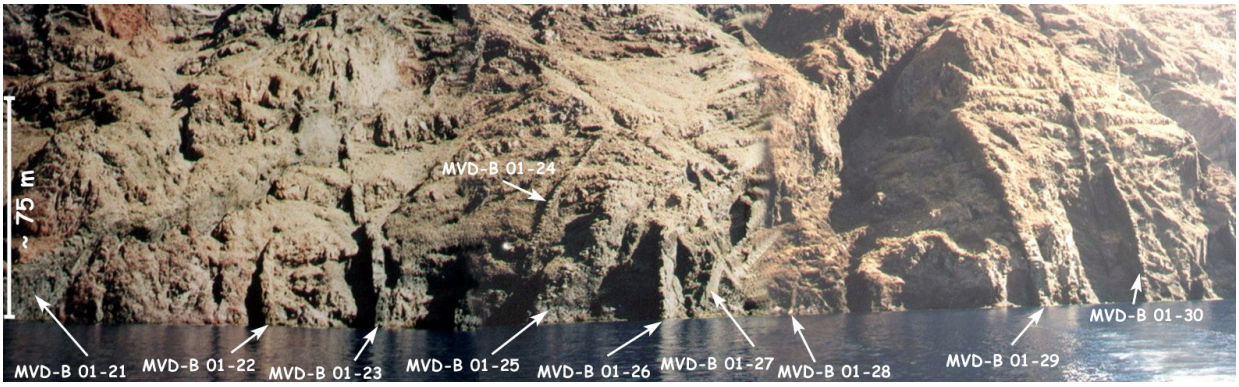


**Fig. 4.14.** A selected area of the caldera wall of Megalo Vouno showing ten of the dikes sampled at sea-level. As can faintly be seen dike MVD-B 01-21 cuts the red dike MVD-B 01-22 but is then itself cut by MVD-B 01-23 (see also Fig. 4.15).

Only in one place has a relationship between dikes been detected in the case of dikes MVD-B 01-21, MVD-B 01-22, and MVD-B 01-23 as can be seen in Figs. 4.14 and 4.15.

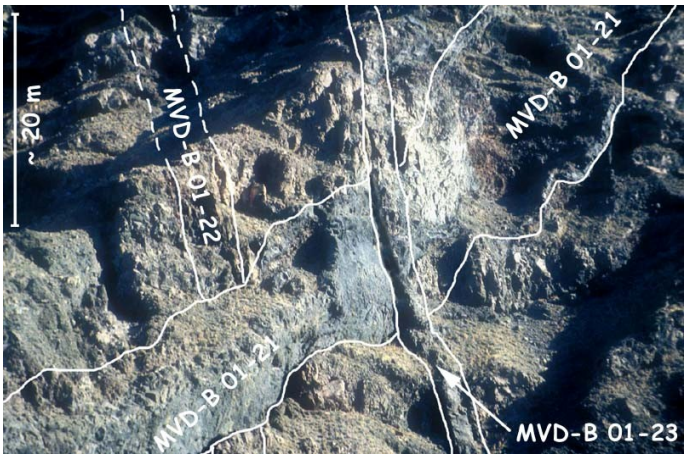


**Fig. 4.15.** Relationship between dikes in the caldera wall. Ca. 40 m above sea-level dike MVD-B 01-21 cross-cuts MVD-B 01-22 and is then itself cut by MVD-B 01-23.
Although MVD-B 01-21 is wider than the other two dikes (Table 4.2) its width is exaggerated visually in this photo due to the strike of the dike and erosion of the caldera wall, which has made some of the dikes stand out like steep wall faces (see also Appendix A).

Photos of all the sampled dikes are provided in Appendix A and a petrographic description is given in Chapter 6 (photos of selected minerals in thin section are placed in Appendix D).

## 4.3. Previous studies of the Megalo Vouno dikes

In 1879, Fouqué made detailed drawings of and described 66 dikes in the caldera wall of north-east Thera (Fig. 4.16) (Fouqué, 1998). Samples of 59 of the dikes were collected, but some could not be sampled because they were impossible to reach or in other ways inaccessible. The orientation and width of the dikes was determined and comments were made on their mutual relations and their relationship to the wall rocks. Finally the dikes were also studied in thin section. The dikes studied varied in thickness from 20 cm up to 10 m but most were found to be between one and two metres wide. Two main trends of the dikes were observed, the majority striking either 30°NW or 30°NE. From the detailed study of thin sections it was concluded that there was no relationship between the mineralogical composition of the dikes and their orientation. On the other hand, Fouqué observed that the dikes trending 30°NW were brownish-yellow, whereas the ones trending 30°NE were dark black and predominantly thinner than the former. Fouqué ascribes this to the 30°NW trending dikes being more viscous at the time they were emplaced as well as having been more strongly oxidised. Neither of these observations has been confirmed in this study, although all the collected dikes of reddish brown colour seem to have a trend close to 30°NW.

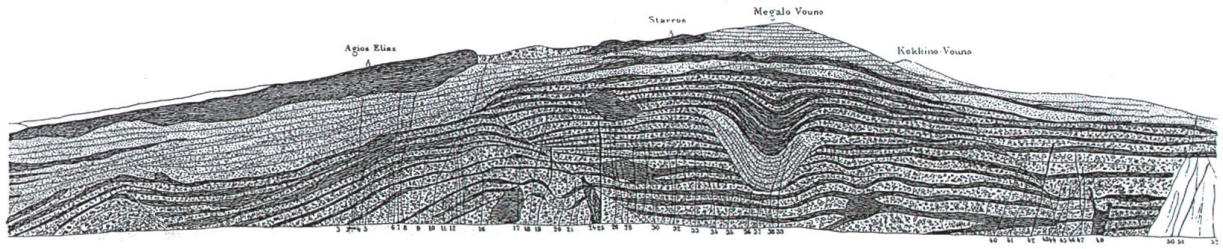


**Fig. 4.16.** Fouqué s'sketch of the Megalo Vouno complex cut by dikes. After Fouqué (1998).

From my own observations it seems likely that there are at least 66 dikes in the caldera wall of north-eastern Thera. Only 49 of the dikes observed by Fouqué, however, cut the Megalo Vouno volcano complex, the rest cut the neighbouring Micros Profitis Ilias. In addition to the 36 dikes sampled for this study, around 14 other dikes were observed along the wall (as indicated on Fig. 4.13) but these were inaccessible from both sea-level and the top, and can only be collected with the aid of climbing equipment (Fig. 4.17).

Nicholls (1971) recognised over 60 dikes in the caldera wall of north-east Thera, ranging in width from ca. 10 cm to 3 m. Four of the nine sampled dikes were basalts, whereas the rest were trachyandesites and trachydacites. The rest of his study describes in further detail the mineralogy and geochemistry of the dikes along with other lavas from Santorini.

Hansen (1997) collected three dike samples and integrated these in a study of the overall petrology and volcanology of the north-eastern volcano centres. As mentioned briefly in Section 4, the study resulted in recognition of two geochemical trends and, based on their geochemistry, her collected dikes were assigned to trend 2. It was furthermore shown that the rocks in trend 2 could not have evolved through fractional crystallisation alone, and magma mixing was suggested as a possible mechanism. In Chapter 7, the two geochemical trends have been compared with the dike geochemistry obtained in the present study.


**Fig. 4.17.** Accessibility of dikes in the caldera wall of north-east Thera. The wide light-grey dike on the right is easily reachable from sea-level, whereas the thin, dark dike on the left outcrops several metres above sea-level. At least five of the observed dikes were unreachable in similar fashion. Other dikes could not be collected because they were near vertical and there was too great a risk of falling rock shards damaging the rubber dinghy, while hammering a sample off the rock.

The dikes sampled by Puchelt et al. (1990) were studied in thin section, and geochemical analyses were carried out showing that the dikes belong to the calc-alkaline suite and range from high-alumina basalts to dacites. Finally the study considers three models for the development of fissures and dike extrusion (Fig. 4.18):

(I) Tensional forces (II) Convex bending (III) Concave bending

Model I was ruled out because they claim tensional forces are not present in this part of the Aegean Sea. Model II was also discarded because convex bending requires either intrusion of magma or compressional forces and would result in dikes being wider at the top than at their lower end.

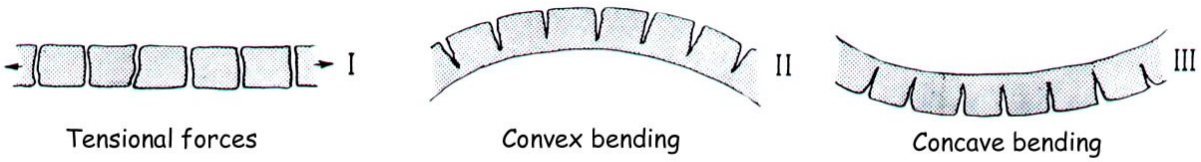


**Fig. 4.18.** Three models of dike extrusion proposed by Puchelt et al. (1990). Concave bending (III) was chosen as the most probable since it reflects the stress pattern in the area and it allows easy access for the dikes up through the strata.

The third model was then accepted as the most likely since it is easier to open fissures in this way. Unfortunately, this model was also chosen on the grounds that the dikes were not thought to penetrate to the surface, which in fact is not the case. However, the dikes I collected at sea-level tended to be wider than dikes collected at the surface, which could indicate that they thin-out slightly towards the top. The concave bending is thought to have arisen when an empty space formed above the underlying magma chamber and subsidence took place, finally leading to caldera collapse. This is in accordance with the model of insliding in the area as suggested by Druitt et al. (1999) (Fig. 4.10). Puchelt et al. (1990) also suggested that the dikes were not extruded all at once but through various periods of magma intrusion. The variable chemistry of the dikes indicated to them that there was a long time span between extrusions or possibly that the material originated from different magma chambers.

Eleftheriadis et al. (1998) studied a selection of dikes in the Santorini caldera wall and found that the majority strike NE-SW; the dip of the dikes is mostly vertical. Major and trace element geochemistry was performed on 17 dikes showing a range in $SiO_2$ composition from 53 to 65 wt.%. Following the classification scheme of Peccerillo & Taylor (1976), the dikes were classified as basaltic andesites, andesites, high-K andesites, dacites and high-K dacites belonging to the calk-alkaline to high-K calc-alkaline series.
Petrographic studies showed a porphyritic texture with plagioclase, clinopyroxene, olivine and orthopyroxene phenocrysts set in a holocrystalline to glassy matrix. Intergranular to intersertal textures and glomeroporphyritic aggregates were reported as common.
Based on the geochemistry the dikes were divided into two groups; a high-silica Group A (59 to 65 wt.% $SiO_2$) and a low-silica Group B (53 to 57 wt.% $SiO_2$). The low-silica group was characterised by the presence of olivine whereas the high-silica group contained orthopyroxenes. As one would expect, the high-silica group was found to have higher SREE, higher LREE enrichment and higher negative Eu anomalies than the low-silica group. On the basis of combined major, trace plus Sr and O isotope data it was concluded that the parental basaltic magma was derived by no more than 10% partial melting of a slightly LILE enriched spinel lherzolite.

Geochemical data for the present study are presented in Chapter 7 plus Appendix E and the petrogenesis of the dikes is discussed in Chapter 8.

# 5. Analytical methods

All sample preparations and geochemical analyses described below were carried out at the Geological Institute, University of Copenhagen.
Procedures followed in the mass spectrometry laboratory are described in detail in Appendix B and analytical uncertainty is given in Appendix C.

## 5.1 Thin section and general preparation

For petrographic analysis, blocks of all samples (except MV-T 01-37; a porous scoria) were cut on a water-cooled diamond saw and handed into the thin section laboratory. Technician Toni Larsen then mounted the samples on glass plates and polished them to the desired thickness of 30 mm for use in a petrological microscope.
Of the remaining rock material individual samples were roughly crushed in a tungsten carbide jaw crusher and further crushed finely by hand using a hammer and a steel mortar. The resulting chips were finely powdered (<4 µm) in a swing mill with an agate mortar shaking at 760 rpm for 30 minutes. The agate mortar was chosen in preference to the tungsten carbide mortar to avoid contamination of the samples with the elements W, C, Co and Ta. The resulting powders were later used in preparation of tablets for XRF analysis, for isotope geochemistry and were handed into laboratories for both major element analysis and ICP-MS data. During preparation, great care was taken to avoid contamination by carefully cleaning all equipment with compressed air and methylated spirits between samples. The greatest risk of contamination was expected to take place in the mechanical agate mortar because of the greater overall surface area of each sample due to the small particle size. To further reduce the risk of cross-contamination among my own samples, the mortar was pre-contaminated with a small amount of the following sample before the main run.

## 5.2 Whole-rock geochemistry by XRF and ICP-MS

Major element oxides ($SiO_2$, $TiO_2$, $Al_2O_3$, FeO, $Fe_2O_3$, MnO, MgO, CaO, $K_2O$ and $P_2O_5$) were analysed by senior chemist Jørgen Kystol (GEUS), using X-ray fluorescence (XRF) on glass discs. In the rock-chemistry laboratory, volatiles were removed by igniting samples at 950 °C and LOI (loss on ignition) was determined. The resulting powders were mixed with sodium tetraborate that facilitates melting and, after heating, the homogenised melt was poured into a Pt-Au mould and cooled to a glass disc. The analyses were carried out on a multi-channel XRF spectrometer (Philips PW1606). Due to the use of sodium tetraborate, $Na_2O$ was analysed by atomic absorption spectrophotometry (AAS) using a Perkin Elmer PE2280 AAS instrument. Total Fe was determined by glass disc analysis, and FeO was determined using the metavanadate technique. $Fe_2O_3$ was finally calculated by subtracting the FeO content from $Fe_{total}$.

Trace elements (Nb, Zr, Sr, Rb, Zn, Ni, Cu, Pb, Ga, V, Cr, Sc, Co, Ba, Cl and S) were analysed by laboratory leader John Bailey (Geological Institute), using XRF on powder tablets. For each powder tablet 1.6 g whole-rock powder was used. A binding agent was added (a 2% PVA solution) and the powder was finally encased in boric acid. The tablet was then pressed into shape using an oil-pressure pump exerting a pressure of 8 tons for ca. 10 seconds.
The results given by the Philips PW1400 spectrometer are in counts per second, so recalculation to concentrations in ppm was done using the formula:

**ppm = net counts per second * mass-absorption coefficient * constant**

The laboratory leader supplied the constant for every trace element (determined by measurement of international standards under the same machine conditions), and the mass-absorption coefficient was calculated from the major element analysis.

Further trace elements (Y, Cs, La, Ce, Pr, Nd, Sm, Eu, Gd, Tb, Dy, Ho, Er, Tm, Yb, Lu, Hf, Ta, Th, and U) were analysed by ICP-MS (inductive coupled plasma-mass spectrometry) by senior chemist Jørgen Kystol (GEUS). Analyses were carried out on a Perkin Elmer ELAN 6100 DRC ICP-MS instrument after samples had been dissolved in HF and aerosolised at $6\text{-}10^4$ °K. Concentrations were obtained by identifying spectral lines and measuring their intensities.

## 5.3 Isotope geochemistry

All isotope analyses were carried out at the Geological Institute, University of Copenhagen.
I performed all separation procedures in the Sr-, Nd- and Pb-laboratories and constructed the filaments for the mass spectrometer. For the final run of samples on the mass spectrometer, I was assisted by laboratory technician Toby Leeper.

For Sr and Nd isotope separation, whole-rock silicate powders (200-300 mg) were dissolved in HBr, HF plus $HNO_3$ and finally HCl. Samples were washed through with 2M HCl and Sr was separated from REE with 2M HCl using AG50W-X8 100-200 mesh resin columns. Rare earth elements (REE) were washed with $H_2O$ and collected with 6M HCl. Sr separates were further washed with 3M $HNO_3$ on columns containing Sr-Specâ (EiChrom SR-B25-A resin) and Sr was collected with $H_2O$. REE were further cleansed for Ba using 2M $HNO_3$ and cleaned with 0.25M HCl before Nd was collected with 0.25M HCl on glass columns containing Bio-Beads SM2 80-180 mesh resin.
For Pb isotope separation, whole-rock silicate powders (100 mg) were dissolved in HBr followed by HF and $HNO_3$. Pb was collected in two steps on columns containing AG1x8 100-200 mesh resin. In the first step Pb was cleaned on glass columns with 1M HBr and 2M HCl

and collected with 8M HCl. After evaporation the same procedure was carried out on smaller glass columns.

Isotope analyses were performed on the TIMS (thermal ionisation mass spectrometer): a VG Sector 54-IT multicollector instrument.

Sr samples were set on a single Ta centre filament with 2 µl 1M $H_3PO_4$ and analysed dynamically. For each Sr sample six blocks (120 ratios) were run at 1250-1300 °C and ca. 3.5 A resulting in a signal between 800 mV and 3 V.

Nd samples were analysed using a three-filament configuration with two Ta side-filaments and a central Re filament. Nd samples were set on the outer Ta filament with 2 µl 0.2M HCl and analysed dynamically. For each Nd sample six blocks (120 ratios) were run at intensities of 3.8 A (centre filament) + 2.7 A (side filament) and temperatures between 1800-1830 °C resulting in a signal of 100 mV-1.2 V.

Pb samples were set on a Re centre filament with 2 µl silica gel plus 2 µl 1M $H_3PO_4$ and analysed statically. For each Pb sample five blocks (100 ratios) were run at 1100-1200 °C and 1.9-2.2 A resulting in a signal of 600 mV-7 V (for $^{208}Pb$).

# 6. Petrography

Thirty-six thin sections of Megalo Vouno dikes were prepared and studied in a petrographic microscope, and selected minerals and textures were later microphotographed. MV-B 01-38, a lava flow from Peristeria volcano, was also studied, while MV-T 01-37 was never prepared for thin section because of its porous nature.

Since mineral chemistry is outside the scope of this thesis, no exact mineral compositions have been obtained.

## 6.1 Petrographic features characteristic of dikes

When sampling the dikes, great care was taken to obtain as fresh rock samples as possible. Thus the glassy cooling-rim often found on dikes intruded through pyroclastic material and lava flows was typically avoided.

Many volcanic rocks show an increase in vesicularity and gas bubble size towards their centre, because the lower cooling rate of the interiors allows a greater time for vesiculation and interaction of gas bubbles (Herd & Pinkerton, 1997). Likewise, phenocrysts tend to accumulate in the centre of a dike, mainly due to the Bagnold effect. Due to the difficulties in sampling from a boat, it was not possible to obtain samples from the same part of each dike, and this has resulted in a mixture of samples from centre parts as well as outermost parts. Because phenocryst and vesicle distribution can vary within a single dike, the amount of phenocrysts and vesicles observed is not strictly typical for the dike in question. The studied rocks do not, therefore, show any correlation between phenocryst or vesicle content and thickness of dikes. However, Fig. 6.1 shows that wide dikes (e.g. >400 cm) tend to have a low to intermediate phenocryst content compared with thin dikes which show amounts from aphyric to phenocryst-rich. This may be due to the fact that wide dikes were sampled at their edges, whereas thin dikes were sampled more randomly because the latter were more easily accessible. Also, the fact that very few wide dikes are represented can blur any possible correlation.

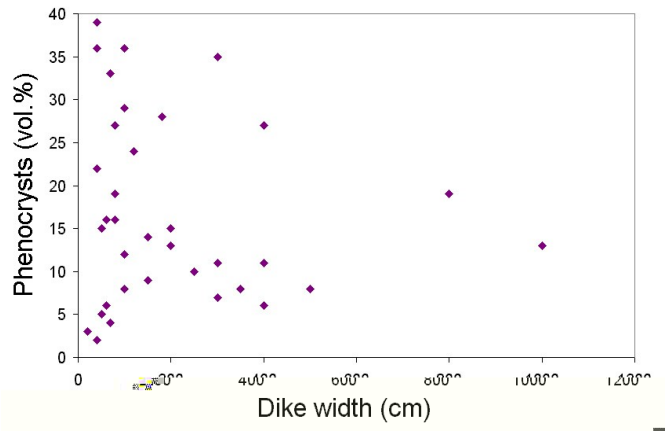


**Fig. 6.1.** Phenocryst content in the Megalo Vouno dikes shows no correlation with dike width. The widest measure of each dike was plotted.

## 6.2 General observations

Table 6.1 gives the visually estimated volume percentage (vol.%) of phenocrysts (on a vesicle-free basis), vesicles and groundmass in the sections, along with the observed groundmass textures. Due to the microcrystalline nature of the groundmass it was not possible to determine

the amount of the individual groundmass minerals, but instead the presence of minerals was indicated with a P. In several cases it was obvious that another groundmass mineral was present besides plagioclase and opaque minerals, but distinction was difficult, so when in doubt such were marked (P). This is also the reason why pyroxenes in the groundmass have not been subdivided into ortho- and clinopyroxenes.

From the table it appears that the total amount of phenocrysts varies from 2 vol.% to 39 vol.%, and that the majority of rocks are moderately vesicular, although some contain up to 40 vol.% vesicles and others hardly contain any. When vesicles have been (partly) filled with secondary minerals (in this case mainly clay minerals or calcite) they are called amygdales. These are so small that they have not been observed in hand specimen but can, however, be seen under the microscope. They are not especially common, occurring in only seven of the studied sections (MVD-B 01-19, MVD-B 01-20, MVD-B 01-23, MVD-B 01-26, MVD-B 01-27, MVD-B 01-28 and MVD-B 01-30) and typically only in few vesicles, never throughout the entire thin section. As can be seen from the sample numbers, amygdales were only observed in dikes sampled at sea-level, which corresponds well with the fact that amygdales typically form at deeper levels.

In hand specimen, all the rocks appear aphanitic, and under the microscope they all have microcrystalline groundmass. Some samples, however, have such a fine-grained groundmass (bordering on cryptocrystalline) that the individual minerals are impossible to determine readily. All the samples furthermore have hypocrystalline and inequigranular groundmass.

One sample (MVD-B 01-16), differed from the others by having a patchy looking groundmass containing ca. 60 vol.% microxenoliths. In hand specimen, the rock looks like any other of the dike rocks, but the thin section reveals that it is actually a tuff, having been emplaced through a dike channel.

The thin sections have been thoroughly searched for the seven kinds of inequigranular textures: (a) seriate; (b) porphyritic; (c) glomeroporphyritic; (d) poikilitic; (e) ophitic; (f) subophitic; and (g) interstitial (intersertal and intergranular) (as suggested by MacKenzie & Guilford, 1994).

The majority of samples contain phenocrysts or glomerocrysts enclosed by fine-grained intergranular and intersertal groundmass (porphyritic and glomeroporphyritic texture).

Photos of selected textures in groundmass and phenocrysts are provided in Fig. 6.2 and Appendix D.

Glomerocrysts, composed of nearly all possible combinations of the four main minerals, were observed but the most common were: plagioclases on their own, clinopyroxenes on their own, plagioclases together with olivines and/or clinopyroxenes and finally plagioclases together with clinopyroxenes and opaque minerals. Orthopyroxenes were only seen lying freely in the groundmass or as the centre part of a jacketed texture (see below).

In two samples (MVD-T 00-10 and MVD-B 01-19), the principal minerals show a continuous range in sizes, resulting in a seriate texture. No poikilitic, ophitic or subophitic textures were observed.

**Table 6.1.** Petrographic characteristics of thirty-seven rocks from the Megalo Vouno volcano complex. B – Basalt; BA – Basaltic andesite; A – Andesite; TA – Trachyandesite; T – Trachyte (based on classification in the TAS diagram, see section 7.3). P indicates that the mineral (or glass) is a constituent of the groundmass, (P) indicates that the mineral may be a constituent of the groundmass but it is too fine-grained to determine the exact mineral.

| Sample no. | Rock Type | Phenocrysts (vol.%) | | | | | | Vesicles (vol.%) | Groundmass | | | | | |
|---|---|---|---|---|---|---|---|---|---|---|---|---|---|---|
| | | Olivine | Plagioclase | Clinopyroxene | Orthopyroxene | Opaque | Total | | Olivine | Plagioclase | Pyroxene | Opaque | Glass | Groundmass textures |
| MVD-T 00-01 | dike/BA | <1 | 4 | 1 | | | 5 | 20 | (P) | P | (P) | P | P | Intersertal, Glomeroporphyritic, Trachytic |
| MVD-T 01-02 | dike/BA | <1 | 3 | <1 | | | 3 | 20 | (P) | P | (P) | P | P | Intersertal, Porphyritic |
| MVD-T 00-03 | dike/BA | 1 | 3 | <1 | | <1 | 4 | 5 | P | P | (P) | P | P | Intersertal, Porphyritic, Trachytic, Intergranular |
| MVD-T 00-04 | dike/BA | <1 | 24 | 12 | <1 | <1 | 36 | 15 | | P | | P | P | Intersertal, Glomeroporphyritic |
| MVD-T 01-05 | dike/BA | 9 | 17 | 3 | | <1 | 29 | 10 | P | P | | P | P | Intersertal, Glomeroporphyritic, Intergranular |
| MVD-T 01-06 | dike/B | 11 | 22 | <1 | | | 33 | 10 | P | P | | P | P | Intersertal, Glomeroporphyritic, Intergranular |
| MVD-T 00-07 | dike/A | <1 | 12 | 5 | <1 | 2 | 19 | <1 | | P | | P | P | Intersertal, Porphyritic, Trachytic, Intergranular |
| MVD-T 01-08 | dike/B | 11 | 22 | 6 | | | 39 | 5 | P | P | | P | P | Intersertal, Glomeroporphyritic, Intergranular |
| MVD-T 00-09 | dike/BA | 7 | 16 | 1 | | <1 | 24 | 5 | P | P | | P | P | Intersertal, Porphyritic, Trachytic, Intergranular |
| MVD-T 00-10 | dike/BA | 2 | 15 | 5 | | | 22 | <1 | (P) | P | | P | P | Intersertal, Seriate |
| MVD-T 00-11 | dike/A | | 8 | 3 | <1 | 2 | 13 | <1 | | P | | P | P | Intersertal, Glomeroporphyritic, Trachytic |
| MVD-T 00-12 | dike/A | | 10 | 4 | <1 | 2 | 16 | <1 | | P | (P) | P | P | Intersertal, Glomeroporphyritic, Intergranular |
| MVD-B 00-13 | dike/BA | 1 | 7 | <1 | | | 8 | 25 | (P) | P | (P) | (P) | P | Intersertal, Glomeroporphyritic |
| MVD-B 00-14 | dike/BA | 1 | 6 | 1 | | | 8 | 10 | (P) | P | (P) | P | P | Intersertal, Glomeroporphyritic |
| MVD-B 00-15 | dike/BA | <1 | 7 | 2 | | | 9 | 15 | (P) | P | (P) | P | P | Intersertal, Glomeroporphyritic, Trachytic, Intergranular |
| MVD-B 01-16 | dike/TA | | 4 | 2 | <1 | 2 | 8 | <1 | | P | (P) | P | P | Intersertal, Porphyritic |
| MVD-B 01-17 | dike/TA | | 5 | 1 | | <1 | 6 | 5 | | P | | P | P | Intersertal, Glomeroporphyritic, Trachytic, Intergranular |
| MVD-B 01-18 | dike/BA | <1 | 12 | 3 | | <1 | 15 | <1 | (P) | P | (P) | P | P | Intersertal, Seriate |
| MVD-B 01-19 | dike/BA | 2 | 28 | 6 | <1 | <1 | 36 | 10 | (P) | P | (P) | P | P | Intersertal, Seriate |
| MVD-B 01-20 | dike/BA | 4 | 8 | <1 | | <1 | 12 | <1 | (P) | P | | P | P | Intersertal, Glomeroporphyritic, Trachytic |
| MVD-B 01-21 | dike/TA | | 6 | 2 | | <1 | 8 | 15 | | P | (P) | P | P | Intersertal, Glomeroporphyritic, Trachytic |
| MVD-B 01-22 | dike/TA | | 12 | 2 | | <1 | 14 | 20 | | P | (P) | P | P | Intersertal, Glomeroporphyritic, Trachytic |
| MVD-B 01-23 | dike/A | | 24 | 2 | <1 | 2 | 28 | 15 | | P | (P) | P | P | Intersertal, Glomeroporphyritic |
| MVD-B 01-24 | dike/T | | 7 | 3 | <1 | <1 | 10 | 25 | | P | (P) | P | P | Intersertal, Porphyritic |
| MVD-B 01-25 | dike/BA | <1 | 16 | 11 | <1 | <1 | 27 | 5 | (P) | P | (P) | P | P | Intersertal, Glomeroporphyritic, Intergranular |
| MVD-B 01-26 | dike/BA | 6 | 21 | 8 | | <1 | 35 | 5 | (P) | P | (P) | P | P | Intersertal, Glomeroporphyritic, Trachytic |
| MVD-B 01-27 | dike/BA | <1 | 2 | <1 | | <1 | 2 | 20 | | P | | P | P | Intersertal, Porphyritic, Trachytic |
| MVD-B 01-28 | dike/TA | | 4 | 2 | | <1 | 6 | 10 | | P | (P) | P | P | Intersertal, Porphyritic, Trachytic |
| MVD-B 01-29 | dike/T | | 11 | 8 | <1 | <1 | 19 | 25 | | P | | P | P | Intersertal, Glomeroporphyritic, Trachytic |
| MVD-B 01-30 | dike/BA | <1 | 12 | 3 | | | 15 | 20 | | P | | (P) | P | Intersertal, Glomeroporphyritic |
| MVD-B 00-31 | dike/TA | | 20 | 7 | <1 | <1 | 27 | 40 | | P | | P | P | Intersertal, Porphyritic |
| MVD-B 00-32 | dike/TA | <1 | 6 | 1 | | <1 | 7 | 35 | | P | | P | P | Intersertal, Porphyritic, Intergranular |
| MVD-B 00-33 | dike/TA | <1 | 5 | 3 | <1 | 3 | 11 | <1 | | P | | P | P | Intersertal, Glomeroporphyritic, Trachytic, Intergranular |
| MVD-B 00-34 | dike/T | | 8 | 2 | | 1 | 11 | 20 | | P | | P | P | Intersertal, Glomeroporphyritic, Trachytic |
| MVD-B 00-35 | dike/T | | 9 | 2 | | 2 | 13 | 10 | | P | | P | P | Intersertal, Glomeroporphyritic, Trachytic, Intergranular |
| MVD-B 00-36 | dike/TA | <1 | 9 | 3 | <1 | 4 | 16 | 10 | | P | | P | P | Intersertal, Glomeroporphyritic, Trachytic, Intergranular |
| MV-B 01-38 | lava/TA | | 26 | 5 | | 3 | 34 | 5 | | P | | P | P | Intersertal, Glomeroporphyritic, Trachytic |

In half of the rocks a trachytic texture was observed, either as alignment of plagioclase laths in (parts of) the groundmass or as subparallel alignment of plagioclase laths around phenocrysts. Selected photos of groundmass textures are shown in Fig. 6.2.

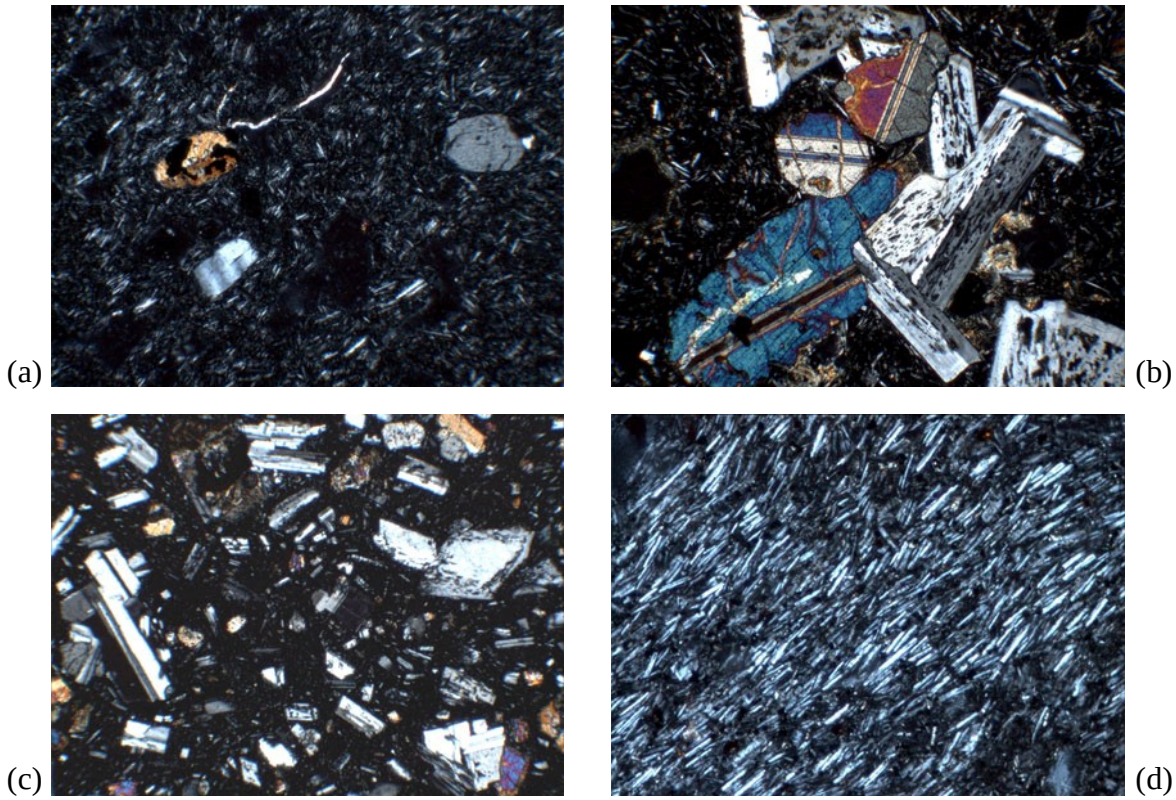


**Fig. 6.2.** The four typical groundmass textures occurring in the studied thin sections: (a) Porphyritic texture – phenocrysts of plagioclase and clinopyroxene lying freely in a fine-grained intersertal groundmass (MVD-B 01-24); (b) Glomeroporphyritic texture – glomerocryst composed of twinned clinopyroxenes and plagioclases set in a fine-grained groundmass (MVD-B 01-23); (c) Seriate texture – principal minerals (olivine, plagioclase and clinopyroxene) occur in a continuous range of sizes (MVD-B 01-19) and (d) Trachytic texture – alignment of plagioclase laths in the groundmass (MVD-B 01-17). Photos are ca. 1.6 mm across.

Alteration is generally restricted to serpentine and iddingsite along cracks in olivine crystals (Fig. 6.3) plus reaction rims around olivines.

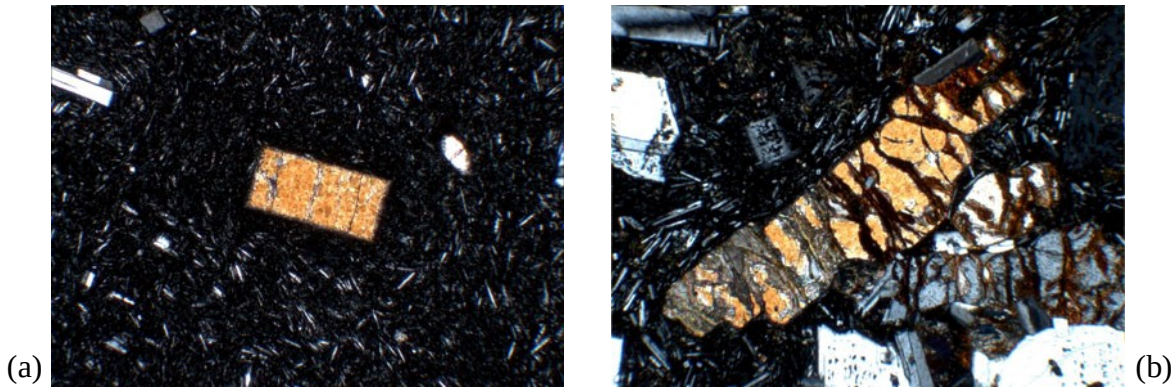


**Fig. 6.3.** (a) Euhedral olivine showing no signs of alteration (MVD-T 00-12). (b) Olivine crystal with alteration products along its cracks. In the lower part of the photo the mineral has been serpentinised, whereas the upper part of the mineral has been partly altered to iddingsite (MVD-B 01-20). Photos are ca. 1.6 mm across.

## 6.3 Phenocrysts

The main minerals occurring as phenocrysts (>0.3 mm and visible with the naked eye) and microphenocrysts (<0.3 mm) are: plagioclase, clinopyroxene, olivine, orthopyroxene and opaque minerals. Plagioclase phenocrysts are up to 3.5 mm long and can be easily seen in hand specimen together with the slightly smaller olivines (up to 1.5 mm) and clinopyroxenes (up to 2.5 mm). Orthopyroxenes and opaque minerals have only been seen under the microscope (<0.5 mm).

*Plagioclase*

As well as being the most abundant mineral in the groundmass, plagioclase is the most common phenocryst phase varying in abundance from 2 to 28 vol.%. The crystals are characterised by their usually euhedral (or subhedral) crystal shape, twinning, zoning and low interference colours (grey-cream). Angular plagioclase crystals are also very common throughout the sections.

Twinning is common in all the thin sections, the most abundant being albite (polysynthetic) twinning followed by Carlsbad twinning. Sometimes these are combined, giving the opportunity to measure the mineral composition using the Carlsbad-albite method. Measurement was carried out on a single crystal (sample MVD-T 01-08) resulting in 70 An%, making the plagioclase a labradorite. Microprobe measurements on plagioclase crystals in rocks from the other northern volcanic centres of Santorini (Thirassia-Skaros) gave results varying between 34-93 An% (Kann, 2004).

Zoning is another common feature occurring within all the thin sections. Ten samples exclusively contain normally zoned crystals and the remaining twenty-seven samples contain both normally and reversely zoned plagioclases. Multiple zoning also occurs in twenty-seven of the samples, mainly as oscillatory zoning and less frequently as convolute zoning (Fig. 6.4.a and b). Sometimes zoning is also picked out by bands of melt inclusions. In most thin sections zoned crystals occur along with plagioclase crystals showing no signs of zoning.

Inclusions in plagioclases are mainly melt (spongy texture) but inclusions of other minerals and of alteration products also occur (Fig. 6.4.f, g and h).

The "spongy texture" is a result of resorption, and was observed in thirty-one samples. The spongy texture is either restricted to the central part of the crystal or more frequently covered the entire crystal (except perhaps for a thin rim). Often spongy crystals occur together with "clear" plagioclases. Care must be taken to consider whether this is in fact a sign of several generations of plagioclase growth, because the positioning of the texture within each crystal may be due to the orientation of the crystal when the section was cut.

Plagioclases often occur as glomerocrysts, often simply in clots with other plagioclase crystals (Fig. 6.4.b), but also together with olivines, clinopyroxenes and opaque minerals – in fact in almost any possible combination of these minerals.

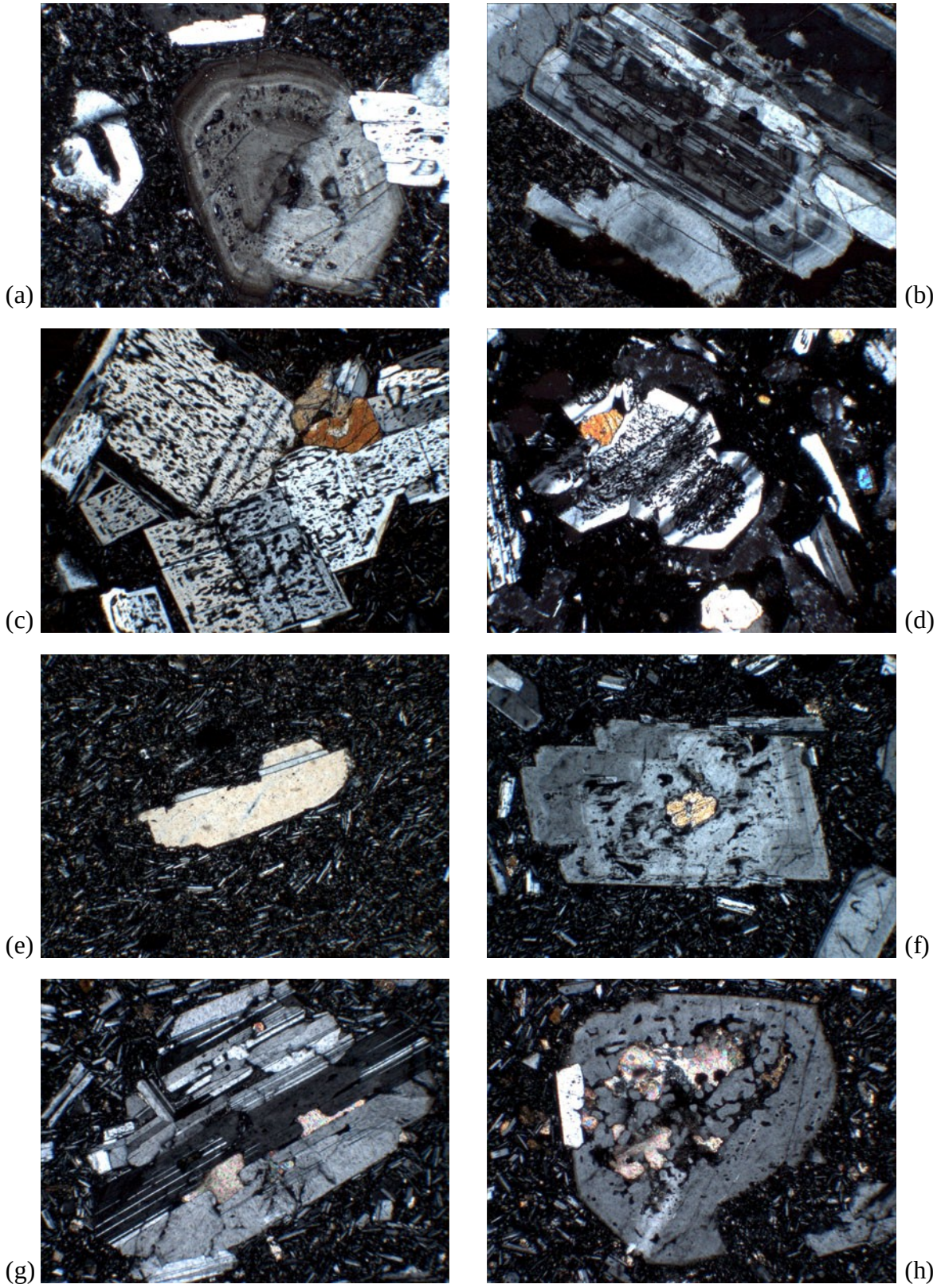


**Fig. 6.4.** Common textures in plagioclases of the studied thin sections. (a) Oscillatory zoning in plagioclase phenocryst (MVD-B 01-38); (b) Convolute zoning in plagioclase crystal in a glomerocryst (MVD-B 00-35); (c) Glomerocryst of clinopyroxene and spongy plagioclase crystals (MVD-B 01-23); (d) Plagioclase crystals with a spongy core and clear rim (MVD-T 00-04); (e) Embayment in plagioclase phenocryst (MVD-B 01-30); (f) Small clinopyroxene included within a zoned plagioclase (MVD-B 01-25); (g) Carbonate occurring as an alteration product along the twin lamellae of a plagioclase and (h) Carbonate occurring as an alteration product in the core of a plagioclase phenocryst. Both (g) and (h) were observed in MVD-B 01-18. Photos are ca. 1.6 mm across.

*Clinopyroxene*

Clinopyroxenes are present in all the samples, occurring in amounts from <1 to 12 vol.%. They are characterised by euhedral to subhedral crystal shape, twinning (Fig. 6.5.d), colour zoning, cleavage and often have a slightly dull green tint in comparison with the almost colourless olivines.

Zoning is fairly common, occurring in twenty of the sections, but is often seen in just one crystal (or a few) within each section. The most common form of zoning is colour zoning, giving the crystal a mottled/speckled appearance. Another common form is sector zoning (Fig. 6.5.f), which was observed in twelve of the rocks, while only one concentrically zoned crystal was seen (showing normal zoning) (MVD-T 00-10) (Fig. 6.5.e).

Clinopyroxenes are commonly occurring in glomerocrysts together with opaque minerals or with both plagioclase and opaque minerals. When lying freely in the matrix, they are often perfectly euhedral, although subhedral crystals are probably most common overall.

A few inclusions of other minerals were observed (e.g., clinopyroxene containing olivine in Fig. 6.5.b), and resorption of a single clinopyroxene was observed in MVD-B 01-25 (Fig. 6.5.a).

In three thin sections (MVD-T 00-04, MVD-B 01-19 and MVD-B 01-25) orthopyroxenes have been jacketed by clinopyroxenes (Fig. 6.5.c).

(a) 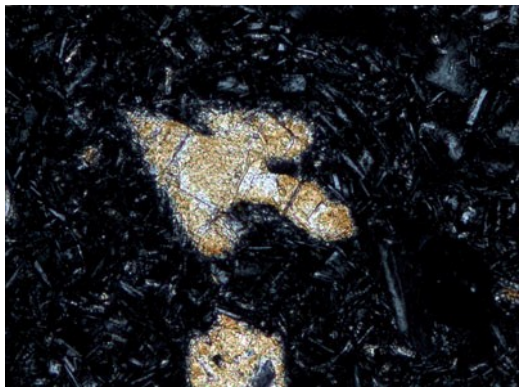  (b)

(c) 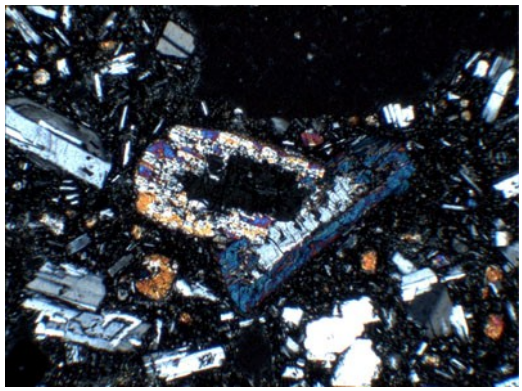 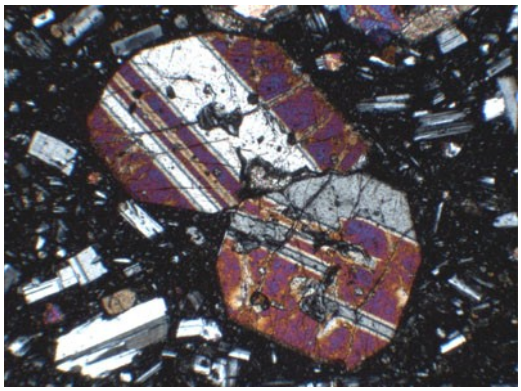 (d)

**Fig. 6.5.** Common textures in clinopyroxenes of the studied thin sections. (a) Resorbed clinopyroxene phenocryst (MVD-B 01-25); (b) Small anhedral olivine included within a large (ca. 1.8 mm long) subhedral clinopyroxene (MVD-T 00-03); (c) Two anhedral orthopyroxenes jacketed by two subhedral clinopyroxenes (MVD-B 01-19); (d) Two subhedral clinopyroxenes showing conspicuous twinning (MVD-B 01-19); **(continues on next page)**

(e) 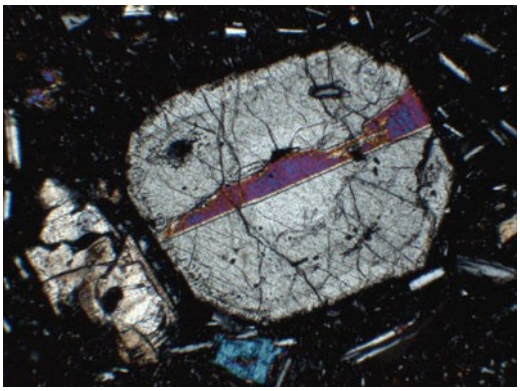 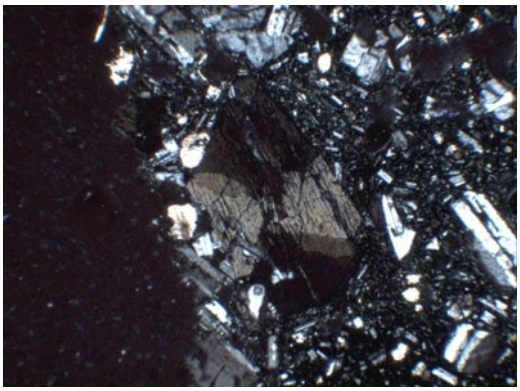 (f)

**Fig. 6.5 (continued from previous page).** (e) Concentrically zoned euhedral clinopyroxene with twinning (MVD-T 00-10) and (f) Subhedral clinopyroxene phenocryst showing sector zoning (hourglass) (MVD-B 01-19). Photos are ca. 1.6 mm across.

*Olivine*

Olivine phenocrysts are present in half of the samples and are characterised by high birefringence, partings (often combined with alteration) and lack of cleavage. All basalts and basaltic andesites contain olivine phenocrysts, and the degree of alteration varies even within a single thin section. In the majority of sections, some olivine crystals show signs of alteration, while others look fresh. However, in a few sections, all olivines present appear to have been altered to some extent. Olivines are also present in a few of the more evolved rocks but are typically partly altered and have reaction rims of clinopyroxene.

In sample MVD-B 00-14 two occurrences of "star-shaped" olivine-clots (composed of three opposite pairs) were observed, and in MVD-T 00-03 a twinned olivine was discovered (Figs. 6.6.a and b). Fairly common features in olivines are embayments and resorption as shown in Fig. 6.6.c and 6.6.d. The amount of olivine phenocrysts varies from 0 to 11 vol.%.

(a) 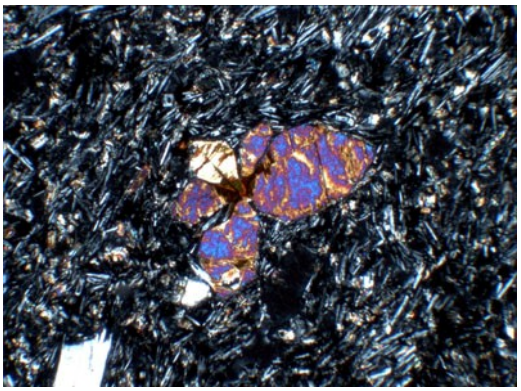 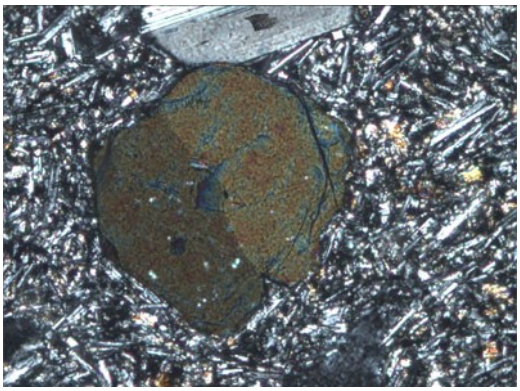 (b)

**Fig. 6.6.** Textures in olivines of the studied thin sections. (a) Star shape formed by three opposite pairs of subhedral olivines (MVD-B 00-14); (b) Twinned olivine (MVD-T 00-03);
**(continues on next page)**

(c)  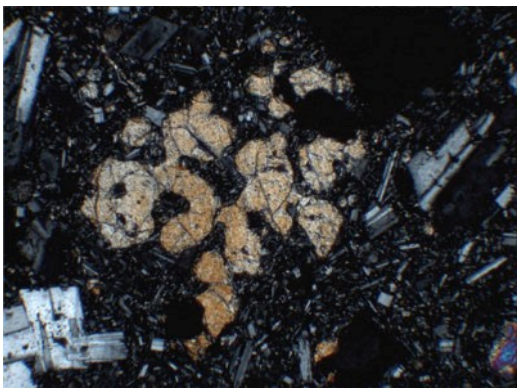 (d)

**Fig. 6.6 (continued from previous page).** (c) Embayments in large, otherwise euhedral olivine phenocryst (MVD-T 00-09) and (d) Highly resorbed olivine (MVD-T 01-08). Photos are ca. 1.6 mm across.

*Orthopyroxene*

Orthopyroxenes are not very common in the samples, but small phenocrysts and microphenocrysts (<0.3 mm) occur in small amounts (<1 vol.%) within thirteen samples. Most of the rocks containing orthopyroxene are trachytes and trachyandesites, although in a few andesites and basaltic andesites one or two grains have been recognised.

The orthopyroxenes are characterised by their pale colour, weak pleochroism (pink-green), euhedral or subhedral eight sided crystal shapes (Fig. 6.7.a), cleavages intersecting near 90° plus parallel extinction. They sometimes occur as jacketed minerals surrounded entirely by clinopyroxene (Fig. 6.7.b).

(a) 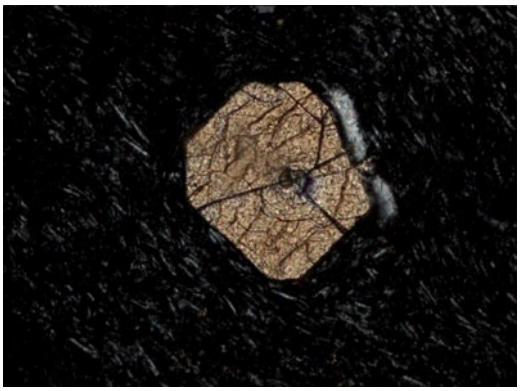  (b)

**Fig. 6.7.** (a) Subhedral orthopyroxene (ca. 0.3 mm in diameter) (MVD-B 00-33). (b) A small orthopyroxene (at extinction) jacketed by clinopyroxene (MVD-T 00-04). Photos are ca. 0.8 mm across.

*Opaque minerals*

The opaque minerals are easily recognised in most sections, because the black stands out against a light-coloured groundmass. However, in some of the sections the opaque minerals are difficult to see because of dark brown/black glass in the groundmass. Tilting the thin section in reflected light where the opaque minerals will gleam easily solves this.

Although constituting part of the groundmass in every single thin section, opaque minerals do not occur as frequently as phenocrysts and microphenocrysts (only <1 to 4 vol.%). The

phenocrysts are typically an- or subhedral crystals seen together with clinopyroxenes and in glomerocrysts along with clinopyroxene and plagioclase. More rarely they occur as euhedral crystals, typically in the shape of a square (Fig. 6.8.a).

Other studies have shown that the opaque minerals are Fe-Ti oxides belonging to the spinel group (Huijsmans, 1985; Kann, 2004).

(a) 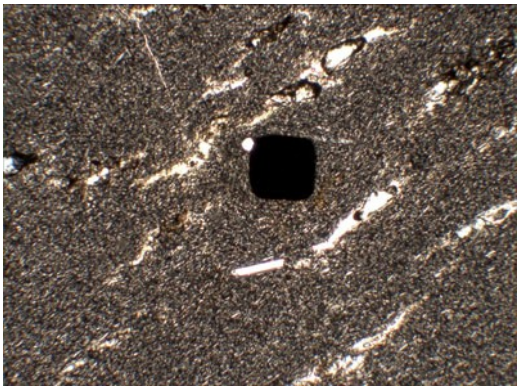 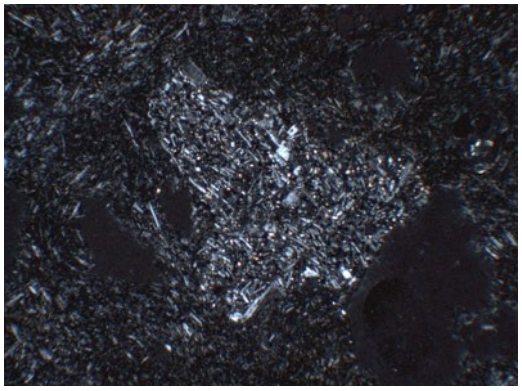 (b)

(c) 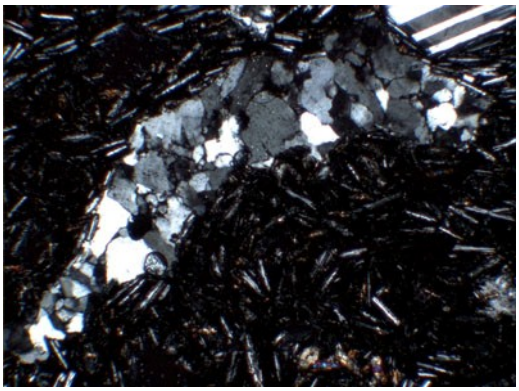

**Fig. 6.8.** (a) Euhedral Fe-Ti oxide (perhaps slightly rounded) in fine-grained, glassy matrix with elongate vesicles (MVD-B 00-36); (b) Microxenolith composed of coarser plagioclase laths and pyroxenes than in the surrounding groundmass (MVD-B 01-17) and (c) Quartzite microxenolith (MVD-B 01-28). Photos are ca. 1.6 mm across.

*Microxenoliths*

Ten thin sections contain microxenoliths (Fig. 6.8.b) and one sample (MVD-B 01-16), a tuff, was composed predominantly of microxenoliths. They are easily recognised because they are composed of a markedly different groundmass (e.g. larger or smaller grains, different minerals or more or less glass) and sometimes contain phenocrysts of other sizes, shapes or even composition than throughout the rest of the sample. In sample MVD-B 01-28 several microxenoliths of quartzite were observed (Fig. 6.8.c).

Xenocrysts are not as easily recognisable, since disequilibrium crystallisation creates some of the same textures (reaction rims, alteration products, roundness) one would usually expect to find enclosing or shaping xenocrysts.

It is not easy optically to tell whether a phenocryst is in fact a xenocryst, though euhedral crystals are expected to be true phenocrysts. No xenocrysts have thus been observed, although they could easily be present since quite a few microxenoliths have been found throughout the sections.

## 6.4 Summary of petrography

Analyses of the minerals from other rocks from the northern volcanic centres have shown that the clinopyroxenes are diopsides and augites, olivines are Mg-rich (>50% Fo) and orthopyroxenes are enstatites. The opaque minerals are Fe-Ti oxides (Ti-magnetite), and plagioclases vary widely in composition from anorthite, bytownite and labradorite to andesine (Huijsmans, 1985; Hansen, 1997; Kann, 2004).

On the basis of rock types obtained from the TAS diagram (Section 7.3.2), the following phenocryst assemblages are found within the Megalo Vouno dikes (and a single Peristeria 1 lava flow (MV-B 01-38)):

| | |
|---|---|
| Basalt: | ol + cpx + plg |
| Basaltic andesite: | ol + cpx + plg ± opx ± op |
| Andesite: | cpx + plg ± opx ± op ± ol |
| Trachyandesite: | cpx + plg + op ± opx ± ol |
| Trachyte: | cpx + plg + op ± opx |

ol olivine
plg plagioclase
cpx clinopyroxene
opx orthopyroxene
op opaque minerals

The order of crystallisation seems to be simultaneous crystallisation of olivine and clinopyroxene immediately followed by plagioclase. Orthopyroxene replaces olivine in the more evolved samples (andesites to trachytes) but there seems to be a considerable overlap, especially in the basaltic andesites where both minerals occur, though in limited amounts. Opaque minerals are present in minute amounts as phenocrysts and microphenocrysts in nearly all rocks (except for basalts). They are most common in the more evolved samples and can be found in the groundmass of every sample. This order of crystallisation is in accordance with the observations obtained by Nicholls (1971), Huijsmans (1985), Hansen (1997) and Kann (2004). The phenocryst assemblage was termed POAM (Plagioclase Olivine/Orthopyroxene Augite – Magnetite) by Gill (1981) and was furthermore suggested to be the most common and extensive fractionation assemblage responsible for generating orogenic andesites.

Huijsmans (1985) observed that glomeroporphyritic and trachytic textures were more common in evolved rocks, but these textures seem to be randomly distributed in the rock types of the thin sections studied here.

Observed textures indicating disequilibrium, whether the result of magma mixing, fractional crystallisation or other processes (e.g. pressure or temperature dependent) are: jacketed orthopyroxenes; resorption and embayments; normally and reversely zoned plagioclases in a single sample; complex zoning; spongy textures in plagioclase plus different textural populations of single minerals.

# 7. Whole-rock geochemistry

Results of analyses are given in Appendix E (Tables E1 and E2) and a table summarising the employed analytical methods is given in Appendix E (Table E3).

## 7.1 Evaluation of sample freshness

Alteration can have an effect on chemical analyses (and subsequent classification) of rock samples, and therefore needs to be evaluated.

All the sampled rocks have been studied in hand specimen as well as thin section, and none show obvious signs of alteration (only a few cases of secondary minerals in vesicles and alteration of olivine to iddingsite).

According to Le Maitre et al. (1989, 2002), all rocks with $H_2O$ contents above 2.0 wt.% and $CO_2$ contents above 0.5 wt.% cannot be plotted in the TAS diagram (Section 7.3, see below) and it was therefore decided to evaluate such samples. Unfortunately, the analyses do not include $H_2O$ and $CO_2$ thus deselection was based on LOI. LOI (mentioned in Section 5.2) is the total amount of volatiles removed from the sample at 950 °C as part of the major element analysis. Altered minerals or devitrified glass in the groundmass typically lead to high LOI in the sample, so this means that all samples having LOI above 2.5 wt.% should be evaluated and perhaps discarded. Only one sample (MVD-B 00-31) has too high a value (2.59 wt.%). On location, the dike stood out like a steep wall, and it was fairly easy to get a fresh sample with minimal chance of having been in direct contact with seawater. In hand specimen the sample appears dark grey and the groundmass is aphanitic containing plagioclase laths. In thin section all minerals look fresh showing no visible signs of alteration.

The degree of alteration can also be reflected in the $Fe_2O_3$/FeO ratio, which indicates alteration of the rock as well as oxidation during eruption. Most samples show low values (<1.0), and only a red, oxidised scoria, MV-T 01-37, shows an expected high value (8.53). It was decided to use both samples after this check.

## 7.2 Introduction to data

All samples were analysed for major and trace elements by XRF, while 30 samples were analysed for further trace elements by ICP-MS and 15 samples had Nd, Sr and Pb isotopes determined (Appendix E, Table E1).

In cases where a given element was available from more than one analysis, the method known to produce the best results was in each case selected. For example in the case of Pb, XRF results were chosen, because they provided data for all samples and the analysis of standards was better than by ICP-MS.

The given analyses have been plotted directly, although an adjustment to 100% on a volatile-free basis is typically undertaken for the major elements. I have chosen not to do so because,

except for one sample having a sum of 98.51 wt.% (MVD-T 00-07 containing hardly any volatiles at all: 0.23 wt.%), all samples have sums within the range 99.22-100.11 wt.%, indicating that they are essentially undisturbed analyses. My argument for using the samples directly with no correction is based on the recommendation from IUGS that "rocks should be classified according to what they are and not what they might have been" (Le Maitre et al., 2002).

**Using data without adjustments applies to all the diagrams in this chapter** (except for the TAS diagram in Section 7.3, since its use is defined by making the adjustment).
Rock names are given on the basis of discrimination in the TAS diagram: basaltic rocks having $SiO_2$ <52 wt.%, basaltic andesites: 52 -57 wt.% $SiO_2$, andesites: 57 -63 wt.% $SiO_2$ and dacites containing 63-77 wt.% $SiO_2$ (at $Na_2O+K_2O=0$).

### *7.2.1 Major elements (wt.% oxides)*

Major elements include $SiO_2$, $TiO_2$, $Al_2O_3$, $Fe_2O_3$, FeO, MnO, MgO, CaO, $Na_2O$, $K_2O$ and $P_2O_5$. (Furthermore $FeO_{total}$ or FeO* was calculated as FeO + 0.89981 * $Fe_2O_3$).

### *7.2.2 Trace elements and volatiles (ppm)*

Trace elements are defined as elements, which are present at less than 0.1 %, volatiles are present in larger amounts. For this study the trace elements have been divided into groups according to similar geochemical behaviour:

*Rare earth elements (REE) and Y (in ppm)*
LREE: La, Ce, Pr, Nd, Sm and Eu.
HREE: Gd, Tb, Dy, Ho, Er, Tm, Yb and Lu (plus Y, which behaves like Ho).

*Large ion lithophile elements (LILE) (in ppm)*
LILE: Rb, Sr, Cs, Ba, Pb, Th and U.

*High field strength elements (HFSE) (in ppm)*
HFSE: Zr, Nb, Hf and Ta.

*Transition metals and Ga (in ppm)*
Zn, Ni, Cu, Cr, Sc, Co, and V (plus Ga).

*Volatile elements*
Cl and S

### *7.2.3 Isotopes*

Isotopic ratios were obtained for $^{87}Sr/^{86}Sr$, $^{143}Nd/^{144}Nd$, $^{206}Pb/^{204}Pb$, $^{207}Pb/^{204}Pb$ and $^{208}Pb/^{204}Pb$. In addition to the 15 analysed samples, five lava flows from a previous study of the Megalo Vouno volcano complex (Hansen, 1997) were analysed for the same five isotopic ratios (Appendix E; Table E2).

Isotopic ratios are characteristic of their source regions and remain unchanged during fractionation events, because the mass difference between the individual radiogenic isotopes, concerned here is so small that no fractionation between them can take place. This signifies that isotopes are an effective means of detecting mixing and contamination processes between isotopically distinct sources.

## 7.3 Classification

The most commonly used diagrams for classifying volcanic rocks from a subduction zone environment have been employed and are shown below.

Trend 1 and Trend 2 recognised by Hansen (1997) have been plotted on all classification diagrams for comparison with the data from this study.

### *7.3.1 CIPW norm*

The CIPW norm is a calculation using a chemical analysis to show the normative mineral assemblage of sampled rocks. The norm thus represents the mineralogical assemblage of an anhydrous magma, with the same chemical composition, crystallising slowly under atmospheric pressure.

The calculation used here is after Holm (1997) based on Kelsey (1965) and Cox et al. (1979) and results are given in Appendix E (Table E4). Major element oxides are recalculated to 100% on a volatile-free basis, and an adjustment of Fe contents is made to obtain an $Fe^{3+}/Fe^{2+}$ ratio representative of the melt.

*Fe correction*

Volcanic rocks are likely to experience oxidation during eruption and later weathering. Through such processes some of the FeO will be converted to $Fe_2O_3$, so that when calculating the norm an increased amount of $Fe_2O_3$ will lead to formation of *magnetite* consisting of equal amounts of $Fe_2O_3$ and FeO. This will result in less available FeO for *olivine* and *hypersthene* and, finally, lead to more normative quartz than is actually the case.

To avoid this quartz enrichment in the norm (risking, in this case, that saturated rocks become oversaturated), an adjustment of the $Fe_2O_3$ content must be made. Several such methods are available, and those considered for the samples studied are briefly discussed.

Correction to an $Fe_2O_3/(Fe_2O_3+FeO)$ ratio of 0.3 was proposed by Gill (1981) as a global average for orogenic andesites. The rocks in this study, however, range in composition from basalts to trachytes (see TAS diagram below), and 11 rocks have initial ratios ($Fe_2O_3/(Fe_2O_3+FeO)$) below 0.3, suggesting that a lower value is needed for at least some of the rocks. A more advanced correction scheme, using correction ratios according to rock type (as classified in the TAS diagram) was set forth by Middlemost (1989). This correction has the advantage that it takes into account the variation in degree of oxidation with differentiation (basalt: 0.2; basaltic andesite: 0.3; andesite: 0.35; trachyandesite: 0.4; trachyte: 0.5). Nevertheless, 45% of the rocks in this study show initial values below the proposed ratios, suggesting that oxidation levels are lower.

The Fe correction used in this study is, therefore, another commonly used method. The lowest $Fe_2O_3/(Fe_2O_3+FeO)$ ratio among the samples has been chosen as the correction factor (sample MVD-T 00-03), because the low value (0.19) suggests that it represents the original magmatic oxidation ratio (Holm, 1997). Furthermore, this sample was collected on top of Megalo Vouno volcano where rocks lack obvious signs of weathering like the rocks at sea-level. It was also checked that this sample was not the only one with a low value, since this could have been a result of analytical error. As can be seen from Table E1 (Appendix E) sample MVD-T 00-11 has an only slightly higher value (0.20) and MVD-T 01-06 and MVD-T 00-07 both have the ratio 0.22. Additionally, two of the latter are andesites, signifying that it is plausible to assume that the oxidation levels have been low.

This last method is preferred because it takes local conditions into account, but the downside is that it does not take into account the probability that oxidation levels may change according to rock type.

When using the 0.3 value suggested by Gill (1981) or the factors proposed by Middlemost (1989), none of the rocks are olivine normative, whereas one sample (MVD-T 01-06) becomes olivine normative using the selected method. Results using the correction factor by Holm (1997) are listed alongside results using the correction factor suggested by Gill (1981) (both Appendix E; Table E4). The olivine normative rock has 0.7 wt.% normative olivine and the remaining 37 samples are all quartz normative with a content of 0.1-14.7 wt.% normative quartz. By definition, the rocks are all tholeiites because they contain normative hypersthene. Only one is an olivine tholeiite; the rest are quartz tholeiites.

### *7.3.2 TAS diagram*

The TAS (Total Alkali Silica) diagram depicts $SiO_2$ content along the abscissa and $Na_2O+K_2O$ content along the ordinate (Fig. 7.1). The diagram is useful for classifying volcanic rocks for which a mineral mode cannot be determined due to the presence of glass, or the fine-grained nature of the groundmass. Analyses are recalculated to 100% on a volatile-free basis, and further subdivisions are carried out using results from the CIPW norm. Classification names are given according to the latest recommendation by IUGS (Le Maitre et al., 2002).

According to the classification, two of the sampled rocks have basaltic composition, and can further be classified as subalkali basalts, since they lack normative nepheline. Basaltic andesites make up most of the rocks with 18 samples, while there are only four andesites. Ten rocks can be classified as trachyandesites, whereof one with further subdivision becomes a latite and the rest are benmoreites on the basis of their content of alkalis. All four rocks plotting in the trachyte/trachydacite field are trachytes, as they all contain less than 20% normative quartz. None of the rocks qualify as peralkaline trachytes because all have mol.% $(Na_2O+K_2O)/Al_2O_3<1$. A line of discrimination can be plotted on the TAS diagram between the two major magma series: the alkaline and subalkaline series. Different authors have located the boundary in slightly different places on the TAS diagram; the line used here is the one suggested by Irvine & Baragar (1971). All 38 samples plot in the subalkaline field and can, therefore, be subdivided further in the $K_2O$ versus $SiO_2$ diagram (Fig. 7.4).

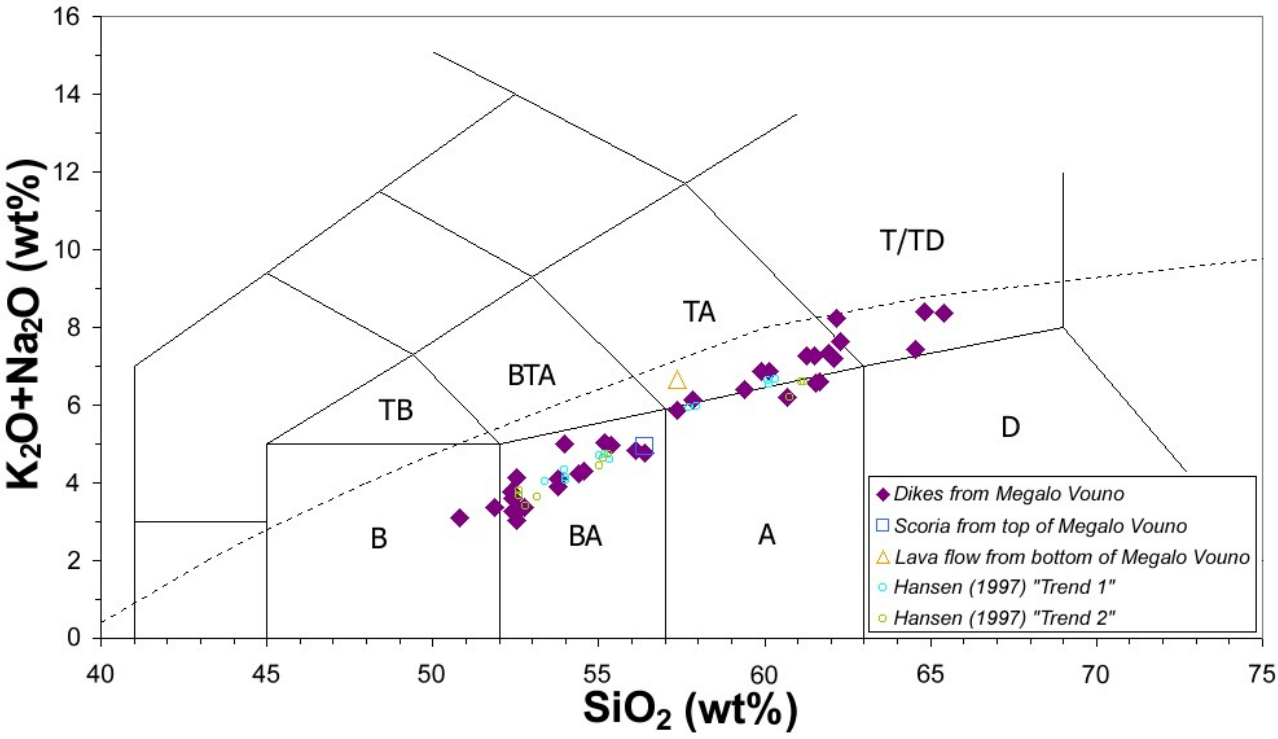


**Fig. 7.1.** TAS diagram showing increasing content of alkalis with degree of differentiation. The dotted line is the divide between alkaline (above) and subalkaline (below) rocks as defined by Irvine & Baragar (1971).
**B**: basalt; **BA**: basaltic andesite; **A**: andesite; **D**: dacite; **TB**: trachybasalt; **BTA**: basaltic trachyandesite; **TA**: trachyandesite; **T/TD**: trachyte/trachydacite. After Le Bas et al. (1986).

### *7.3.3 Discrimination between the tholeiitic and calc-alkaline series*

Subalkaline rocks can be further subdivided into the tholeiitic and calc-alkaline series, and several diagrams can be used to discriminate between the two series as shown below. Dividing lines in the diagrams are not definitive but can be useful when separating or contrasting magma series.

Previous studies of volcanic products from Santorini have shown that samples are transitional in composition (Huijsmans, 1985; Hansen, 1997; Druitt et al., 1999; Pe-Piper & Piper, 2002). The possible reason for this behaviour is discussed in Chapter 8.

*FeO*/MgO versus $SiO_2$ diagram*

In the FeO*/MgO versus $SiO_2$ diagram proposed by Miyashiro (1974) (Fig. 7.2), the majority of samples plot in the tholeiitic field and samples furthermore cross the dividing line, giving the impression that rocks evolve from a calc-alkaline to a tholeiitic composition with increased degree of magmatic differentiation. It is, however, more important that the samples show a steeper slope than the dividing line and the significance of this is discussed in Chapter 8.

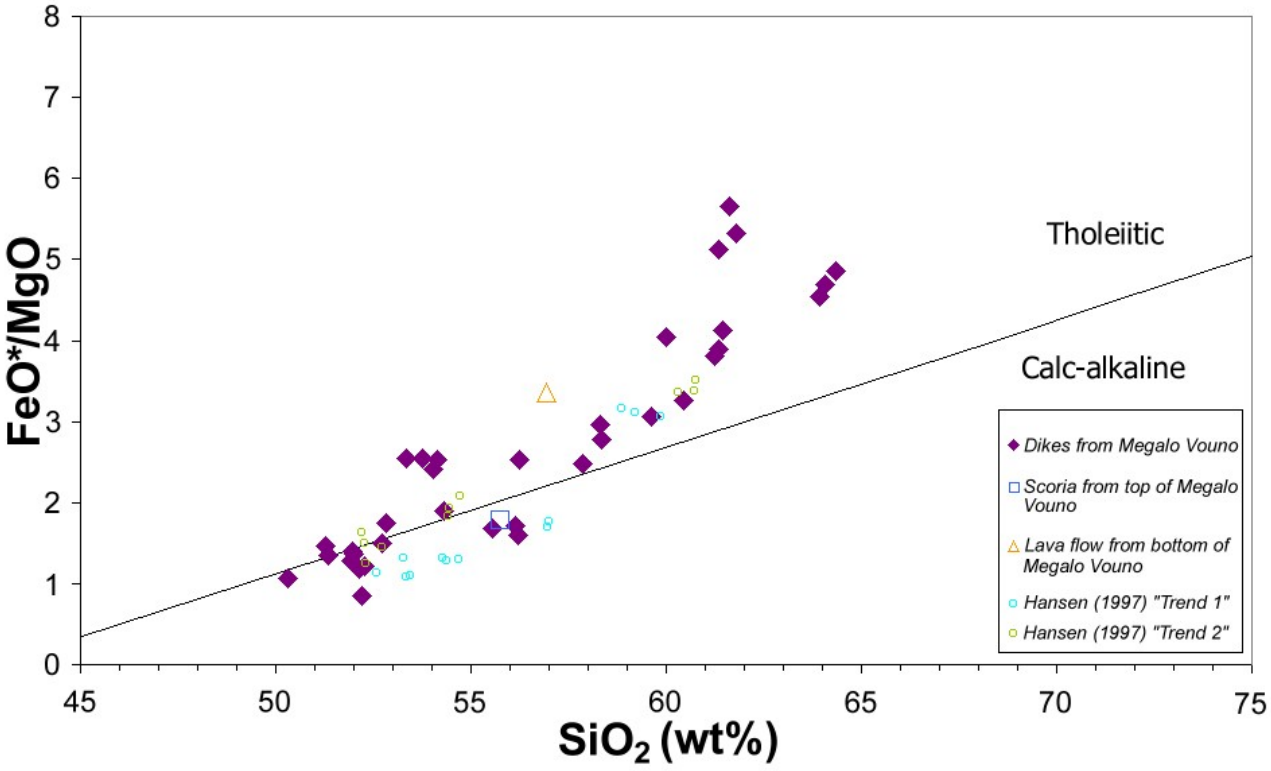


**Fig. 7.2.** FeO*/MgO versus $SiO_2$ diagram for separation of tholeiitic from calc-alkaline rocks. FeO* is total Fe calculated as FeO + 0.89981 * $Fe_2O_3$. After Miyashiro (1974).

*AFM diagram*

The AFM diagram (Fig. 7.3) has the oxides $Na_2O+K_2O$, FeO* and MgO at the three apices of a triangle, and a separation line between calc-alkaline and tholeiitic rocks defined by Irvine & Baragar (1971).

The majority of the rock samples plot in the calc-alkaline field, but four samples (MVD-B 00-13, 01-17, 00-32, 00-33) plot in the tholeiitic field and eight of the remaining samples plot directly on or close to the dividing line. Because of these iron-enriched samples the series shows slightly more pronounced iron-enrichment than would be expected in a calc-alkaline evolution trend.

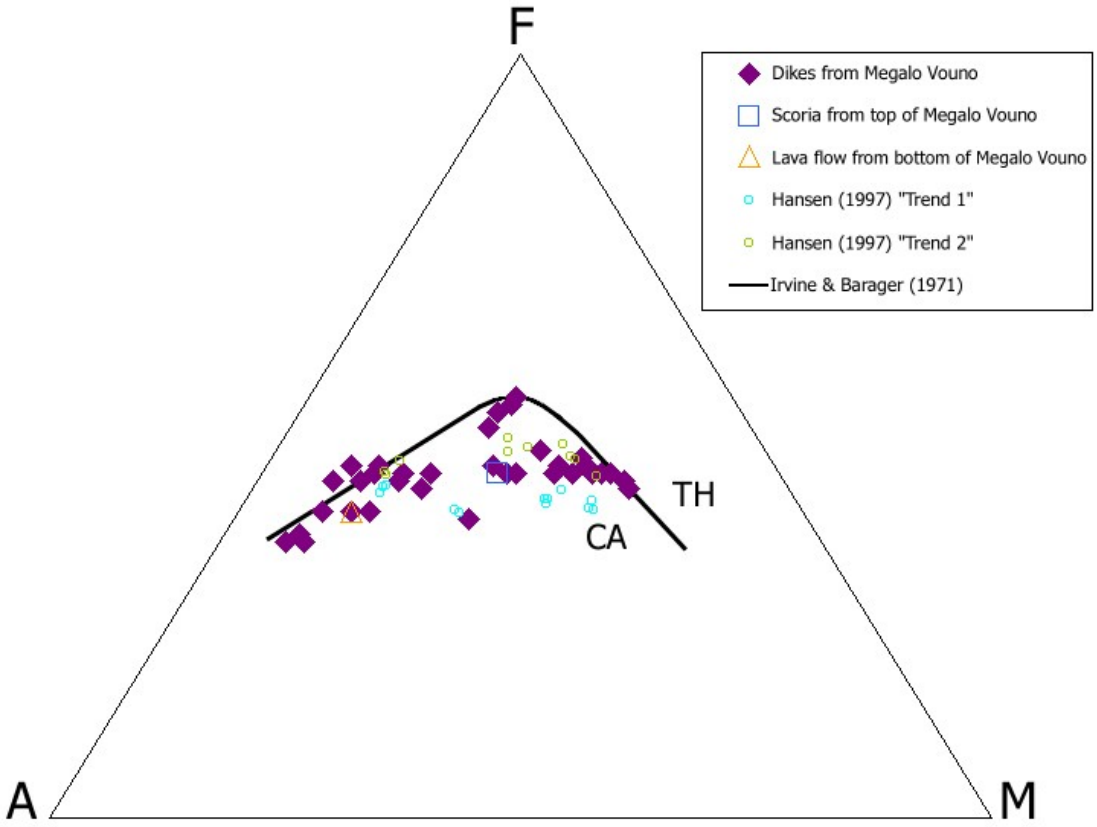


**Fig. 7.3.** AFM diagram for discrimination between tholeiitic and calc-alkaline rock series. **CA**: calc-alkaline and **TH**: tholeiitic. The letters at the three apexes stand for: **A**: $Na_2O+K_2O$; **F**: FeO* (FeO + 0.89981 * $Fe_2O_3$); **M**: MgO. The thick, black line separating tholeiitic from calc-alkaline rocks was defined by Irvine & Baragar (1971).

*$K_2O$ versus $SiO_2$*

The $K_2O$ versus $SiO_2$ diagram divides rocks into four separate series on the basis of their $K_2O$ content (Fig. 7.4).

On the diagram, three samples plot transitionally between low-K tholeiites and the medium-K calc-alkaline series; the majority of samples (17) plot in the medium-K calc-alkaline series; six

samples plot transitionally between the medium-K calc-alkaline and the high-K calc-alkaline series, and the last 12 samples plot in the high-K calc-alkaline field.

The diagram furthermore shows an increase in $K_2O$ content with increased degree of magmatic differentiation and the samples cross the lines defining the individual series. This behaviour will be discussed in Chapter 8.

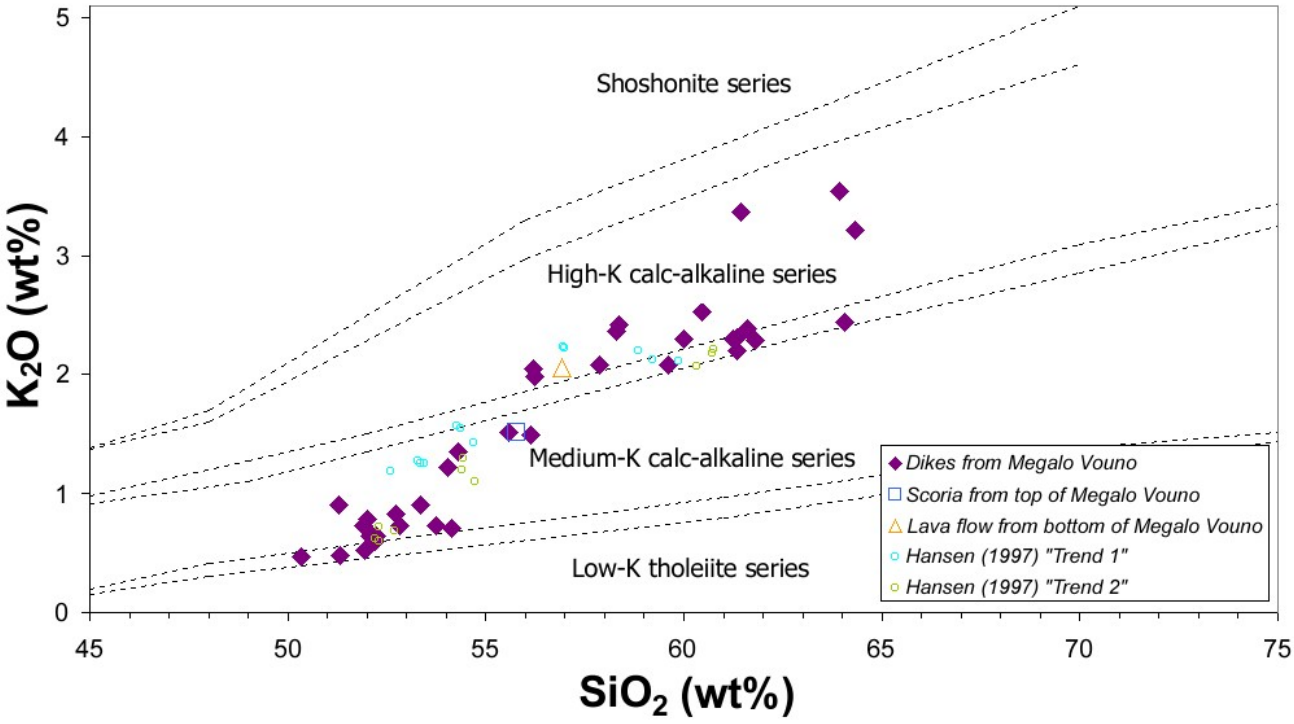


**Fig. 7.4.** $K_2O$ versus $SiO_2$ diagram subdividing subalkaline rocks into four separate series: Low-K tholeiite series, Medium-K calc-alkaline series, High-K calc-alkaline series and Shoshonite series. Subdivisions and nomenclature after Rickwood (1989).

*Pseudo-ternary phase diagrams (Ol-Cpx-Qtz and Ol-Plg-Qtz)*

Two diagrams developed by Grove & Baker (1984) can be used to show the calc-alkaline and tholeiitic evolution trends of basaltic melts. Both diagrams (Ol-Cpx-Qtz and Ol-Plg-Qtz) are projections from the pseudo-quaternary system Ol-Cpx-Qtz-Plg, which has been simplified from ten-component space. Although some information is lost during these procedures, the diagrams are still useful for discriminating between typical tholeiitic and calc-alkaline differentiation trends.

Fig. 7.5 shows that rocks from the Megalo Vouno volcano complex follow a calc-alkaline differentiation trend, i.e. avoidance of reaction point A, crystallisation at elevated pressure (>1 atm) and early crystallisation of olivine + augite + plagioclase, with olivine + augite dominant over plagioclase.

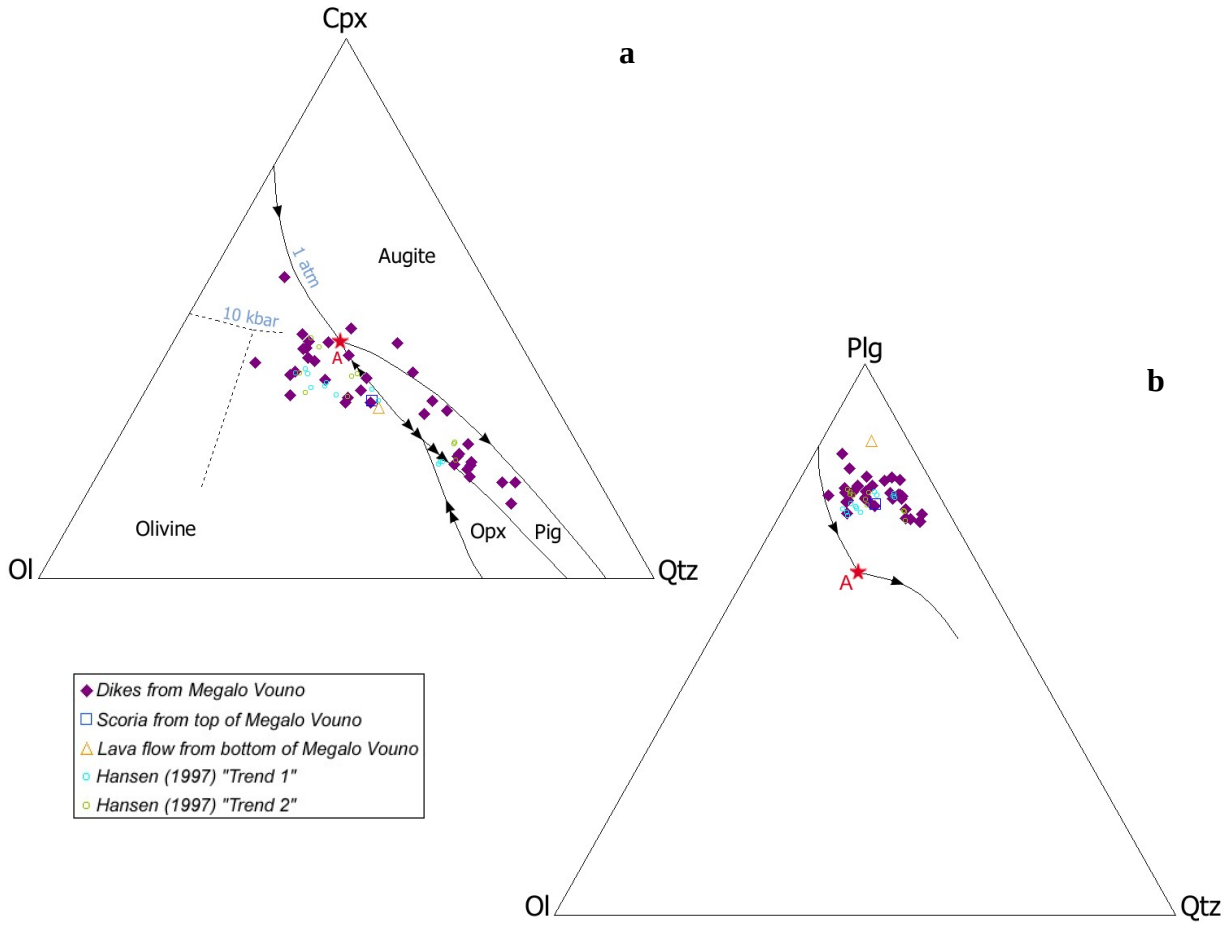


**Fig. 7.5.** Pseudo-ternary phase diagrams for discrimination between tholeiitic and calc-alkaline rock series. After Grove & Baker (1984). Analyses have been recalculated from weight percent oxides to oxygen-normalised molar mineral components (Ol olivine, Cpx clinopyroxene, Qtz silica and Plg plagioclase). Diagram **a** shows the 1 atm and 10 kbar plagioclase-saturated boundaries in the Ol-Cpx-Qtz system. Diagram **b** shows the 1 atm clinopyroxene-saturated boundaries in the Ol-Plg-Qtz system. Reaction point A marks the reaction *olivine+liquid=pigeonite+augite+plg*. Abbreviations: **Opx** orthopyroxene and **Pig** pigeonite. Data are listed in Appendix E, Table E5a and Table E5b.

## 7.4 Variation in major and trace elements

Processes in subduction zone magma series generally result in great variation in $SiO_2$ content among the samples. This makes $SiO_2$ a valuable oxide for plotting along the abscissa against other oxides and trace elements, because the $SiO_2$ content increases with magmatic differentiation.

Trend 1 and Trend 2 recognised by Hansen (1997) were plotted in as many variation diagrams as possible in order to compare these with the dike samples from the Megalo Vouno volcano complex (see also Section 7.5).

From the major element diagrams (Fig. 7.6), it can be seen that increasing $SiO_2$ is accompanied by increasing $K_2O$. $Na_2O$ and $P_2O_5$ both increase up to ca. 62 wt.% $SiO_2$ and then flatten and decrease, respectively. $TiO_2$ looks relatively constant but a slight increase up to 55 wt.% $SiO_2$

followed by a slight decrease can be faintly seen. CaO and MgO both decrease with increasing $SiO_2$, whereas $Al_2O_3$ decreases rapidly up to ca. 54 wt.% $SiO_2$ and then remains relatively constant at higher levels. MnO shows a flat trend, whereas FeO* shows a slight decrease and some scatter.

*When using ICP-MS data for the trace element variation diagrams, only the 30 analysed samples could be plotted, whereas all 38 samples are represented on the diagrams when using XRF data.*

The LREE (Fig. 7.7) in general show a flattened, slightly increasing trend up until about 54 wt.% $SiO_2$ followed by a marked increase with further differentiation. Eu is an exception showing an increase up until 60 wt.% $SiO_2$ where it flattens out.

In Fig. 7.8, the HREE and Y all increase with increasing $SiO_2$ content and seem to flatten above ca. 61 wt.% $SiO_2$.

The LILE (Fig. 7.9), like the LREE, generally show a flattened trend until about 54 wt.% $SiO_2$ followed by an abrupt increase in content with degree of differentiation. The only exception is Sr which shows more scatter and an apparent decrease in content with increasing $SiO_2$.

In Fig. 7.10, all HFSE show an increase in content with degree of magmatic differentiation but perhaps a fairly flat trend up until about 54 wt.% $SiO_2$.

The volatile elements in Fig. 7.11. show very different trends. Cl shows a flat trend with only a few samples above 5000 ppm (plus two samples well above), whereas the samples scatter throughout the S diagram. A rise and fall in S contents is visible despite the scatter.

In Fig. 7.12, the transition metals Sc, V, Cr, Co, Ni and Cu show a decrease with increasing $SiO_2$ content. Sc and V show flat trends up until about 53 wt.% $SiO_2$ followed by a marked decrease. Four samples in the V diagram, however, plot well above the other samples and correlate with four samples rich in FeO* and in FeO*/MgO (Fig. 7.2), giving the impression that there could be a second series with an early V enrichment. Cr and Ni show a rapid decrease to ca. 54 wt.% $SiO_2$ followed by flattened, slightly decreasing trends. Co and Cu both show a continuous decrease throughout the diagrams. Scatter in the Cu diagram makes it difficult to determine whether there is in fact a flat trend or slight increase until 54 wt.% $SiO_2$ prior to the decrease. Zn and Ga show relatively flat patterns but there seems to be some scatter in the Zn diagram, which gives the impression that there is a slight increase with increasing $SiO_2$.

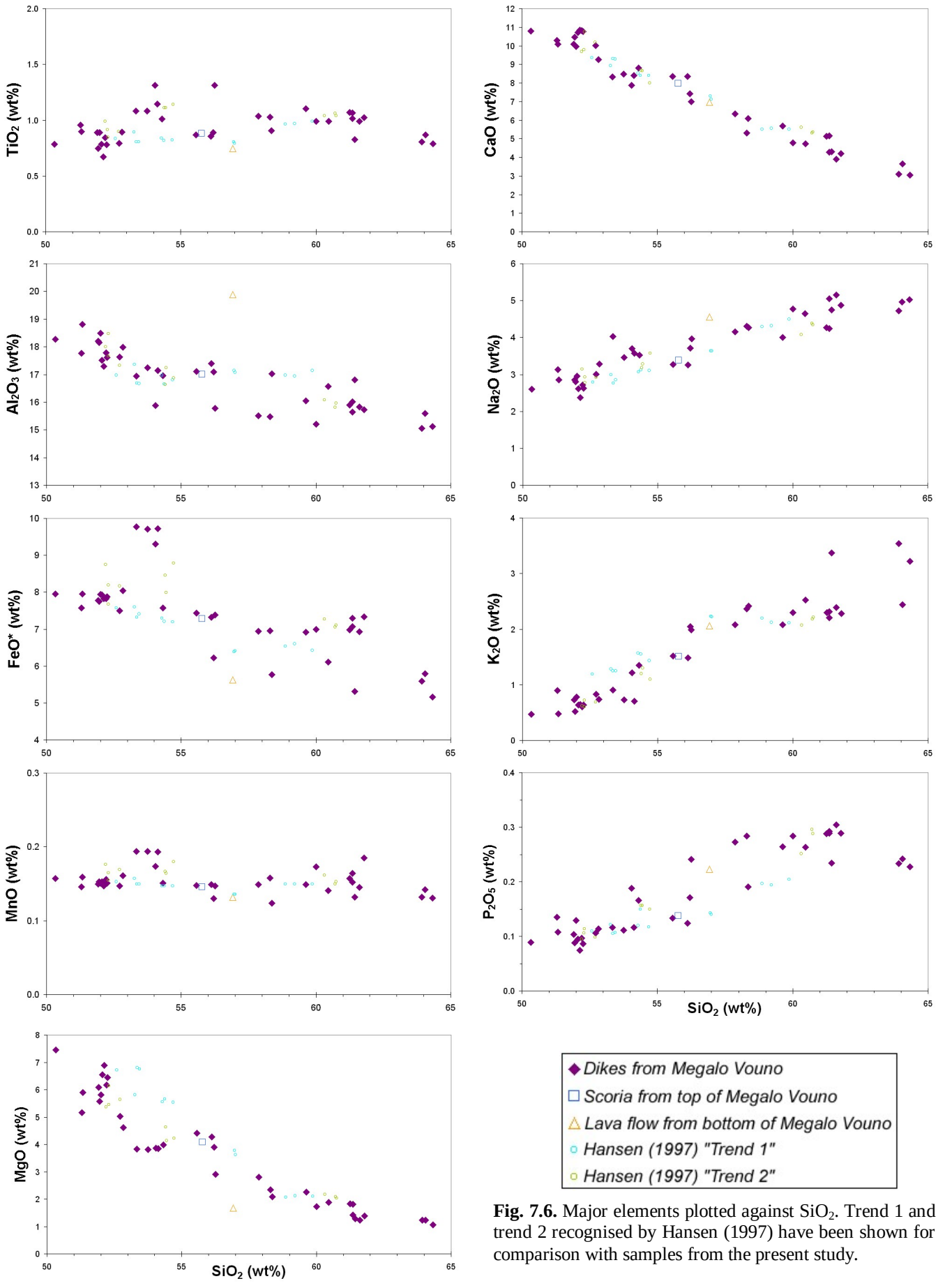


**Fig. 7.6.** Major elements plotted against $SiO_2$. Trend 1 and trend 2 recognised by Hansen (1997) have been shown for comparison with samples from the present study.

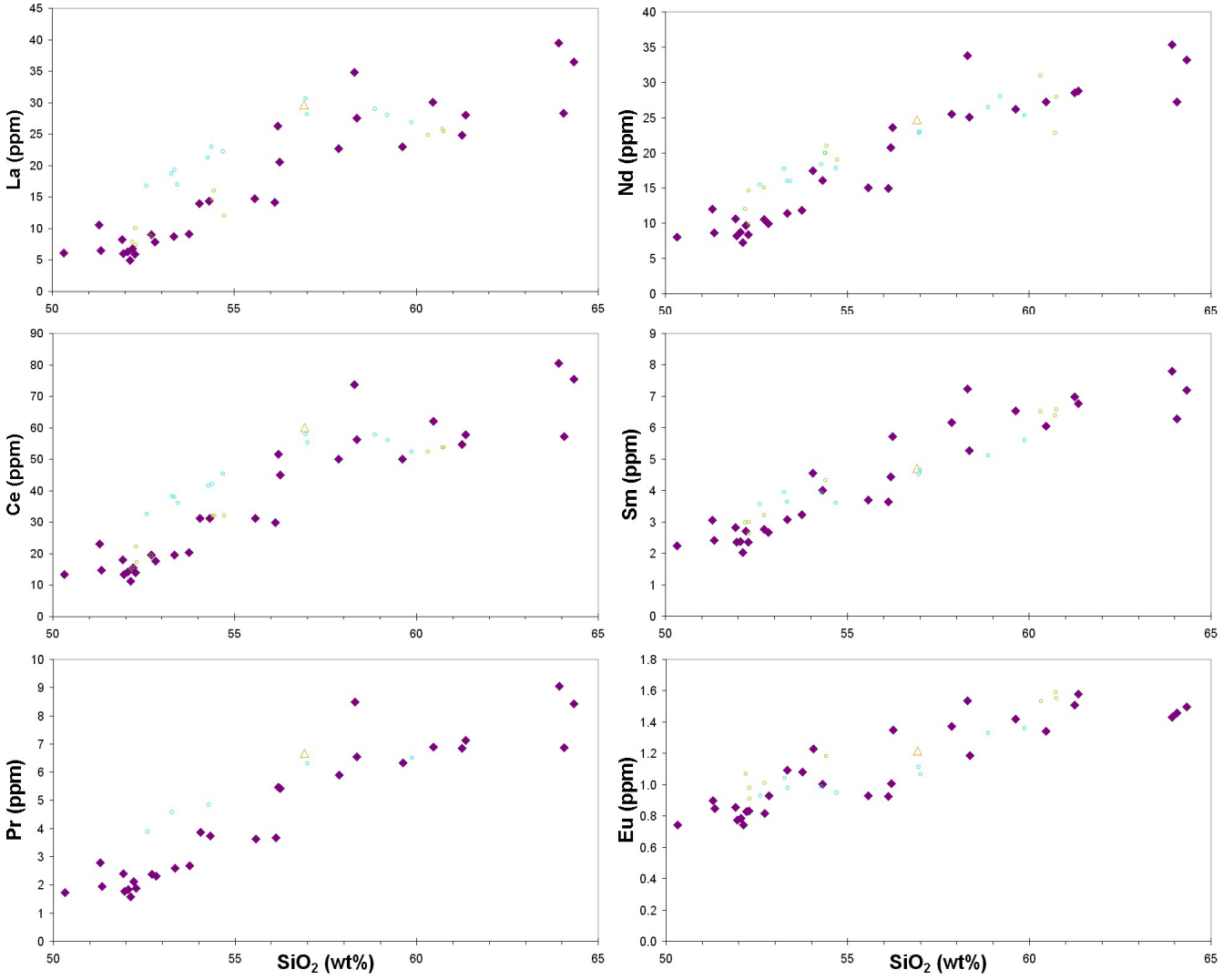


**Fig. 7.7.** Light rare-earth elements (LREE) plotted against $SiO_2$.
Trend 1 and trend 2 data from Hansen (1997) were analysed by INAA and XRF except for samples MV104, MV108, MV109, MV110 and MV115, which have been re-analysed by ICP-MS (Table E2, Appendix E). Some of Hansen s'(1997) samples were not analysed for Sm and Eu and only the above mentioned ICP-MS data were available for Pr.

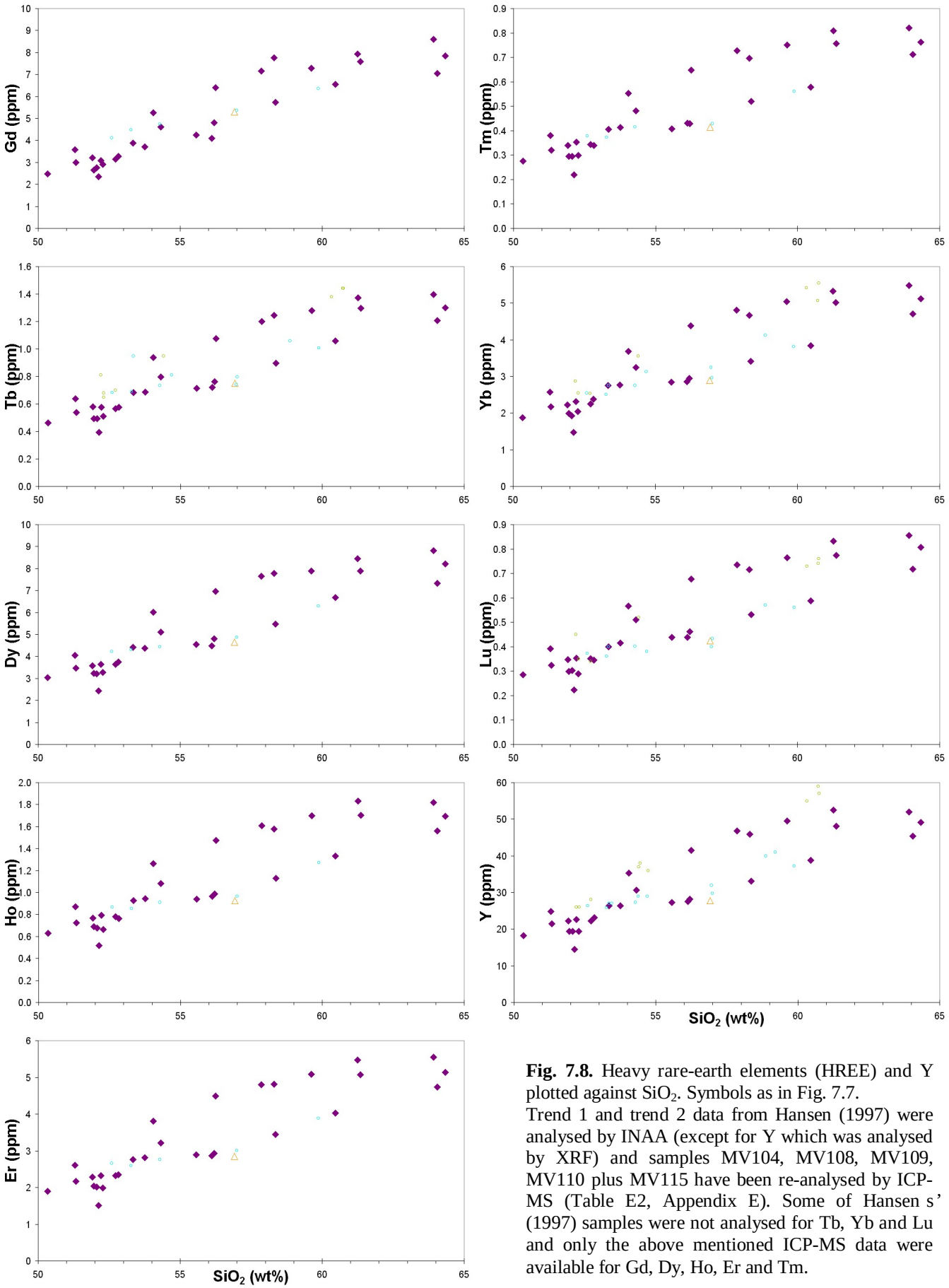


**Fig. 7.8.** Heavy rare-earth elements (HREE) and Y plotted against $SiO_2$. Symbols as in Fig. 7.7.
Trend 1 and trend 2 data from Hansen (1997) were analysed by INAA (except for Y which was analysed by XRF) and samples MV104, MV108, MV109, MV110 plus MV115 have been re-analysed by ICP-MS (Table E2, Appendix E). Some of Hansen s' (1997) samples were not analysed for Tb, Yb and Lu and only the above mentioned ICP-MS data were available for Gd, Dy, Ho, Er and Tm.

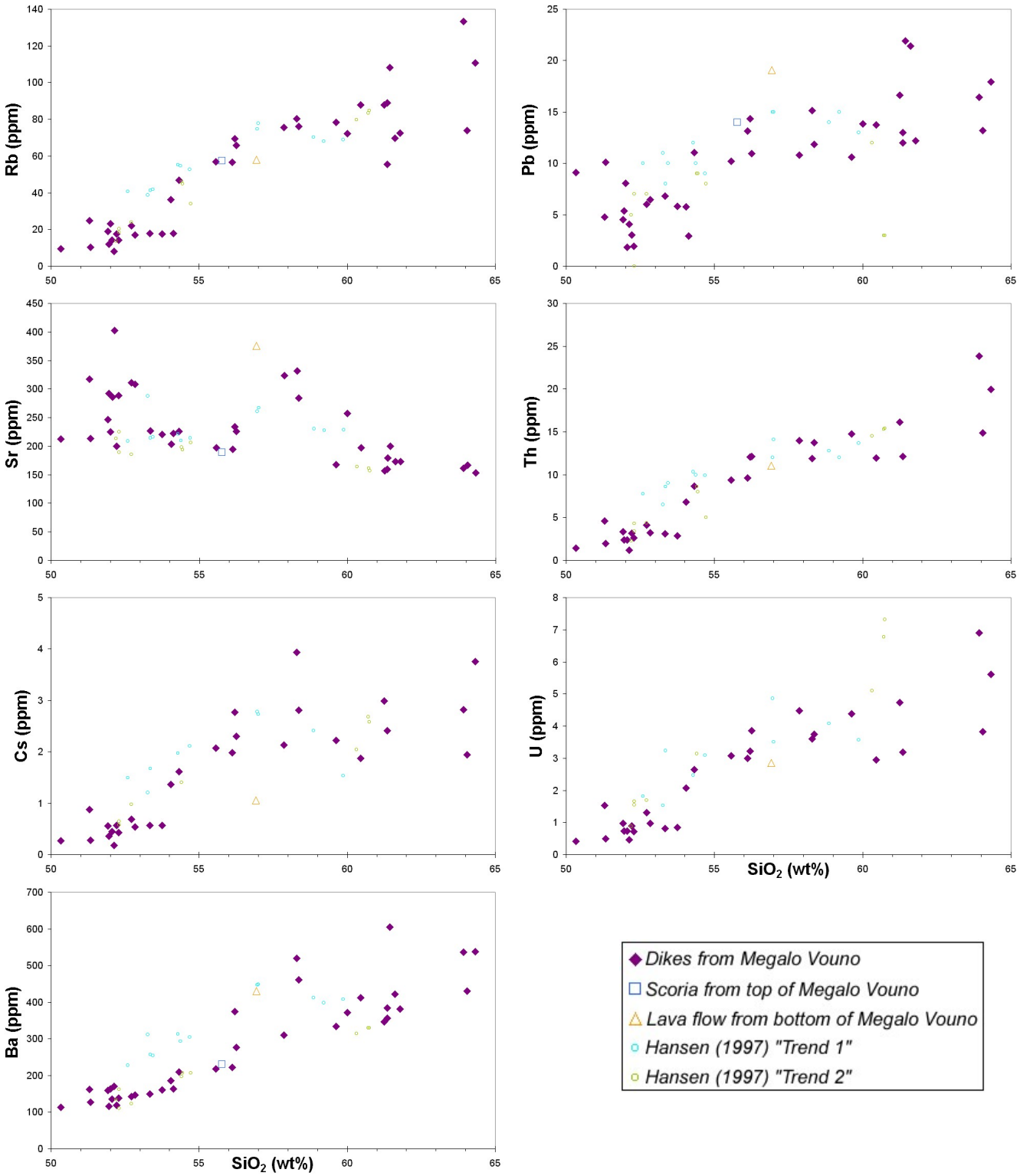


**Fig. 7.9.** Large ion lithophile elements (LILE) plotted against $SiO_2$.
Trend 1 and trend 2 data from Hansen (1997) were analysed by INAA and XRF. New ICP-MS data were used for Th, U and Cs on samples MV104, MV108, MV109, MV110 and MV115 (Table E2, Appendix E). Some of Hansen s (1997) samples were not analysed for U and Cs.

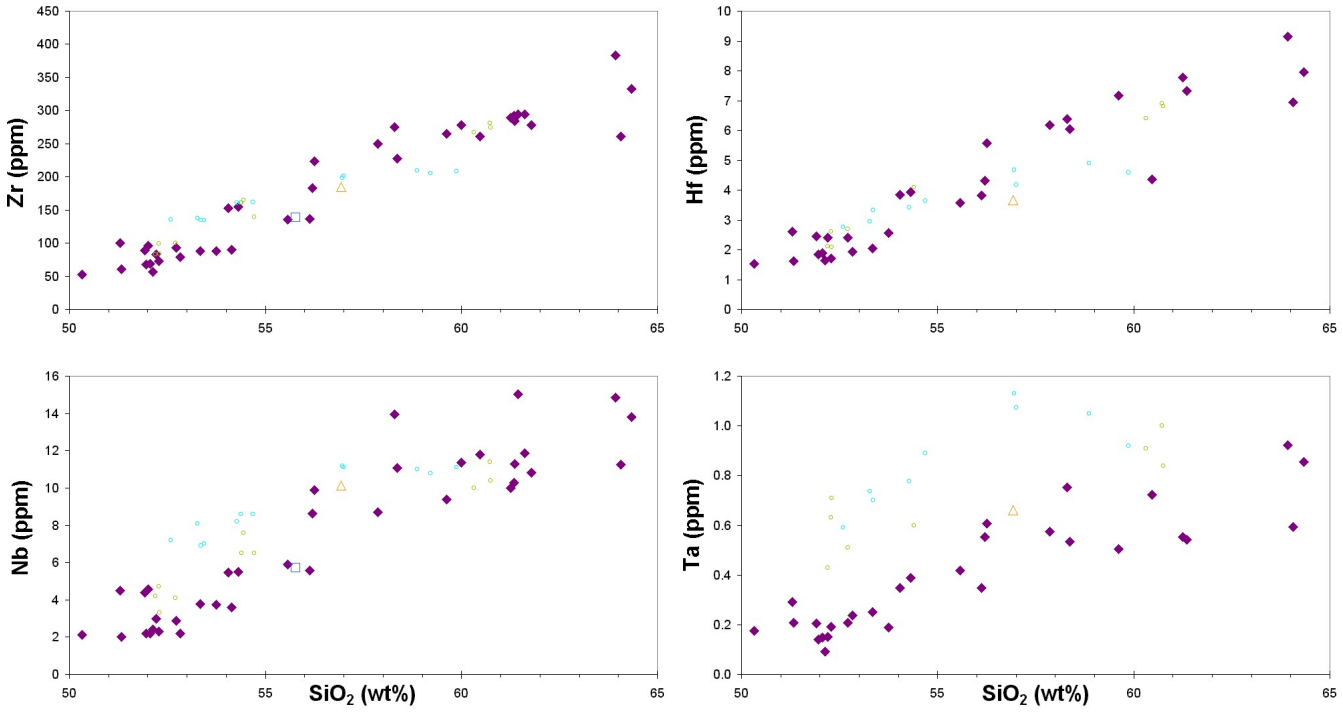


**Fig. 7.10.** High field strength elements (HFSE) plotted against $SiO_2$.
Trend 1 and trend 2 data from Hansen (1997) were analysed by XRF and INAA. New ICP-MS data were used for Hf on samples MV104, MV108, MV109, MV110 and MV115 (Table E2, Appendix E). Some of Hansen s'(1997) samples were not analysed for Hf. Due to contamination from the tungsten-carbide mortar, Ta data from Hansen (1997) have not been plotted.

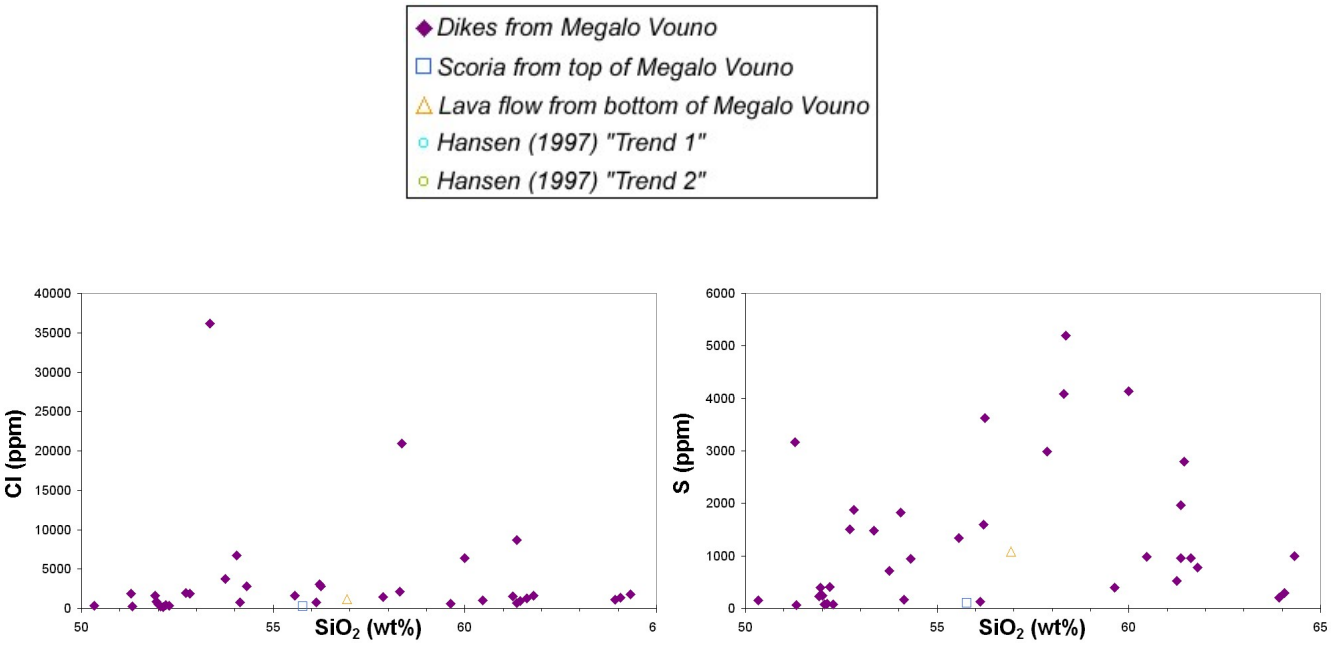


**Fig. 7.11.** Volatile elements plotted against $SiO_2$.
Cl and S analyses were not available from Hansen (1997).

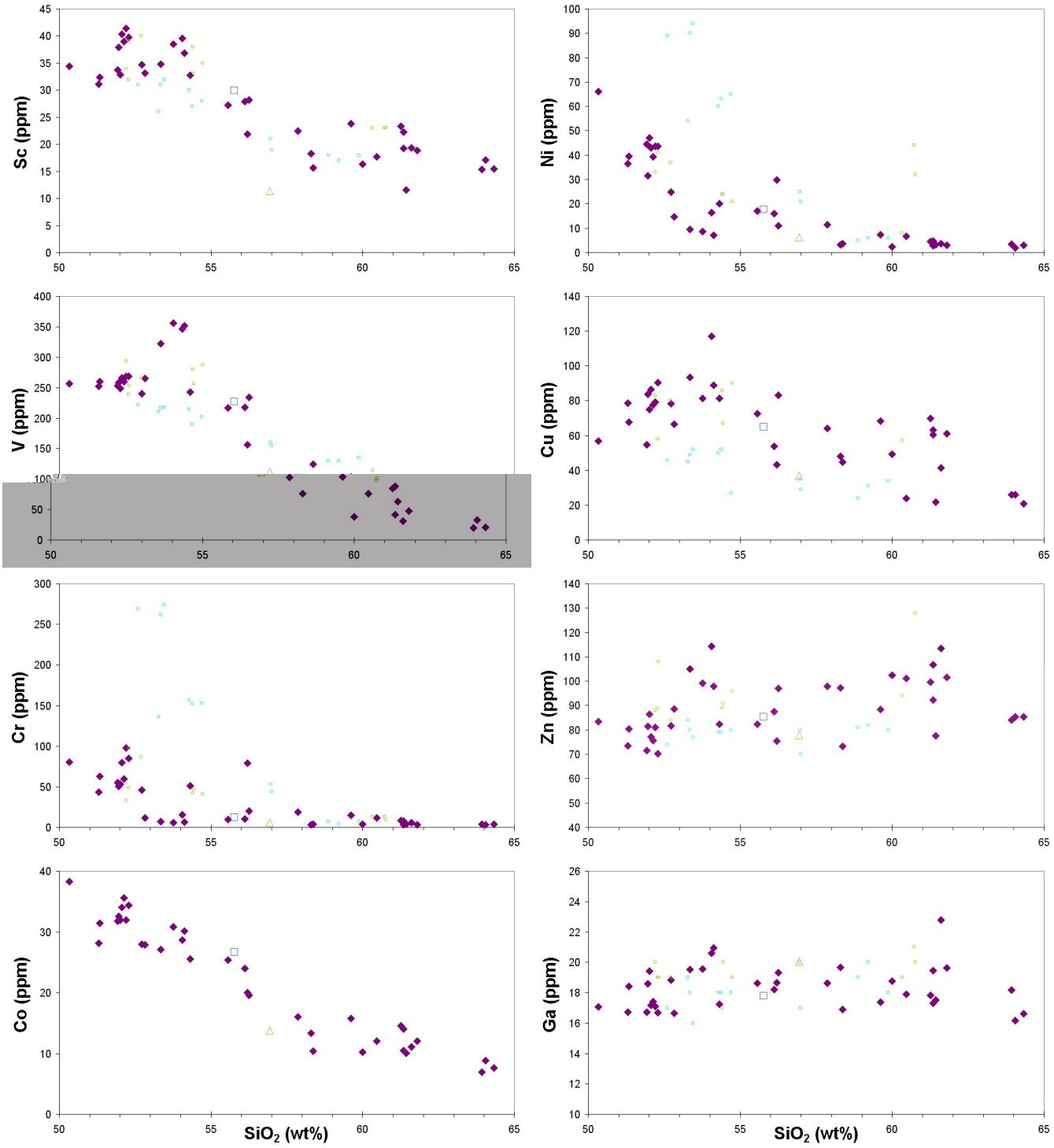


**Fig. 7.12.** Transition metals and Ga plotted against $SiO_2$. Trend 1 and trend 2 data from Hansen (1997) were analysed by INAA.
In the Ni versus $SiO_2$ diagram sample MVD123 is not shown because of its anomalously high Ni content (216 ppm) and in the Cu versus $SiO_2$ diagram samples MVD121, MVD122 and MVD123 are not shown because of their anomalously high Cu contents (296 ppm, 364 ppm and 441 ppm, respectively) (all from Hansen, 1997). Due to contamination from the tungsten-carbide mortar Co data from Hansen (1997) have not been plotted.

Fig. 7.13 shows ratios of HFSE and LILE plotted against $SiO_2$. The element pairs Zr-Hf and Nb-Ta are chemically very similar and have been expected to behave congruently in fluids and melts (Weyer et al., 2003). However, improved analytical techniques have resulted in observed variations in these ratios. In Fig. 7.13 the majority of samples have Nb/Ta values lower than chondritic (17.6; Weyer et al., 2002) and N-MORB values (17.7; Sun & McDonough, 1989), and show significant scatter in the least evolved rocks. Ten samples have ratios above chondritic values, the highest at 26.5. Zr/Hf values are slightly higher than chondritic values (34.2; Weyer et al., 2002) and nearly constant (only sample MVD-T 01-06 is marginally lower: 34.1). Data from Hansen (1997) generally show slightly higher values (the majority >40.0). The highest ratio is represented by sample MVD-B 01-16 at 60.0. Both Nb/Ta and Zr/Hf appear to show only a slight increase with increasing $SiO_2$. Th and U, on the other hand, have vastly different chemical properties and thus vary in different geochemical reservoirs (Weyer et al, 2003). Th/U shows a slight increase with increasing $SiO_2$, the majority of samples having values near 3.5, which is between the 4.0 continental crust value proposed by Rudnick & Fountain (1995) and the 2.5 depleted upper mantle value from Sun & McDonough (1989). There is more scatter among the data from Hansen (1997), which is probably due to the less precise analytical method available at that time.

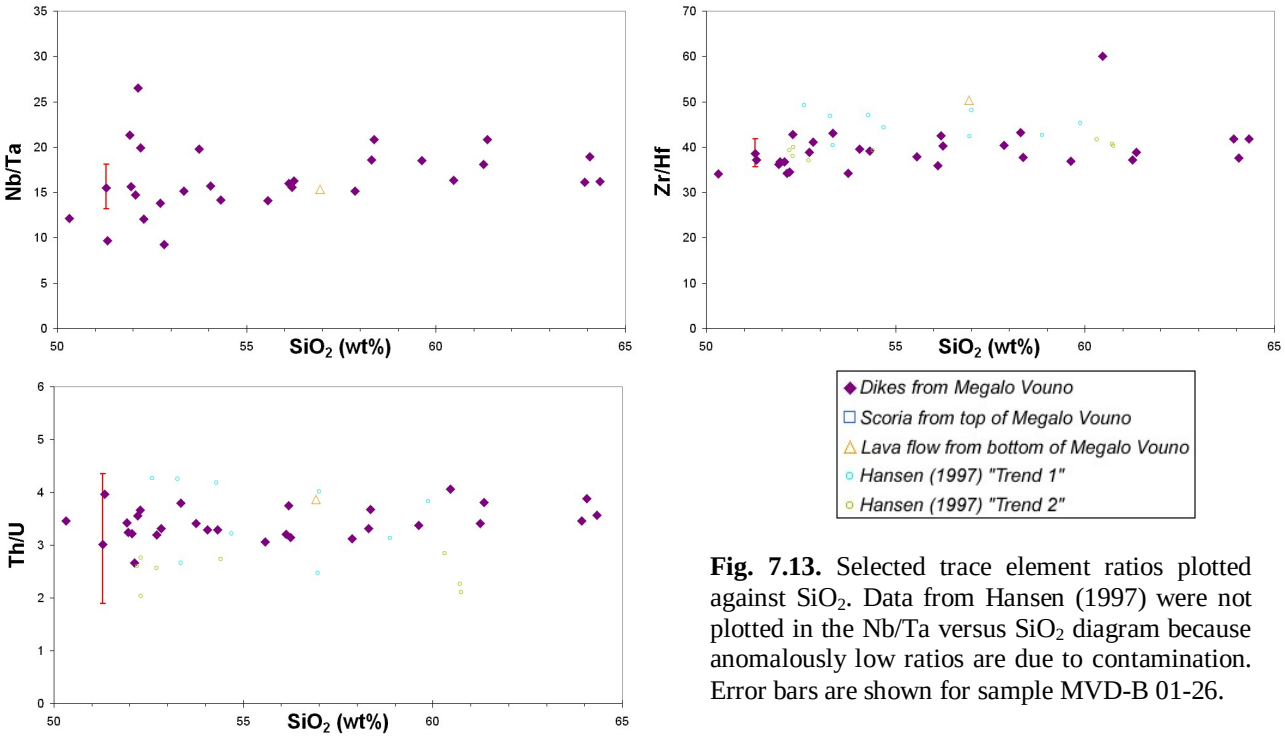


**Fig. 7.13.** Selected trace element ratios plotted against $SiO_2$. Data from Hansen (1997) were not plotted in the Nb/Ta versus $SiO_2$ diagram because anomalously low ratios are due to contamination. Error bars are shown for sample MVD-B 01-26.

## 7.5 Recognition of trends

Hansen (1997) showed that samples from Megalo Vouno and adjacent volcanoes plot along two distinct trends which she argued were controlled mainly by fractional crystallisation (trend 1) and possibly magma mixing (trend 2).

The diagrams in Figs. 7.6, 7.7, 7.8, 7.9, 7.10, 7.11 and 7.12 all show data from the present study, and when data were available the two trends recognised by Hansen (1997) were inserted. From comparison with Hansen s'(1997) samples and careful testing of geochemical coherence throughout the diagrams it was tried to establish whether the sampled dikes also belong to these two series or are, perhaps, only representative of one of the series.

Data from Santorini form at least two distinct trends on a $TiO_2$ versus $SiO_2$ diagram; one trend showing a marked $TiO_2$ enrichment followed by decrease, and the other showing slight enrichment throughout the diagram. When the two series suggested by Hansen (1997) were plotted on the diagram, it was realised that a possible third trend could also be recognised among the compiled Santorini data (Fig. 7.14).

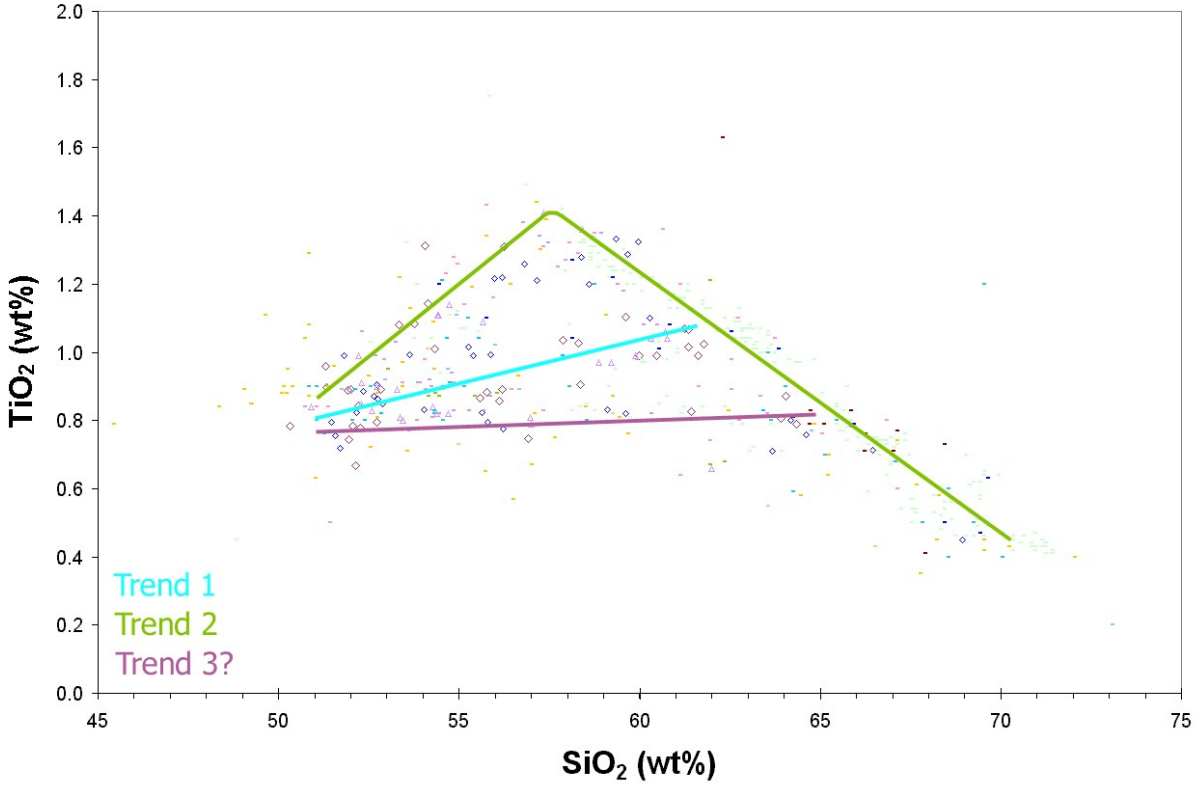


**Fig. 7.14.** Data from Santorini plot along at least two trends on a $TiO_2$ versus $SiO_2$ diagram. Trend 1 and trend 2 recognised by Hansen (1997) can be matched with trends elsewhere on Santorini, but a large number of samples do not fit these trends. It seems that many samples have ca. 0.75 wt.% $TiO_2$ and fit a third trend. The plotted data (ca. 600 samples) were compiled by Kann (2004).

Unfortunately, these trends are not clear in the $TiO_2$ diagram in Fig. 7.6, though it can be seen, that some rocks seem to be enriched in $TiO_2$ compared with others with the same $SiO_2$ content.

To establish which series the sampled dikes could be representative of, the following reasoning was used: if the least evolved and the most evolved samples in the $TiO_2$ diagram represent end-members of two possible series, then only the samples in between these can be used to define the individual series. Thus, five dike samples showing increasing $TiO_2$ content with degree of magmatic differentiation, and three dike samples with near-constant $TiO_2$ content with degree

of magmatic differentiation were chosen as possible representatives of the two trends recognised by Hansen (1997):

Trend 1: Samples 04, 23 and 25 (symbols shown with blue rims on diagrams)
Trend 2: Samples 13, 14, 15, 27 and 28 (shown with green rims on diagrams)
(For ease of reading and clarity on diagrams, samples were named only by their two last digits).

Fig. 7.15 shows how the eight chosen samples plot on selected major and trace element diagrams, along with the two trends. After plotting, the following problems were found: samples 04 and 25 plot on or near the other trend on the $K_2O$, Ba and La diagrams -even well to the far side of trend 2 on the Nb diagram; sample 28, likewise, plots nearer to trend 1 and on the far side of this in the $K_2O$, La and Nb diagram (and well off trend 2 on Ba) and finally, samples 13 and 15 plot on trend 1 in the Tb diagram. It is evident that there are too many discrepancies between samples and trends throughout the diagrams, and it was concluded that the Megalo Vouno dikes cannot belong strictly to the two trends of Hansen (1997). This situation will be discussed further in Chapter 8.

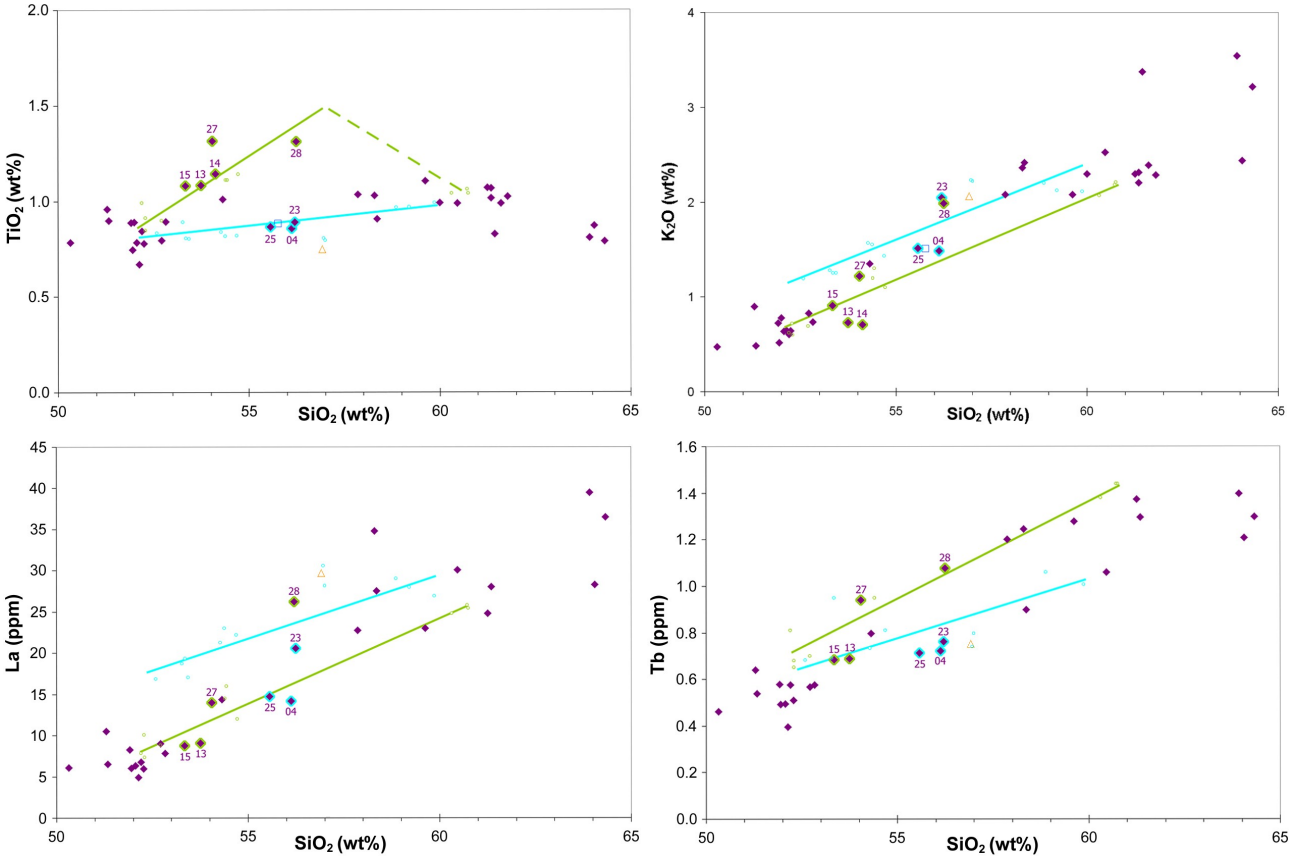


**Fig. 7.15.** Comparison of Megalo Vouno dikes with trend 1 and trend 2 (Hansen, 1997) on selected major and trace element variation diagrams **(continues on next page)**

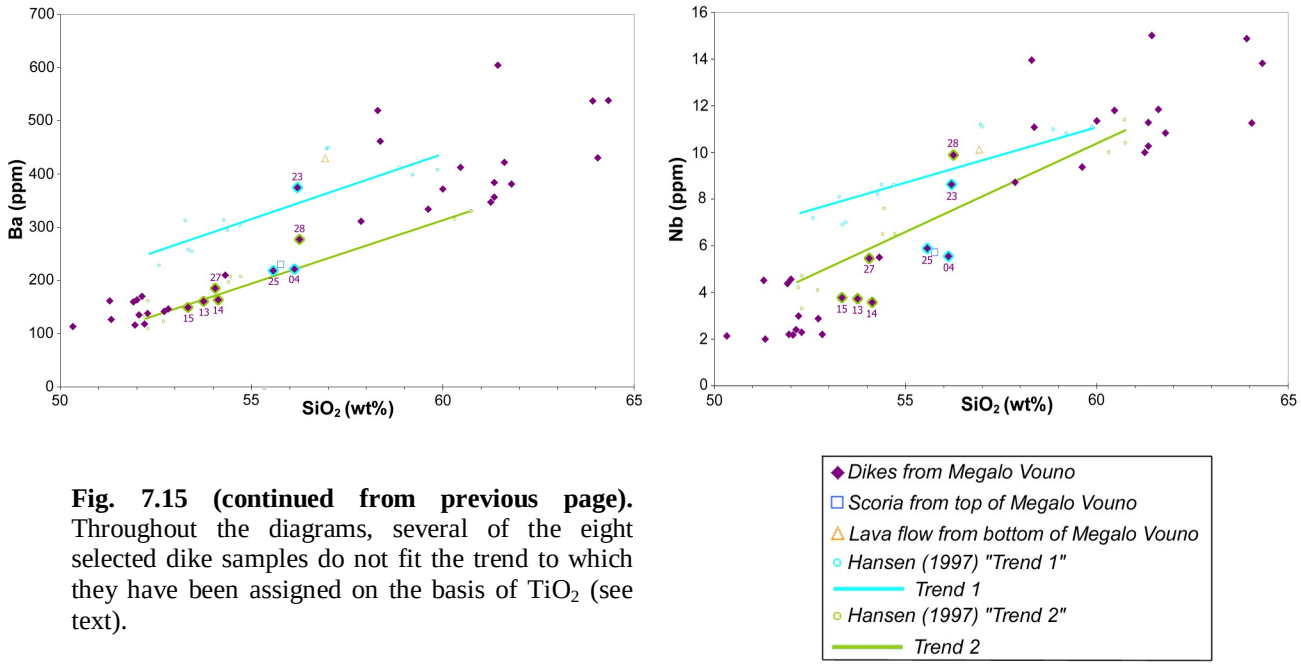


**Fig. 7.15 (continued from previous page).** Throughout the diagrams, several of the eight selected dike samples do not fit the trend to which they have been assigned on the basis of $TiO_2$ (see text).

## 7.6 REE patterns

The distribution of trace elements between phases can be described by the partition coefficient $Kd = C_{mineral}/C_{melt}$ (where $C$ is the concentration of the trace element). A mineral/melt partition coefficient larger than 1.0 means that the element has a preference for the mineral (solid phase) and can be described as compatible, whereas an incompatible element will have a partition coefficient below 1.0.

REE compete with other elements for space in the crystal structure of minerals. They are therefore useful in determining which minerals have been involved in partial melting or fractional crystallisation processes. An example is the element Eu, which is readily partitioned into plagioclase as $Eu^{2+}$ (under relatively reducing conditions), whereas $Eu^{3+}$ is less readily incorporated. This means that fractional crystallisation of plagioclase will deplete the melt in $Eu^{2+}$ creating a negative Eu-anomaly between Gd and Sm in the REE pattern. The size of the Eu anomaly is given by Eu/Eu* (where Eu* is an interpolation between $Sm_N$ and $Gd_N$). Taylor & McLennan (1985; 1995) recommend calculating the geometric mean: $Eu/Eu^* = Eu_N/(Sm_N * Gd_N)^{½}$, where Eu/Eu*>1.0 = positive anomaly and Eu/Eu*<1.0 = negative anomaly. A negative Eu anomaly is pronounced in the evolved rocks in Fig. 7.16.

Besides the negative Eu anomaly, Fig. 7.16 also shows how the REE become fractionated relative to each other. The LREE in the studied rocks behave more incompatibly during crystallisation processes than the HREE (LREE: ca. 20-160 times chondritic values and HREE ca. 10-35 times chondritic values). This is easily recognised because the elements along the abscissa have been organised according to atomic number: the elements furthest to the left on

the diagram are, therefore, most incompatible in the differentiating minerals of the studied rocks.

For the LREE, the slope of the patterns becomes steeper from the least evolved to the most evolved rocks, whereas the slopes trend almost parallel for the HREE.

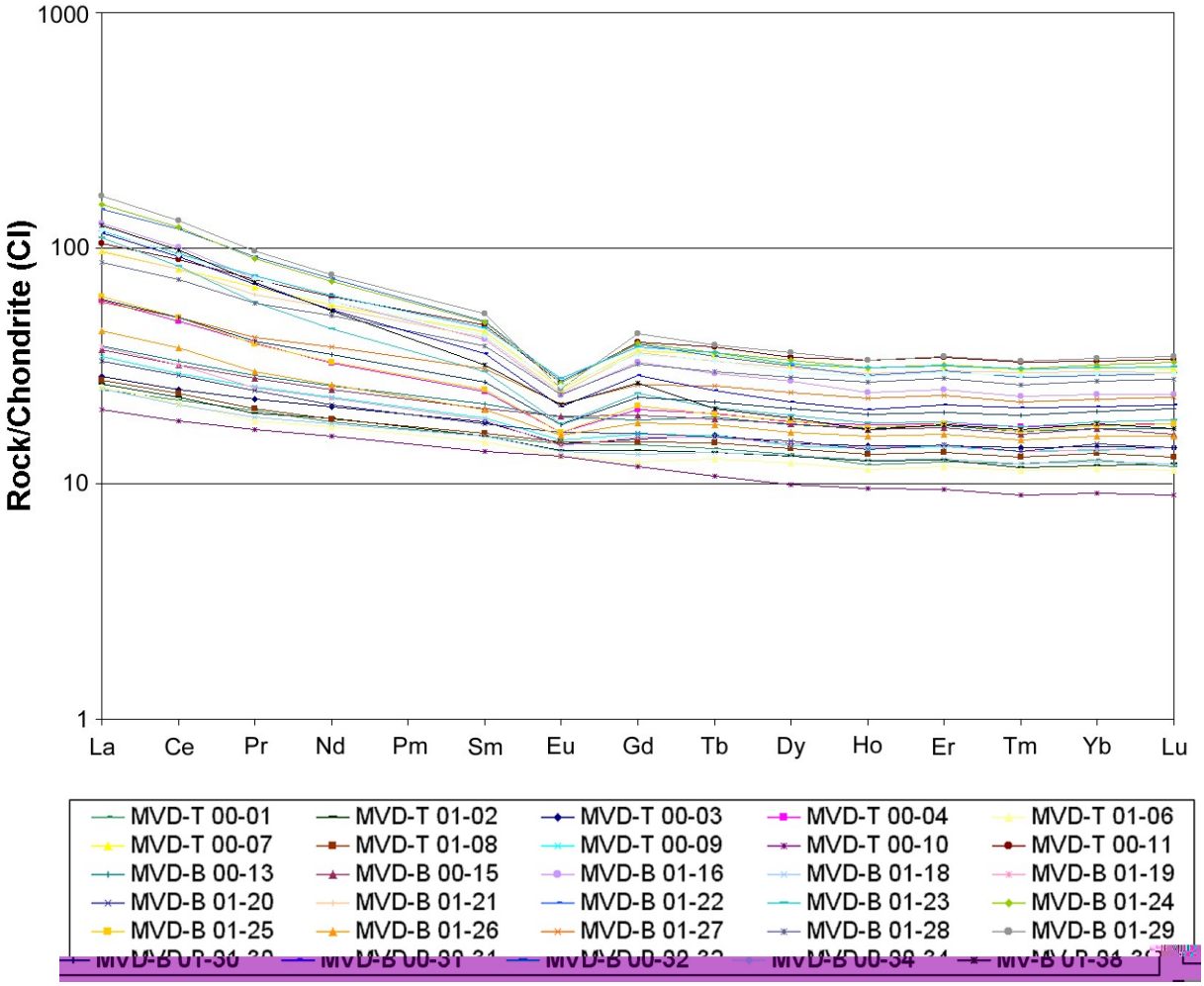


**Fig. 7.16.** REE abundances normalised to average composition of CI carbonaceous chondrites (McDonough & Sun, 1995).

Fractionation among the REE is graphically presented in Fig. 7.17, where normalised ratios of combined LREE (La-Sm) and HREE (Gd-Yb) have been plotted against $SiO_2$. In accordance with Fig. 7.16, the $(La/Sm)_N$ diagram shows an increase with magmatic differentiation and an even greater increase can be seen on the $(La/Yb)_N$ diagram. In both diagrams it seems that there could be two trends. The $(Gd/Yb)_N$ diagram shows an almost flat, only slightly increasing trend, and, finally, the $(Eu/Eu^*)_N$ diagram shows how the negative Eu anomaly is developed from ca. 54-58 wt.% $SiO_2$. Below 54 wt.% $SiO_2$, the trend is nearly flat and the ratio just below 1.0 (except for a single sample >1.0 and four samples <<1.0). The pattern is nearly flat above 58 wt.% $SiO_2$.

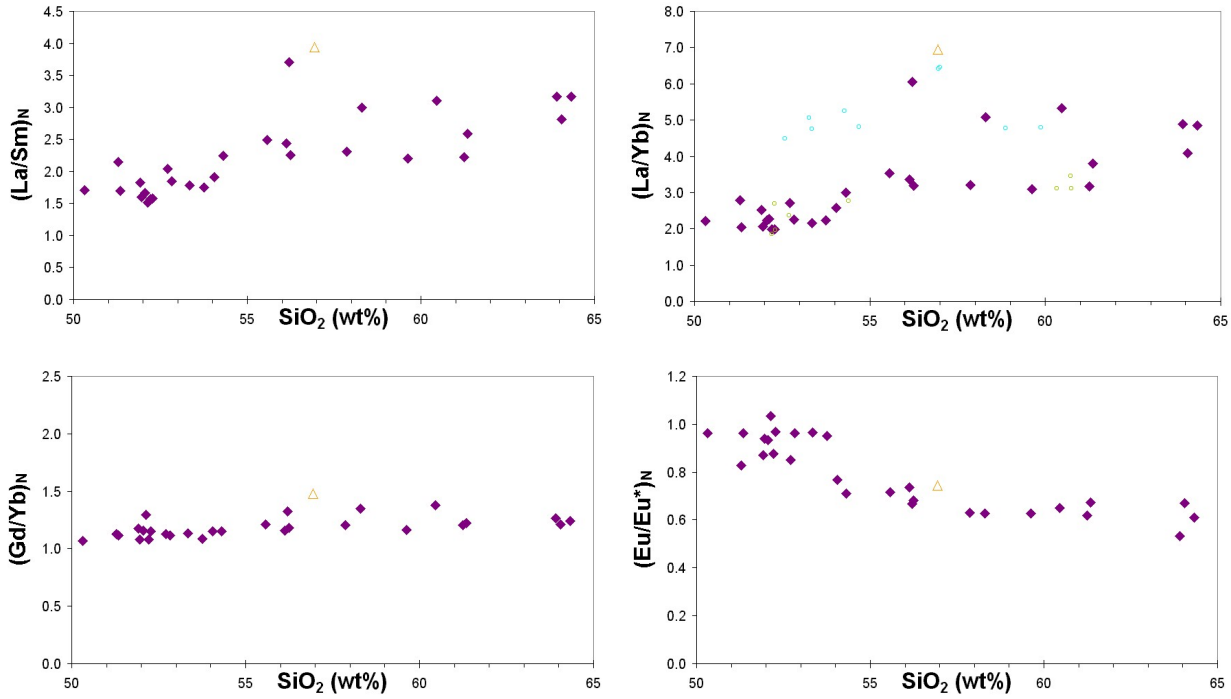


**Fig. 7.17.** Normalised REE ratios and Eu/Eu* versus $SiO_2$. Trend 1 and trend 2 samples from Hansen (1997) are clearly separated on $(La/Yb)_N$ versus $SiO_2$. Symbols as in Fig. 7.15.

## 7.7 Spider diagrams

Spider diagrams (or normalised multi-element diagrams) are widely used to compare basaltic rock chemistry with either a possible mantle source or with the most abundant volcanic rock (MORB). As a mantle source (or rather a primitive undifferentiated earth), Rollinson (1993) recommends using chondrite data because these are measured directly (as opposed to estimated primordial mantle values). The normalising values for chondrite used here are from McDonough & Sun (1995) and for MORB from Pearce (1983).

Some of the basaltic samples from Megalo Vouno were not analysed by ICP-MS and could not be plotted in the spider diagrams because of lack of data. Instead, six of the borderline basaltic andesites were plotted along with the basalts (the most silicic having an $SiO_2$ content of 52.83 wt.%). This resulted in 11 samples which were chosen as basaltic representatives for the Megalo Vouno dikes throughout the diagrams (Fig. 7.18).

The spider diagrams (Fig. 7.18) show the sþiky þattern expected in rocks from a subduction zone. The basalts representing the Megalo Vouno dikes show uniform, almost parallel patterns in both normalisations, and only in a few cases do some of the samples stand out. Whereas the majority have less $Nb_N$ than $Ta_N$, the opposite is the case with samples MVD-T 00-03, MVD-T 00-09 and MVD-T 00-10 in the MORB normalisation. In general, the samples show positive anomalies in Rb, Th and Ce (except MVD-T 00-10 having a different LILE pattern).

In the chondrite normalised diagram, the greatest discrepancies among the samples are seen between Cs-Pb-Rb. Some of the rocks have a pronounced negative Pb anomaly, whereas others almost show a weak positive anomaly. In general, the samples show high values in Ba-Th-U, a strong negative P anomaly, a weak negative Ti anomaly and weak positive anomalies in La and Sr.

An average of the basaltic dike samples was compared with basalts from other volcanic centres in the Aegean arc as well as with basalts from other tectonic settings. The Aegean basalts show overall similar patterns and the average of the Megalo Vouno dike basalts lies slightly below the other volcanic centres.

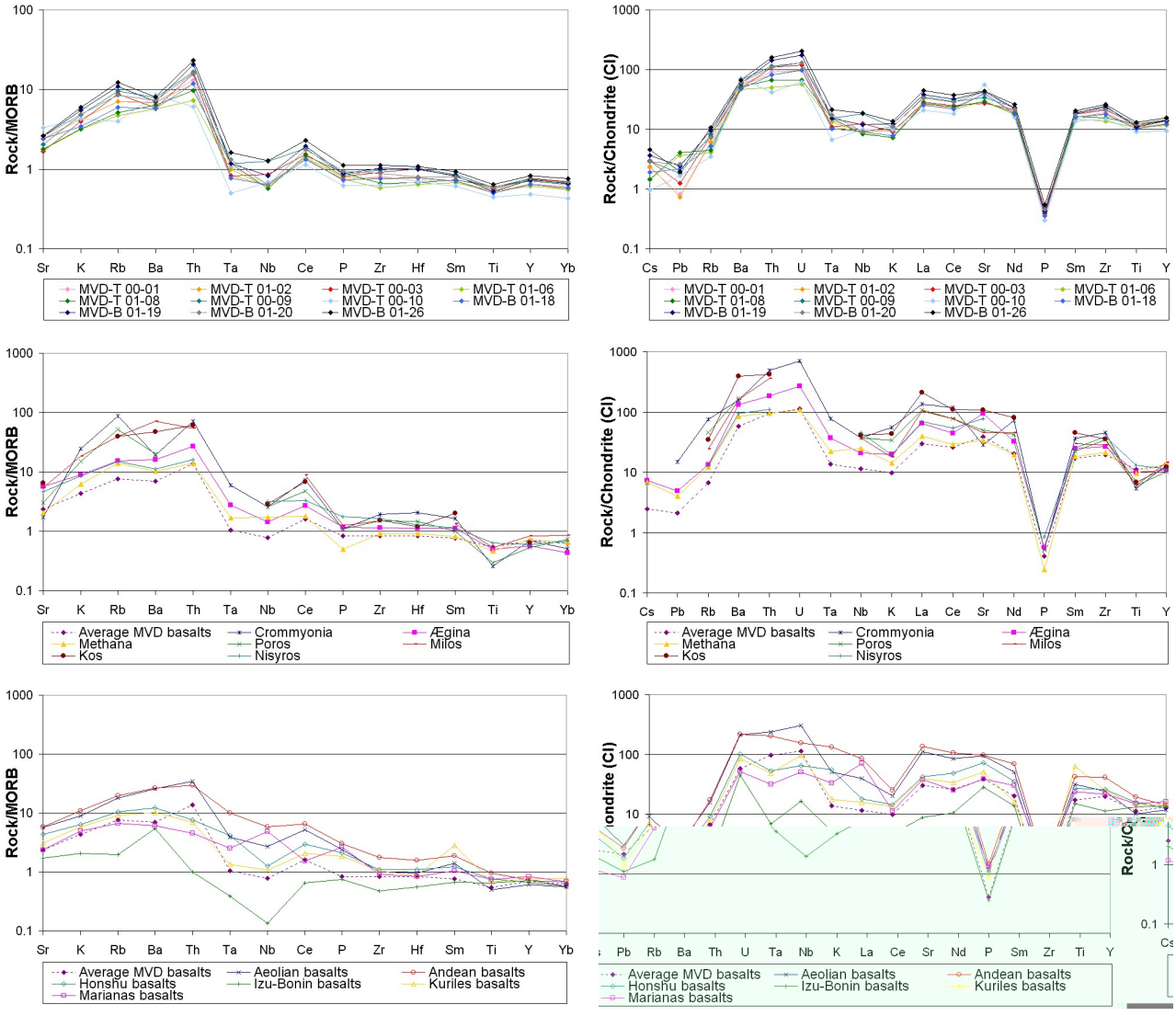


**Fig. 7.18.** MORB normalised (left column) and CI chondrite normalised (right column) spider diagrams. Eleven basaltic dike samples from Megalo Vouno have been plotted in the two top diagrams and an average was calculated for comparison with basalts from other volcanic centres in the Aegean arc (middle row) and with basalts from other tectonic settings (bottom row). Some of the latter are representative of active continental margins and others of oceanic island arcs. Geochemical data from the Aegean arc and other arc settings are from various authors listed along with the data sets in Appendix E (Table E6 - MORB and Table E7 - CI chondrite).

In the bottom figures (Fig. 7.18), the Izu-Bonin oceanic island-arc basalts show lower values than average Megalo Vouno dike basalts and the samples generally show quite different patterns. Only the negative anomalies in Pb and P (CI normalisation) seem to be common. The basaltic dikes from Megalo Vouno have the most in common with the pattern shown by Aeolian arc basalts, but the latter show overall higher values.

## 7.8 Tectonic discrimination diagrams

From field work as well as the literature presented in the first few chapters it is obvious that the setting of Santorini and the Megalo Vouno dikes is in a subduction zone. However, to learn more about the processes leading to the types of volcanism found on Santorini, and to see whether the samples are typical for this tectonic setting or they are transitional as seen elsewhere in the geochemistry, various diagrams discriminating between different tectonic settings have been studied.

The so-called tectono-magmatic diagrams can be used to identify tectonic settings from the geochemistry of rock samples and can be subdivided roughly into two main groups: diagrams using elements which reflect the source of the magmas and diagrams showing the effect of the subsequent processes, i.e. degree of melting and fractional crystallisation.

Belonging to the first group are two diagrams by Bailey (1981), which use Sc/Ni and Th versus La/Yb to group four types of andesites (Fig. 7.19).

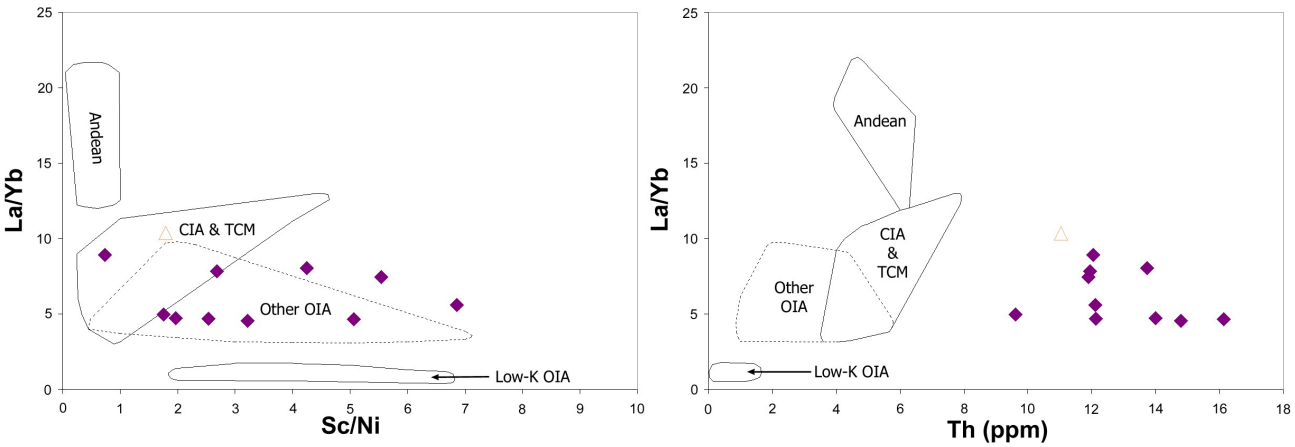


**Fig. 7.19.** Tectonic discrimination using trace elements and trace element ratios to discriminate between four types of andesites: Low-K OIA *low-K oceanic island-arc andesites*; Other OIA *other oceanic island-arc andesites*; CIA & TCM *continental island-arc andesites and thin continental margins* and finally representative of thick continental margins: Andean *Andean andesites*. Symbols as in Fig. 7.1. After Bailey (1981).

Ten andesitic dikes (56> wt.% $SiO_2$ <63; following Peccerillo & Taylor (1976)) plus a scoria of andesitic composition were plotted in the diagrams. The samples show a wide variation in Th content and lie outside the four andesite types in the La/Yb versus Th diagram. They are, however, level with "other" and "CIA" in La/Yb content, but have too high Th content to belong to any of these groups. In the La/Yb versus Sc/Ni diagram most of the samples plot in

other" and a few in "CIA & TCM," which was expected since these groups contain oceanic island arcs and island arcs partly formed on thin continental crust ("other"), plus island arcs on well developed continental crust and island arcs on thin continental margins ("CIA & TCM")."
Gorton & Schandl (2000) also developed diagrams that reflect the source of the magmas. The first diagram (Fig. 7.20) was based on Pearce (1982, 1983), and uses trace element ratios (Th/Yb versus Ta/Yb) to group felsic and intermediate rocks (covering $SiO_2$ ranges from 54 to 77 wt.%) into three tectonic settings: oceanic arcs, active continental margins and within-plate volcanic zones. Besides discriminating among different tectonic settings, the diagrams can be used to interpret the tectonic evolution of a region and the geochemical evolution of rocks (e.g., transition from subduction to rift-related volcanism) (Gorton & Schandl, 2000).

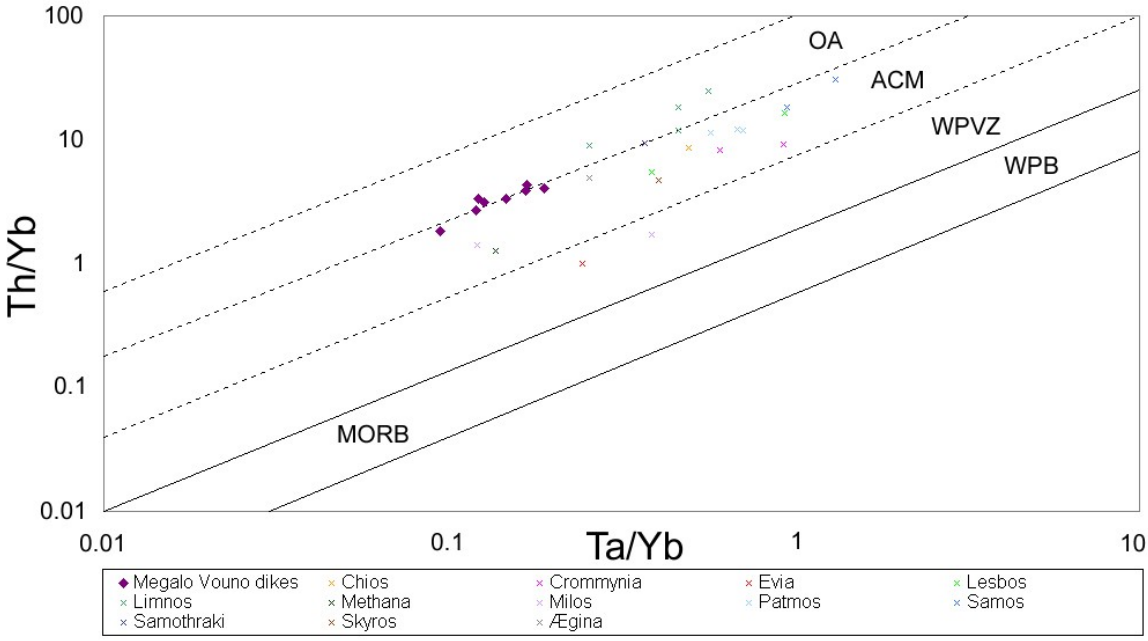


**Fig. 7.20.** OA – *oceanic arcs*; ACM – *active continental margins*; WPVZ – *within-plate volcanic zones*; MORB – *mid-ocean ridge basalts*; WPB – *within-plate basalts*. The field WPB and MORB represents the zones previously defined by Pearce (1982). After Pearce (1982, 1983) and revised by Gorton & Schandl (2000).

Eight dikes from Megalo Vouno could be plotted in the diagram together with representatives from other volcanic centres in the Aegean arc. The dikes group in a straight line directly on the division between OA (oceanic arcs) and ACM (active continental margins). As mentioned by Gorton & Schandl (2000), rocks in a suite are expected to plot parallel to (though not necessarily directly on) the division lines between tectonic settings, since Th and Ta will be enriched relative to Yb to about the same degree during magmatic processes. This is clear for the Megalo Vouno dikes but not as pronounced for the other volcanic centres in the arc. The dikes are generally lower in Ta/Yb than the other centres, but plot centrally or to the lower side regarding the Th/Yb values.

The Th/Ta versus Yb diagram (Fig. 7.21) shows the same 12 volcanic centres and the same eight dikes, and, again, the samples plot near the division line between oceanic arcs and active continental margins. However, the majority of the dike samples plot in the oceanic arc field and generally have higher Yb values than the other centres but plot intermediate on Th/Ta values.
Because both diagrams use Ta as a discriminator one must take care during sample preparation when samples crushed in a tungsten carbide mill can result in significant Ta contamination. Since all samples for this study were crushed in the agate mill none of the samples have been discarded. The anomalously high contents of Th in the Santorini magmas make any interpretation using the diagrams of Gorton & Schandl (2000) uncertain.

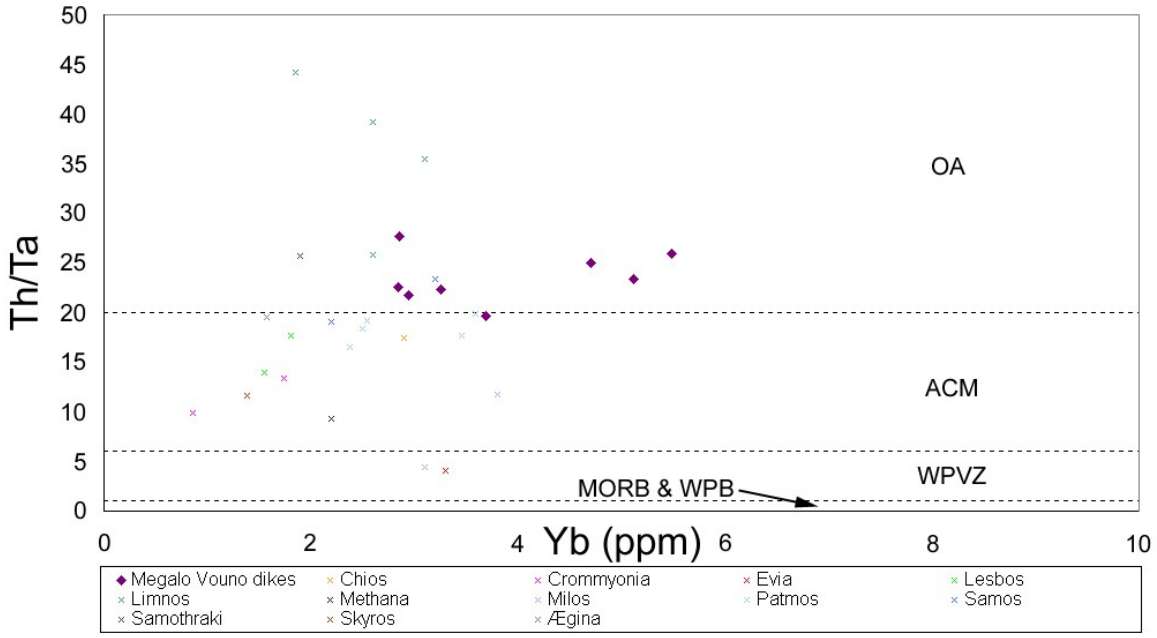


**Fig. 7.21.** OA *oceanic arcs*; ACM *active continental margins*; WPVZ *within-plate volcanic zones*; MORB *mid-ocean ridge basalts*; WPB *within-plate basalts*. After Gorton & Schandl (2000).

Belonging to the second category are discrimination diagrams using elements which discriminate between tectonic settings resulting from the different geochemical processes taking place in the different environments.
The ternary diagram developed by Wood (1980) was originally constructed for use with basalts, and uses Hf, Th and Ta to discriminate between volcanic arcs, MORB, within-plate tholeiites and within-plate alkaline basalts (Fig. 7.22) According to Rollinson (1993), it is particularly useful for identifying volcanic arc basalts and it can be applied to intermediate and silicic lavas as well as basalts. All samples from Megalo Vouno plot well within the field of volcanic arc basalts. Again, the high Th contents of Megalo Vouno dikes add uncertainty to the interpretation of this diagram.

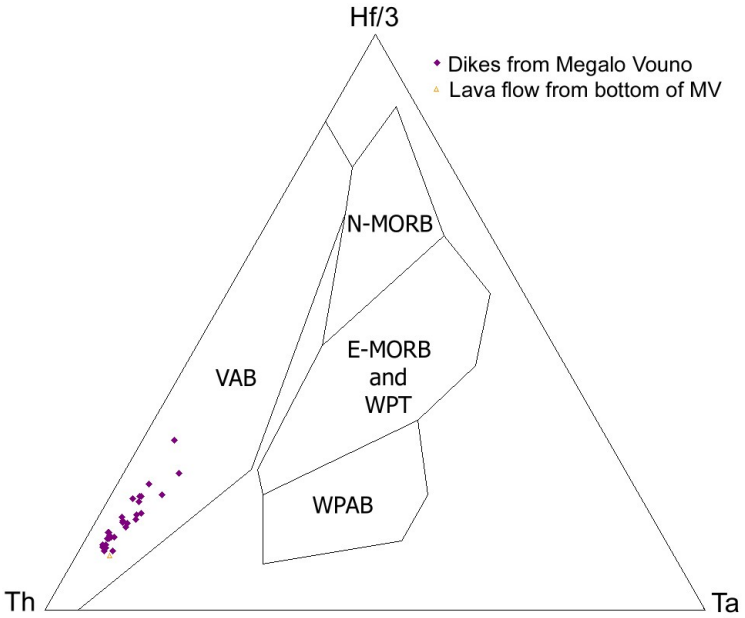


**Fig. 7.22.** Discrimination diagram using immobile HFSE to discriminate between N-MORB ~~*normal mid-ocean ridge basalts*~~; E-MORB ~~*enriched mid-ocean ridge basalts*~~; WPT ~~*within-plate tholeiites*~~; WPAB ~~*within-plate alkaline basalts*~~ and VAB ~~*volcanic arc basalts*~~. Symbols as in Fig. 7.1. After Wood (1980).

The tectonic discrimination diagram by Shervais (1982) (Fig. 7.23) groups basalts according to their V and Ti content. Variations of V relative to Ti can be taken as a measure of the crystal fractionation processes as well as the oxygen activity of a magma. This is because V can exist in reduced or oxidised states in a magma, whereas Ti only exists in one state. Five basalts have been plotted and all but one plot within the field for calc-alkaline basalts. The fields, however, have great overlap, and all the Megalo Vouno basalts also plot within the fields of arc tholeiites, MORB and back-arc basalts.

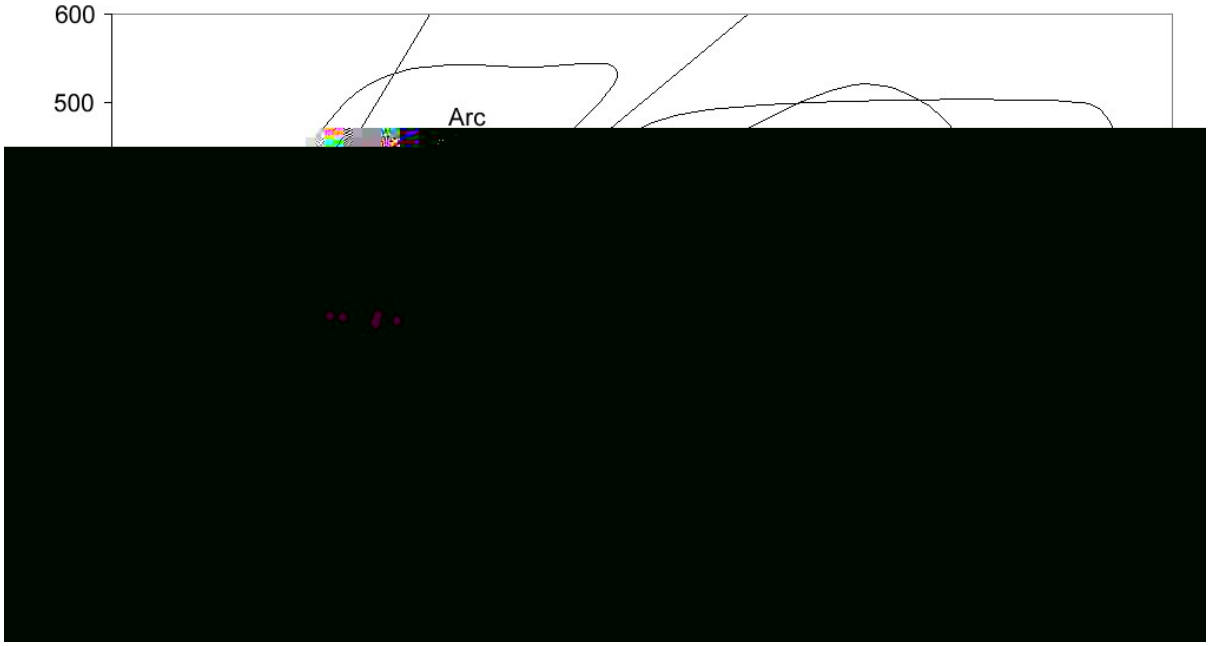


**Fig. 7.23.** Tectonic discrimination diagram using V versus Ti. Abbreviations: CFB ~~*continental flood basalts*~~; MORB ~~*mid-ocean ridge basalts*~~ and BAB ~~*back-arc basalts*~~. Symbols as in Fig. 7.1. After Shervais (1982).

## 7.9 Isotope geochemistry

Primary magmas produced beneath subduction zones are believed to be varying mixtures of different components or sources arising from melting of the peridotitic mantle, subducted sediments and slab fluids (from the altered oceanic crust and sediments) (e.g., Ellam & Hawkesworth, 1988; Schmidt & Poli, 1998; Macdonald et al., 2000). Since isotopic ratios are not altered by subsequent fractional crystallisation, they may reveal something about this mixing of components which is thought to take place in the sub-arc mantle. However, isotopic ratios can also change subsequently as a consequence of mixing between magmas with different isotopic composition or by contamination with crustal rocks, and this will mask the information provided by primary source melts.

Isotopic data for 20 samples are presented in Table 7.1 and uncertainties are presented in Tables C4 and C5 (Appendix C).

**Table 7.1.** Isotopic ratios for 14 dikes, one Peristeria 1 lava flow and five lavas from Peristeria 3. The latter five samples were collected by Hansen (1997) but analysed for this study, while the rest are all from this study.

| Sample No | $^{87}Sr/^{86}Sr$ | $^{143}Nd/^{144}Nd$ | $^{206}Pb/^{204}Pb$ | $^{207}Pb/^{204}Pb$ | $^{208}Pb/^{204}Pb$ |
|---|---|---|---|---|---|
| MVD-T 00-01 | 0.703783 | 0.512844 | 18.917 | 15.652 | 38.884 |
| MVD-T 01-06 | 0.704345 | 0.512826 | 18.891 | 15.669 | 39.064 |
| MVD-T 00-07 | 0.704225 | 0.512784 | 18.914 | 15.679 | 38.964 |
| MVD-T 01-08 | 0.704544 | 0.512788 | 18.873 | 15.654 | 39.084 |
| MVD-T 00-10 | 0.703656 | 0.512751 | 18.992 | 15.639 | 39.048 |
| MVD-B 00-15 | 0.704880 | 0.512740 | 18.906 | 15.671 | 38.989 |
| MVD-B 01-18 | 0.704056 | 0.512833 | 18.927 | 15.660 | 39.012 |
| MVD-B 01-20 | 0.705046 | 0.512785 | 18.910 | 15.656 | 38.971 |
| MVD-B 01-21 | 0.705037 | 0.512799 | 18.876 | 15.640 | 38.848 |
| MVD-B 01-22 | 0.707115 | 0.512558 | 18.901 | 15.673 | 38.940 |
| MVD-B 01-23 | 0.706043 | 0.512558 | 18.896 | 15.674 | 38.940 |
| MVD-B 01-24 | 0.704538 | 0.512711 | 18.895 | 15.664 | 38.916 |
| MVD-B 01-25 | 0.705004 | 0.512700 | 18.859 | 15.673 | 38.940 |
| MVD-B 00-32 | 0.704912 | 0.512711 | 18.892 | 15.667 | 38.910 |
| MV-B 01-38 | 0.705029 | 0.512645 | 18.907 | 15.674 | 38.957 |
| MV104 | 0.705625 | 0.512613 | 18.921 | 15.673 | 38.958 |
| MV108 | 0.706172 | 0.512523 | 18.903 | 15.688 | 39.009 |
| MV109 | 0.706376 | 0.512531 | 18.799 | 15.640 | 38.824 |
| MV110 | 0.705658 | 0.512566 | 18.886 | 15.683 | 39.004 |
| MV115 | 0.704693 | 0.512636 | 18.873 | 15.668 | 38.932 |

The five samples from Megalo Vouno/Peristeria 3 (MV104-MV115) all belong to trend 1 of Hansen (1997). At the time of isotopic analysis it had not yet been discovered that the two geochemical trends produced by the Peristeria 3 lavas (Hansen, 1997) differed from trends produced by the dikes (Section 7.5). Since it was only possible to analyse isotopic compositions

for a total of 20 samples, it would not have been possible to obtain a good coverage of both trend 1 and 2 from Hansen (1997), as well as the dikes.

Table 7.2 compares the ranges of Sr-, Nd- and Pb-isotopes obtained in this study with previously published isotopic data from Santorini. From the table it appears that the Sr- and Nd-isotope ranges in this study are slightly wider than in most other studies (except for Briqueu et al. (1986)).

**Table 7.2.** Isotopic ratios of Santorini rocks.

| Author | $^{87}Sr/^{86}Sr$ | $^{143}Nd/^{144}Nd$ | $^{206}Pb/^{204}Pb$ | $^{207}Pb/^{204}Pb$ | $^{208}Pb/^{204}Pb$ |
|---|---|---|---|---|---|
| Pe & Gledhill (1975) | 0.7048-0.7060 | | | | |
| Barton et al. (1983) | 0.70472-0.70620 | | | | |
| Briqueu et al. (1986) | 0.70376-0.70762 | 0.512473-0.512888 | | | |
| Eleftheriadis et al. (1998) | 0.70472-070520 | | | | |
| Zellmer (1998) | 0.7035-0.7052 | 0.51285-0.51267 | | | |
| Druitt et al. (1999) | 0.704331-0.705425 | 0.512630-0.512794 | 18.708-18.951 | 15.647-15.728 | 38.741-39.083 |
| This Study | 0.703656-0.707115 | 0.512523-0.512844 | 18.799-18.992 | 15.639-15.688 | 38.824-39.084 |

The important effect of post-eruptive contamination upon Sr isotopic ratios was reported by Barton et al. (1983) who showed that an increase of 0.0008 in $^{87}Sr/^{86}Sr$ is possible. Thus, the reason for the high upper value in the studied rocks could most likely be that dikes sampled at sea-level have been contaminated with seawater. This is supported by the fact that dikes collected on top of Megalo Vouno represent the lowest Sr isotopic values, and that a dike collected at sea-level has the highest ratio. There is, however, a considerable overlap and two of the lava flows collected by Hansen (1997) on top of Megalo Vouno (belonging to Peristeria 3) showed the second and third highest values (0.706376 and 0.706172).

Druitt et al. (1999) studied isotopic variation with stratigraphic height of the pyroclastics throughout the entire Santorini volcano complex, and found that there is a decrease in $^{87}Sr/^{86}Sr$ with time until Upper Scoriae 1 & 2 followed by an increase in the Cape Riva and Minoan eruptions. The opposite tendency was found in the $^{143}Nd/^{144}Nd$ ratios, whereas the Pb isotopes showed no clear variation with stratigraphic height. On the basis of these data, they suggested that both trace element and isotopic variations were due to temporal changes in the extent of crustal interaction and perhaps the composition of the assimilant. Thus, the change to higher Sr isotopic ratios and lower Nd isotopic ratios in the final eruptives may be due to assimilation of remobilised plutonic rocks from the first phase of volcanism on Santorini.

Among the studied samples it is not possible to make out any stratigraphic variation, because a single lava flow from Peristeria 1 represents the lowest levels, and the highest levels are represented by five lava flows from Peristeria 3 sampled by Hansen (1997). The remaining

samples are dikes sampled at different levels in the caldera wall; only the dikes sampled on top of the complex could represent a stratigraphically higher level.

Overall, isotopic ratios plotted against $SiO_2$ (Fig. 7.24) show no clear correlations and seem to be dominated by scatter. However, trend 1 samples from Hansen (1997), and two dikes (MVD-B 01-22 and MVD-B 01-23), are displaced to lower $^{143}Nd/^{144}Nd$ ratios than the rest of the samples. On this basis, these rocks are collectively termed the "low-Nd" series. It is, however, not possible to determine whether all trend 1 samples belong to this series until further isotopic data are obtained. The "high-Nd" series is defined by the remaining 12 dike samples. Although no isotopic data are available for trend 2 samples (Hansen, 1997), it is suspected that these may belong to the "high-Nd" series. This is purely based on the variation diagrams (Section 7.4), in which dikes generally show more geochemical similarity with trend 2 than trend 1 (Figs. 7.6-7.12). This cannot be proven without isotopic data for trend 2 samples.

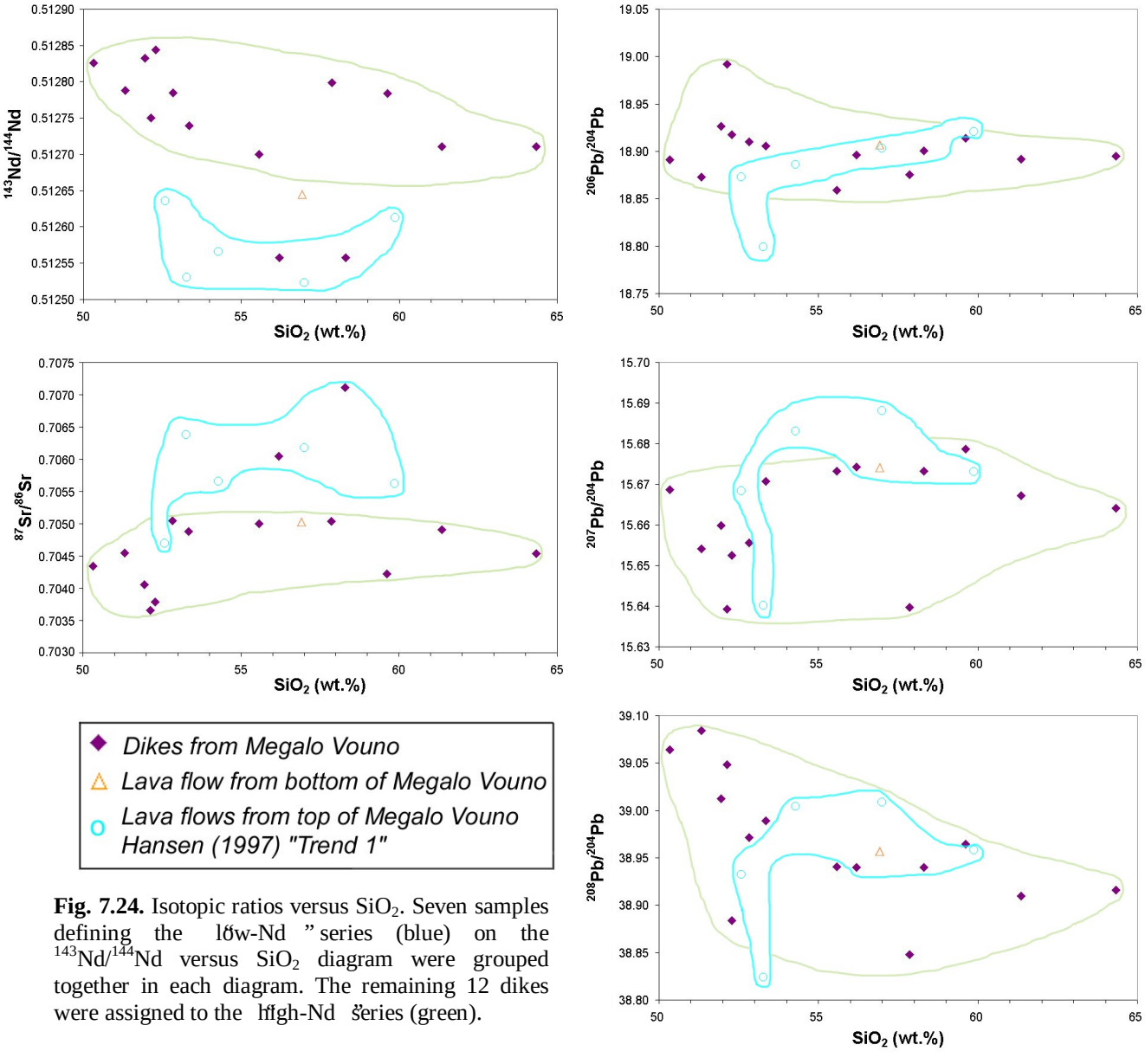


**Fig. 7.24.** Isotopic ratios versus $SiO_2$. Seven samples defining the "low-Nd" series (blue) on the $^{143}Nd/^{144}Nd$ versus $SiO_2$ diagram were grouped together in each diagram. The remaining 12 dikes were assigned to the "high-Nd" series (green).

The Peristeria 1 lava flow (orange triangle) plots in between the two series on the Nd isotope diagram, and within the high-Nd series on the Sr isotope diagram. However, on the three Pb isotope diagrams it plots within both series. It must be pointed out, that this lava flow represents a much older eruption than the dikes, and may be unrelated isotopically.
Samples belonging to the low-Nd series are characterised by higher $^{87}Sr/^{86}Sr$ ratios than the high-Nd series (except sample MV 115). Sr isotopic ratios show a vague positive correlation with $SiO_2$, whereas no correlation can be seen on the Nd isotope diagram. The samples show no clear difference from the high-Nd series in Pb isotopic ratios, but they show a marked increase with $SiO_2$ without producing a clear trend.
Samples belonging to the high-Nd series show a positive correlation with Sr isotopic ratios but a negative correlation with Nd ratios. In contrast to the unclear trends shown by the low-Nd series, the high-Nd dikes appear to correlate negatively with $SiO_2$ on $^{206}Pb/^{204}Pb$ and $^{208}Pb/^{204}Pb$ isotopic plots.

Most dikes and Peristeria lava flows plot together with other Santorini isotopic data on combined isotopic diagrams (Figs. 7.25, 7.26 and 7.27). Fig. 7.25 shows $^{143}Nd/^{144}Nd$ plotted against $^{87}Sr/^{86}Sr$ for the analysed rocks along with rocks from other geological settings and mantle reservoirs. The data form a negative trend and plot well below the MORB field, as is common for other arc rocks. Most samples plot within the field defined by Aegean arc rocks and to the right of the mantle array. Their slope is lower than that of the mantle array and trends almost parallel to Aeolian arc rocks (and slightly lower than Aegean arc data).
The inset in Fig. 7.25 displays only the two series defined above, and shows that these can be separated completely on the diagram. The low-Nd rocks, furthermore, appear to have a slightly lower slope than the high-Nd rocks. Most high-Nd dikes have Sr and Nd isotopic ratios similar to Western USA, whereas the low-Nd rocks trend towards high Sr isotopic and low Nd isotopic ratios displayed also by both the Aeolian arc and Aegean arc. In the Aegean arc this high-Sr low-Nd isotopic area is produced by samples from Milos (Barton et al., 1983) but similar values have not been previously recognised on Santorini. This suggests that the samples defining this Sr-Nd trend were influenced by components which are present at other localities along the Aegean Arc.

Druitt et al. (1999) observed that lavas and pyroclastics from Santorini overlap isotopically, but that the lavas extend to lower Sr and higher Nd isotopic ratios. This was interpreted as a result of their less evolved average compositions. The lavas in this study, however, extend to higher Sr isotopic ratios and lower Nd isotopic ratios than any pyroclastics studied by Druitt et al. (1999).

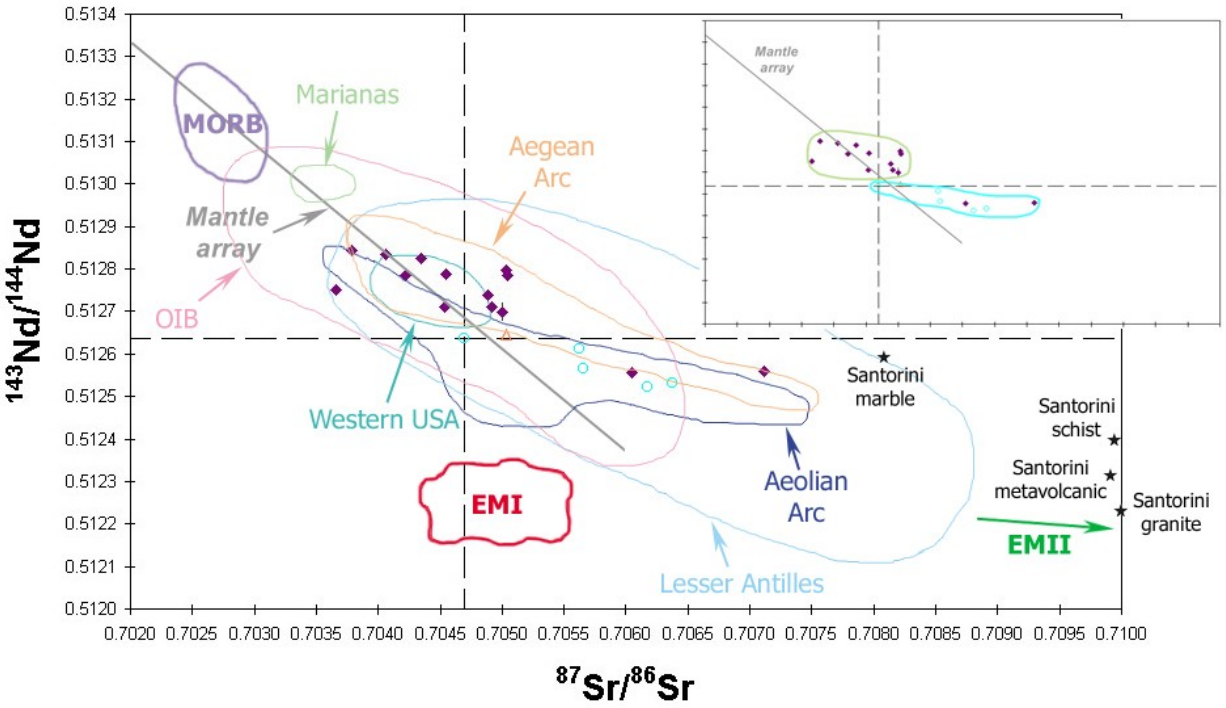


**Fig. 7.25.** $^{143}Nd/^{144}Nd$ versus $^{87}Sr/^{86}Sr$ plot showing Megalo Vouno volcano complex lavas and dikes along with various mantle sources, mantle reservoirs and other volcanic arcs. MORB, OIB, Marianas, Western USA and Lesser Antilles data from Rollinson (1993); EMI and EMII mantle reservoirs from Zindler & Hart (1986) (explained in Fig. 7.28). The EMII reservoir as defined by Zindler & Hart (1986) plots approximately within the values: $^{143}Nd/^{144}Nd$: 0.51170-0.51210, $^{87}Sr/^{86}Sr$: 0.7168-0.7205; Aeolian Arc data from Ellam et al. (1988), Peccerillo & Wu (1992), Francalanci et al. (1993), Del Moro et al. (1998), De Astis et al. (2000) and Gertisser & Keller (2000); Aegean Arc is represented by Milos and Santorini data from Barton et al. (1983) and further Santorini data from Zellmer (1998) and Druitt et al. (1999). Santorini basement is represented by a marble, a schist, a metavolcanic rock (Briqueu et al., 1986) and a granite (Altherr & Siebel, 2002). Since no isotopic data were available for the Santorini granite, an average of granites from the Aegean area having similar geochemistry was used ~~see~~ text. The intersection between $\varepsilon_{Sr}=0$ and $\varepsilon_{Nd}=0$ (broken lines) represents bulk earth composition. $\varepsilon_{Nd}=0$: Chondrite uniform reservoir for Nd, the present-day value of which is 0.512638 (Faure, 1986; Rollinson, 1993). $\varepsilon_{Sr}=0$: Uniform reservoir for Sr, the present-day value of which is not known accurately, but the value 0.7047 (Taylor & McLennan, 1985) was chosen. Straight grey line is mantle array (also known as mantle correlation line) from DePaolo & Wasserburg (1976). For clarity, uncertainty is only given for sample MVD-B 01-25, but error crosses for all samples are shown in Appendix C. Symbols as in Fig. 7.24.

All Megalo Vouno samples fall within the area defined by the Lesser Antilles. The large isotopic variation displayed by this island arc is attributed to a relatively high contribution (ca. 2%) from subducted local seafloor sediment, followed by subsequent high-level assimilation of crust (AFC) (Thirlwall et al., 1996). This overlap could indicate that the same processes may have influenced the Santorini samples.

Basement samples (represented by a marble, a schist, a granite and a metavolcanic rock ~~all~~ from Santorini) plot in the bottom right corner of the diagram, indicating that any of these materials could represent a contaminant.

Besides this study, only Druitt et al. (1999) has published Pb isotopic data from Santorini, and no Pb isotopic data from other volcanic Aegean islands have been found in the literature. On a $^{207}Pb/^{204}Pb$ versus $^{206}Pb/^{204}Pb$ diagram (Fig. 7.26), samples plot in a small field above NHRL,

along with other arc data. They plot to the lower $^{207}Pb/^{204}Pb$ side of other Santorini data, and generally have lower $^{206}Pb/^{204}Pb$ ratios but similar $^{207}Pb/^{204}Pb$ ratios when compared to data from the Aeolian Arc and Lesser Antilles. All samples plot within the field for EMII defined by Zindler & Hart (1986). The "low-Nd" series appears to define a trend whereas the "high-Nd" samples do not.

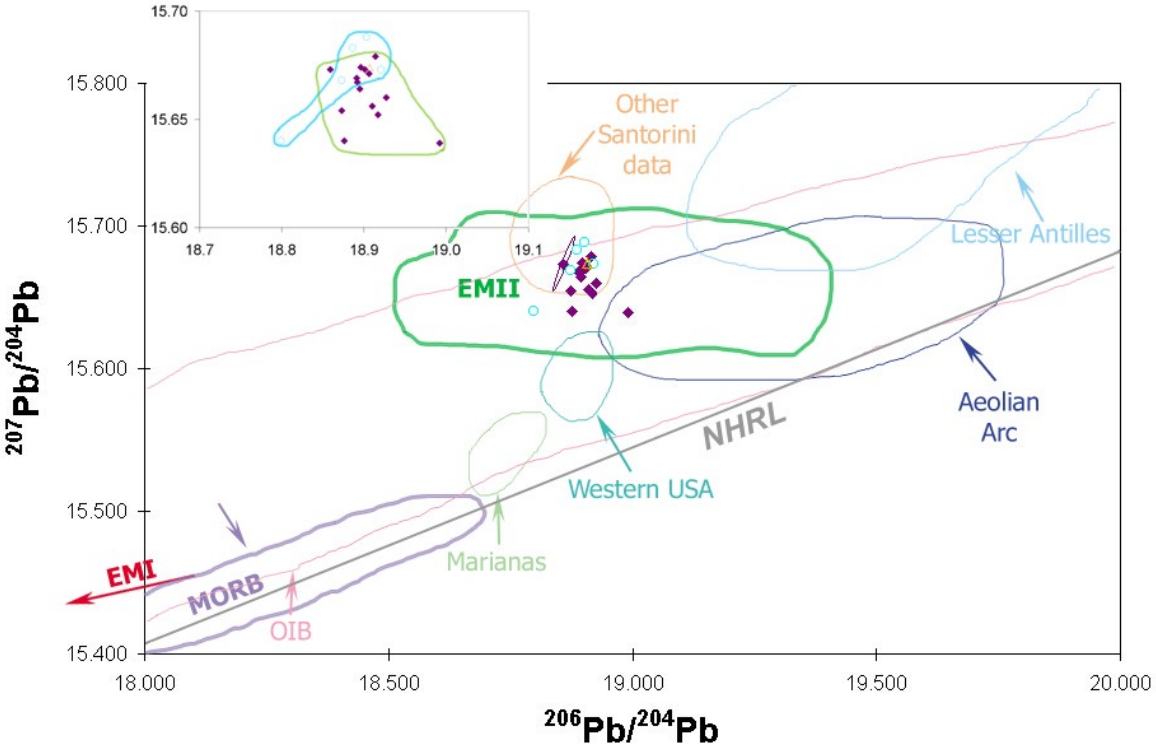


**Fig. 7.26.** $^{207}Pb/^{204}Pb$ versus $^{206}Pb/^{204}Pb$ plot showing Megalo Vouno lavas and dikes along with various mantle sources, mantle reservoirs and other volcanic arcs. MORB, OIB, Marianas, Western USA and Lesser Antilles data from Rollinson (1993); EMI and EMII mantle reservoirs from Zindler & Hart (1986) (explained in Fig. 7.28). The EMI reservoir as defined by Zindler & Hart (1986) plots approximately within the values: $^{207}Pb/^{204}Pb$: 15.35-15.51, $^{206}Pb/^{204}Pb$: 16.30-17.40; Aeolian Arc data from Ellam et al. (1988), Francalanci et al. (1993), Del Moro et al. (1998), De Astis et al. (2000) and Gertisser & Keller (2000); Other Santorini data are from Druitt et al. (1999). Grey line is NHRL (northern hemisphere reference line) after Hart (1984). For clarity, uncertainty is only given for sample MVD-B 01-25, but error ellipses for all samples are shown in Appendix C. Inset shows enlarged area of the diagram with samples divided into the "high-Nd" (green) and "low-Nd" (blue) series. Symbols as in Fig. 7.24.

On a $^{208}Pb/^{204}Pb$ versus $^{206}Pb/^{204}Pb$ diagram (Fig. 7.27), samples again plot above the NHRL along with the majority of other arc data. They plot to the high end of $^{206}Pb/^{204}Pb$ compared with other Santorini data, but have lower $^{206}Pb/^{204}Pb$ ratios than data from the Aeolian Arc and Lesser Antilles. The inset shows that "low-Nd" samples define a clearer trend than the "high-Nd" samples.

Zindler & Hart (1986) constructed diagrams showing the main isotopic mantle reservoirs (Fig. 7.28). In both diagrams, Santorini data plot at rather uniform Pb isotopic compositions ($^{206}Pb/^{204}Pb$), but with a wide range in both $^{87}Sr/^{86}Sr$ and $^{143}Nd/^{144}Nd$ ratios. One end of the

trend appears to point towards the MORB reservoir, whereas the other end points towards the EMII reservoir. In agreement with Fig. 7.25, most "low-Nd" samples plot closer to EMII than "high-Nd" samples. This indicates that the EMII reservoir may have influenced the source of "low-Nd" samples to a larger degree than the remaining dikes.

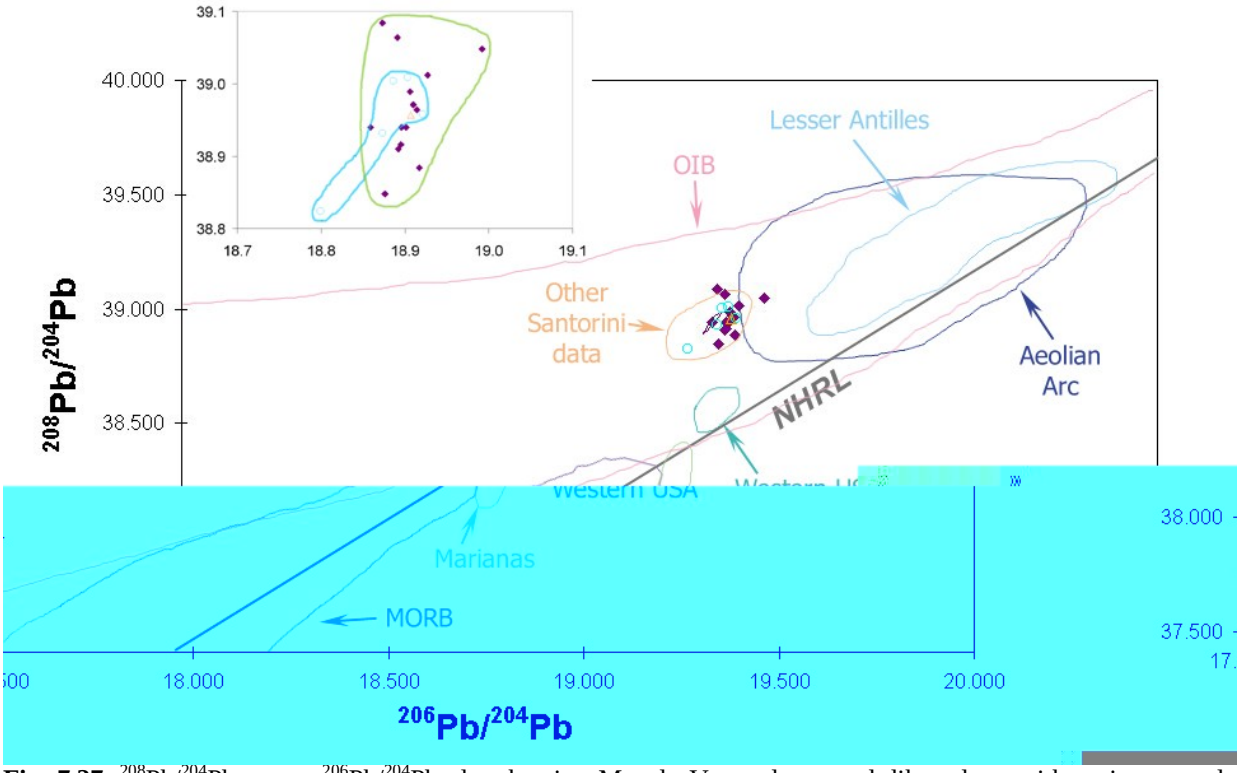


**Fig. 7.27.** $^{208}Pb/^{204}Pb$ versus $^{206}Pb/^{204}Pb$ plot showing Megalo Vouno lavas and dikes along with various mantle sources and other volcanic arcs. Mantle reservoir data are not available for $^{208}Pb/^{204}Pb$. MORB, OIB, Marianas, Western USA and Lesser Antilles data from Rollinson (1993); Aeolian Arc data from Ellam et al. (1988), Francalanci et al. (1993), Del Moro et al. (1998), De Astis et al. (2000) and Gertisser & Keller (2000); other Santorini data are from Druitt et al. (1999). Grey line is NHRL (northern hemisphere reference line) after Hart (1984). For clarity, uncertainty is only given for sample MVD-B 01-25, but error ellipses for all samples are shown in Appendix C. Inset shows enlarged area of the diagram with samples divided into the "high-Nd" (green) and "low-Nd" (blue) series. Symbols as in Fig. 7.24.

The reservoir concept is usually employed in the study of mantle plumes (OIB), but it has been shown that enriched mantle (sometimes in the form of plumes) may be present beneath subduction zones (Ellam et al., 1988). Hence it seems relevant to study the samples in this context. Since the reservoirs are a working hypothesis defined strictly upon isotopic compositions, no trace element data were published for the different reservoirs.

The suspicion that the five trend 1 lavas, plus two dikes could be grouped into a "low-Nd" series was backed up when plotting incompatible elements and incompatible element ratios against $^{143}Nd/^{144}Nd$ or $^{87}Sr/^{86}Sr$ ratios. In Fig. 7.17, two trends could be made out on the $(La/Yb)_N$ versus $SiO_2$ plot. The two same trends are even more pronounced on a $(La/Yb)_N$

versus $^{143}Nd/^{144}Nd$ plot (Fig. 7.29), where samples with high $(La/Yb)_N$ have the lowest Nd isotopic ratios.

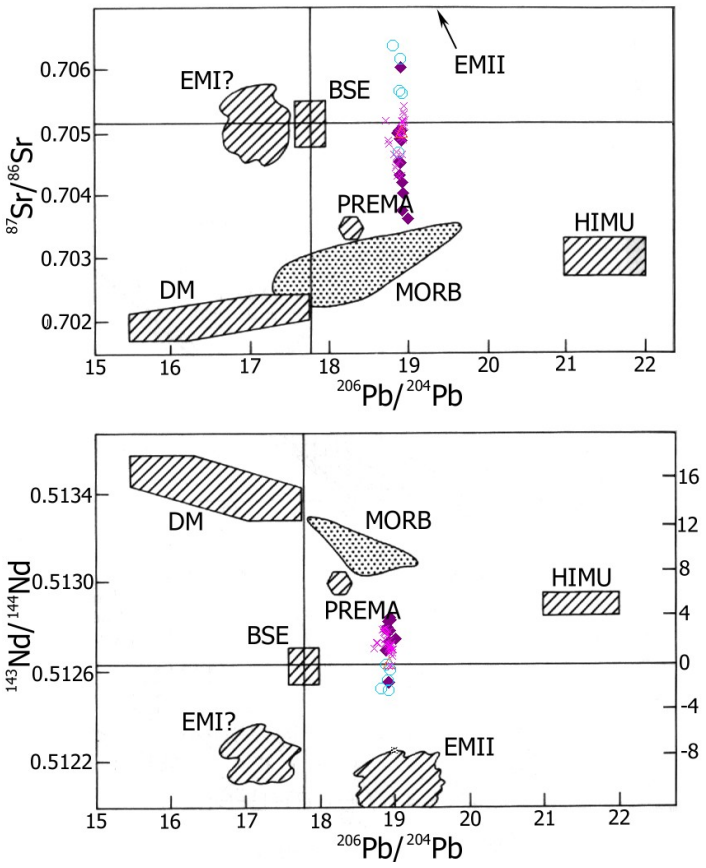


**Fig. 7.28.** $^{87}Sr/^{86}Sr$ versus $^{206}Pb/^{204}Pb$ and $^{143}Nd/^{144}Nd$ versus $^{206}Pb/^{204}Pb$ isotope correlation diagrams with positions of hypothetical mantle reservoirs as based upon OIB data. After Zindler & Hart (1986).
The compiled Santorini data set consists of 20 samples from the present study and 29 samples from Druitt et al. (1999).
Reservoirs are: DM, depleted mantle; MORB, mid-ocean ridge basalts; PREMA, frequently observed PREvalent MAntle composition; BSE, bulk silicate earth; HIMU, mantle with high U/Pb ratio; EMI and EMII, enriched mantle with low $^{143}Nd/^{144}Nd$ combined with low and high $^{87}Sr/^{86}Sr$, respectively. Both EMI and EMII are believed to reflect recycled crustal materials (e.g., Carlson, 1995).
The EMII reservoir plots approximately within the values: $^{87}Sr/^{86}Sr$: 0.7168-0.7205, $^{206}Pb/^{204}Pb$: 18.5-19.6.

◆ *Dikes from Megalo Vouno*
△ *Lava flow from bottom of Megalo Vouno*
○ *"Trend 1" Hansen (1997)*
× *Druitt et al. (1999)*

**Fig. 7.29.** $^{143}Nd/^{144}Nd$ versus $(La/Yb)_N$. All available Santorini data (Zellmer, 1998) were plotted along with the studied rocks in order to elucidate the series (no REE data were available from Druitt et al. (1999) and no $(La/Yb)_N$ data were available for basement rocks). Santorini rocks split into two separate series on the diagram. The 'low-Nd' series is defined by the five trend 1 lavas plus two dikes, and a single sample from Zellmer (1998) also plots within the field. These samples are characterised by having low $^{143}Nd/^{144}Nd$ and high $(La/Yb)_N$. The 'high-Nd' series is defined by the remaining dikes plus the remaining samples from Zellmer (1998). Symbols as in Fig. 7.30b.

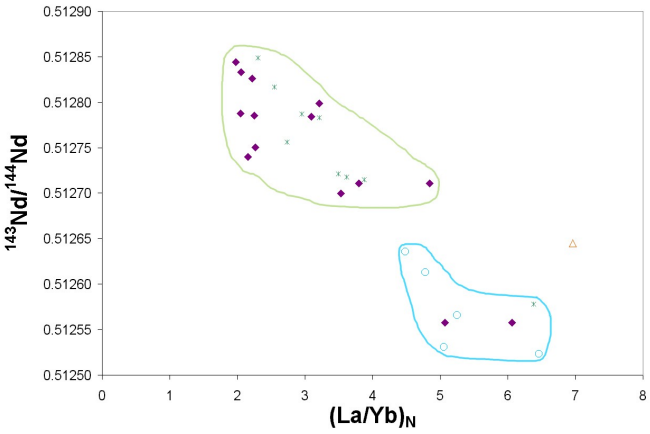

### *7.9.1 Effects of sediment and crustal contamination*

The Rb/Sr versus Nd and Sr isotopic ratio diagrams (Figs. 7.30a and 7.30b) show that a marked increase in Rb/Sr dominates the "high-Nd" series, whereas the "low-Nd" series is not affected to the same degree. The marked increase in Rb/Sr ratios in the "high-Nd" series takes place during magmatic evolution. A similar marked increase in Rb/Sr ratios is not oberved for the "low-Nd" series but unfortunately the latter is not represented by quite as evolved samples as the "high-Nd" series. Crustal contamination by different basement rocks could, perhaps, explain the observed trends, hence such rocks from Santorini were studied in order to test the possibility of crustal contamination.

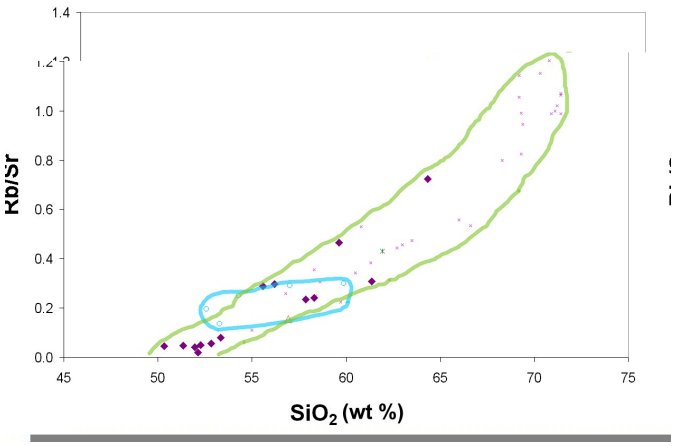


**Fig. 7.30a.** Rb/Sr versus $SiO_2$. The increase in Rb/Sr with magmatic evolution is more pronounced for "high-Nd" samples (green) than for "low-Nd" samples (blue). Symbols as in Fig. 7.30b.

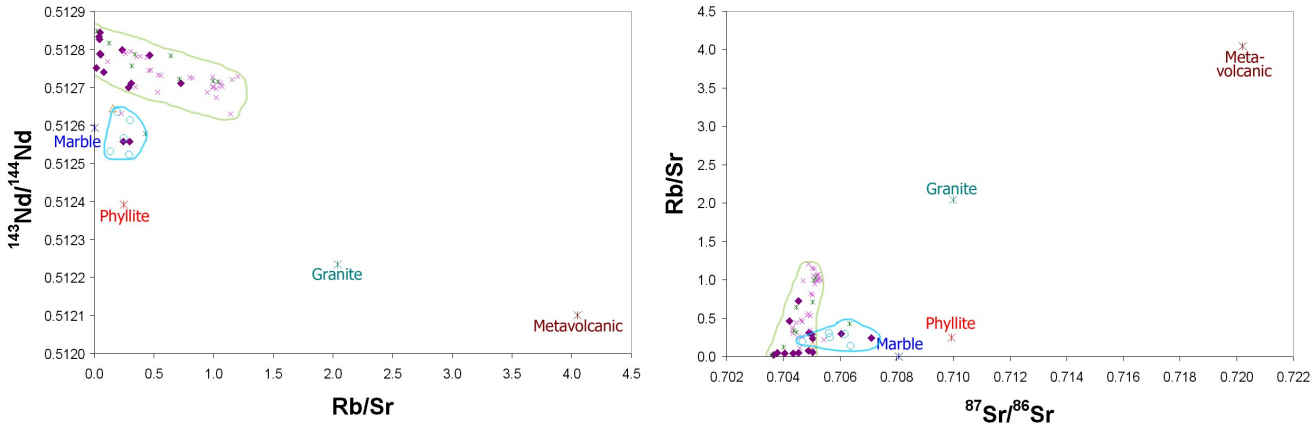


**Fig. 7.30b.** $^{143}Nd/^{144}Nd$ versus Rb/Sr and Rb/Sr versus $^{87}Sr/^{86}Sr$ for compiled Santorini data and four different basement rocks. The increase in Rb/Sr in the "high-Nd" series is accompanied by an increase in Sr isotopic ratios and a decrease in Nd isotopic ratios. The "low-Nd" series does not seem to be affected much by high- or low- Rb/Sr components and trends instead towards a phyllite basement sample. A high Rb/Sr component has on Santorini been found in granitic and metavolcanic rocks. See text for data sources.

- *Dikes from Megalo Vouno*
- *Lava flow from bottom of Megalo Vouno*
- *"Trend 1" Hansen (1997)*
- *Zellmer (1998)*
- *Druitt et al. (1999)*

Unfortunately, only a few studies of the geochemical composition of Santorini basement rocks have been published. In the case of a marble and a schist (phyllite), isotopic data from Briqueu et al. (1986) were combined with major and trace element data analysed by Kann (pers. commun., 2004). All data for a metavolcanic rock were taken from Druitt et al. (1999). Unfortunately, only a few trace element data were published for this rock sample. Granite major and trace element data were taken from the study of a 9.55 ± 0.3 Ma granite sampled via a borehole on Santorini (Skarpelis et al., 1992). No isotopic data are available for this granite, so in order to get an estimate of its isotopic composition, data from granitoids sampled on other Aegean volcanic islands were used (Altherr & Siebel, 2002). Four granites had major and trace element geochemistry that resembled the Santorini sample, and an average isotopic composition was chosen as a representative for the granite.

In Fig. 7.9 and 7.19 it was noticed that the Th content among the studied samples is anomalously high for arc volcanics. High Th in primitive and evolved samples is a general characteristic in Santorini and was previously commented on by Mitropoulos et al. (1987) and Kann (2004). Isotopically, the hïgh-Nd šeries shows a marked increase in Th content with decreasing Nd isotopic ratios (Figs. 7.31). When plotting data on a Th versus $SiO_2$ diagram (Fig. 7.32), it is seen that an increase in Th up to ca. 25 ppm takes place during magmatic evolution. Basalts and basaltic andesites have high Th contents (1.22-9.61 ppm) and trend 1 samples have higher Th content than trend 2 samples (Hansen, 1997) at the same $SiO_2$ contents.

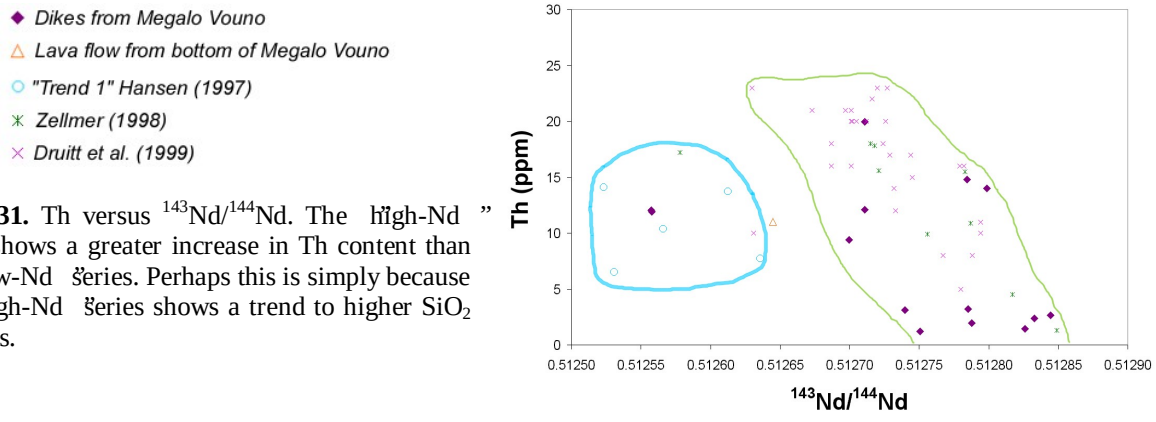


**Fig. 7.31.** Th versus $^{143}Nd/^{144}Nd$. The hïgh-Nd " series shows a greater increase in Th content than the löw-Nd šeries. Perhaps this is simply because the hïgh-Nd šeries shows a trend to higher $SiO_2$ contents.

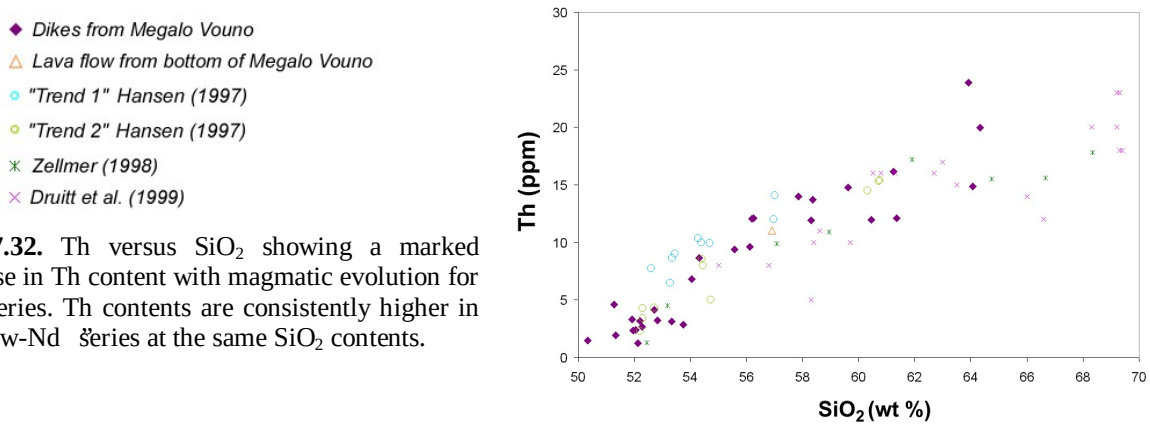


**Fig. 7.32.** Th versus $SiO_2$ showing a marked increase in Th content with magmatic evolution for both series. Th contents are consistently higher in the löw-Nd šeries at the same $SiO_2$ contents.

Three of the four basement lithologies plotted in Fig. 7.30b could be plotted on a Th versus $^{143}Nd/^{144}Nd$ diagram (Fig. 7.33). It can be seen that while the "low-Nd" series possibly trends towards a component with an intermediate Th content (ca. 10-15 ppm), the "high-Nd" series trends towards a component with elevated Th content, possibly represented by a Santorini granite.

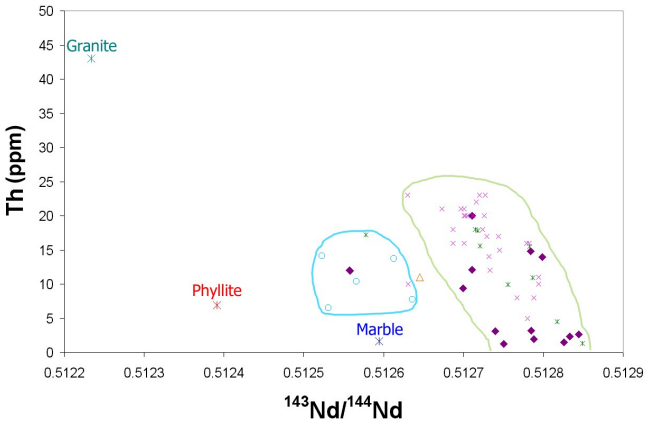


**Fig. 7.33.** Th versus $^{143}Nd/^{144}Nd$ showing that the majority of data plot towards a high Th component which on Santorini has been found in a granite (no Th data were published for the metavolcanic rock). The "low-Nd" series does not seem to be affected to the same degree and may trend towards the composition of the basement phyllite. Symbols as in Figs. 7.31. See text for data sources.

According to the two-component mixing equations by Langmuir et al. (1978), data plotted on an isotopic ratio versus trace element diagram with a common denominator will define a straight line between the two mixing end-members. In the case of a $^{87}Sr/^{86}Sr$ versus $1/^{86}Sr$ diagram, the $^{86}Sr$ abundance can be approximated by total Sr (ppm) without introducing significant errors (Dickin, 1995). The studied samples can be seen in Fig. 7.34, where data from Zellmer (1998) and Druitt et al. (1999) were added in order to get a better representation of the overall isotopic evolution of Santorini. It seems that two straight lines can be recognised in the diagram; one defined by "low-Nd" series samples, and one defined by the "high-Nd" series. There is, however, considerable scatter, especially among samples belonging to the "high-Nd" series.

It is important to note that in the case of AFC, the linear mixing trend cannot be used to determine the composition of the contaminant on this type of diagram, because the composition of the contaminant does not lie on the magma evolution trajectory (Mensing et al., 1984).

Briqueu & Lancelot (1979) showed through schematic modelling how selective Sr contamination and fractionation of magmas plot on diagrams with Sr isotopic ratios versus $1/^{86}Sr$ (Fig. 7.35). Comparison of these models with Fig. 7.34 gives an indication of the different types of contamination that could lead to the trends produced by the two series. This immediately suggests that the "low-Nd" series results from simple two-component mixing between a primitive magma and a crustal contaminant (e.g., phyllite), while the "high-Nd" series could have been contaminated with a metavolcanic rock or perhaps undergone simultaneous contamination (by e.g., a granite) and fractionation (AFC). However, the model

(Fig. 7.35) is based on contamination with crustal rocks high in Sr which is not the case for either the analysed basement phyllite, metavolcanic, marble or granite.

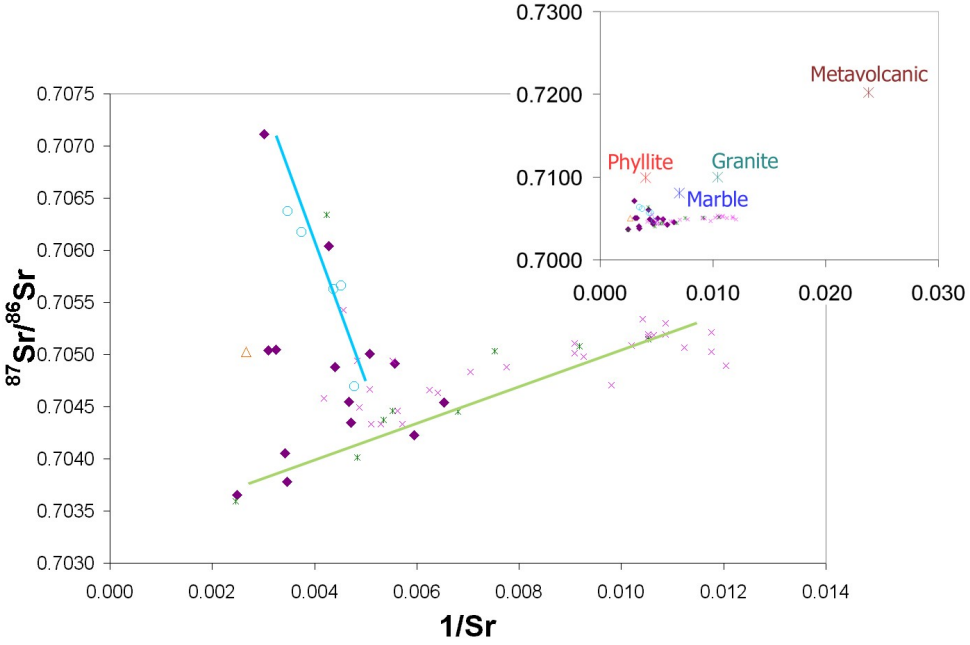


**Fig. 7.34.** $^{87}Sr/^{86}Sr$ versus 1/Sr. Samples from both the "high-Nd" and "low-Nd" series produce straight lines in the diagram, suggesting that the two series were contaminated with compositionally distinct sources. The trends suggest that two different crustal contaminants are required in order to produce the observed trends. The inset shows the composition of Santorini basement rocks (see text). Symbols as in Fig. 7.31.

In AFC modelling, the bulk distribution coefficient (D) and the rate of assimilation to the rate of fractional crystallisation (r) can be varied to produce a best fit (e.g., DePaolo 1981; Roberts & Clemens, 1995). However, during fractional crystallisation the bulk distribution coefficient for the element under investigation can change drastically (e.g., in the case of Sr), adding further variables to the modelling. The effects of AFC upon a primitive magma could not be studied without the aid of a specialised computer program, but preliminary modelling using the equations from DePaolo (1981) was attempted and is discussed further in Section 8.3.3.

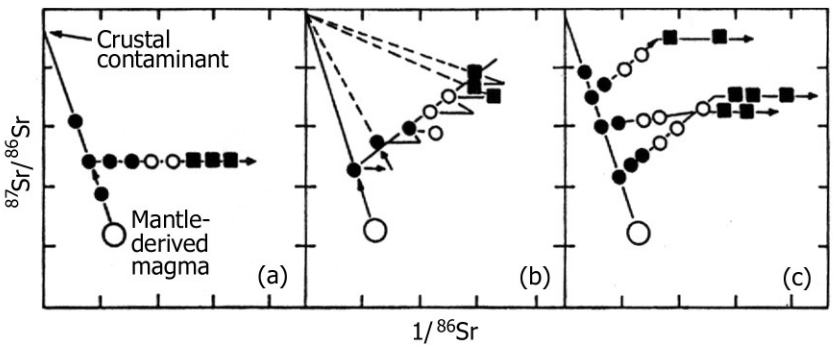


**Fig. 7.35.** $^{87}Sr/^{86}Sr$ versus $1/^{86}Sr$ showing schematic modelling of selective Sr contamination and fractionation of magmas.
**a**: contamination followed by fractionation; **b**: sequential contamination and fractionation events; **c**: simultaneous contamination and fractionation followed by fractionation.
Modified after Briqueu & Lancelot (1979).

Finally, it was tested whether the "low-Nd" series could, perhaps, be the result of basement rock contamination of the "high-Nd" series. For this purpose the simple two-component mixing

model was tested in the $^{143}Nd/^{144}Nd$ versus $^{87}Sr/^{86}Sr$ diagram in Fig. 7.36. The equation used (Faure, 1986) was derived from the hyperbolic mixing equations from Langmuir et al. (1978):

$$\left(\frac{^{87}Sr}{^{86}Sr}\right)_m = \frac{\left(\frac{^{87}Sr}{^{86}Sr}\right)_c [Sr]_c f + \left(\frac{^{87}Sr}{^{86}Sr}\right)_p [Sr]_p (1-f)}{[Sr]_c f + [Sr]_p (1-f)}$$

subscripts *m*, *c* and *p* denote the mixed magma, the contaminant and the parental magma, respectively, and *f* is the fraction of contaminant.

The modelling shows that the trend produced by the low-Nd series could be approximated by simple two-component mixing between the composition of a primitive high-Nd sample and a basement phyllite. Rather high degrees of melting of the phyllite (ca. 20-40%) are required to produce the trend. See discussion (Section 8.3.3).

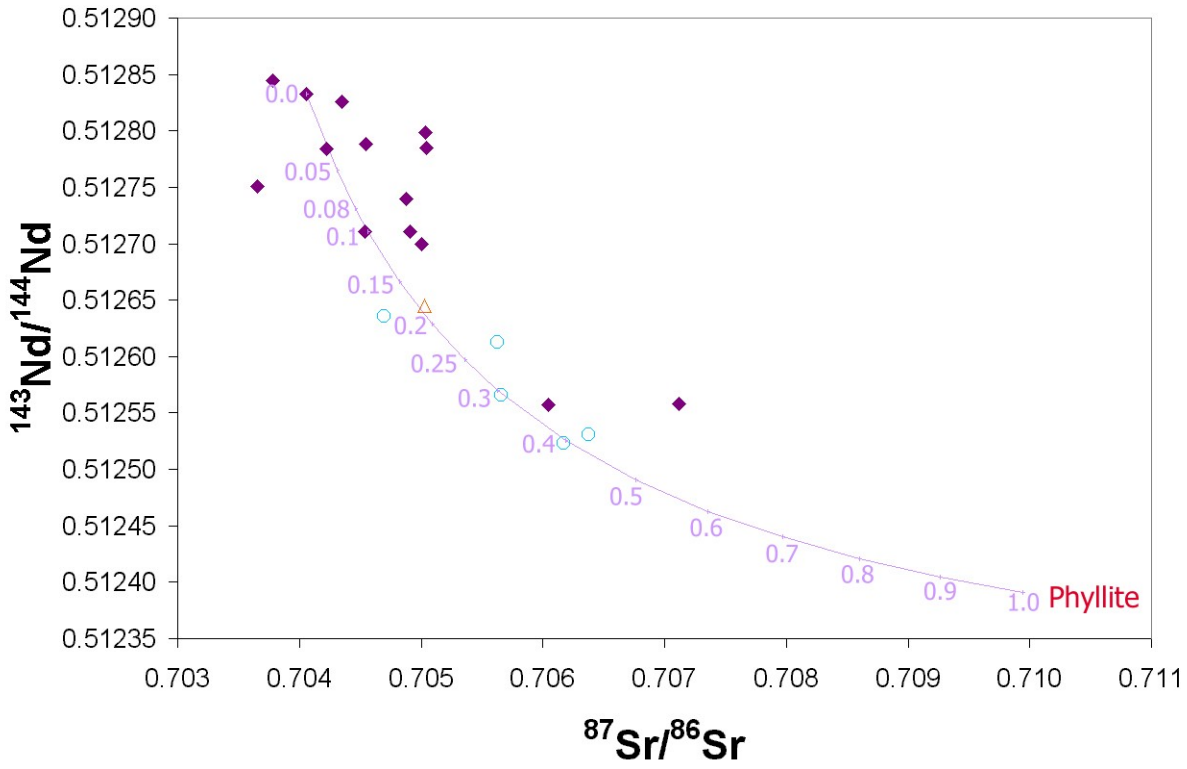


**Fig. 7.36.** Two-component mixing between a primitive dike sample (represented by MVD-B 01-18) and a phyllite basement rock shown on a $^{143}Nd/^{144}Nd$ versus $^{87}Sr/^{86}Sr$ plot. Numbers indicate degree of contamination. Trend 1 samples and two dikes (low-Nd series) lie close to the mixing line. The mixing hyperbola has the equation:
3165.8071($^{87}Sr/^{86}Sr$) + 6180.2600($^{143}Nd/^{144}Nd$)($^{87}Sr/^{86}Sr$) 4339.2352($^{143}Nd/^{144}Nd$) + 2222.7444 = 0
Symbols as in Fig. 7.31.

# 8. Discussion

The discussion consists of three parts. The first part gives a short overview of the processes involved in the generation of primary magmas and the role of mantle source heterogeneity. The second part explores dike emplacement and the significance of the Megalo Vouno dikes in the evolution of the northern volcanic centres. Finally, the third part concentrates on uncovering the magma chamber processes giving rise to the observed geochemical trends.

## 8.1 Melt generation in subduction zones

The structure of the Aegean subduction zone was presented in Chapter 2. The following section will briefly touch upon the mineralogical and geochemical processes that take place during subduction leading to primary melts and subsequently volcanic arc rocks.

It has been argued that three separate principal components can be identified in the source of most island arc lavas: subducted sediments, fluids derived from the altered oceanic crust and, finally, the mantle wedge (e.g., Perfit et al., 1980; McCulloch & Gamble, 1991; Macdonald et al., 2000).

### *8.1.1 The mantle wedge, slab fluids and sediments*

It is widely accepted that partial melting beneath subduction zones is induced by the release of slab fluids to the overlying mantle wedge. Direct melting of subducted oceanic crust and the resulting adakitic magmatism may only occur when very hot young crust is subducted and is rare on the modern Earth (Martin, 1986). However, as mentioned in Section 2.2, Aegean subduction is taking place in two separate flanks and it has been suggested that slab melting may occur at plate edges where upwelling of hot asthenosphere can take place (Vanek et al., 1987; Yogodzinski et al., 2001). This is important, considering the location of Santorini centrally in the volcanic arc and, hence, it cannot be ruled out that upwelling hot asthenosphere may induce melting of sediments and/or oceanic crust at the plate edges.

When the African oceanic lithosphere attained negative buoyancy and began to sink, several materials were introduced into the subcontinental Aegean mantle. The slab itself consists of oceanic mantle, oceanic crust (which has been hydrothermally altered due to interaction with seawater) and an uppermost layer of sediments.

Most of the water initially subducted is contained in sediments (up to 20% water by volume) (You et al., 1996). However, according to Peacock (2000), pore waters are expelled by early diagenetic processes at relatively shallow depths (<10 km). During progressive subduction, altered oceanic crust and those sediments which have not been scraped off are heated and compacted in the trench. At ca. 20 km depth fluids are released as a result of the breakdown of hydrous minerals undergoing metamorphic reactions (Fig. 8.1). Some of these fluids are believed to be taken up by newly formed hydrous minerals. The latter are transported to greater

depths where they subsequently dehydrate and release fluids (You et al., 1996). Although there is some dispute about the degree of involvement of different mineral phases, amphibole, chloritoid, zoisite and lawsonite are generally believed to be the hydrous phases of greatest importance (e.g., Peacock, 1993; Schmidt & Poli, 1998; Forneris & Holloway, 2003).

It is suggested that mantle is dragged down with the descending slab, because the slab surface is initially coupled to the overlying mantle (van Keken, 2003). As a result of this process, mantle is drawn in from below the overriding continental lithosphere, and this zone of viscous deformation defines the mantle wedge. Fluids released from the slab may be carried deeper into the mantle by this circulation.

Most experimental studies show that dehydration reactions take place over a wide interval as opposed to at a distinct depth (e.g., Schmidt & Poli, 1998). The majority of the hydrous minerals are believed to break down completely between 100-200 km depth (You et al., 1996), and new experimental data from Forneris & Holloway (2003) show that dehydration of the crustal part of the slab would take place between ca. 90-110 km for most types of intermediate to cold subduction zones. This is in accordance with the observation that generally volcanic arcs are located 128 ± 38 km above the subducting slab (Gill, 1981).

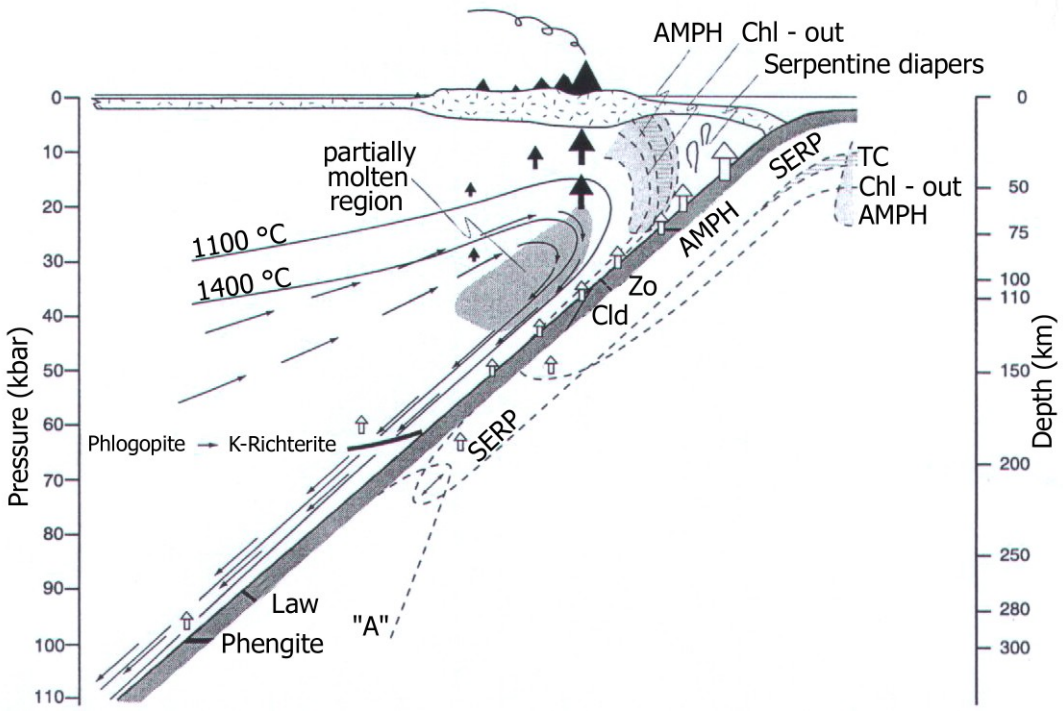


**Fig. 8.1.** Model for the formation of a volcanic front in a subduction zone environment. Continuous dehydration of the oceanic crust takes place down to ca. 150-200 km depth releasing fluids (open arrows) to the overlying mantle. The location of the volcanic front depends on the position of the 1300 °C isotherm in the metasomatised mantle wedge, because this is most likely the temperature necessary for mechanical extraction of melts (indicated by solid, black arrows) (Schmidt & Poli, 1998). Sufficiently high temperatures for melt extraction to take place are obtained by convection in the mantle wedge. Model after Schmidt & Poli (1998).

During subduction the oceanic crust passes first through a blueschist facies stage (10-50 km depth) and progressive heating and increased pressure finally transforms the initially basaltic crust into eclogite. This process results in the gradual decrease in bulk water content of the crust from ca. 5-6 wt.% $H_2O$ to 0.2-0.5 wt.% $H_2O$ (Schmidt & Poli, 1998). While no dehydration takes place in the peridotitic mantle below the subducting oceanic crust in cold subduction zones, it is believed that dehydration of the peridotitic layer above the oceanic crust may also supply the mantle with fluids (Schmidt & Poli, 1998). The high Cl content in arc magmas is also believed to have been supplied by gradual release from the altered oceanic crust of the subducting slab, since the oceans are the primary source of this element (Scambelluri & Philippot, 2001).

When fluids are released into the overlying mantle, the mantle solidus is lowered. At the same time, fluid mobile LILE and LREE are introduced into the mantle, which is generally believed to be depleted in incompatible trace elements because of previous melt extractions (You et al., 1996). However, it has also been suggested that trace element enriched material may be present in the continental mantle lithosphere along continental margins due to delamination of the lower crust (DeBari & Sleep, 1991; Hawkesworth et al., 1993).

Metasomatism of mantle by slab fluids can explain the slight enrichment in LREE relative to HREE observed in basaltic rocks in Fig. 7.16, while the high levels of LILE observed in the MORB normalised spider diagrams in Fig. 7.18 and low levels of HFSE (and HREE) compared with both LREE and LILE can be explained by two different processes: a) HFSE are fluid immobile, and hence not added to the mantle via slab fluids as apposed to LILE (e.g., Pearce, 1983; McCulloch & Gamble, 1991; Thirlwall et al., 1994) and b) HFSE are retained in a titanate phase in the mantle during melting (e.g., Green, 1980; Morris & Hart, 1983).

In the case of partial melting of the slab it is suggested that HFSE can be retained by a distinctive HFSE-bearing residual phase (rutile and/or ilmenite) in the slab (Saunders et al., 1980). However, at the depth where such slab melting should occur, experiments have shown that the slab consists of eclogite (Schmidt & Poli, 1998), and low degrees of melting of this slab composition would result in a steeper HREE pattern than that observed, because the HREE are retained by garnet. Therefore, the trace element data support the model of generation of primary melts in the mantle wedge, as opposed to slab melting.

In Fig. 7.18, an average of all basaltic dike samples was compared with basalts from other volcanic centres in the Aegean arc. This dike average generally plots at lower abundances than the other volcanic centres, suggesting that the degree of melting beneath Santorini may have been larger than beneath the other islands. This could, perhaps, be a consequence of the complex geometrical nature of the subduction in the shape of two crossing flanks (Fig. 2.11). In a study of geochemical variation among islands in the Aegean arc, Mitropoulos et al. (1987) came to the conclusion that the less LREE enriched nature of Santorini could be ascribed to

upwelling of hot asthenospheric mantle material as a consequence of the greater crustal extension in the central part of the Aegean arc.

In comparison with other island arcs (Fig. 7.18), the pattern of the average dike sample lies in between those of basalts erupted through continental crust (Andes and Aeolian arc) and thin oceanic crust (Izu-Bonin and to some extent the Marianas). The patterns and abundances of the Kuriles and Honshu resemble that of the dike average, indicating that the mantle beneath these settings may be similar to that beneath Santorini.

Zellmer (1998) showed that 15-20% melting of a spinel lherzolite mantle, possibly containing small amounts of amphibole, could account for the observed HREE contents in the Second Eruptive Cycle on Santorini. Such a degree of melting was, however, not believed to be induced by the water flux alone, since modelling showed that primary basalts had low water contents of less than 0.7 wt.% $H_2O$. As a solution to this problem, he suggested that either other volatiles than $H_2O$ had an influence (e.g., $CO_2$) or that melting could be in part due to decompression by mantle diapirism.

It is generally assumed that high values of $^{87}Sr/^{86}Sr$ for a given $^{143}Nd/^{144}Nd$ ratio, in relation to the mantle array defined by oceanic basalts (as seen in Fig. 7.25), are diagnostic of the presence of a component of altered oceanic crust or sediment in island arc volcanics (Hofmann & White, 1982). Slab fluids from the altered oceanic crust are believed to shift isotopic compositions to the right of the mantle array, while mixing between sediment and depleted mantle may or may not lead to samples which cross through the mantle array. Thus, samples falling within the mantle array are not indicative of the presence or absence of a sedimentary component (Ben Othman et al., 1989).

The Nd isotopic ratios of island arc rocks are consistently lower than those of MORB, and this is generally interpreted in terms of a small sediment contribution (Faure, 1986; Hawkesworth et al., 1993). Zellmer (1998) suggested that in the case of Santorini, partial sedimentary melts may have infiltrated the wedge only to a very low degree. This was based on low Nd/Th ratios, and the relatively unradiogenic Nd isotopic composition. It was found that only 0.2-0.4% sediment melt addition was required to account for the observed Th and HREE abundances in a modelled primary basaltic composition, when GLOSS (global subducted sediment composition) from Plank & Langmuir (1998) was used in the modelling.

The data from the present study also indicate that only small amounts of sediments can have affected the primary melts, since larger input in the form of bulk sediment or sediment melt would be in disagreement with the observed Pb isotopic ratios (Figs. 7.26 and 7.27). According to Ben Othman et al. (1989), the great difference in Pb content in mantle (ca. 0.05 ppm) and terrigeneous sediment (ca. 25 ppm), means that addition of even less than a percent of sediment to the mantle significantly affects mantle Pb isotopic ratios. Therefore, the mantle takes on the Pb isotopic characteristics of the sediment with several percent addition. Since isotopic

differences between mantle and sediments are much greater for $^{207}Pb/^{204}Pb$ ratios than for $^{206}Pb/^{204}Pb$ ratios, the primary effect of mixing sediment with mantle will be to increase the $^{207}Pb/^{204}Pb$ ratios. Thus, if sediment is involved, steeper $^{206}Pb/^{204}Pb$-$^{207}Pb/^{204}Pb$ arrays than for oceanic basalts are expected. Although this was shown by the "low-Nd" series, the "high-Nd" samples plot at the same relative abundances, but show no trend (Fig. 7.26). This observation, combined with the fact that trend 1 samples (Hansen, 1997) plot at higher Pb contents than trend 2 samples in Fig. 7.9, indicates that sediment may have had a greater influence on the "low-Nd" series than the "high-Nd" series. To test this, Th/Ce was plotted against $^{143}Nd/^{144}Nd$ in Fig. 8.2. According to Hawkesworth et al. (1997) and Ishizuka et al. (2003), high Th contents are most likely supplied with subducted sediments. It was shown that Th cannot be considered fluid mobile because Th/Ce ratios vary inversely with $^{143}Nd/^{144}Nd$ in a compilation of island arc volcanics. They concluded that high Th/Ce ratios in rocks with low Nd isotope ratios are a result of sediment contribution. In the present study, such a co-variation can perhaps be detected among the "high-Nd" samples, but the lowest Nd isotopic ratios do not coincide with the highest Th/Ce ratios, implying that sediment did not have a greater effect on the "low-Nd" series.

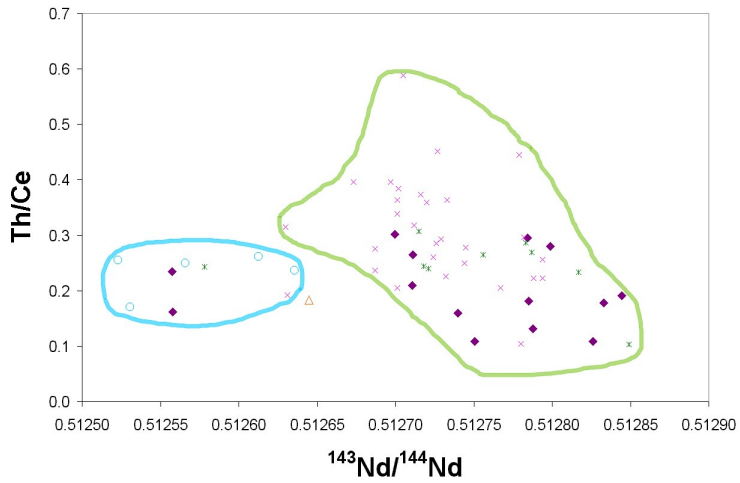


**Fig. 8.2.** Th/Ce versus $^{143}Nd/^{144}Nd$. According to Hawkesworth et al. (1997), rocks with low Nd isotopic ratios have correspondingly high Th/Ce ratios when Th is supplied by sediment. The "low-Nd" samples do not have the highest Th/Ce ratios indicating that their source was not affected by sediments to a larger degree than the source of "high-Nd" samples.

The Th/U ratios of dike samples (Fig. 7.13) lie in between those of depleted upper mantle and continental crust. U is readily mobilised in fluids, whereas Th is believed to be supplied by sediment. Hence, high Th/U ratios, relative to depleted mantle, could indicate that sediment was added to the mantle during subduction. It appears that the two series from Hansen (1997) are separated in the diagram, suggesting that sediments affected "low-Nd" samples more. This did not appear to be true in Fig. 8.2, indicating, perhaps, that trend 1 samples were derived from a less depleted mantle source than trend 2 samples. On the other hand, this could be the effect of analytical uncertainty, since trend 1 and trend 2 samples were analysed using a different method than for the dikes. It must also be pointed out that four out of the five reanalysed trend 1 samples that were originally below the detection limit could be easily analysed using ICP-MS.

The high Th contents observed in primitive Santorini samples indicate that the mantle source was somehow enriched in Th. It seems likely that this enrichment was supplied by subducted sediments. Th versus $SiO_2$ (Fig. 7.32) shows that trend 1 samples have higher Th contents (at the same $SiO_2$ content) than trend 2 samples and most dikes. This is not believed to be a result of different degrees of sediment input, but it supports the theory that the two series from Hansen (1997) were derived from geochemically different sources. It likewise suggests that the source of the "low-Nd" series is less depleted than that of the "high-Nd" series. This is backed up by observations from Hawkesworth et al. (1997), that rocks with high Th tend to have high Sr isotopic ratios, indicating that the mantle wedge may have been supplied with old trace element enriched material.

Likewise, the high Sr isotopic ratios combined with low Nd isotopic ratios and high $(La/Yb)_N$ ratios (Fig. 7.29) displayed by the "low-Nd" series suggests that some component enriched these samples in LREE/HREE relative to the "high-Nd" series.

### *8.1.2 Source heterogeneity*

It was shown in Section 2.2 that a subducted microcontinent was trapped underneath Crete ca. 19 Ma ago. This is taken as good evidence for previous subductions in the Aegean, and it could explain how parts of the upper mantle may have been enriched by subducted material. Mitropoulos et al. (1987) argued that the "complex make-up of the underlying lithosphere" results from a long history of subductions. They furthermore suggested that differences in the geochemistry of Santorini lavas, compared with those of other Aegean islands, could result from the greater crustal thinning in the central Aegean, leading to replacement of the subcontinental lithosphere with asthenospheric mantle material. The latter model seems to be at variance with the MORB normalised spider diagram patterns (Fig. 7.18), which indicate that the mantle source of most dikes is depleted in HFSE and HREE relative to average MORB.

The location of samples on Pb isotopic plots (Figs. 7.26 and 7.27) indicates that the source of all samples is of EMII-like composition. The EMII reservoir has affinities with the upper continental crust and may represent the recycling of continentally derived sediment, continental crust, altered oceanic crust or ocean-island crust (Rollinson, 1993). This indicates that the EMII reservoir could be the result of enrichment of the mantle by previous subduction events. Carlson (1995) suggested that the EMII reservoir is derived from upper continental crust, probably through the subduction and recycling of sediments of continental origin.

The relatively small Pb isotopic variations suggest that all analysed samples were extracted from a common source. However, the absence of a clear linear array among the "high-Nd" series (Figs. 7.26 and 7.27) contrasts with the array shown by "low-Nd" samples, indicating that either different source compositions, or different processes affected the Pb isotopic compositions of the two series. Although the variation in $^{87}Sr/^{86}Sr$ ratios and $^{143}Nd/^{144}Nd$ ratios

points towards mixing between a MORB-like source and the EMII reservoir, samples plot far from the EMII reservoir on Fig. 7.25. The "low-Nd" series, that would seem to have been affected the most by the EMII reservoir (Fig. 7.28), plots together with the "high-Nd" series on Pb-Pb isotopic plots (Figs. 7.26 and 7.27). It is suspected that this contrast among the isotopic data results from Pb isotopic ratios being much more easily influenced by sediment input than Sr and Nd isotopic ratios.

The large variation in $^{87}Sr/^{86}Sr$ ratios (Fig. 7.25) displayed by both series can be partly due to contamination with seawater in high-level magma chambers, and/or by slab fluids from the altered oceanic crust of the subducted slab. The trend 1 samples from Hansen (1997) were collected ca. 200 metres above sea-level, implying that it is unlikely that these were post-eruptively contaminated by seawater.

In the variation diagrams in Fig. 7.15 (Section 7.5) it was shown that many dikes could not be strictly assigned to the two series defined by Hansen (1997). On the other hand, the isotopic section showed that two dikes share the isotopic characteristics displayed by five trend 1 samples (Hansen, 1997). Careful checks of these two dike samples have shown that MVD-B 01-23 can be followed through in all variation diagrams with only slight deviations from trend 1. Most importantly, the dike sample does not alternate between the two series, as was shown for other samples in Fig. 7.15. It is also the only dike sample that can be safely assigned to trend 1 in the Cr and Ni versus $SiO_2$ diagrams (Fig. 7.12), which are among the diagrams where the two trends diverge the most. In the REE diagram (Fig. 7.16), this dike also stands out by having higher LREE/MREE.

Dike MVD-B 01-22 on the other hand, clearly does not belong to trend 1 (Hansen, 1997) since it plots on trend 2 in most major and trace element variation diagrams (most markedly on $P_2O_5$, Cs, Zn and HREE versus $SiO_2$). This indicates that the extreme isotopic ratios shown by this sample (highest Sr isotopic ratios of all the sampled rocks combined with relatively low Nd isotopic ratios) requires another explanation. In Appendix C it is shown that this deviation cannot be due to analytical uncertainty, since the analysis of the sample was reliable. It is possible that crustal contamination was the cause of the observed isotopic compositions, but it is also likely that contamination by seawater or magmatic water increased the Sr isotopic ratio. Although the sample looks fresh in thin section, alteration could have affected the specific area of the sample that was crushed into powder and later analysed for isotopic composition. This suspicion is confirmed by the high LOI (2.43 wt.%) shown by the sample (Appendix E; Table E1). The low Nd isotopic ratio of sample MVD-B 01-22 strongly suggest that the sample belongs to the "low-Nd" series, although it clearly does not belong to trend 1.

Diagrams in Fig. 7.15 showed that trend 1 samples (Hansen, 1997) have high La, Ba and Nb at low $SiO_2$ contents. This signifies that none of the basaltic dikes (<53 wt.% $SiO_2$) can belong to trend 1. On spider diagrams, basaltic samples show varying abundances of most elements, and

the variation among the HFSE is of special interest. In Fig. 7.18, eight dike samples have Nb contents below MORB (and some of these dikes are also depleted in Zr, Hf and Ta). These lów-HFSE ÞpatternsÓ contrast with samples having higher Ta and Nb contents than MORB and higher Zr and Hf abundances than the lów-HFSE ÐdikesÑ (Fig. 8.3 top left).

Assuming that the effect of crustal contamination upon basaltic samples can be ignored, the geochemistry of dikes (this study) and lava flows from the northern volcanic centres (Hansen, 1997; Kann, 2004) indicates that the mantle below Santorini produces basaltic magmas with significant trace element variations (Figs 7.29 and 8.3). It is suspected that the variation displayed in spider diagrams indicates that volcanics from northern Santorini may possibly have been derived from as many as four different source compositions:

The four possible sources of the volcanics were named after the characteristics shown by their representative basaltic samples in Fig. 8.3:

Low-Th: Represented by a single dike relatively high in LILE (Sr, Ba) and low in HFSE compared with other samples and MORB. This sample may be isotopically related to the "high-Nd" series, but low $^{143}Nd/^{144}Nd$ ratios could signify a different source (see text).

Low-HFSE: Represented by eight dikes having HFSE abundances lower than MORB (except for Ta). Five of these dikes were isotopically analysed and all belong to the "high-Nd" series.

Medium-HFSE: Represented by two dikes having HFSE levels similar to or just above MORB. No isotopical analyses available. Based on the spider diagrams, it is possible that trend 2 samples from Hansen (1997) were derived from this source (also no available isotopic analyses).

High-HFSE: Represented by a trend 1 lava flow (Hansen, 1997) high in HFSE in comparison with both MORB and all basaltic dikes. The sample belongs to the "low-Nd" series along with all other isotopically analysed trend 1 samples.

In Fig. 8.3, the pattern shown by sample MVD-T 00-10 ( lów-Th )"deviates from all other dikes by having higher Sr, a negative anomaly at Rb, a positive anomaly at Ba, lower Th and a trough at Ta (less pronounced troughs are shown by samples MVD-T 00-03 and MVD-T 00-09). Initially, little emphasis was given to this single sample, but it was discovered that a basaltic sample from the Thirassia-Skaros complex ( aÞ5-Nod-Oia Ñ from Zellmer (1998)) (Fig. 8.3 top right) shows a very similar pattern to dike MVD-T 00-10 (except that the trough lies at Nb in sample aÞ5-Nod-Oia )."This could indicate that the two samples reflect a distinct source composition with a differing LILE pattern and lower HFSE abundances than displayed by any other samples (the lów-Th Ñsource). Although the sample appears to have a deviating isotopic composition (discussed below), additional samples of this type are needed in order to make conclusions about such a source.

Most basaltic dikes from this study belong to the lów-HFSE Ñsource (Fig. 8.3 top left).

The patterns displayed by five basaltic trend 2 samples (Fig. 8.3 top right) from Hansen (1997) seem to resemble those of the two "medium-HFSE" dikes (Fig. 8.3 top left). The high Ta contents in trend 2 samples (Hansen, 1997) are the result of contamination during the crushing process.

The "high-HFSE" source is represented by a single trend 1 sample (Hansen, 1997), plotting at higher HFSE abundances than dikes and trend 2 lavas (Fig. 8.3 top right). Unfortunately, none of the dikes show a similar pattern but it appears that such a pattern is represented among Thirassia-Skaros lavas by sample TR 0014 (Kann, 2004) (Fig. 8.3 bottom left). The remaining Thirassia-Skaros lavas have patterns resembling that of the "low-HFSE" source, except sample TS 0101 showing the characteristics of the "medium-HFSE" source.

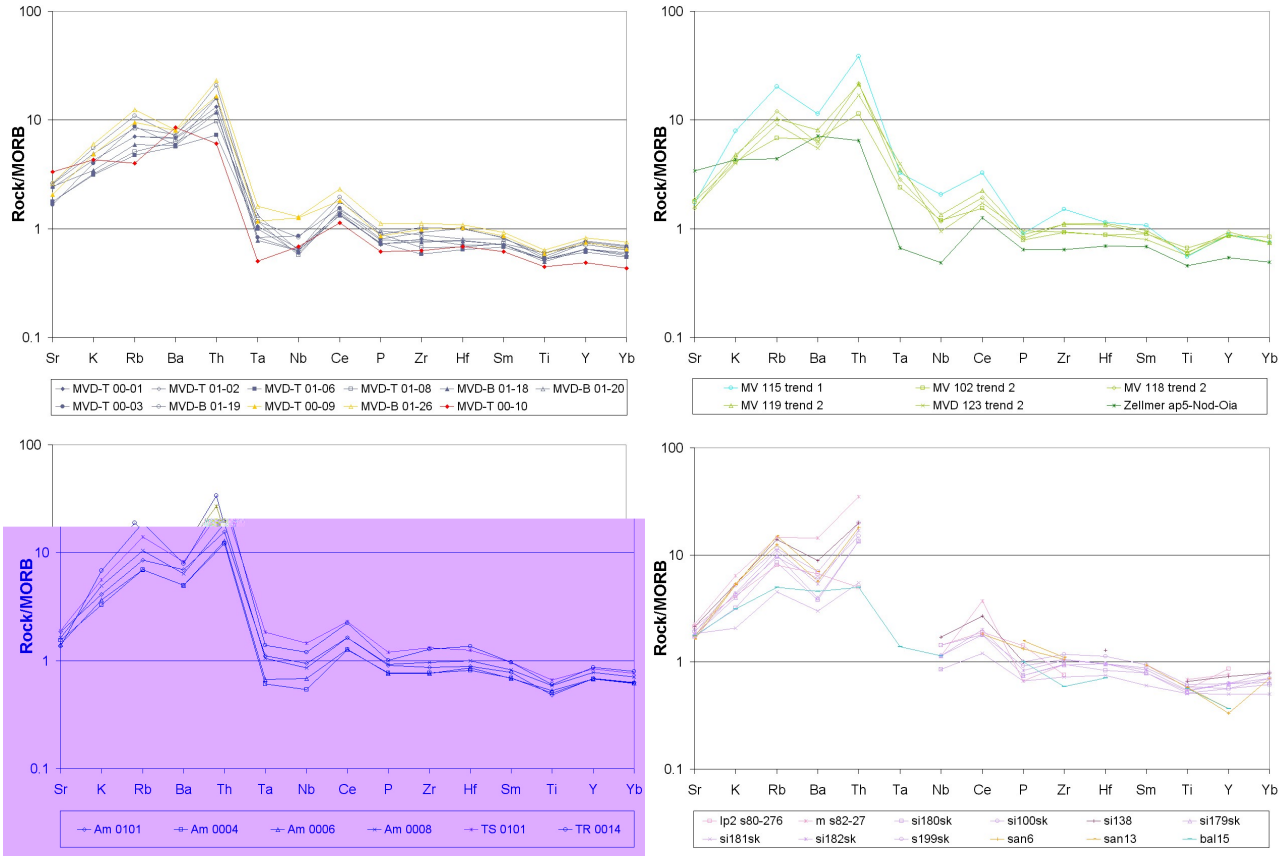


**Fig. 8.3.** Spider diagrams showing that possibly four different mantle sources gave rise to basaltic samples from Santorini. *Top left*: Eleven basaltic dike samples (this study) were divided into three separate series on the basis of their LILE and HFSE patterns ("low-Th" in red; "low-HFSE" in blue and "medium-HFSE" in yellow). *Top right*: Basaltic trend 1 ("high-HFSE") and trend 2 samples ("medium-HFSE") from Hansen (1997) plus a basaltic sample from Zellmer (1998) ("low-Th"). *Bottom left*: Basaltic samples from Kann (2004) represent the "low-HFSE," "medium-HFSE" and "high-HFSE" sources. *Bottom right*: Twelve basaltic samples from other Santorini localities generally resembling "medium-HFSE." Data from other Santorini studies (except trend 2 from Hansen, 1997) are listed in Appendix E, Table E8. See text for discussion.

Basaltic samples from other Santorini localities generally lack trace element data (Appendix E; Table E8), but twelve basaltic samples could be plotted (Fig. 8.3 bottom right). The patterns of most of these samples resemble those typical of the "medium-HFSE" source. Sample "m s82-

27 (Druitt et al., 1999) shows a resemblance to the high-HFSE pattern, but has much lower Nb, while sample s181sk (Huijsmans & Barton, 1989) could have been derived from the low-HFSE source.

Unfortunately, there are no isotopic data from basaltic samples belonging to the medium-HFSE series. It is possible that such isotopic data could confirm the existence of the four different source compositions, or reveal that some of the sources are isotopically similar.

Processes that may have influenced the trace element patterns displayed by the spider diagrams could be: variable depletion of the source as a consequence of melt extractions, variation in sediment input and slab fluid flux, and/or different degrees of melting of a mantle source which was HFSE depleted relative to MORB. It is conceivable that these processes varied systematically over a period of time. However, a careful study of data from Kann (2004) showed that this does not seem to be the case for the low-HFSE and the high-HFSE series. His combined data and stratigraphy showed that basalts belonging to both series were erupted simultaneously in the Thirassia-Skaros complex. It cannot be ruled out, however, that the distinct pattern shown by MVD-T 00-10 ( low-Th )is a result of either of the suggested time-dependent processes.

The resemblance between low-HFSE and medium-HFSE patterns could indicate that medium-HFSE samples were merely derived by smaller degrees of melting of the low-HFSE source. If this were the case, the two sources would have similar isotopic compositions. This could not be confirmed because none of the basalts with medium-HFSE patterns were analysed isotopically.

The high-HFSE pattern (defined by trend 1 sample MV 115 from Hansen (1997)) is believed to represent a distinct mantle source, and this is supported by the isotopic composition of this sample. Perhaps, mixing between this source and a depleted source component could produce the intermediate patterns. Since the patterns shown by the low-Th samples (Fig. 8.3 top left+right) deviate significantly from those of the remaining samples these are not likely candidates for an end-member source composition. However, the medium-HFSE series could, possibly, result from mixing between the low-HFSE source and the high-HFSE source.

This is the first reported evidence for different parent magmas on Santorini.

Spider diagrams as well as isotopic data indicate that the mantle source is heterogenous. The simplest model that appears to satisfy both types of data (prior to the effects of magma chamber processes) is given in Fig. 8.4.

Although sample MVD-T 00-10 was suspected to belong to the high-Nd series, the combination of a low Sr isotopic value and a relatively low Nd isotopic value (Fig. 8.4) could indicate derivation from a distinct source. This suspicion was supported by spider diagrams, in which this sample defines the low-Th source by having higher LILE and lower HFSE

abundances than other dikes (Fig. 8.3 top left). Furthermore, the sample stands out Pb isotopically by having the highest $^{206}Pb/^{204}Pb$ and lowest $^{207}Pb/^{204}Pb$ ratios of all the studied rocks. The fact that both the isotopic composition and trace element pattern deviate from the other studied samples strongly suggests that the sample had a different source. A distinct source composition cannot, however, be based on a single sample.

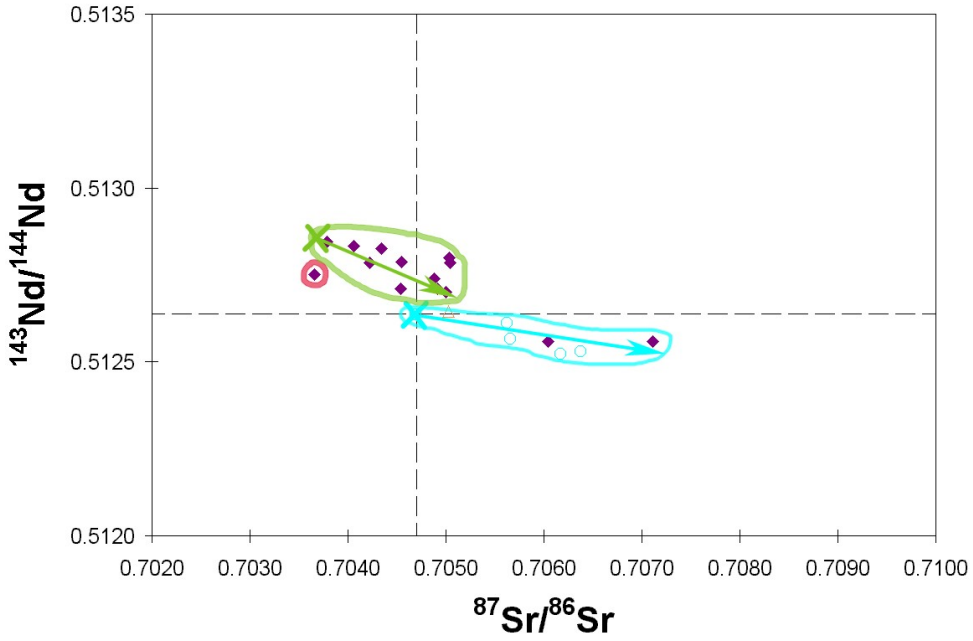


**Fig. 8.4**. Model of at least two distinct source compositions as interpreted from isotopic and trace element data. The possible isotopic source compositions of both the low-Nd and high-Nd series are marked with an "x" and arrows indicate isotopic variations which can be ascribed to processes in the mantle source or subsequent crustal contamination or most likely a combination of both. The single sample marked with a red circle is MVD-T 00-10 (defining the low-Th source in Fig. 8.3 top left) and its isotopic composition at low Sr isotopic values combined with a rather low Nd isotopic ratio (in comparison with the high-Nd series) indicates that this sample could have a distinct source. See text for further explanation.

Both the low-Nd and the high-Nd series show variations in Nd and Sr isotopic ratios that are believed to result from similar processes. The low-Nd series, however, appears to have been slightly more affected by a Sr isotopic contaminant than the high-Nd series (Fig. 8.4). Isotopic data and spider diagrams, in combination, confirm that the sources of the low-Nd " and high-Nd series were different.

The high-Nd samples are believed to have been derived from a more depleted mantle source having an isotopic composition closer to MORB (i.e. a weakly enriched isotopic signature) (Fig. 8.4). The variation in isotopic ratios within the series can be explained by a combination of sediment addition, seawater infiltration (in the shape of slab fluids from altered oceanic crust and/or subsequent contamination/alteration) and assimilation of upper crustal basement rocks.

The low-Nd "samples are believed to have been derived from a mantle source with an enriched character in trace elements as well as isotopic ratios relative to both MORB and the high-Nd samples (Fig. 8.4). It was shown that sediment addition probably did not affect one

series more than the other (Fig. 8.2). Addition of adakitic melts from the subducted slab is expected to result in a steep HREE pattern, which is not the case (Fig. 7.16). It appears, instead, that the enrichment relative to the hfgh-Nd "series can be explained by small degrees of mixing with an EMII reservoir existing in the mantle, possibly, in the form of relics of an older, terminated subduction. The isotopic variation in the lw-Nd "series does not differ much from that displayed by hfgh-Nd "samples. The larger Sr isotopic variation of the lw-Nd "series is most likely due to crustal contamination by basement rocks differing in composition from those which may have affected the hfgh-Nd "series (Section 8.3.3), or, in the case of sample MVD-B 01-22, a consequence of seawater contamination.
The effects of subsequent magma chamber processes upon the primitive magmas are discussed in Section 8.3 below.

To summarise, there appears to be good evidence for at least two distinct mantle sources ( lw-HFSE "and hfgh-HFSE )"that can be linked to the two source compositions shown by isotopic data ( hfgh-Nd "and lw-Nd ,"respectively). This is supported by Fig. 8.5 confirming that basaltic hfgh-Nd "samples all have low HFSE contents (in this case shown by Ta), while the basaltic lw-Nd "sample has high HFSE contents. The lw-Th "sample seems to have a distinct isotopic signature, but due to the lack of data a source cannot easily be defined. The mdium-HFSE "samples may not represent a distinct source, as it appears possible that such samples can be derived either directly from the lw-HFSE "source (smaller degree of melting), or from mixing between the lw-HFSE "and hfgh-HFSE "sources. Isotopic data are required to monitor these possibilities.

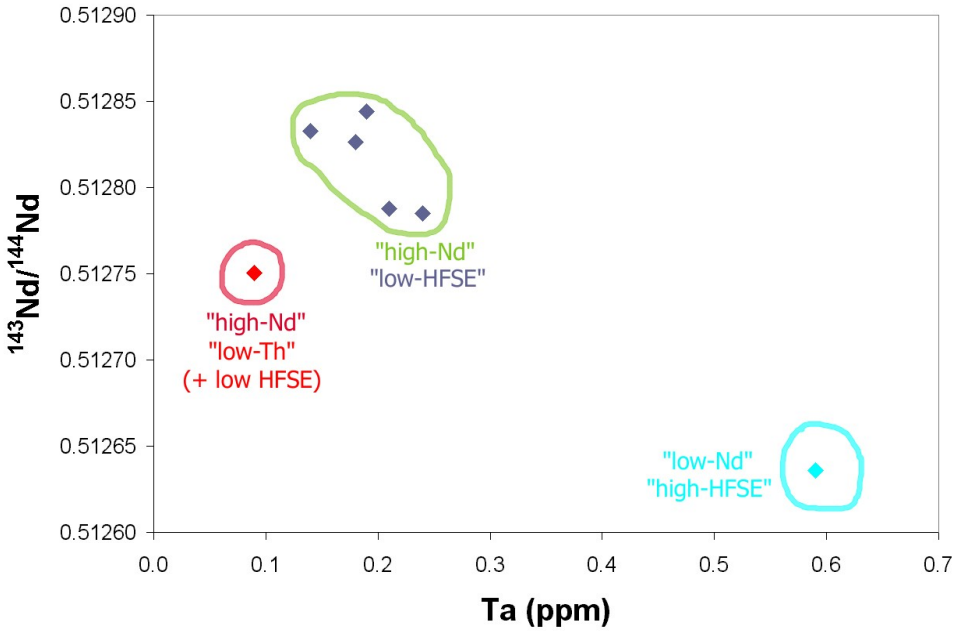


**Fig. 8.5.** Nd isotopic ratios versus Ta linking the lw-Nd "sample with the hfgh-HFSE "source and the hfgh-Nd "samples (except lw-Th )" with the lw-HFSE "source.

In Fig. 7.13, ratios of HFSE were plotted in order to learn more about the composition of the mantle source. Nb/Ta and Zr/Hf ratios are considered characteristic for the source, and most magmatic rocks have ratios that are indistinguishable from chondritic values (Prouteau et al., 2000). Nb/Ta ratios of most dikes are slightly subchondritic and closely resemble the depleted mantle value of 15.5 ± 1 (Jochum et al., 1997) (continental crust has subchondritic values ca. 12-13 (Barth et al., 2000)). The scatter to high Nb/Ta ratios observed among the least evolved rocks does not appear to be the result of analytical uncertainty (Fig. 7.13). It could, perhaps, reflect the existence of a superchondritic Nb/Ta reservoir in the mantle as proposed by Schmidt et al. (2004). Stolz et al. (1996) interpreted superchondritic Nb/Ta values (up to 33) as evidence that such rocks (from the Sunda arc) were derived from a mantle which had been modified by silicic melts derived from the partial melting of the subducted slab.

When Nb/Ta ratios of studied samples were compared with the spider diagrams it was discovered that both a „low-HFSE" sample (MVD-T 00-03) and a „medium-HFSE" sample (MVD-T 00-09) have high Nb/Ta ratios (Figs. 7.13, 7.18 and 8.3). The „low-Th" sample MVD-T 00-10 also has high Nb/Ta although its spider diagram pattern is relatively depleted in comparison with other dikes. Furthermore, sample MVD-B 01-26, which has the most enriched pattern of all basaltic dike samples, has intermediate Nb/Ta (15.5), while sample MV 115 (displaying the most enriched pattern of all Santorini samples) has even lower Nb/Ta (12.2) indicating that a high Nb/Ta ratio cannot be considered a characteristic feature of an enriched mantle source in the case of Santorini. Experimental studies by Schmidt et al. (2004) showed that superchondritic Nb/Ta ratios do not form as a result of partial melting of subducted oceanic crust, and Prouteau et al. (2000) reported that adakites are most likely to have chondritic Nb/Ta and Zr/Hf values. Their data suggest that high Nb/Ta ratios may instead result from smaller degrees of melting, or may be linked to hydrous fluid-metasomatism beneath island arcs.

Zr/Hf ratios in the studied rocks are superchondritic (Fig. 7.13) and, except for a single sample with an anomalously high ratio (MVD-B 01-16), samples do not scatter as seen for Nb/Ta ratios. Thus, it is suspected that superchondritic values are merely a consequence of analytical uncertainty. Zr/Hf ratios were calculated in this study, whereas the chondritic ratio was measured directly using a new analytical method (Weyer et al., 2002) that introduces less error.

## 8.2 Dike emplacement

Absolute ages have not yet been established for the dikes in the Megalo Vouno volcano complex. It is, however, certain that the dikes are younger than the products through which they have intruded. The latter range between 551 ± 12 ka (oldest Peristeria 1) and 54 ka ± 23 ka (youngest products on Megalo Vouno) (Druitt et al., 1999). It seems safe to conclude that the dikes must have been emplaced when the Megalo Vouno volcano complex was a complete edifice (as previously suggested by Puchelt et al. (1990)).

*How and when were the dikes erupted?*

Puchelt et al. (1990) suggested that the fissures, through which the dikes erupted, formed as a consequence of subsidence (Fig. 4.18). Caldera collapse is typically thought to take place in response to an empty space forming above magma in a chamber. Formation of such an empty space could be a good explanation for subsidence, resulting in fissures opening just prior to either caldera 2 (Fira caldera ca. 70 ka) or caldera 3 (Cape Riva caldera ca. 22 ka). Another possibility is that tremors prior to a large eruption could have triggered activity along existing faults (related to the overall NNE tectonic lineament on Santorini as well as to previous subsidence events), and that dikes could have intruded along these faults.

The majority of dikes outcrop like wall surfaces and are now visible in the caldera wall because the complex was ripped apart by a tremendous caldera formation. It is, therefore, certain that all dikes were intruded prior to the Cape Riva eruption (caldera 3), and are thus older than ca. 22 ka. This is evident from stromatolites that were ejected from the water-filled caldera during the Minoan eruption (caldera 4); the stromatolites could only have formed if there was water in the north-eastern area after the Cape Riva eruption and, thus, the dikes must have been part of a complex which had formed prior to the Cape Riva eruption. This conclusion is based on the lack of evidence for caldera formations between the Cape Riva and Minoan eruptions.

Nicholls (1971) observed that several dikes acted as feeders for lava flows in Peristeria volcano (the youngest Peristeria 3 lava flow in the Megalo Vouno volcano complex yielding an age of 480 ± 5 ka; Druitt et al. (1999)), and this can be concluded if dikes are observed to have an end point at levels where they can clearly be related to a lava flow. This was not observed during the present field work but may well occur. An observation of crossing dikes (Fig. 4.15) supports the idea that there were several intrusive events.

Many of the dikes sampled on top of the complex have scoria welded to their edges, suggesting that the cinder cones had formed prior to their intersection. These dikes seem to be the only products in the Megalo Vouno volcano complex which could have been extruded through young fissures formed just prior to caldera 3 (ca. 22 ka). It seems, therefore, that the dikes may cover a considerable time span: the oldest dikes could possibly be related to the Peristeria 1 volcano, some fed the >480 ka Peristeria 3 lava flows, whereas the youngest dikes were erupted after the cinder cones had formed. This implies that there were at least three intrusive events.

Any dikes feeding lava flows in the Peristeria 3 complex were derived from either of the two Peristeria magma chambers that Hansen (1997) suggested produced the two trends (shown to be two different sources in this study). Dikes extending all the way to the top, plus the cinder cones, were most likely related to the Thirassia-Skaros complex which was active in the northern part of Santorini between formation of caldera 2 and caldera 3 (Fig. 3.5). Puchelt et al. (1990) concluded that the compositional range of the dikes argued against derivation from a homogeneous magma chamber, and suggested two possible explanations: either that different

magma chambers were sources for the dikes, or that the intrusive events were so far apart in time that the magma chamber had evolved considerably and/or received new melts between the intrusions.

From the geochemical data (Chapter 7), it can be concluded that the sampled scoria from Megalo Vouno cinder cone does not differ markedly in geochemistry from the sampled dikes. Furthermore, data from Hansen (1997) support the fact that Peristeria 3 products (Megalo Vouno lava flows) and dikes do not show great discrepancies in their geochemistry. Critically, however, the dikes generally do not to fit the two trends observed among Peristeria 3 lavas by Hansen (1997) (Section 7.5). An obvious explanation could be that whereas dikes derived from the two separate Peristeria 3 magma chambers (shown to be two different sources) are expected to show either of the two trends, it is likely that dikes cutting to the top (MVD-T 00-01 to MVD-T 00-12) could have originated from the Thirassia-Skaros magma chamber which need not show the two trends (Fig. 8.6).

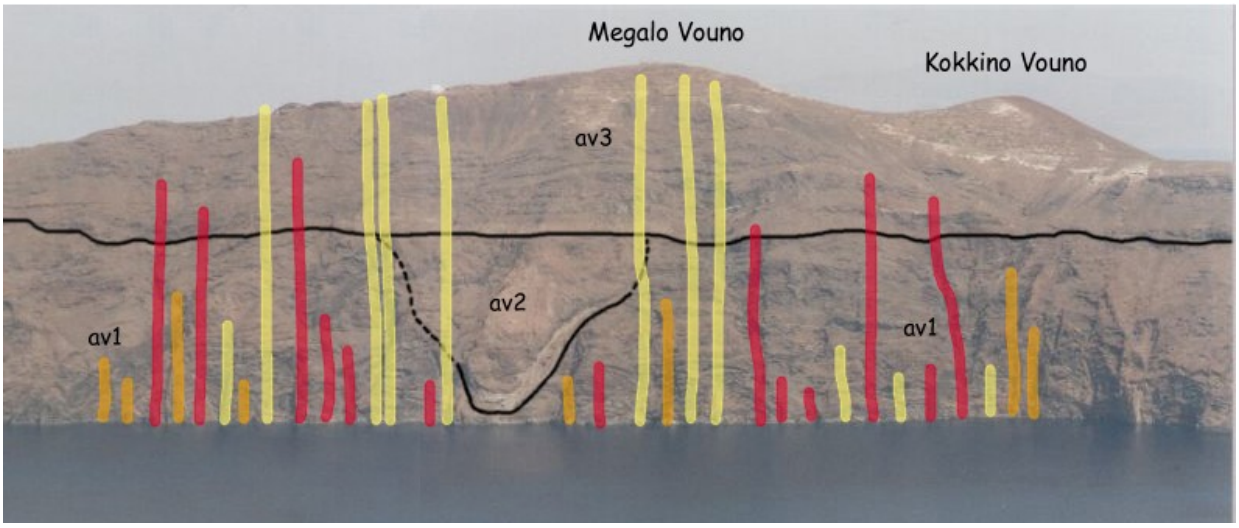


**Fig. 8.6.** A section of the Megalo Vouno volcano complex showing a possible explanation why the sampled dikes do not fit the two geochemical trends recognised throughout Peristeria 3 lavas (av3) by Hansen (1997). The yellow dikes are from a young intrusive event and stop at different levels in the wall, but some extend all the way to the top. The red dikes are from an older event and, although they also stop at different levels in the wall, they do not rise higher than Peristeria 3 (av3), where Nicholls (1971) observed that some of the dikes fed lava flows. It is impossible to say which of the dikes sampled at sea-level belong to which intrusive event, but the yellow dikes sampled on top of the complex must, certainly, belong to a younger intrusive event (possibly even more than one) than the red dikes feeding lava flows in av3. Orange dikes indicate that possibly even older dikes exist, but this is purely speculative. Only red dikes would decisively belong to the Peristeria 3 magma chambers, showing the two geochemical trends (Hansen, 1997) (shown, in fact, to be two different sources). As indicated in the sketch, most dikes could not be followed far above sea-level and, likewise, the yellow dikes reaching the top could not be followed all the way down to sea-level, but this is shown for clarity in the sketch. The fact that the red dikes have fed Peristeria 3 lava flows was based purely on observations by Nicholls (1971). The seven yellow dikes reaching the top were depicted as close as possible to their actual outcrop, whereas all other dikes were positioned to support the above ideas, since it was not possible to assign the dikes at sea-level to any intrusive event.

Kann (2004) studied the geochemistry of the Thirassia-Skaros complex and noticed that at least two trends could be observed in diagrams showing $TiO_2$ and FeO* versus $SiO_2$ but the two trends could not be followed through into trace element variation diagrams. It was concluded

that at least two different mechanisms (fractional crystallisation and magma mixing) controlled the evolution of the Thirassia-Skaros magmas (Kann, 2004). The same geochemical relations were found for the dikes in this study, and this is taken as strong evidence that the youngest dikes were derived from the Thirassia-Skaros magma chamber.

Nicholls (1971) emphasised the similarity in petrographic and chemical characteristics among the northern volcano centres, and grouped the products of Peristeria, Micros Profitis Ilias, Thirassia, Skaros and Megalo Vouno (including dikes) into a single volcanic series – the Main Series. Trace element and isotopic data from this study are, however, at variance with the conclusions of Nicholls (1971). The new data show that lavas and dikes from the northern centres were derived from a heterogeneous mantle (Section 8.1.2).

Integrating dike chronology with the geochemical data has proved to be difficult. Relatively young dikes collected on top of the complex appear to have been derived from two, or perhaps three, sources represented by the "low-HFSE" and the "medium-HFSE" samples (Fig. 8.3) plus a "low-Th" sample, if the latter is valid. In order to produce the two geochemical trends observed in Peristeria 3 lavas, Hansen (1997) concluded that two smaller magma chambers, above a common chamber, were needed. This study has shown that two magma chambers cannot explain the observed trace element variation among basaltic samples, and it is suggested that the two trends from Hansen (1997) were instead results of derivation from different mantle sources. This study has shown that Peristeria 3 lavas represent two different source compositions, namely the "high-HFSE" and the "medium-HFSE". Although the latter could not be shown to represent a distinct source (due to the lack of isotopic data), it still differs in trace element composition from the "high-HFSE" source.

To summarise, it seems evident from the geochemical data and age relations that the youngest dikes (at least twelve) were derived from the Thirassia-Skaros magma chamber. These dikes are generally similar in geochemistry to lava samples from the Thirassia-Skaros complex studied by Kann (2004). There is only evidence for one dike (sampled at sea-level) belonging to trend 1 from Peristeria 3 (Hansen, 1997). Except for this single sample, the two trends of Hansen (1997) are not consistently reproduced by the geochemistry of the dikes. While three variation diagrams (Ba, La and Nb versus $SiO_2$) in Fig. 7.15 indicated that basaltic dikes do not belong to trend 1 (Hansen, 1997), spider diagrams (Fig. 8.3) indicate that the majority of basaltic dikes were not derived from the same source as trend 2 samples either. This would explain why most dikes do not fit either of the two trends recognised by Hansen (1997). Isotopic data for trend 2 samples would have been helpful in determining whether geochemical differences between dikes and the trends recognised by Hansen (1997) are in fact due to different mantle sources or if subsequent magma chamber processes were also of importance.

Finally, it was not possible to establish whether additional older dikes intruded the complex prior to formation of Peristeria 3, and whether any of these have been sampled. This speculation is depicted in Fig. 8.6.

The data indicate that a heterogeneous mantle existed beneath the northern volcanic complex over a long period of time, and that magmas with different trace element and isotopic compositions were more or less continuously, and at times simultaneously, extracted from these different sources. Whereas isotopic and trace element data indicate the existence of two distinct (but possibly as many as four different) source compositions, the overall similarity in major element geochemistry among northern volcanics suggests that similar differentiation processes influenced the primary magmas (Section 8.3).

A solution as to how magmas may be simultaneously extracted from sources of distinctly different geochemical compositions is not immediately obvious, but this problem could perhaps be accommodated by the existence of enriched relic veins or patches from older subduction events, or the penetration of deeper asthenospheric melts as plumes in the mantle. The biggest problem seems to be how to avoid subsequent mixing between these sources in crustal-level magma chambers. Perhaps, mixing in the magma chamber is never taken to completion prior to eruption, or magmas from one source are transmitted more or less directly to the surface along fault-controlled channels. Otherwise a rather complicated model with several magma chambers within a relatively small area beneath the northern volcanic centres seems to be the only solution to this problem.

## 8.3 Magma chamber processes

As elegantly articulated by Neumann et al. (1999), only minerals faithfully record information about the changing chemical compositions in the magmas from which they grow. Since only whole-rock analyses were obtained for this study, and because they merely give an average result of the processes to which magmas have been subjected, they were combined with the petrography (Chapter 6) and mineral chemistry from other studies of Santorini volcanics.

As shown below, geochemical analyses of the dikes predominantly support conclusions about magma chamber processes obtained in former studies of the Santorini volcanic products.

*How were primary magmas modified in the magma chamber?*

Huijsmans et al. (1988), Zellmer (1998) and Druitt et al. (1999), among others, showed that the overall chemical variations displayed by lavas and pyroclastics from Santorini can be explained by a combination of three main effects: crystal fractionation, magma mixing and assimilation of crustal rocks.

- It is evident that fractional crystallisation played a major role in the differentiation of volcanic products from Santorini. For example, Mann (1983) found evidence for fractional

crystallisation among Main Series volcanics and Hansen (1997) showed that the main process in generating trend 1, observed in the Peristeria 3 lavas, was fractional crystallisation. Zellmer (1998) found that the differentiation trends of samples <60 wt.% $SiO_2$ were dominated by simple crystal fractionation, Druitt et al. (1999) explained much of the compositional variation in the Thera pyroclastics by fractional crystallisation and least squares calculations from Kann (2004) showed that lavas following trend 2 (see Fig. 7.14) were related by fractional crystallisation.

- Zellmer (1998) explained samples with relatively low $P_2O_5$ and $TiO_2$ abundances at intermediate compositions by mixing of relatively mafic (< ~58 wt.% $SiO_2$) with much more felsic material (> ~65 wt.% $SiO_2$). The effects of magma mixing were backed up by Druitt et al. (1999) who suggested that magma mixing played a role in producing mildly calc-alkaline volcanics by chemical mixing of a silicic component with a more mafic component of basaltic or mafic andesite composition. This was based on geochemical as well as textural observations (e.g., banding of pumices) and disequilibrium phenocryst assemblages. Kann (2004) explained that calc-alkaline volcanics could result from input and mixing of mafic tholeiitic magma into a magma chamber already containing an evolved tholeiitic magma.

- Zellmer (1998) showed a good positive correlation of Sr isotopes with $SiO_2$ at high silica abundances, implying that crustal contamination was most pronounced for the dacites and rhyolites, whereas only slight crustal contamination was thought to have occurred within the basaltic andesites. Druitt et al. (1999) argued that crustal assimilation played a major role in producing the geochemical time-variations observed in the Thera pyroclastics.

The effects of these processes upon the studied dikes are discussed in the three following sections.

### *8.3.1 Fractional crystallisation*

In this study, the effects of fractional crystallisation can be observed in several of the major and trace element variation diagrams in Figs. 7.6-7.12. Non-linear trends can reflect the build-up and then removal of elements as different mineral phases appear. Linear (or near-linear) trends are less diagnostic and can be typically explained by incompatible elements being accumulated in the residual melt or, in the exact opposite case, by the removal of elements which are compatible in the crystallising phases. However, magma mixing can also produce linear trends on variation diagrams (see Section 8.3.2).

Thus, the increase in $K_2O$ and $Na_2O$ with differentiation (Figs. 7.1, 7.4 and 7.6) is thought to represent accumulation in the melt, implying that K and Na are not incorporated significantly in the crystal structure of the observed crystallising phases. $Na_2O$ is, however, progressively incorporated into plagioclase, and this is reflected by a slightly flattened curve. $P_2O_5$ shows a

similar trend, and the kink at the evolved end could reflect crystallisation of apatite. Although this was not observed in the petrography of the dikes, both Mann (1983) and Huijsmans (1985) recorded the occurrence of apatite in some Main Series lavas with >63 wt.% $SiO_2$.

$Al_2O_3$, FeO*, MgO and CaO all decrease with differentiation, which is consistent with fractional crystallisation of the observed phenocryst phases (Chapter 6): plagioclase, clinopyroxene and olivine. The $H_2O$ content of a cooling magma strongly influences the onset and extent of plagioclase crystallisation (Grove & Baker, 1984; Grove & Kinzler, 1986; Zellmer, 1998). The observed early decrease in $Al_2O_3$ indicates early crystallisation and removal of plagioclase, which suggests that $H_2O$ contents were low in the primitive melt. MnO shows a flat trend, probably reflecting that it to a small degree is concentrated in olivine plus plagioclase, and in larger amounts in pyroxenes. The possible kink at ~62 wt.% $SiO_2$ could reflect crystallisation and removal of orthopyroxene. $TiO_2$ shows a fairly straight trend at first sight but, as suggested in Section 7.5, at least two different evolutionary trends seem to be represented in the diagram. One trend is represented by a marked increase in $TiO_2$ up to 55 wt.% $SiO_2$ followed by decrease. A second trend is characterised by only a slight increase with magmatic differentiation, while a possible third trend shows constant levels throughout the diagram (Fig. 7.14). The trends, which can also be vaguely seen in the FeO* versus $SiO_2$ diagram, can be described as characteristic of tholeiitic (trend 2) and calc-alkaline (trends 1 and 3) fractionation. Possible explanations of how calc-alkaline and tholeiitic trends can have developed, apparently simultaneously, are given in Section 8.3.2.

The REE (and Y) (Figs. 7.7 and 7.8) all seem to be incompatible in the crystallising phases and are thus concentrated in the melt. Eu is an exception, and the only mild increase with $SiO_2$ is thought to reflect incorporation into plagioclase. The development of a negative Eu anomaly, shown in Fig. 7.16, supports removal of plagioclase, and the $(Eu/Eu^*)_N$ versus $SiO_2$ diagram in Fig. 7.17 shows that the anomaly is developed above ca. 54 wt.% $SiO_2$ and stabilises from ca. 58 wt.% $SiO_2$ upwards. The other three diagrams in Fig. 7.17 show the degree of fractionation among the REE. As seen in Fig. 7.16, the LREE are fractionated relative to the HREE and this fractionation increases with differentiation as illustrated by $(La/Yb)_N$ ratios. Likewise, the $(La/Sm)_N$ diagram shows that the LREE are fractionated relative to each other, and that the ratio increases with differentiation, whereas the HREE in the $(Gd/Yb)_N$ diagram show hardly any change with differentiation and are only slightly fractionated relative to each other. The REE are all incompatible in olivine, clinopyroxene and orthopyroxene in basaltic and andesitic liquids and are only slightly fractionated. However, in more evolved liquids the partition coefficients increase by an order of magnitude from La to Lu in the mentioned minerals, and this may cause fractionation of the LREE relative to HREE (Rollinson, 1993).

The LILE (Fig. 7.9), except Sr, all increase with differentiation, reflecting accumulation in the residual melt. Pb increases only mildly which could reflect minor incorporation into

plagioclase. The decrease in Sr is, likewise, thought to reflect incorporation into plagioclase and subordinately into clinopyroxene. The high Sr values (ca. 300-400 ppm) shown by some samples will be discussed in Section 8.3.2 below.

The HFSE (Fig. 7.10) all increase, although some Nb and Ta is expected to be removed by Fe-Ti oxides. The volatiles (Fig. 7.11) do not show any clear indication of magmatic processes. All samples >5000 ppm Cl were collected at sea-level, and probably reflect contamination with sea water.

The decrease in most of the transition metals (Fig. 7.12) is thought to reflect incorporation into pyroxenes (Ni, Sc, Cr, V), titanomagnetite (V, Co, Ni) and olivine (Co, Ni). Cu is accumulated until it is incorporated into augite, and Zn is probably mainly affected by the removal of olivine. Two trends seem to be discernible in the Zn versus $SiO_2$ diagram and, in accordance with what was observed for $TiO_2$, this can be explained by a vaguely decreasing calc-alkaline trend (due to removal of magnetite), but an increasing tholeiitic trend (Bailey, 1991). Ga is only removed in limited amounts (by plagioclase, pyroxenes and titanomagnetite). There is, however, considerable scatter throughout the diagrams (as previously noted by Huijsmans et al. (1988)), and while some of this could be explained by the phyric nature of some of the rocks (e.g., Sr, Ni, Cr, Co) it seems evident that processes other than fractional crystallisation were involved in the differentiation of the products.

### *8.3.2. Magma mixing*

Magma mixing is consistent with disequilibrium textures in the studied thin sections (Chapter 6), but it is not possible to establish that magma mixing was the sole cause of these textures, since other processes (e.g., contamination by assimilation of crust) may also produce disequilibrium textures.

Geochemical data from this study suggests that magma mixing may have been present, and this is best seen in $P_2O_5$ and $TiO_2$ versus $SiO_2$ diagrams (Fig. 7.6). Linear trends in these diagrams can be explained by magma mixing as previously suggested by Zellmer (1998).

The high Sr content (Fig. 7.9) shown by the single Peristeria 1 lava flow and some of the dikes (MVD-T 00-01, MVD-T 01-02 and MVD-T 00-10) may also be indicative of magma mixing. Huijsmans et al. (1988) suggested that long-term depletion in LILE observed among the volcanic centres of Santorini could be explained by processes taking place in the upper mantle. However, Huijsmans & Barton (1990) subsequently found that not all samples from the Megalo Vouno volcano complex could fit this time-related depletion trend. The same deviation was observed in the present study, where a lava flow from the old Peristeria 1 volcano shows a high Sr value (376 ppm) along with one of the youngest dikes (>400 ppm) collected on top of Megalo Vouno. Two other young dikes have values above 250 ppm, signifying that some of the dikes are anomalously enriched in Sr. Huijsmans & Barton (1990) concluded that high Sr

values among young Megalo Vouno lavas were the result of mixing between relatively evolved liquid compositions and a Sr-rich component ~~-~~possibly a plagioclase-phyric basaltic liquid or a plagioclase-rich crystal mush. Unfortunately, Huijsmans & Barton (1990) did not publish any data so it is not possible to compare the geochemistry of the high Sr lavas with that of the high Sr dikes to see if their chemistry is broadly similar.

Druitt et al. (1999) argued that mixing between a silicic component and a mafic component would produce anomalously low levels of $TiO_2$ and FeO*/MgO at intermediate compositions compared with samples generated solely through fractional crystallisation. They furthermore plotted Cr versus Zr to show how magma mixing affects a highly compatible element versus an incompatible one. Cr is rapidly removed from the basaltic melt by fractional crystallisation of augite (and olivine), and will thus fall in the early stages of differentiation. Zr, being incompatible, will increase in the residual melt while Cr remains low, and hence fractional crystallisation produces a strongly curved trend in this diagram (Fig. 8.7). Druitt et al. (1999) in this way showed that an anomalously high Cr content among Cape Riva and Cape Therma 1 andesites was the result of magma mixing.

The dikes were plotted in the same two diagrams (Fig. 8.7), and it seems evident that fractional crystallisation was not the only process in development of all dikes. It, furthermore, appears that magma mixing mostly controlled the development of trend 1 lavas from Hansen (1997) along with a few dikes.

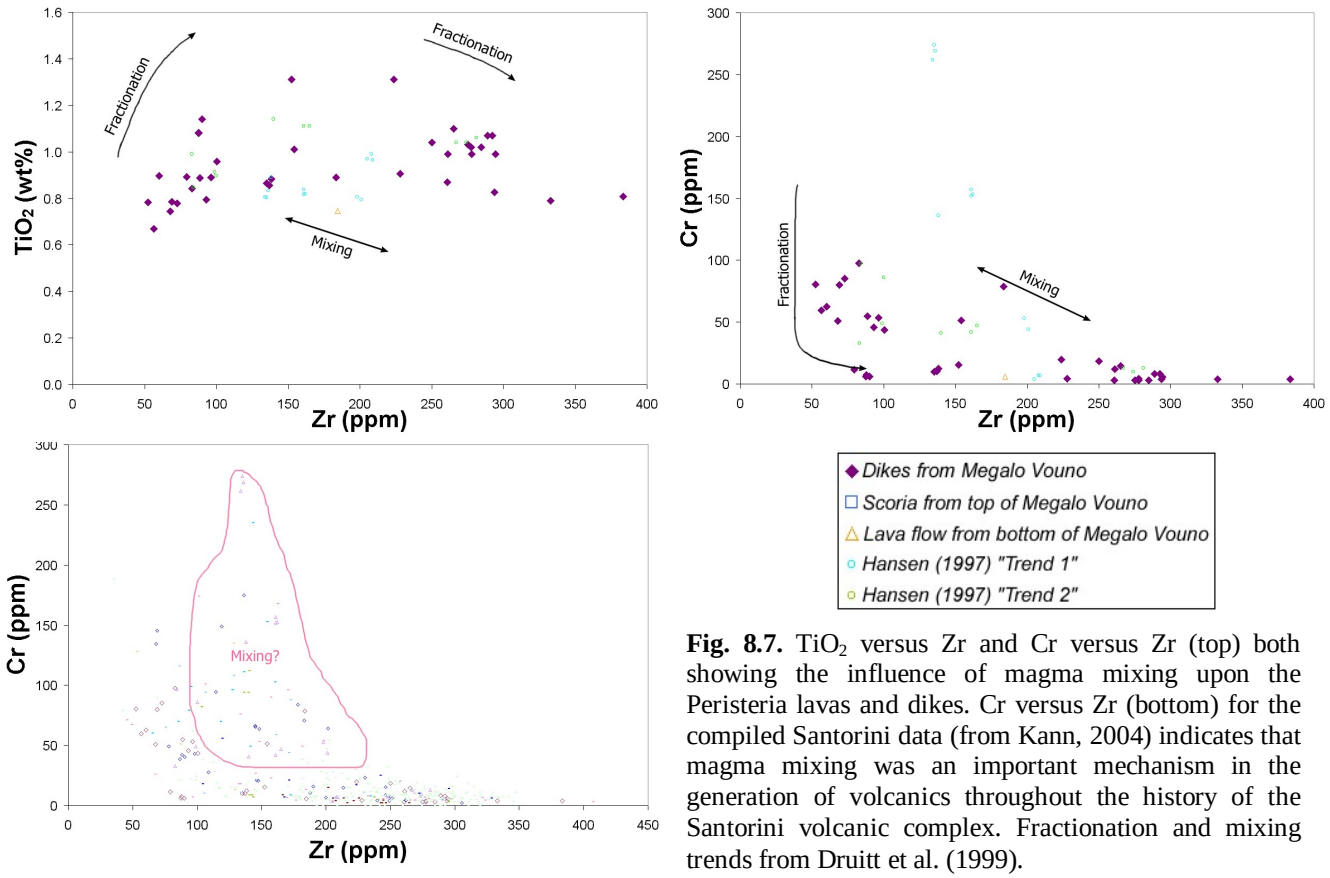


**Fig. 8.7.** $TiO_2$ versus Zr and Cr versus Zr (top) both showing the influence of magma mixing upon the Peristeria lavas and dikes. Cr versus Zr (bottom) for the compiled Santorini data (from Kann, 2004) indicates that magma mixing was an important mechanism in the generation of volcanics throughout the history of the Santorini volcanic complex. Fractionation and mixing trends from Druitt et al. (1999).

It seems probable that magma mixing may also be a valid mechanism in producing a third trend on the $TiO_2$ versus $SiO_2$ diagram (Fig. 7.14), to which only a few of the dikes appear to belong. Overall, magma mixing could be the main reason for the presence of calc-alkaline volcanics on Santorini. The presence of both tholeiitic and calc-alkaline volcanic products that seem to overlap in time does not seem to be common in subduction zone settings, and in the Aegean has only been observed on Santorini. While most scientists merely observe that volcanic products from Santorini are calc-alkaline, or perhaps transitional in composition, some have commented on the two different evolution trends. Huijsmans et al. (1988) suggested that there is an evolution towards tholeiitic compositions with time, whereas Druitt et al. (1999) and Kann (2004) believe that the calc-alkaline trends are mainly the result of magma mixing.

Field evidence from Santorini suggests that, overall, the eruptive style is typical of calc-alkaline volcanism, because large amounts of pyroclastic material are associated with the lava flows. However, it is not possible to determine whether any pyroclastic material has been associated with eruption of the dikes themselves, since most dikes thin out and stop at different levels in the wall, and only a few cut through the uppermost eruptions of the Megalo Vouno cinder cone.

The above examination of the geochemical data showed that both the calc-alkaline and tholeiitic series are only weakly developed, since not all typical traits of the two series can be seen in the geochemistry. The same can be argued from the petrography where the two series also resemble each other. For example, the rocks show a similar overall mineralogy, and the calc-alkaline rocks do not contain any indicator minerals such as hornblende or mica.

*Could processes other than magma mixing explain the evolution of volcanics along calc-alkaline differentiation trends?*

In most discrimination diagrams (Section 7.3: Figs. 7.2, 7.3 and 7.4), samples from the Megalo Vouno volcano complex plot in an intermediate position between typical calc-alkaline and tholeiitic series or cross the discrimination lines. In Miyashiro s'diagram (Fig. 7.2), the slope of the differentiation trend is more important with respect to which series the samples belong to, than the position of individual samples on either side of the discrimination line (Miyashiro, 1974; *definition number 1*). In this diagram, the slope produced by the samples is steeper than the dividing line, thus signifying that the rocks are tholeiitic. In the AFM diagram (Fig. 7.3), some of the rocks seem to follow a weak tholeiitic evolution trend characterised by a greater initial iron-enrichment (increase in Fe/Mg ratio) during fractionation than typical calc-alkaline series. Others follow a weak calc-alkaline trend showing no particular Fe enrichment, but instead a slight alkaline enrichment during fractionation. However, discrimination between the two series can be difficult, and the samples from this study are no exception. According to Grove & Kinzler (1986) "..it has been realised that clear-cut distinctions do not exist and that subtle differences separate a continuum of rock series from calc-alkaline to tholeiitic ."

One explanation for the development along tholeiitic or calc-alkaline differentiation trends was given by Grove & Baker (1984) using their pseudo-ternary diagrams (Fig. 7.5) (subsequently discussed by Grove & Kinzler (1986)). Experimental studies (Grove & Baker, 1984) showed that tholeiitic trends develop by fractional crystallisation at low pressures, and that the calc-alkaline series develop by fractional crystallisation at moderate crustal-level pressures (ca. 5 kbar and above) as well as in continental environments where basaltic magmas risk being contaminated with silicic crustal material. Thus, the main process in determining whether a basaltic melt will develop along the calc-alkaline or the tholeiitic trend is the pressure at which fractional crystallisation begins to take place (Grove & Baker, 1984).

Fig. 8.8 demonstrates that at low pressures (ca. 1 atm) the dominant crystallising phase is plagioclase together with some olivine. Later on, crystallisation of plagioclase+olivine+augite increases the proportions of total iron in the melt during fractional crystallisation. Further iron enrichment occurs at the reaction point A (Fig. 7.5a and 7.5b), when olivine reacts with the melt. At this point, crystallisation of augite and pigeonite with higher Mg/Fe ratios than the dissolving olivine combined with further crystallisation of plagioclase causes iron enrichment and a modest decline in silica content in the residual liquid. The appearance of titanomagnetite late in the crystallising assemblage eventually causes iron depletion.

At higher pressure (Fig. 8.8), combined olivine and augite dominate the crystallisation assemblage over minor amounts of calcic plagioclase, and the melts produced hereby will be of basaltic to basaltic andesite compositions. It is proposed that the residual liquid will then rise to a shallower magma chamber and produce andesitic-dacitic-rhyolitic lavas by continued fractional crystallisation (Grove & Baker, 1984). Iron enrichment is avoided because of the early precipitation of silicate phases in proportions that differ from those characteristic of the tholeiitic series, and by avoidance of the reaction point A.

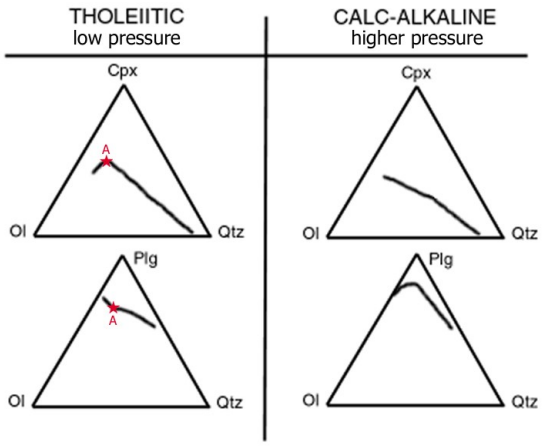


**Fig. 8.8.** Simplified pseudo-ternary phase diagrams showing typical tholeiitic (low pressure) versus calc-alkaline (higher pressure) differentiation trends from a single olivine tholeiitic parent melt in the Ol-Cpx-Qtz and Ol-Plg-Qtz diagrams.
After Grove & Baker (1984).

This could imply that, at Santorini, volcanic products are derived from two separate chambers residing at different crustal levels. Although the rest of the Aegean volcanoes show a calc-

alkaline affinity, the lower crustal thickness beneath Santorini may simply result in differentiation in a shallow chamber (or perhaps chambers) at the boundary between preferred tholeiitic and calc-alkaline crystallisation trends. This may explain why the tholeiitic and calc-alkaline trends at Santorini are not pronounced.

Sisson & Grove (1993) showed that $H_2O$ can effectively drive crystallisation along a calc-alkaline trend at low, upper crustal-level pressures (ca. 2 kbar) if the basaltic magmas (or basaltic andesite magmas) contain ca. 4-6 wt.% $H_2O$. However, Zellmer (1998) found that this process was unlikely (for the studied Thera products), since basaltic andesites contained less than 1.5 wt.% $H_2O$. He furthermore concluded that because geobarometry limits the pressure to less than 3 kbar for the basalts (Huijsmans, 1985), and because the observed crystallising assemblage is dominated by plagioclase, it seems unlikely that the calc-alkaline magmatism originates from fractionation at higher pressures.

Another way of producing tholeiitic and calc-alkaline products was proposed by Gill (1981) (Fig. 8.9). He showed that different degrees of melting of a common mantle source can produce calc-alkaline (10% melting) and tholeiitic (25% melting) suites. This theory is supported by Pe-Piper & Piper (2002) who suggested that whereas calc-alkaline products are common along the entire Aegean arc, the occurrence of tholeiitic rocks only on Santorini could be the result of a greater component of asthenospheric melting (Fig. 7.18) due to the lower crustal thickness below Santorini. However, this does not explain why both suites are found on Santorini.

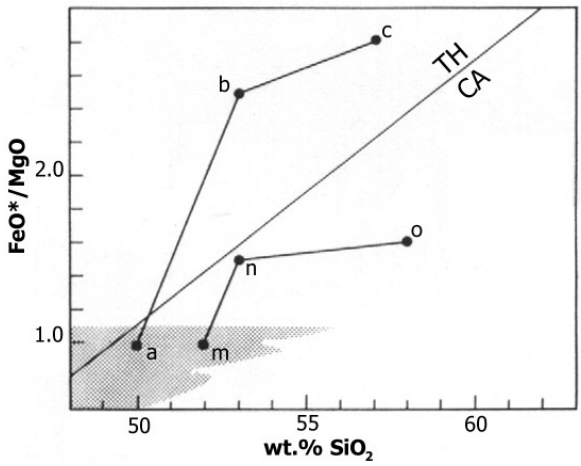


**Fig. 8.9.** A model proposed by Gill (1981) showing generation of tholeiitic and calc-alkaline suites by 25% and 10% melting, respectively, of a common peridotite source.
Line **abc** is a tholeiitic fractionation trend producing a low-K tholeiitic andesite and line **mno** is a calc-alkaline fractionation trend producing a medium-K calc-alkaline andesite. Modified after Gill (1981).

Although it may be possible to generate the two suites in this way, it seems more likely that different degrees of melting would result from time-related changes in the source region. For example, it could be argued that an increase in the release of slab fluids with time would result in progressively larger degrees of melting and thus enable the shift from one suite (calc-alkaline) into the other (tholeiitic). However, both suites were erupted throughout most of the history of the Santorini complex, and the products overlap in Peristeria 3 (Hansen, 1997) and in the Thirassia-Skaros complex (Kann, 2004). If the two suites have a common source, it seems that a more complicated process is needed to simultaneously initiate different degrees of

melting. In general, for Santorini, authors seem to favour the model of one large plus perhaps several smaller magma chambers below the volcanic complex, thus complicating the theory of differentiation of primitive melts derived by different degrees of melting.

As noted briefly above, crustal assimilation combined with fractional crystallisation can also drastically alter the composition of a magma, and generate liquids which follow the calc-alkaline trend upon continued fractional crystallisation (Grove & Baker, 1984). The effect of crustal contamination upon Santorini magmas has been demonstrated with isotope studies, and the model suggested by Druitt et al. (1999) for the Thera magma chamber builds partly on assimilation of crustal rocks (Section 8.3.3).

The different models above all give suggestions to how tholeiitic and calc-alkaline trends may develop from a common mantle source. This study has shown on the basis of HFSE data that trend 2 and trend 1 lavas of Hansen (1997) are derived from compositionally distinct sources. Furthermore, HFSE and Nd isotopic data indicate that the source of calc-alkaline trend 1 lavas from Hansen (1997) was enriched relative to the source of most dikes. However, mixing trends in Fig. 8.7 present good evidence for the calc-alkaline trend developing as the result of magma mixing. Mixing, likewise, holds a possible explanation to the anomalously high Sr contents observed among relatively young dikes.

### *8.3.3 Assimilation of crustal material*

Section 8.1.2 demonstrated that the isotopic differences displayed by the ‘low-Nd’ and the ‘high-Nd’ series arise from their different source compositions. It appears, however, that the isotopic variation within each series could have been enhanced by crustal contamination. This was backed up by Fig. 7.24 showing correlation between $SiO_2$ and Nd and Sr isotopic ratios, especially among ‘high-Nd’ samples.

Assimilation of crustal material during ascent, and/or storage in subvolcanic magma chambers are well documented processes, especially when magmas are erupted through thickened crust (e.g., Davidson, 1985; Bacon et al., 1989). The latter is not the case on Santorini where extension has approximately halved the crustal thickness in the central part of the arc. The volcanics have, nevertheless, erupted through continental crust.

Tectonic discrimination diagrams (Figs. 7.19-7.23) show that the geochemistry of the dikes is largely typical of volcanic arcs. In Figs. 7.20 and 7.21, the reduced crustal thickness beneath Santorini is reflected in the geochemistry of the volcanics; in Fig. 7.20 the dikes plot close to the division line between oceanic arcs and active continental margins, and in Fig. 7.21 most samples plot as oceanic island volcanics. In Fig. 7.19, the same intermediate tectonic environment is reflected in the La/Yb versus Sc/Ni diagram, whereas the La/Yb versus Th diagram shows the anomalously high Th content of the samples. High Th contents in basalts

(Fig. 7.32) suggests that the overall high Th contents in Santorini volcanics is a property of the source (Section 8.1.1).

In Fig. 7.32 it was observed that further enrichment in Th takes place during magmatic evolution. Although Figs. 7.20 and 7.21 indicate that crustal contamination is not reflected markedly in the geochemistry, contamination by a crustal component high in Th, Rb/Sr ratios and Sr isotopic ratios seems necessary to explain the observed enrichment in the "high-Nd" series (Figs. 7.30, 7.31 and 7.33). The "low-Nd" series appears, on the other hand, to have been less affected by this component (Figs. 7.24, 7.30, 7.31 and 7.33), or was perhaps contaminated by another type of basement rock as indicated by Figs. 7.30 and 7.34.

According to Macdonald et al. (2000), crustal contamination typically results in covariation in Sr and Nd isotopes (and displacement away from the MORB field). Hence it is suspected that crustal contamination has enhanced the extent of isotopic variation as shown for both the "low-Nd" series and the "high-Nd" series in Fig. 8.4. A similar conclusion was reached by Zellmer (1998), although his study did not include samples with isotopic characteristics of the "low-Nd" series. The modelling of Zellmer (1998) on the effects of different contaminating components upon samples from the Second Eruptive Cycle (SEC) showed that neither wedge fluids nor sediment (either as bulk sediment or as a melt) could change the Sr isotopic compositions in the direction of the samples. However, the data could be modelled satisfactorily by combined assimilation and fractional crystallisation (AFC), when using upper continental crust data from Taylor & McLennan (1995) as the contaminant (Fig. 8.10).

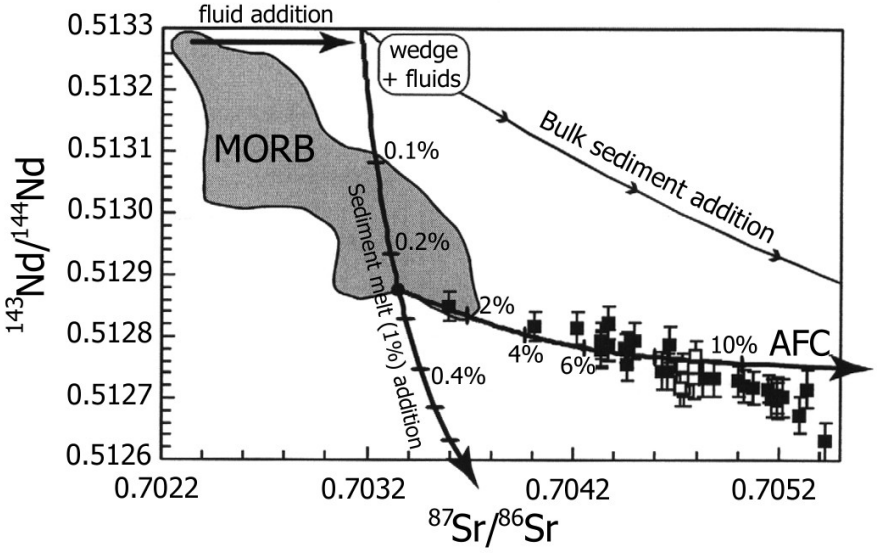


**Fig. 8.10.** Modelling showing the effects of contamination by different components upon samples from the Second Eruptive Cycle. See text for explanation. Diagram from Zellmer (1998).

Another indicator of assimilation combined with fractional crystallisation is the positive and negative correlation of Sr and Nd isotopic ratios, respectively, with $SiO_2$ (Fig. 7.24). Such a correlation was previously demonstrated by Zellmer (1998) and Druitt et al. (1999), both

studies displaying similar isotopic variation to that displayed by the "high-Nd" series from this study.

AFC modelling was also carried out by Druitt et al. (1999), and this demonstrated that basement rocks from Naxos could not fit the Santorini data, and that granitoids from Laurium, Serifos, Mykonos, Delos, Naxos, Kos and Samos all seemed to have too high Sr contents. They concluded that a contaminant with high $K_2O$, Rb, Ba, Zr and low Sr was needed. Such contents were found in metavolcanic rocks on Santorini and, thus, three samples of this rock type were used in their modelling. It was pointed out that the $SiO_2$ contents were too low for the rock type to be the actual assimilant. They finally suggested that the data point to the contaminant being a leucogranite or rhyolite, probably in the form of a partial melt. Druitt et al. (1999) furthermore showed that contamination by AFC was consistent with slightly elevated $\delta^{18}O$ (compared with mantle values). They concluded that some crustal contamination occurred in high-level magma chambers because plagioclase phenocrysts were generally less radiogenic than the corresponding melt phases.

Barton et al. (1983), on the other hand, reported scatter in their Sr isotopic data and observed no correlation with $SiO_2$. They concluded that assimilation of crustal material had taken place prior to low-pressure fractional crystallisation. Perhaps a similar process could explain why the "low-Nd" series lacks a positive correlation between Sr isotopic ratios and $SiO_2$ (Fig. 7.24).

The anomalous enrichment in $K_2O$ with magmatic differentiation (shown in Figs. 7.1 and 7.4) could also reflect crustal contamination. Huijsmans et al. (1988) found it unlikely that fractional crystallisation alone could generate compositional variations from low-K tholeiite to high-K andesite. Since the most primitive rocks have low $K_2O$ contents the evolution to high-K is most likely the result of crustal assimilation as opposed to being a source characteristic.

In Fig. 7.34 preliminary modelling showed that simple two-component mixing between a primitive "high-Nd" sample and a basement phyllite approximates the isotopic variations displayed by the "low-Nd" samples. However, trace element data show that the two series were derived from sources with distinct isotopic compositions, and thus the result of Fig. 7.34 is merely regarded as a coincidence. This was backed up when mixing was modelled using different trace elements versus isotopic ratios as seen in Fig. 8.11. This diagram shows that the Th content (along with other trace elements: e.g., Rb, La, Ba) of the "low-Nd" series cannot be explained by simple mixing between a "high-Nd" sample and a phyllite basement rock.

Fig. 8.12, on the other hand, shows that the Th enrichment observed in the separate series can be approximated by contaminating a primitive sample from each series with different basement rocks: the variation within the "high-Nd" series can be approximated by contamination of a primitive sample with a granite basement rock, while the most primitive "low-Nd" sample may have assimilated a phyllite basement rock. The Th enrichment in the "low-Nd" series is not

satisfactorily explained by this model, indicating that perhaps assimilation of granite also affected the low-Nd samples, although to a lesser extent.

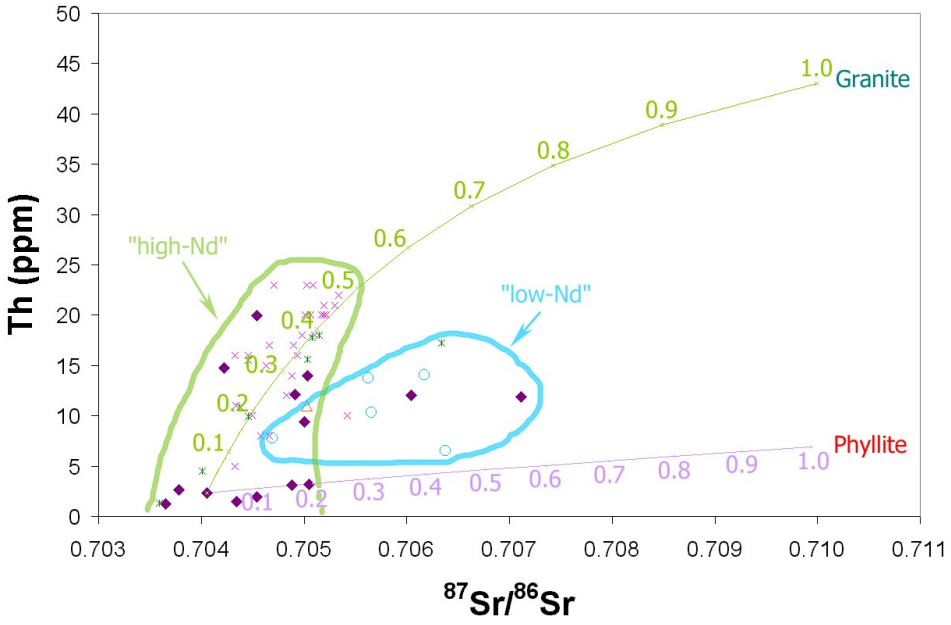


**Fig. 8.11**. Two-component mixing between a primitive high-Nd sample (MVD-B 01-18) and a granite approximates the variation shown by the high-Nd series. Mixing between the same primitive sample and a phyllite does not explain the variation in trace elements and isotopic compositions shown by the low-Nd series.

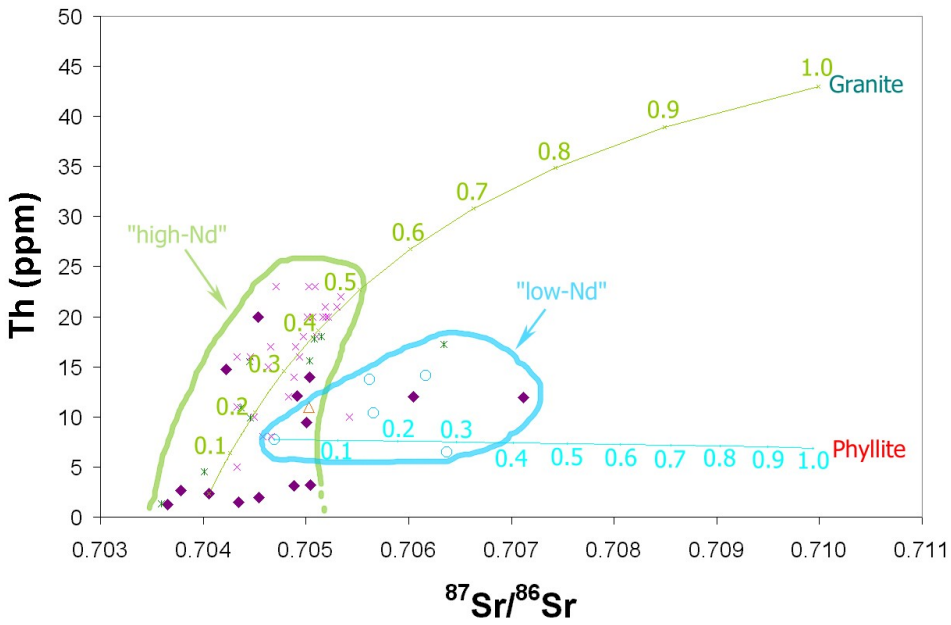


**Fig. 8.12**. Simple two-component mixing between the most primitive sample in the low-Nd series and a phyllite approaches the variation shown by the low-Nd series. The slight Th increase in the low-Nd series, however, cannot be explained. This indicates that either the low-Nd series could have assimilated small amounts of the granite or that the effect of AFC solves this problem (see text).

Figs. 7.24, 7.34 and 7.35 all indicated that AFC is a more likely process than two-component mixing in producing the variation shown by high-Nd samples. It also seems unlikely that any process could create up to 50% melting of a basement rock, as required in order to produce the variations in the high-Nd series in Figs. 8.11 and 8.12. To test whether assimilation combined

with fractional crystallisation could produce the observed variations by a smaller, and more realistic, degree of basement rock assimilation, preliminary AFC modelling was carried out using the following equation:

$$R_L = R_O + (R_C - R_O)\left(1 - \frac{X_O}{X_L} F^{-K}\right)$$

$X_L$ = concentration of the trace element in the contaminated liquid
$X_O$ = concentration of the trace element in the original magma
$X_C$ = concentration of the trace element in the assimilant
$R_L$ = isotope ratio of the contaminated liquid
$R_O$ = isotope ratio of the original magma
$R_C$ = isotope ratio of the assimilant
r = ratio (rate of assimilation)/(rate of fractional crystallisation)
D = bulk distribution coefficient of the fractionating assemblage
F = fraction of magma remaining

$$K = \frac{r - 1 + D}{r - 1}$$

The modelling proved difficult because of the changes that take place in bulk distribution coefficients during fractional crystallisation. The attempt was furthermore complicated by changes in the variables r and F, but it is expected that computer programs specifically created for AFC modelling can handle this problem.

It was pointed out by Roberts & Clemens (1995) that there are some general problems with AFC modelling, because it is based on mathematical models attempting to reproduce trends shown by a specific data set. Although data arrays on variation diagrams are typically assumed to be petrogenetically significant, these may not always reflect a particular process. If samples in a data set were shown *not* to be comagmatic, AFC modelling could falsely indicate that they were comagmatic simply because of the nature of the mathematical equations. Therefore, they concluded that AFC modelling should only be undertaken with robust initial constraints on the compositions of the parent magma and the proposed assimilant. Furthermore, in AFC modelling crystal-liquid partition coefficients are typically chosen so that they produce the best fit with the data set rather than founding these on reliable petrologic and experimental data. Naturally, partition coefficients should always be used in so far as they are known. Finally, the possibility of the involvement of more than one assimilant is neglected in AFC modelling.

Roberts & Clemens (1995) conclude that the results of AFC modelling should only be accepted if the isotope-based model parameters are consistent with those derived from major and trace element variations, and there should be some hard evidence for the existence of the proposed magma and assimilant.

On these grounds, it was decided to avoid further interpretation about the method of assimilation, because it has already been shown that crustal contamination is a likely process in creating the variety in isotopic ratios within both the lów-Nd ánd the hígh-Nd séries.

# 9. Conclusions

Thirty-six dikes cutting the Megalo Vouno volcano complex in northern Santorini were collected in the years 2000 and 2001. Furthermore, an old Peristeria 1 lava flow was sampled by boat and a piece of scoria from the Megalo Vouno cinder cone was collected near the top of the volcano complex. Dikes reaching the top of the complex are believed to be related to the Thirassia-Skaros complex which was active in northern Santorini between ca. 85-22 ka. The majority of dikes, however, thin out and stop at different levels in the caldera wall, and some of these may have fed lava flows in the older Peristeria 3 unit. Hence, lava flows from Peristeria 3 sampled by Hansen (1997) were studied along with the dikes.
The dikes vary in composition from basalt to trachyte, the majority being basaltic andesites.

Spider diagrams indicate on the basis of HFSE contents that four different mantle source compositions gave rise to basaltic samples in northern Santorini: low-HFSE, medium-HFSE, high-HFSE and low-Th.
The low-HFSE series comprises eight basaltic dike samples, characterised by generally low HFSE levels compared with MORB. Four samples from Kann (2004) show a similar pattern.
Only two basaltic dikes appear to have been derived from a mantle source with medium-HFSE characteristics. However, spider diagram patterns suggest that all four basaltic, trend 2 samples from Hansen (1997) were also derived from this source. Since none of these samples were analysed isotopically, it was not possible to confirm the existence of a distinct mantle source composition for the medium-HFSE rocks. It is possible that these may instead result from smaller degrees of melting of the low-HFSE source, or mixing between the low-HFSE and the high-HFSE sources.
The enriched high-HFSE mantle source is defined by a single trend 1 lava flow of Hansen (1997), and a similar pattern is displayed by a single sample from Kann (2004).
The low-Th mantle source is defined by a single dike sample plus a basaltic sample from the Thirassia-Skaros complex collected by Zellmer (1998). This source is characterised by a differing LILE pattern combined with low HFSE levels in comparison to both MORB and the three other mantle sources.

This study is the first to suggest that distinct mantle sources played a role in the geochemistry of the northern volcanic centres on Santorini. The existence of different parent magmas is supported by Nd isotopic data which confirm that at least two isotopically distinct sources, low-Nd and high-Nd, are present among the data. On the basis of isotopic compositions a third group can be distinguished.
The low-Th basalt displays a distinct isotopic composition at low Nd and low Sr isotopic ratios and has the highest $^{206}Pb/^{204}Pb$ and lowest $^{207}Pb/^{204}Pb$ ratios of all the studied rocks.

The high-Nd series comprises eleven samples of basaltic to trachytic composition, displaying high Nd isotopic ratios at 0.512844-0.512700, i.e. from a depleted mantle source.
The low-Nd series is defined by seven samples, ranging from basaltic andesite to trachyandesite, displaying lower Nd isotopic ratios at 0.512636-0.512558. The data strongly suggest that the low-Nd source was at some point enriched relative to the high-Nd source, perhaps by mixing between relics of a former, terminated subduction and a relatively depleted mantle.
The large variation in Sr isotopic composition, within both the low-Nd (0.704693-0.707115) and high-Nd (0.703783-0.705004) series, can be ascribed to a combination of seawater contamination and assimilation of upper crustal lithologies. Preliminary modelling suggested that assimilation of different types of basement rocks from Santorini could to some extent explain the varying trace element and isotopic compositions displayed by the low-Nd and high-Nd series. The high-Nd rocks are believed to have been affected to a larger degree by basement rocks of granitic composition than the low-Nd samples. Differences between the low-Nd and high-Nd series are not pronounced on Pb-Pb isotopic plots, possibly because Pb isotopic ratios of both sources were affected by the same subducted sediment.

Both a tholeiitic and a calc-alkaline evolution trend can be recognised in variation diagrams. However, dikes generally do not reproduce the calc-alkaline trend 1 and tholeiitic trend 2 recognised by Hansen (1997). This is suspected to be a consequence of the distinct mantle source compositions. Trend 2 lavas from Hansen (1997) are believed to have been derived from the medium-HFSE source, along with only few dikes, while trend 1 lavas were derived from the high-HFSE source. The majority of dikes were, however, derived from the low-HFSE source, and this would explain why the majority of dikes do not consistently follow trend 1 or trend 2 of Hansen (1997) in their geochemistry. While the tholeiitic trend is believed to mainly result from fractional crystallisation, there is good evidence that magma mixing produces the calc-alkaline trend.

*Implications for further studies*
High-quality trace element analyses of additional basaltic samples are required to confirm the existence of the low-Th mantle source. Unfortunately, basaltic rocks are not very common on Santorini.
Only a few studies of Santorini include isotopic analyses of samples. Additional isotopic data could, hopefully, confirm the existence of the low-Th source and reveal whether the medium-HFSE samples have a distinct isotopic composition suggestive of a distinct mantle source.
Computer modelling for AFC plus acquisition of $\delta^{18}O$ data could prove helpful in determining the importance of crustal contamination. In addition, high-quality major and trace element data and isotopic data are required for a more comprehensive collection of Santorini basement rocks.

# Acknowledgements

I would like to address a special thanks to Kristian Kann for proof reading, constructive criticism and enormous support during field work as well as during the writing process. It would have been dangerous, and practically impossible, to collect samples in the caldera on my own (from a boat with a dodgy motor and only one oar!). Most of all, thank you for keeping up the high spirits during your illness, and for having the energy and strength to finish this project that we started on together.

I would also like to thank

- The laboratory technicians at the Geological Institute, Copenhagen: especially Birthe Møller for producing beakers for isotopical analyses as well as for many pleasant conversations in the very early hours. Maria Jankowski for overall help in the laboratories, Jørgen Kystol for analysing whole-rock samples, and finally Toby F. Leeper for his assistance on the mass spectrometer.

- Walther Friedrich, Aarhus University, for showing me around on Santorini, for extinguishing fires in Greek restaurants, and for giving me the opportunity for treading wine with the Gavalas family.

- My supervisors: Erik Schou Jensen, Geological Museum, for a pleasant and instructive week on Santorini and John Bailey, Geological Institute, for XRF results, criticism, praise and quick replies to even the most trivial questions.

- Svend Pedersen, Geological Institute, for editing our VARV article, and for showing a genuine interest in our work on Santorini.

- Professor Cenka Christova for tremendous helpfulness with retrieving articles, and for many interesting conversations via e-mail.

- Lukas and Vasilis for letting me rent Atlantis Diving s'primitive (but usable) motorised rubber dinghy at a reasonable price – without it I could never have sampled 24 dikes at sea-level.

- Henrik Faaborg, Hillerød Handelsskole, for retrieving otherwise lost data on my old hard drive, and for giving me access to beautiful, top quality colour prints.

- Students with the Petrological Department, Geological Institute, and colleagues at the Geological Museum for endless, encouraging conversations.

- Lea & Christina for our marvellous cookery- and theatre club as well as long-lasting friendship.

- Abdah Ghulam for always being there even though we never have time to meet.

- Karina D. Hansen for your cheerful self, beautiful gifts and for always finding time to drop by the office for a chat. Also many thanks for the lovely evenings spent in the company of your family.

- Charles Frazer Pedersen for supporting both of us during busy times with his fabulous Gambian cuisine, and for providing us both with lots of adventures.

- Mara Lenz for proof reading of most chapters, for checking the punctuation I was never taught correctly, for letting Tavs sort out the piles of paper and most of all thank you for keeping up my spirits when things got too tough. Also thank you to Henrik Sørensen for letting us borrow Miv, who certainly made sure that we never got up late during the final months of hard work.

- Birgit & Torben Kann, for lovely trips to Bakken and Sønderjylland, for Torben s' fabulous stews ;o) and everything wonderful you both have done for us during our studies. A special thanks to Birgit for your ever fantastic support and faith in us, it was such a shame that you did not get to see the final results.

- Marc S. Curtis for preliminary proof reading of the opening chapters, and to Anette and Pernille for always being there and for keeping me in a good mood with great stories and Pernille s 'wonderful phrases.

Most of all thank you to my Mum and Dad for enormous support throughout my studies, and for cosy weekends, vacations together, indispensable "relief aid" and for providing washing machine for piles of laundry. It would all have been impossible without your wonderful, old, red Toyota!

And finally, thank you to everybody who is not listed above, but has in any way contributed to the project and made it all possible.

Copenhagen, November 2004

# References

Altherr, R. & Siebel, W. 2002. I-type plutonism in a continental back-arc setting: Miocene granitoids and monzonites from the central Aegean Sea, Greece. *Contributions to Mineralogy and Petrology*, vol. **143**; 397–415.

Avigad, D., Baer, G. & Heimann, A. 1998. Block rotations and continental extension in the central Aegean Sea: Palaeomagnetic and structural evidence from Tinos and Mykonos (Cyclades, Greece). *Earth and Planetary Science Letters*, vol. **157**; 23–40.

Avigad, D. & Garfunkel, Z. 1991. Uplift and exhumation of high-pressure metamorphic terrains; the example of the Cycladic blueschist belt (Aegean Sea). *Tectonophysics*, vol. **188**, no. 3-4; 357–372.

Bacon, C.R., Adami, L.H. & Lanphere, M.A. 1989. Direct evidence for the origin of low-$^{18}$O silicic magmas: quenched samples of a magma chamber's partially-fused granitoid walls, Crater Lake, Oregon. *Earth and Planetary Science Letters*, vol. **90**; 199–208.

Bailey, J.C. 1981. Geochemical criteria for a refined tectonic discrimination of orogenic andesites. *Chemical Geology*, vol. **32**; 139–154.

Bailey, J.C. 1991. *Geochemistry of igneous rocks: Second edition*. Copenhagen University; 287 p.

Bailey, J.C., Larsen, O. & Frolova, T.I. 1987. Strontium isotope variations in lower Tertiary-Quaternary volcanic rocks from the Kurile island arc. *Contributions to Mineralogy and Petrology*, vol. **95**, no. 2; 155–165.

Bard, E., Hamelin, B., Fairbanks, R. G. & Zindler, A. 1990. Calibration of the $^{14}$C timescale over the past 30.000 years using mass spectrometric U-Th ages from Barbados corals. *Nature*, vol. **345**, no. 6274; 405–409.

Bardot, L., Thomas, R. & McClelland, E. 1996. Emplacement temperatures of pyroclastic deposits on Santorini deduced from palaeomagnetic measurements: constraints on eruption mechanisms. In: Morris, A. & Tarling, D.H. (eds.): *Palaeomagnetism and tectonics of the Mediterranean region*. Geological Society Special Publication No. **105**, London; 345–357.

Barth, M.G., McDonough, W.F. & Rudnick, R.L. 2000. Tracking the budget of Nb and Ta in the continental crust. *Chemical Geology*, vol. **165**; 197–213.

Barton, M. & Huijsmans, J.P.P. 1986. Post-caldera dacites from the Santorini volcanic complex, Aegean Sea, Greece: An example of the eruption of lavas of near-constant composition over a 2.200 year period. *Contributions to Mineralogy and Petrology*, vol. **94**, no. 4; 472–495.

Barton, M., Salters, V.J.M. & Huijsmans, J.P.P. 1983. Sr isotope and trace element evidence for the role of continental crust in calc-alkaline volcanism on Santorini and Milos, Aegean Sea, Greece. *Earth and Planetary Science Letters*, vol. **63**, no. 2; 273–291.

Ben Othman, D., White, W.M. & Patchett, J. 1989. The geochemistry of marine sediments, island arcs magma genesis, and crust-mantle recycling. *Earth and Planetary Science Letters*, vol. **94**, no. 1-2; 1–21.

Bertagnini, A., Metrich, N., Landi, P. & Rosi, M. 2003. Stromboli Volcano (Aeolian Archipelago, Italy); an open window on the deep-feeding system of a steady state basaltic volcano. *Journal of Geophysical Research*, vol. **108** no. B7, 2336; 15 p.

Bohnhoff, M., Makris, J., Papanikolaou, D. & Stavrakakis, G. 2001. Crustal investigation of the Hellenic subduction zone using wide aperture seismic data. *Tectonophysics*, vol. **343**; 239–262.

Bougault, H., Maury, R.C., El Azzouzi, M., Joron, J.L., Cotton, J. & Treuil, M. 1982. Tholeiites, basaltic andesites, and andesites from Leg 60 sites; geochemistry, mineralogy, and low partition coefficient elements. In: Marianna, L. & Powell, R. (eds.): *Leg 60 of the cruises of the drilling vessel Glomar Challenger; Apra, Guam to Apra, Guam; March-May 1978. Initial Reports of the Deep Sea Drilling Project*, vol. **60**; 657–677.

Briqueu, L., Javoy, M., Lancelot, J.R. & Tatsumoto, M. 1986. Isotope geochemistry of recent magmatism in the Aegean Arc: Sr, Nd, Hf and O isotope ratios in the lavas of Milos and Santorini – geodynamic implications. *Earth and Planetary Science Letters*, vol. **80**, no. 1-2; 41 – 54.

Briqueu, L. & Lancelot, J.R. 1979. Rb-Sr systematics and crustal contamination models for calc-alkaline igneous rocks. *Earth and Planetary Science Letters*, vol. **43**; 385 – 396.

Carlson, R.W. 1995. Isotopic inferences on the chemical structure of the mantle. *Journal of Geodynamics*, vol. **20**, no. 4; 365 – 386.

Christova, C. & Nikolova, S.B. 1993. The Aegean region: deep structures and seismological properties. *Geophysical Journal International*, vol. **115**; 635 – 653.

Christova, C. & Nikolova, S.B. 1998. New results on the contemporary plate tectonics in the Aegean region from seismological investigations. *Physics and Chemistry of the Earth*, vol. **23**, no. 7-8; 785 – 798.

Churikova, T., Dorendorf, F. & Woerner, G. 2001. Sources and fluids in the mantle wedge below Kamchatka, evidence from across-arc geochemical variation. *Journal of Petrology*, vol. **42**, no. 8; 1567 – 1593.

Cox, K.G., Bell, J.D. & Pankhurst, R.J. 1979. *The interpretation of igneous rocks*. George Allen & Unwin, London; 450 p.

Crawford, A.J., Beccaluva, L., Serrie, G. & Dostal, J. 1986. Petrology, geochemistry and tectonic implications of volcanics dredged from the intersection of the Yap and Mariana trenches. *Earth and Planetary Science Letters*, vol. **80**, no. 3-4; 265 – 280.

Davidson, J.P. 1985. Mechanism of contamination in Lesser Antilles island arc magmas from radiogenic and oxygen isotope relationships. *Earth and Planetary Science Letters*, vol. **72**, 2-3; 163 – 174.

Davidson, J.P., McMillan, N.J., Moorbath, S., Worner, G. Harmon, R.S. & Lopez-Escobar, L. 1990. The Nevados de Payachata volcanic region (18S, 69W, N. Chile); II. Evidence for widespread crustal involvement in Andean magmatism. *Contributions to Mineralogy and Petrology*, vol. **105**, no. 4; 412-432.

Davis, E.N. & Bastas, C. 1978. Petrology and geochemistry of the metamorphic system of Santorini. In: Doumas, C. (ed.): *Thera and the Aegean World I.* Thera Foundation, London; 61 – 80.

De Astis, G., Peccerillo, A., Kempton, P.D., La Volpe, L. & Wu, T.W. 2000. Transition from calc-alkaline to potassium-rich magmatism in subduction environments: geochemical and Sr, Nd, Pb isotopic constraints from the island of Vulcano (Aeolian Arc). *Contributions to Mineralogy and Petrology*, vol. **139**; 684 – 703.

De Silva S.L., Davidson, J.P., Croudace, I.W. & Escobar, A. 1993. Volcanological and petrological evolution of Volcan Tata Sabaya, SW Bolivia. *Journal of Volcanology and Geothermal Research*, vol. **55**, no. 3-4; 305 – 335.

DeBari, S.M. & Sleep, N.H. 1991. High-Mg, low-Al bulk composition of the Talkeetna island arc, Alaska – implications for primary magmas and the nature of arc crust. *Geological Society of America Bulletin*, vol. **103**; 37 – 47.

Del Moro, A., Gioncada, A., Pinarelli, L., Sbrana, A. & Joron, J.L. 1998. Sr, Nd, and Pb isotope evidence for open system evolution at Volcano, Aeolian Arc, Italy. *Lithos*, vol. **43**, no. 2; 81 – 106.

DePaolo, D.J. 1981. Trace elements and isotopic effects of combined wallrock assimilation and fractional crystallization. *Earth and Planetary Science Letters*, vol. **53**; 189 – 202.

DePaolo, D.J. & Wasserburg, G.J. 1976. Nd isotopic variations and petrogenetic models. *Geophysical Research Letters*, vol. **3**; 249 – 252.

Dickin, A.P. 1995. *Radiogenic isotope geology*. Cambridge University Press, Cambridge; 490 p.

Dietrich, V., Emmermann, R., Oberhaensli, R. & Puchelt, H. 1978. Geochemistry of basaltic and gabbroic rocks from the West Mariana Basin and the Mariana Trench. *Earth and Planetary Science Letters*, vol. **39**, no. 1; 127 – 144.

Doutsos, T. & Kokkalas, S. 2001. Stress and deformation patterns in the Aegean region. *Journal of Structural Geology*, vol. **23**; 455 – 472.

Druitt, T.H., Edwards, L., Mellors, R.M, Pyle, D.M., Sparks, R.S.J, Lanphere, M., Davies, M. & Barriero, B. 1999. *Santorini Volcano*. Geological Society Memoir no. 19, Geological Society, London; 165 p.

Druitt, T.H. & Francaviglia, V. 1990. An ancient caldera cliff line at Phira, and its significance for the topography and geology of Pre-Minoan Santorini. In: Hardy, D.A. (ed.): *Thera and the Aegean World III*, vol. **2**. Thera Foundation, London; 362 – 369.

Druitt, T.H., Mellors, R.A., Pyle, D.M. & Sparks, R.S.J. 1989. Explosive volcanism on Santorini, Greece. *Geological Magazine*, vol. **126**, no. 2; 95 – 126.

Eleftheriadis, G., Christofides, G. Esson, J. Soldatos, T. & Koroneos, A. 1998. Petrology and geochemistry of the volcanic dykes from the Santorini caldera walls. In: Casale, R., Fytikas, M., Sigvaldasson, G. and Vougioukalakis, G. (eds.): *Volcanic Risk – The European laboratory volcanoes, proceedings of the second workshop Santorini, Greece. –EUR 18161*; 137 – 156.

Ellam, R.M. & Hawkesworth, C.J. 1988. Elemental and isotope variations in subduction related basalts: evidence for a three component model. *Contributions to Mineralogy and Petrology*, vol. **98**; 72 – 80.

Ellam, R.M., Menzies, M.A., Hawkesworth, C.J., Leeman, W.P., Rosi, M. & Serri, G. 1988. The transition from calc-alkaline to potassic orogenic magmatism in the Aeolian Islands, Southern Italy. *Bulletin of Volcanology*, vol. **50**, no. 6; 386 – 398.

Elliott, T., Plank, T., Zindler, A., White, W. & Bourdon, B. 1997. Element transport from slab to volcanic front at the Mariana Arc. *Journal of Geophysical Research*, vol. **102 B**, no. 7; 14991 – 15019.

Ergün, M. & Özel, E. 1995. Structural relationship between the Sea of Marmara Basin and the North Anatolian Fault Zone. *Terra Nova*, vol. **7**; 278 – 288.

Eriksen, U., Friedrich, W.L., Buchardt, B., Tauber, H. & Thomsen, M.S. 1990. The Stronghyle caldera: geological, palaeontological and stable isotope evidence from radiocarbon dated stromatolites from Santorini. In: Hardy, D.A. (ed.): *Thera and the Aegean World III*, vol. **2**. Thera Foundation, London; 139 – 150.

Faccenna, C., Funiciello, F., Giardini, D. & Lucente, P. 2001. Episodic back-arc extension during restricted mantle convection in the Central Mediterranean. *Earth and Planetary Science Letters*, vol. **187**; 105 – 116.

Faure, G. 1986. *Principles of isotope geology*. John Wiley & Sons, New York; 589 p.

Forneris, J.F. & Holloway, J.R. 2003. Phase equilibria in subducting basaltic crust: implications for $H_2O$ release from the slab. *Earth and Planetary Science Letters*, vol. **214**; 187 – 201.

Fouqué, F.A. 1998. *Santorini and its eruptions*. Translated and annotated by McBirney, A.R. Foundation of natural history. Johns Hopkins, University Press, Baltimore. 495 p.

Francalanci, L., Taylor, S.R., McCulloch, M.T. & Woodhead, J.D. 1993. Geochemical and isotopic variations in the calc-alkaline rocks of Aeolian arc, southern Tyrrhenian Sea, Italy; constraints on magma genesis. *Contributions to Mineralogy and Petrology*, vol. **113**, no. 3; 300 – 313.

Friedrich, W.L. 2000. *Fire in the sea. Volcanism and the natural history of Santorini*. Cambridge University Press, Cambridge; 256 p.

Fytikas, M., Innocenti, F., Manetti, P., Mazzuoli, R., Peccerillo, A. & Villari, L. 1984. Tertiary to Quaternary evolution of volcanism in the Aegean region. In: Dixon, J.E. & Robertson, A.H.F. (eds.): *The geological evolution of the Eastern Mediterranean.* Geological Society Special Publication No. 17, London; 687–699.

Fytikas, M., Kolios, N. & Vougioukalakis, G. 1990. Post-Minoan volcanic activity of the Santorini volcano. Volcanic hazard and risk, forecasting possibilities. In: Hardy, D.A. (ed.): *Thera and the Aegean World III*, vol. **2**. Thera Foundation, London; 183–198.

Garfunkel, Z. 1998. Constrains on the origin and history of the Eastern Mediterranean basin. *Tectonophysics*, vol. **298**; 5–35.

Gautier, P., Brun, J-P., Moriceau, R., Sokoutis, D., Martinod, J. & Jolivet, L. 1999. Timing, kinematics and cause of Aegean extension: a scenario based on a comparison with simple analogue experiments. *Tectonophysics*, vol. **315**; 31–72.

Gertisser, R. & Keller, R. 2000. From basalt to dacite: origin and evolution of the calc-alkaline series of Salina, Aeolian Arc, Italy. *Contributions to Mineralogy and Petrology*, vol. **139**; 607–626.

Gill, J. 1981. *Orogenic andesites and plate tectonics.* Springer-Verlag, Berlin-Heidelberg; 390 p.

Gorton, M.P. & Schandl, E.S. 2000. From continents to island arcs: a geochemical index of tectonic setting for arc-related and within-plate felsic to intermediate volcanic rocks. *The Canadian Mineralogist*, vol. **38**; 1065–1073.

Green, T.H. 1980. Island arc and continent-building magmatism – a review of petrogenetic models based on experimental petrology and geochemistry. *Tectonophysics*, vol. **63**; 367–385.

Grove, T.L. & Baker, M.B. 1984. Phase equilibrium controls on the tholeiitic versus calc-alkaline differentiation trends. *Journal of Geophysical Research*, vol. **89**, no. B5; 3253–3274.

Grove, T.L. & Kinzler, R.J. 1986. Petrogenesis of andesites. *Annual Review of Earth and Planetary Science*, vol. **14**; 417–454.

Gust, D.A., Arculus, R.J. & Kersting, A.B. 1997. Aspects of magma sources and processes in the Honshu Arc. *The Canadian Mineralogist*, vol. **35**, no. 2; 347–365.

Hammer, C.U., Clausen, H.B., Friedrich, W.L. & Tauber, H. 1987. The Minoan eruption of Santorini in Greece dated to 1645 BC? *Nature*, vol. **328**, no. 6130; 517–519.

Hansen, A. 1997. *Megalo Vouno volcano in the northern part of Santorini.* Kandidatafhandling, Københavns Universitet, Danmark; 117 p.

Hart, S.R. 1984. A large-scale isotope anomaly in the southern hemisphere mantle. *Nature*, vol. **309**; 753–757.

Hawkesworth, C.J., Gallagher, K. Hergt, J.M. & McDermott, F. 1993. Mantle and slab contributions in arc magmas. *Annual Review of Earth and Planetary Sciences*, vol . **21**; 175–204.

Hawkesworth, C.J., Turner, S.P., McDermott, F., Peate, D.W. & van Calsteren, P. 1997. U-Th isotopes in arc magmas: Implications for element transfer from the subducted crust. *Science*, vol. **276**; 551–555.

Heiken, G. & McCoy, F. 1984. Caldera development during the Minoan eruption, Thira, Cyclades, Greece. *Journal of Geophysical Research*, vol. **89**, no. b10; 8441–8462.

Herd, R.A. & Pinkerton, H. 1997. Bubble coalescence in basaltic lava: Its impact on the evolution of bubble populations. *Journal of Volcanology and Geothermal Research*, vol. **75**, no. 1-2; 137–157.

Hofmann, A.W. & White, W.M. 1982. Mantle plumes from ancient oceanic crust. *Earth and Planetary Science Letters*, vol. **57**, no. 2; 421–436.

Hole, M.J., Saunders, A.D., Marriner, G.F. & Tarney, J. 1984. Subduction of pelagic sediments; implications for the origin of Ce-anomalous basalts from the Mariana Islands. *Journal of the Geological Society of London*, vol. **141**, no. 3. 453 - 472.

Holm, P.M. 1997. *Beregning og anvendelse af CIPW-normen*. Geologisk Institut, København; 11 p.

Huijsmans, J.P.P. 1985. Calc-alkaline lavas from the volcanic complex of Santorini, Aegean Sea, Greece; a petrological, geochemical and stratigraphic study. *Geologica Ultraiectina*, vol. **41**; 316 p.

Huijsmans, J.P.P. & Barton, M. 1989. Polybaric geochemical evolution of two shield volcanoes from Santorini, Aegean Sea, Greece: evidence for zoned magma chambers from cyclic compositional variations. *Journal of Petrology*, vol. **30**, no. 3; 583 625.

Huijsmans, J.P.P. & Barton, M. 1990. New stratigraphic and geochemical data for the Megalo Vouno complex: a dominating volcanic landform in Minoan Times. In: Hardy, D.A. (ed.): *Thera and the Aegean World III*, vol. **2**. Thera Foundation, London; 433 441.

Huijsmans, J.P.P., Barton, M. & Salters, V.J.M. 1988. Geochemistry and evolution of the calc-alkaline volcanic complex of Santorini, Aegean Sea, Greece. *Journal of Volcanology and Geothermal Research*, vol. **34**; 283 306.

Ikeda, Y. 1998. Geochemistry of Miocene back-arc basin basalts from Northeast Hokkaido, Japan. *Journal of the Geological Society of Japan*, vol. **104**, no. 2; 99 106.

Irvine, T.N. & Baragar, W.R.A. 1971. A guide to the chemical classification of the common volcanic rocks. *Canadian Journal of Earth Sciences*, vol. **8**; 523 548.

Ishizuka, O., Taylor, R.N., Milton, A. & Nesbitt, R.W. 2003. Fluid-mantle interaction in an intra-oceanic arc: constraints from high-precision Pb isotopes. *Earth and Planetary Science Letters*, vol. **211**; 221 236.

Jackson, J. 1994. Active tectonics of the Aegean region. *Annual Reviews of Earth and Planetary Sciences*, vol. **22**; 239 271.

Jochum, K.P., Pfänder, J., Snow, J.E. & Hofmann, A.W. 1997. Nb/Ta in mantle and crust. *EOS (Transactions, American Geophysical Union)*, vol. **78**; 804.

Jolivet, L. & Patriat, M. 1999. Ductile extension and the formation of the Aegean Sea. In: Durand, B., Jolivet, L., Horváth, F. & Séranne, M. (eds.): *The Mediterranean Basins: Tertiary extension within the Alpine Orogen*. Geological Society Special Publication No. 156, London; 427 456.

Kahle, H-G., Straub, C., Reilinger, R., McClusky, S., King, R., Hurst, K., Veis, G., Kastens, K. & Cross, P. 1998. The strain rate fields in the eastern Mediterranean region, estimated by repeated GPS measurements. *Tectonophysics*, vol. **294**; 237 252.

Kann, K. 2004. *Et petrologisk, geokemisk og vulkanologisk studie af Thirassia vulkankomplekset, Santorini*. Kandidatafhandling, Københavns Universitet, Danmark; 110 p.

Kann, K. & Petersen, A.D.J. 2003. Santorinis eksplosive historie. *Varv*, no. **2**; 9 23.

Kastens, K.A. 1991. Rate of outward growth of the Mediterranean Ridge accretionary complex. *Tectonophysics*, vol. **199**, no. 1; 25 50.

Keller, J. 1981. Quaternary tephrochronology in the Mediterranean region. In: Self, S. & Sparks, R.S.J. (eds.): *Tephra studies; proceedings of the NATO Advanced Study Institute "Tephra studies as a tool in Quaternary research*"; 227 244.

Keller, J., Rehren, T.H. & Stadlbauer, E. 1990. Explosive volcanism in the Hellenic Arc: a summary and review. In: Hardy, D.A. (ed.): *Thera and the Aegean World III*, vol. **2**. Thera Foundation, London; 13 26.

Kelsey, C.H. 1965. Calculation of the C.I.P.W. norm. *Mineralogical Magazine*, vol. **34**; 276 282.

Kissel, C. & Laj, C. 1988. The Tertiary geodynamical evolution of the Aegean arc: A paleomagnetic reconstruction. *Tectonophysics*, vol. **146**; 183–201.

Kraemer, B. 1999. Eine geochemische Traverse quer zum mittelmiozänen magmatischen Bogen im südlichen Bereich der Zentralen Vulkanischen Zone der Anden (ZVZ, 25°-26°30 S; 67°30 -69°W). *Berliner Geowissenschaftliche Abhandlungen,* **A 200**, Dissertation am Fachbereich Geowissenschaften, Freie Universität Berlin; 174 p.

Kraemer, B., Adelmann, D., Alten, M., Schnurr, W., Erpenstein, K., Kiefer, E., van den Boegaard, P. & Görler, K. 1999. Incorporation of the Paleogene foreland into the Neogene Puna plateau: The Salar de Antofalla area, NW Argentina. *Journal of South American Earth Sciences*, vol. **12**; 157–182.

Kystol, J. & Larsen, L. M. 1999. Analytical procedures in the rock geochemical laboratory of the Geological Survey of Denmark and Greenland. *Geology of Greenland Survey Bulletin*, vol. **184**; 59–62.

Langmuir, C.H., Vocke, Jr., R.D., Hanson, G.N. & Hart, S.R. 1978. A General mixing equation with applications to Icelandic basalts. *Earth and Planetary Science Letters*, vol. **37**; 380–392.

Le Bas, M.J., Le Maitre, R.W., Streckeisen, A. & Zanettin, B.A. 1986. Chemical classification of volcanic rocks based on the total alkali-silica diagram. *Journal of Petrology*, vol. **27**, no. 3; 745–750.

Le Maitre, R.W., Bateman, P., Dudek, A., Keller, J., Lemeyre, J., Le Bas, M.J., Sabine, P.A., Schmid, R. Sørensen, H., Streckeisen, A., Wooley, A.R. & Zanettin, B. 1989. *A classification of igneous rocks and glossary of terms.* Blackwell Scientific; 193 p.

Le Maitre, R.W., Streckeisen, A., Zanettin, B., Le Bas, M. J., Bonin, B., Bateman, P., Bellieni, G., Dudek, A., Efremova, S., Keller, J., Lameyre, J., Sabine, P. A., Schmid, R., Sørensen, H. & Woolley, A. R. 2002. *Igneous rocks: a classification and glossary of terms: recommendations of the International Union of Geological Science Subcommission on the systematics of igneous rocks. Second edition.* University Press, Cambridge; 236 p.

Le Pichon, X. & Angelier, J. 1981. The Aegean Sea. *Philosophical Transactions of the Royal Society of London*, vol. **A 300**; 357–372.

Limonov, A.F., Woodside, J.M., Cita, M.B. & Ivanov, M.K. 1996. The Mediterranean Ridge and related mud diapirism: a background. *Marine Geology*, vol. **132**; 7–19.

Lister, G.S., Banga, G. & Feenstra, A. 1984. Metamorphic core complex of Cordilleran type in the Cyclades, Aegean Sea, Greece. *Geology*, vol. **12**; 221–225.

Ludwig, K.R. 2003. *User's manual for Isoplot 3.00: a geochronological toolkit for Microsoft Excel*. Berkeley Geochronology Center Special Publication No. **4**, Berkeley; 59 p.

Macdonald, R., Hawkesworth, C.J. & Heath, E. 2000. The Lesser Antilles volcanic chain; a study in arc magmatism. *Earth-Science Reviews*, vol. **49**, no. 1-4; 1–76.

MacKenzie, W.S. & Guilford, C. 1994. *Atlas of rock-forming minerals in thin section.* Longman Scientific & Technical, Essex; 98 p.

Makris, J. 1978. The crust and upper mantle of the Aegean region from deep seismic soundings. *Tectonophysics*, vol. **46**; 269–284.

Makropoulos, K.C. & Burton, P.W. 1984. Greek tectonics and seismicity. *Tectonophysics*, vol. **106**; 275–304.

Mann, A.C. 1983. Trace element geochemistry of high alumina basalt–andesite–dacite–rhyodacite lavas of the Main Volcanic Series of Santorini Volcano, Greece. *Contributions to Mineralogy and Petrology*, vol. **84**, no. 1; 43–57.

Martin, H. 1986. Effect of steeper Archean geothermal gradient on geochemistry of subduction-zone magmas. *Geology*, vol. **14**; 753 – 756.

McCoy, F.W. & Heiken, G. 2000. Tsunami generated by the Late Bronze Age eruption of Thera (Santorini), Greece. *Pure and Applied Geophysics*, vol. **157**; 1227 – 1256.

McCulloch, M.T. & Gamble, A.J. 1991. Geochemical and geodynamical constraints on subducton zone magmatism. *Earth and Planetary Science Letters*, vol. **102**, no. 3-4; 358 – 374.

McDonough, W.F. & Sun, S.S. 1995. The composition of the Earth. *Chemical Geology*, vol. **120**; 223 – 253.

McKenzie, D.P. 1970. Plate tectonics of the Mediterranean region. *Nature*, vol. **226**; 239 – 243.

McKenzie, D.P. 1978. Active tectonics of the Alpine-Himalayan belt; the Aegean Sea and surrounding regions. *Geophysical Journal of the Royal Astronomical Society*, vol. **55**, no. 1; 217 – 254.

Mellors, R.A. & Sparks, R.S.J. 1991. Spatter-rich pyroclastic flow deposits on Santorini, Greece. *Bulletin of Volcanology*, vol. **53**, no. 5; 327 – 342.

Mensing, T.M., Faure, G., Jones, L.M., Bowman, J.R. & Hoefs, J. 1984. Petrogenesis of the Kirkpatrick Basalt, Solo Nunatak, Northern Victoria Land, Antarctica, based on isotopic compositions of strontium, oxygen and sulfur. *Contributions to Mineralogy and Petrology*, vol. **87**, 101 – 108.

Mercier, J.L. 1981. Extensional – compressional tectonics associated with the Aegean Arc: Comparison with the Andean Cordillera of south Peru – north Bolivia. *Philosophical Transactions of the Royal Society of London*, vol. **A 300**; 337 – 355.

Middlemost, E.A.K. 1989. Iron oxidation ratios, norms and the classification of volcanic rocks. *Chemical Geology*, vol. **77**, no. 1; 19 – 26.

Mitropoulos, P. & Tarney, J. 1992. Mineral composition variation in the Aegean Island Arc. *Journal of Volcanology and Geothermal Research*, vol. **51**; no. 4; 283 – 303.

Mitropoulos, P., Tarney, J., Saunders, A.D. & Marsh, N.G. 1987. Petrogenesis of Cenozoic volcanic rocks from the Aegean Island Arc. *Journal of Volcanology and Geothermal Research*, vol. **32**; 177 – 193.

Miyashiro, A. 1974. Volcanic rock series in island arcs and active continental margins. *American Journal of Science*, vol. **274**; 321 – 355.

Morris, A. 2000. Magnetic fabric and palaeomagnetic analyses of the Plio-Quaternary calc-alkaline series of Aegina Island, South Aegean volcanic arc, Greece. *Earth and Planetary Science Letters*, vol. **176**; 91 – 105.

Morris, J.D. & Hart, S.R. 1983. Isotopic and incompatible element contraints on the genesis of island arc volcanics from Cold Bay and Amak Island, Aleutians, and implications for mantle structure. *Geochimica et Cosmochimica Acta*, vol. **47**, no. 11; 2015 – 2030.

Neumann, E.-R., Wulff-Pedersen, E., Simonsen, S.L., Pearson, N.J., Mart, J. & Mitjavila, J. 1999. Evidence for fractional crystallization of periodically refilled magma chambers in Tenerife, Canary Islands. *Journal of Petrology*, vol. **40**, no. 7; 1089 – 1123.

Nicholls, I.A. 1971. Petrology of Santorini volcano, Cyclades, Greece. *Journal of Petrology*, vol. **12**; 67 – 119.

Papadopoulos, G.A., Kondopoulou, D.P., Leventakis, G.A. & Pavlides, S.B. 1986. Seismotectonics of the Aegean region. *Tectonophysics*, vol. **124**, no. 1-2; 67 – 84.

Papazachos, B.C. 1990. Long- and short-term predictions of volcanic eruptions in Santorini. In: Hardy, D.A. (ed.): *Thera and the Aegean World III*, vol. **2**. Thera Foundation, London; 224 – 228.

Papazachos, B.C. & Comninakis, P.E. 1971. Geophysical and tectonic features of the Aegean Arc. *Journal of Geophysical Research*, vol. **76**, no. 35; 8517 8533.

Papazachos, B.C. & Comninakis, P.E. 1978. Deep structure and tectonics of the eastern Mediterranean. *Tectonophysics*, vol. **46**; 286 296.

Papazachos, B.C., Karakostas, V.G., Papazachos, C.B. & Scordilis, E.M. 2000. The geometry of the Wadati-Benioff zone and lithospheric kinematics in the Hellenic Arc. *Tectonophysics*, vol. **319**; 275 300.

Papazachos, B.C. & Panagiotopoulos. 1993. Normal faults associated with volcanic activity and deep rupture zones in the southern Aegean volcanic arc. *Tectonophysics*, vol. **220**; 301 308.

Pe, G.G. & Gledhill, A. 1975. Strontium isotope ratios in volcanic rocks from the south-eastern part of the Hellenic arc. *Lithos*, vol. **8**; 209 214.

Peacock, S.M. 1993. Large-scale hydration of the lithosphere above subducting slabs. *Chemical Geology*, vol. **108**; 49 59.

Peacock, S.M. 2000. Thermal structure and metamorpic evolution of subducting slabs. http://www.margins.wustl.edu/Eugene_PDF/SubFac_abstract_Peacock.pdf, October 21st 2004; 1 9.

Pearce, J.A. 1982. Trace element characteristics of lavas from destructive plate boundaries. In: Thorpe R.S. (ed.), *Andesites; orogenic andesites and related rocks*. Wiley, Chichester; 525 548.

Pearce, J.A. 1983. Role of the sub-continental lithosphere in magma genesis at active continental margins. In: Hawkesworth, C.J. & Norry M.J. (eds.): *Continental basalts and mantle xenoliths*. Shiva, Nantwich; 230 249.

Peccerillo, R. & Taylor, S.R. 1976. Geochemistry of Eocene calc-alkaline volcanic rocks from the Kastamonu area, northern Turkey. *Contributions to Mineralogy and Petrology*, vol. **58**; 63 81.

Peccerillo, A. & Wu, T.W. 1992. Evolution of calc-alkaline magmas in continental arc volcanoes; evidence from Alicudi, Aeolian Arc (southern Tyrrhenian Sea, Italy). *Journal of Petrology*, vol. **33**, no. 6; 1295 1315.

Pe-Piper, G. & Piper, D.J.W. 2002. The igneous rocks of Greece The anatomy of an orogen. In: Bender, F., Jacobshagen, V. & Lüttig, G. (eds.): *Beiträge zur regionalen geologie der Erde*, vol. **30**, Gebrüder Borntraeger, Berlin Stuttgart; 573 p.

Perfit, M.R., Gust, D.A., Bence, A.E., Arculus, R.J. & Taylor, S.R. 1980. Chemical characteristics of island-arc basalts: implications for mantle sources. *Chemical Geology*, vol. **30**, no. 3; 227 256.

Perissoratis, C. 1995. The Santorini volcanic complex and its relation to the stratigraphy and structure of the Aegean arc, Greece. *Marine Geology*, vol. **128**; 37 58.

Pichler, H. & Friedrich, W.L. 1976. Radiocarbon dates of Santorini volcanics. *Nature*, vol. **262**; 373 374.

Pichler, H. & Friedrich, W.L. 1980. Mechanism of the Minoan eruption of Santorini. In: Doumas, C. (ed.): *Thera and the Aegean World II*. The Thera Foundation, London; 15 30.

Pichler, H. & Kussmaul, S. 1980. Comments on the geological map of the Santorini islands. In: Doumas, C. (ed.): *Thera and the Aegean World II*. The Thera Foundation, London; 413 427.

Plank, T. & Langmuir, C.H. 1998. The chemical composition of subducting sediment and its consequences for the crust and mantle. *Chemical Geology*, vol. **145**, no. 3-4; 325 394.

Prouteau, G., Maury, R.C., Sajona, F.G., Cotton, J. & Joron, J-L. 2000. Behavior of niobium, tantalum and other high field strength elements in adakites and related lavas from the Philippines. *The Island Arc*, vol. **9**; 487 498.

Puchelt, H., Hubberten, H.-W. & Stellrecht, R. 1990. The geochemistry of the radial dykes of the Santorini caldera and its implications. In: Hardy, D.A. (ed.): *Thera and the Aegean World III*, vol. **2**. Thera Foundation, London; 229 236.

Pyle, D.M. 1990. New estimates for the volume of the Minoan eruption. In: Hardy, D.A. (ed.): *Thera and the Aegean World III*, vol. **2**. Thera Foundation, London; 113 121.

Pyle, D.M. 1997. The global impact of the Minoan eruption of Santorini, Greece. *Environmental Geology*, vol. **30**, no. 1/2; 59 61.

Rickwood, P.C. 1989. Boundary lines within petrologic diagrams which use oxides of major and minor elements. *Lithos*, vol. **22**, no. 4; 247 263.

Roberts, M.P. & Clemens, J.D. 1995. Feasibility of AFC models for the petrogenesis of calc-alkaline magma series. *Contributions to Mineralogy and Petrology*, vol. **121**, no. 2; 139 147.

Robertson, A.H.F., Dixon, J.E., Brown, S., Collins, A., Morris, A., Pickett, E.A., Sharp, I. & Ustaömer, T. 1996. Alternative tectonic models for the Late Palaeozoic-Early Tertiary development of Tethys in the Eastern Mediterranean region. In: Morris, A. & Tarling, D.H. (eds.): *Palaeomagnetism and tectonics of the Mediterranean region*. Geological Society Special Publication No. 105, London; 239 263.

Robertson, A.H.F. & Grasso, M. 1995. Overview of the Late Tertiary Recent tectonic and palaeo-environmental development of the Mediterranean region. *Terra Nova*, vol. **7**; 114 127.

Rollinson, H. 1993. *Using geochemical data: evaluation, presentation, interpretation*. Longman Scientific and Technical, UK; 352 p.

Rosi, M., Bertagnini, A. & Landi, P. 2000. Onset of the persistent activity at Stromboli Volcano (Italy). *Bulletin of Volcanology*, vol. **62**, no. 4-5; 294 300.

Rudnick, R.L. & Fountain, D.M. 1995. Nature and composition of the continental crust: a lower crustal perspective. *Reviews of Geophysics*, vol. **33**, no. 3; 267 309.

Sachpazi, M., Kontoes, C., Voulgaris, N., Laigle, M., Vougioukalakis, G., Sikioti, O., Stavrakakis, G., Baskoutas, J., Kalogeras, J. & Lepine, J.C. 2002. Seismological and SAR signature of unrest at Nisyros caldera, Greece. *Journal of Volcanology and Geothermal Research*, vol. **116**; 19 33.

Saunders, A.D., Tarney, J. & Weaver, S.D. 1980. Transverse geochemical variations across the Antarctic Peninsula: implications for the genesis of calcalkaline magmas. *Earth and Planetary Science Letters*, vol. **46**; 344 360.

Scambelluri, M. & Philippot, P. 2001. Deep fluids in subduction zones. *Lithos*, vol. **55**, no. 1-4; 213 227.

Schmidt, M.W., Dardon, A., Ghazot, G. & Vannucci, R. 2004. The dependence of Nb and Ta rutile-melt partitioning on melt composition and Nb/Ta fractionation during subduction preocesses. *Earth and Planetary Science Letters*, vol. **226**; 415 432.

Schmidt, M.W. & Poli, S. 1998. Experimentally based water budgets for dehydrating slabs and consequences for arc magma generation. *Earth and Planetary Science Letters*, vol. **163**; 361 379.

Seward, D., Wagner, G. A. & Pichler, H. 1980. Fission track ages of Santorini volcanics. In: Doumas, C. (ed.): *Thera and the Aegean World II*. The Thera Foundation, London; 101 108.

Shervais, J.W. 1982. Ti-V plot and the petrogenesis of modern and ophiolitic lavas. *Earth and Planetary science Letters*, vol. **59**; 101 118.

Sisson, T.W. & Grove, T.L. 1993. Experimental investigations of the role of $H_2O$ in calc-alkaline differentiation and subduction zone magmatism. *Contributions to Mineralogy and Petrology*, vol. **113**, no. 2; 143 166.

Skarpelis, N., Kyriakopoulos, K. & Villa, I. 1992. Occurence and $^{40}Ar/^{39}Ar$ dating of a granite in Thera (Santorini, Greece). *Geologische Rundschau*, vol. **81**, no. 3; 729 – 735.

Skarpelis, N. & Liati, A. 1990. The prevolcanic basement of Thera at Athinios: metamorphism, plutonism and mineralization. In: Hardy, D.A. (ed.): *Thera and the Aegean World III*, vol. **2**. Thera Foundation, London; 172 – 182.

Spakman, W., van der Lee, S. & van der Hilst, R. 1993. Travel-time tomography of the European-Mediterranean mantle down to 1400 km. *Physics of the Earth and Planetary Interiors*, vol. **79**; 3 – 74.

Spakman, W., Wortel, M.J.R. & Vlaar, N.J. 1988. The Hellenic subduction zone: a tomographic image and its geodynamic implications. *Geophysical Research Letters*, vol. **15**, no. 1; 60 – 63.

Stampfli, G.M. & Borel, G.D. 2002. A plate tectonic model for the Paleozoic and Mesozoic constrained by dynamic plate boundaries and restored synthetic oceanic isochrons. *Earth and Planetary Science Letters*, vol. **196**; 17 – 33.

Stanley, D.J. & Sheng, H. 1986. Volcanic shards from Santorini (upper Minoan ash) in the Nile Delta, Egypt. *Nature*, vol. **320**, no. 6064; 733 – 735.

Stern, C.R., Frey, F.A., Futa, K., Zartman, R.E., Peng, Z. & Kyser, T.K. 1990. Trace element and Sr, Nd, Pb and O isotopic composition of Pliocene and Quaternary alkali basalts of the Patagonian Plateau lavas of southernmost South America. *Contributions to Mineralogy and Petrology*, vol. **104**, no. 3; 294-308.

Stolz, A.J., Jochum, K.P., Spettel, B. & Hofmann, A.W. 1996. Fluid- and melt-related enrichment in the subarc mantle: evidence from Nb/Ta variations in island-arc basalts. *Geology*, vol. **24**, no. 7; 587 – 590.

Sun, S.S. & McDonough, W.F. 1989. Chemical and isotopic systematics of oceanic basalts: implications for mantle composition and processes. In: Saunders, A.D. & Norry, M.J. (eds.): *Magmatism in the Ocean Basins*, Geologocal Society Special Publication No. **42**; 313 – 345.

Takagi, T., Orihashi, Y., Naito, K. & Watanabe, Y. 1999. Petrology of a mantle-derived rhyolite Hokkaido, Japan. *Chemical Geology*, vol. **160**, no. 4; 425 – 445.

Taylor, S.R. & McLennan, S.M. 1985. *The continental crust: its composition and evolution*. Blackwell Scientific Publications, Oxford; 312 p.

Taylor, S.R. & McLennan, S.M. 1995. The geochemical evolution of the continental crust. *Reviews of Geophysics*, vol. **33**, no. 2; 241 – 265.

Taylor, R.N. & Nesbitt, R.W. 1998. Isotopic characteristics of subduction fluids in an intra-oceanic setting, Izu-Bonin Arc, Japan. *Earth and Planetary Science Letters*, vol. **164**, no. 1-2; 79 – 98.

Ten Veen, J.H. & Meijer, P.T. 1998. Late Miocene to recent tectonic evolution of Crete (Greece): Geological observations and model analysis. *Tectonophysics*, vol. **298**; 191 – 208.

Thirlwall, M.F., Graham, A.M., Arculus, R.J., Harmon, R.S. & Macpherson, C.G. 1996. Resolution of the effects of crustal assimilation, sediment subduction, and fluid transport in island arc magmas: Pb-Sr-Nd-O isotope geochemistry of Grenada, Lesser Antilles. *Geochimica et Cosmochimica Acta*, vol. **60**, no. 23; 4785 – 4810.

Thirlwall, M.F., Smith, T.E., Graham, A.M., Theodorou, N, Hollings, P., Davidson, J.P. & Arculus, R.J. 1994. High field strength element anomalies in arc lavas: source or process? *Journal of Petrology*, vol. **35**, no. 3; 819 – 838.

Todt, W., Chauvel, C., Arndt, N.T. & Hofmann, A.W. 1984. Pb isotopic composition and age of Proterozoic komatiites and related rocks from Canada. AGU 1984 fall meeting. *Eos, Transactions, American Geophysical Union*, vol. **65**; 1129 p.

Ujike, O. & Stix, J. 2000. Geochemistry and origins of Ueno and On-take basaltic to andesitic rocks (<3 Ma) produced by distinct contributions of subduction components, central Japan. *Journal of Volcanology and Geothermal Research*, vol. **95**, no. 1-4; 49 64.

Vanek, J., Hanus, V., Christova, C. & Simeonova, S. 1987. Morphology of the Wadati-Benioff zone in the Hellenic arc. *Journal of Geodynamics*, vol. **8**, no. 1; 79 93.

van Keken, P.E. 2003. The structure and dynamics of the mantle wedge. *Earth and Planetary Science Letters*, vol. **215**; 323 338.

Vitaliano, C.J., Taylor, S.R., Norman, M.D., McCulloch, M.T. & Nicholls, I.A. 1990. Ash layers of the Thera volcanic series: Stratigraphy, petrology and geochemistry. In: Hardy, D.A. (ed.): *Thera and the Aegean World III*, vol. **2**. Thera Foundation, London; 53 78.

Volti, T. K. 1999. Magnetotelluric measurements on the Methana Peninsula (Greece): modelling and interpretation. *Tectonophysics*, vol. **301**; 111 132.

Weyer, S., Münker, C. & Mezger, K. 2003. Nb/Ta, Zr/Hf and REE in the depleted mantle: implications for the differentiation history of the crust-mantle system. *Earth and Planetary Science Letters*, vol. **205**; 309 324.

Weyer, S., Münker, C., Rehkämper, M. & Mezger, K. 2002. Determination of ultra-low Nb, Ta, Zr and Hf concentrations and the chondritic Zr/Hf and Nb/Ta ratios by isotope dilution analyses with multiple collector ICP-MS. *Chemical Geology*, vol. **187**; 295 313.

Wittenbrink, R. 1997. Einfluß der neogenen Krustenentwicklung auf die Genese andiner Magmen im südlichen Teil der CVZ. *Berliner Geowissenschaftliche Abhandlungen*, **A 193**, Dissertation am Fachbereich Geowissenschaften, Freie Universität Berlin; 135 p.

Wood, D.A. 1980. The application of a Th-Hf-Ta diagram to problems of tectonomagmatic classification and to establishing the nature of crustal contamination of basaltic lavas of the British Tertiary volcanic province. *Earth and Planetary Science Letters*, vol. **50**; 11 30.

Woodhead, J.D. 1989. Geochemistry of the Mariana Arc (western Pacific); source composition and processes. *Chemical Geology*, vol. **76**, no. 1-2; 1 24.

Yogodzinski, G.M., Lees, J.M., Churikova, T.G., Dorendorf, F., Wöerner, G. & Volynets, O.N. 2001. Geochemical evidence for the melting of subducting oceanic lithosphere at plate edges. *Nature*, vol. **409**; 500 – 504.

You, C.F., Castillo, P.R., Gieskes, J.M., Chan, L.H. & Spivack, A.J. 1996. Trace element behavior in hydrothermal experiments: Implications for fluid processes at shallow depths in subduction zones. *Earth and Planetary Science Letters*, vol. **140**; 41 52.

Zellmer, G. 1998. *Petrogenetic processes and their time scales beneath Santorini, Aegean Volcanic Arc, Greece*. PhD Thesis, Open University, UK; 270 p.

Zindler, A. & Hart, S. 1986. Chemical geodynamics. *Annual Review of Earth and Planetary Sciences*, vol . **14**; 493 571.